Author:
Vaccari Cardoso, Barbara

Title:
Novel molecular tools to selectively inhibit astrocyte-to-neurone L-lactate signalling

Novel molecular tools to selectively inhibit astrocyte-to-neurone L-lactate signalling

Barbara Vaccari Cardoso

A dissertation submitted to the University of Bristol in accordance with the requirements for award of the degree of Doctor of Philosophy in the Faculty of Life Sciences

School of Physiology, Pharmacology and Neuroscience
Faculty of Life Sciences

August 2019

Word count: 63,640

Abstract

Astrocyte-derived L-lactate (LL) is thought to metabolically support neurones during periods of high activity. LL also has signalling roles in the brain and its release can affect sleep/wake cycle, learning and memory, and cardiorespiratory control. We have previously shown that astrocyte-derived LL induces noradrenaline release in the locus coeruleus *in vitro*, and that this action was abolished by the enantiomer D-lactate. Moreover, LL application in the brainstem or pons *in vivo* increased sympathetic nerve activity, or caused cortical desynchronization, respectively. A new route for LL release in the brain mediated by connexin hemichannels has been described, raising the possibility that these conduits actively participate in LL effects in the brain.

During this project, I have developed a range of molecular tools to selectively limit astrocyte-derived LL release and actions in the brain, in order to better understand its roles. These vectors induce expression of bacteria-derived enzymes that either reduce the intracellular LL pool by metabolising LL (LL monooxygenase – LMO; LL oxidase – LOX), or interfere with LL -noradrenaline signalling by production of D-lactate (D-lactate dehydrogenase – DLDH). Moreover, a tool to drive astrocyte-selective knock-down of connexin-43 was created in order to investigate hemichannel-mediated LL release from astrocytes.

Functional validation of the novel molecular tools *in vitro* showed that the enzymes of bacterial origin are active when expressed in mammalian cells. Constitutive and forced LL release were reduced in primary dissociated cultured astrocytes as well as in organotypic brainstem slices. Moreover, expression of the DLDH-based molecular tool induced production and release of D-lactate by astrocytes. Evaluation of the impact of the new constructs on noradrenaline release suggested that expression of LOX inhibits LL -induced noradrenaline release from locus coeruleus neurons.

Therefore, these novel tools show promise for future studies into the roles of astrocytic LL in the brain *in vivo*.

Acknowledgements

First, I would like to thank my supervisors Dr Anja Teschemacher and Professor Sergey Kasparov for the opportunity to work in this challenging and innovative project. Their incessant support, guidance and encouragement were crucial for the conclusion of my PhD. I have learnt a lot from them, and it was a privilege to have been their student.

Thanks to my sponsor, the National Council for Scientific and Technological Development (CNPq) of the Ministry of Science, Technology and Innovation of Brazil - Science without Borders programme (Grant number: 206427/2014-0).

My sincere gratitude to Dr Beihui Liu, for her endless support and great expertise that assisted me in this research project, and for always motivating me. I am also very grateful to Dr Valentina Mosienko, who provided a huge support on my laboratory work and for her insightful comments.

I thank Lesley Arberry, for the enormous technical support with the molecular cloning. Thanks also to Dr Ali Seyed Rasooli-Nejad, for helping me with the brain slice culture preparation. I thank Dr Iliana Barrera for running and analysing the Western Blots. Many thanks also to Roba Sofi, for the daily sharing of the ups and downs of a PhD life.

Thanks to Dr Melina Fernandes Figueiredo, for helping me in the beginning of my PhD and the continued friendship. I thank Dr Ana Paula Abdala Sheikh for all the professional mentoring provided.

A very special thanks to Yit, who has made this a way more pleasurable ride. I am grateful to all the support and encouragement, especially in the very end of my PhD. I am also immensely thankful to each of my dear friends that have been part of my life during the past years.

Finally, I would like to express my deepest gratitude to my family. My mom and dad have unconditionally supported and encouraged me to peruse my goals. They have put the greatest efforts towards my education and celebrated each of my achievements. Thanks also to my brother Adu for the excellent example he sets and for all the support he gives. They were very important to me in the pursuit of this PhD and I dedicated this thesis to them.

Declaration

I declare that the work in this dissertation was carried out in accordance with the requirements of the University's *Regulations and Code of Practice for Research Degree Programmes* and that it has not been submitted for any other academic award. Except where indicated by specific reference in the text, the work is the candidate's own work. Work done in collaboration with, or with the assistance of, others, is indicated as such. Any views expressed in the dissertation are those of the author.

SIGNED:..... DATE:.....

Table of Contents

List of Figures

List of Tables

List of Abstracts

B Vaccari Cardoso, V Mosienko, AV Gourine, S Kasparov, AG Teschemacher. Novel viral vector tools selectively inhibit astrocytic L-lactate release. Poster communication in: **XIV European Meeting on Glial Cells in Health and Disease**, 2019, Porto.

B Vaccari Cardoso, V Mosienko, S Kasparov, AG Teschemacher. New molecular tools to selectively inhibit astrocyte-to-neurone L-lactate signalling. Poster communication in: **13th International Conference on Brain Energy Metabolism**, 2018, Valdivia.

S Kasparov, BH Liu, V Mosienko, **B Vaccari Cardoso**, AG Teschemacher. Prosaposin mediates glio- and neuroprotection via GPR37L1 and GPR37 expressed by astrocytes. Poster communication in: **13th International Conference on Brain Energy Metabolism**, 2018, Valdivia.

B Vaccari Cardoso, V Mosienko, BH Liu, S Kasparov, AG Teschemacher. Validation of molecular tools to limit astrocytic L-lactate release and action. Poster communication in: **KAUST Research Workshop on Innovative Technologies to Study Brain Energy Metabolism**, 2018, Thuwal.

AG Teschemacher, **B Vaccari Cardoso**, V Mosienko, BH Liu, S Kasparov. Viral vector tools for selective inhibition of lactate release from astrocytes. Oral communication in: **KAUST Research Workshop on Innovative Technologies to Study Brain Energy Metabolism**, 2018, Thuwal.

B Vaccari Cardoso, S Kasparov, AV Gourine, AG Teschemacher. Development of a novel molecular tool to selectively inhibit astrocyte-to-neurone L-lactate signalling. Poster communication in: **XIII European Meeting on Glial Cells in Health and Disease**, 2017, Edinburgh.

List of Publication

Liu, B., Mosienko, V., Vaccari Cardoso, B., Prokudina, D., Huentelman, M., Teschemacher, A. G., & Kasparov, S. (2018). Glio- and neuro-protection by prosaposin is mediated by orphan G-protein coupled receptors GPR37L1 and GPR37. *Glia*, *66*(11), 2414–2426. https://doi.org/10.1002/glia.23480

List of Abbreviations

1,3-BPG: 1,3-biphosphoglycerate
AAV: adeno-associated viral vectors
ANLS: astrocyte-to-neurone LL shuttle
AVV: adenoviral vector

BDNF: brain-derived neurotrophic factor
BSA: bovine serum albumin

CIAP: calf intestine alkaline phosphatase
CMV: Cytomegalovirus
CNiFER: cell-based neurotransmitter fluorescent engineered reporter
CNS: central nervous system
CPE: cytopathic effect
CREB: cAMP response element-binding
Cx43: Connexin 43

DAB: 1,4-dideoxy-1,4-imino-d-arabinitol
DAB: 3,3-Diaminobenzidine
DBH: dopamine β-hydroxylase
DHAP: dihydroxyacetone phosphate
DL: D-lactate
DLDH: D-lactate dehydrogenase
DMEM: Dulbecco′s Modified Eagle Medium
dNTP: deoxynucleotide triphosphate
DREADDs: designer receptors exclusively activated by designer drugs
ds: double-stranded

EF1α: Human elongation factor-1α
EGFP: enhanced green fluorescent protein
EmGFP: emerald green fluorescent protein

F-1,6-BP: fructose 1,6-biphosphate
F-6P: fructose 6-phosphate
FACS: fluorescence-activated cell sorting
FAD: flavin adenine dinucleotide
FBS: foetal Bovine Serum
FMN: flavin mononucleotide
FRET: Förster Resonance Energy Transfer

G-1P: glucose 1-phosphate
G-6P: glucose 6-phosphate
GAP: glyceraldehyde 3-phosphate
GAPDH: 3-phosphate dehydrogenase
GFAP: Glial fibrillary acidic protein
GFP: green fluorescent protein
GSH: glutathione

HBS: HEPES-buffered solution
HCA1: hydroxycarboxylic receptor 1
HEK293: human embryonic kidney 293
HIV: human immunodeficiency virus
HRP: horseradish peroxidase

IEG: immediate early genes
IF: immunofluorescence
IGF-1: insulin-like growth factor 1
IRES: internal ribosomal entry site

Km: Michaelis constant

Laconic: FRET-based L-lactate nanosensor
LB: Luria Bertani
LC: locus coeruleus
LDH: L-lactate dehydrogenase
LL: L-lactate
LMO: L-lactate 2-monooxygenase
LOX: L-Lactate oxidase
LP: lentiviral particle
LVVs: lentiviral vectors

MAS: malate-aspartate shuttle
MCT: monocarboxylate transporter
MDH: malate dehydrogenase
miRNAs: microRNAs
MOI: multiplicity of infection

NA: noradrenaline
NAD: nicotinamide adenine dinucleotide
NADP: nicotinamide adenine dinucleotide phosphate
nt: nucleotide

OR51E2: Olfactory Receptor Family 51 Subfamily E Member 2
ORF: open reading frame

PBS: phosphate buffered saline
PCR: polymerase chain reaction
PDH: pyruvate dehydrogenase
PEP: phosphoenolpyruvate
PFK: phosphofructokinase
PFKFB3: 6-phosphofructose-2-kinase/fructose-2,6-bisphosphatase-3
Pi: inorganic phosphate
PKA: protein kinase A
PPP: phosphate-pentose pathway
pre-miRNA: precursor microRNA
pri-miRNA: primary precursor miRNA
PYR: pyruvate
Pyronic: FRET-based pyruvate nanosensor

RFP: red fluorescent protein
RNAi: RNA interference
ROS: reactive oxygen species
RT: room temperature
RVLM: rostral ventrolateral medulla

ss: single-stranded

TCA: tricarboxylic acid cycle
TU: transducing unit

UDP: uridine diphosphate
UTP: uridine triphosphate
UTR: untranslated region

VEGFA: vascular endothelial growth factor A
Vmax: maximum rate of reaction
VSVG: vesicular stomatitis virus glycoprotein G

WPRE: woodchuck hepatitis post-transcriptional regulatory element

Chapter 1 – General Introduction

1.1 Glia-neuronal network

Glial cells have been classically assigned a secondary role in information coding and cognitive processing. Whilst neuronal activity is widely acknowledged as being mainly responsible for information processing and transmission, astrocytic activity was assigned the role of providing structural, trophic, and metabolic support to surrounding neurones. Over the last decade, however, an increasing amount of evidence has challenged the subservient view of glia functions, showing that these cells are directly involved in synaptic activity and neurotransmitter release (Allen & Lyons, 2018; Perea, Sur, & Araque, 2014). In fact, findings have shown that astrocytes can detect and modulate the activity of noradrenergic neurones, which in turn are involved in the regulation of many brain functions (Bekar, He, & Nedergaard, 2008; Tang et al., 2014). A particularly interesting expanding field is the relevance of brain energy metabolism in the information processing, and the consequent metabolic and signalling coupling between astrocytes and neurones.

1.1.1 Astrocytes

Understanding of the cell biology of astrocytes is in its infancy. Most of our knowledge about astrocytic function presumes that astrocytes are a homogenous group of cells, without considering the different properties of brain regions and circuits in which astrocytes are situated (Mederos, González-Arias, & Perea, 2018). In reality, a range of recent evidence has demonstrated that astrocytes are a strikingly heterogenous group, comprising of cells with different gene expression patterns and complexity of cellular architecture, displaying brain region-specific features and activity (Khakh & Deneen, 2019; Oberheim, Goldman, & Nedergaard, 2012; Zhang et al., 2016).

Although the term astrocytes originated from initial observations in the end of 19th century of cells with star-like appearance, it is becoming increasingly evident that astrocytic morphology is much more diverse and complex. Morphology and location of astrocytes in the brain was initially used to categorize astrocytes into protoplasmic and fibrous (Miller & Raff, 1984). Protoplasmic astrocytes, i.e. astrocytes localized in the gray matter, generally exhibit a spongiform shape with approximately 4 to 10 major branches that ramify to form thousands of smaller processes, which can contact

different synapses as well as the vascular endothelium, integrating the neurovascular unit (Chai et al., 2017; Khakh & Sofroniew, 2017). Surprisingly, a single astrocyte in the hippocampus stratum radiatum is estimated to contact over 100,000 synapses (Chai et al., 2017; Khakh & Deneen, 2019). On the other hand, fibrous astrocytes contain fewer branches, although they are still able to reach blood vessels, and they are situated in the white matter in contact with the nodes of Ranvier (Miller & Raff, 1984; Souza, Almeida, Souza, & Zimmer, 2019). This simplistic classification of astrocytes is likely to be expanded in the near future in face of increasing number of studies unveiling the heterogeneity of these cells (Chai et al., 2017; Khakh & Sofroniew, 2017). Astrocytes can establish interconnections through gap junctions, allowing dynamic exchange of ions and metabolites along an astrocytic network (Savtchouk & Volterra, 2018).

Differently from neurones, astrocytes are electrically silent cells. Absence of propagated electrical signal that can be used as readouts of different functions prevent assessment of astrocytic roles using electrophysiology (Khakh & Deneen, 2019). On the other hand, astrocytes are consistently shown to respond to various stimuli by altering intracellular Ca^{2+} concentration ($[Ca^{2+}]i$ transients or waves), which has been considered a form of excitability by which astrocytes communicate *in vitro* and *in vivo* (Oberheim et al., 2009; Schummers, Yu, & Sur, 2008; Smith, 1992). Different molecular mechanisms were described to underlie astrocytic Ca^{2+} fluctuations, including IP_3 type 2 receptor, TRPV4 channel-mediated Ca^{2+} entry, or transient opening of the mitochondrial permeability transition pore (Agarwal et al., 2017; Haustein et al., 2014; Straub & Nelson, 2007). In fact, Ca^{2+} signalling in astrocytes is remarkably diversified. By using Ca^{2+} indicators, researchers have identified spontaneous – without any identifiable external stimulation – as well as neuronal-mediated Ca^{2+} signalling, which can take place in either localized microdomains in a single astrocyte or widespread throughout the astrocytic network (Di Castro et al., 2011; Haustein et al., 2014; Khakh & Deneen, 2019). The role of Ca^{2+} signalling in astrocytes is also very broad, which includes functions such as release of signalling molecules and trophic factors, modulation of neurotransmitters and K^+ uptake, and regulation of gene expression (Khakh & Deneen, 2019; Verkhratsky & Nedergaard, 2018). Overall, astrocytes take part in all essential CNS functions and are primarily regarded as the key regulators of brain homeostasis.

1.1.2 Communication between astrocytes and neurones

Astrocytes are key cells in the modulation of neuronal function, actively participating in neuronal processing and information coding. Expression of many receptors to neurotransmitters and neuromodulators have been described in astrocytes, such as glutamate, serotonin, dopamine, adenosine, GABA, and adrenergic receptors (Doengi, Deitmer, & Lohr, 2008; Khan, Koulen, Rubinstein, Grandy, & Goldman-Rakic, 2001; Latour, Gee, Robitaille, & Lacaille, 2001; Sandén, Thorlin, Blomstrand, Persson, & Hansson, 2000; Shao & Sutin, 1991; Vélez-Fort, Audinat, & Angulo, 2012; Verkhratsky & Nedergaard, 2018). Neuronal activity mediated by various signalling molecules can, therefore, be perceived by astrocytes through activation of intracellular signalling cascades, which in turn are implicated in the control of intracellular Ca^{2+} levels. (Bazargani & Attwell, 2016). In fact, astrocytes have been suggested to be able to distinguish between the different synaptic inputs and display different Ca^{2+} signals in response (Perea & Araque, 2005; Perea et al., 2014).

By processing the neuronal information, astrocytes can actively modulate neuronal network function. One of the astrocytic mechanisms of response to synaptic activity is the uptake of neurotransmitters, as it occurs with astrocytes wrapping the vicinity of glutamatergic neurones (Poulain, Oliet, & Piet, 2001). In addition, astrocytes can control neuronal function through the release of neuroactive substances – the gliotransmitters – such as glutamate, GABA, D-serine, and ATP (Araque et al., 2014; Bezzi & Volterra, 2001). Neuronal activity-driven Ca^{2+} elevations in astrocytes has been associated with gliotransmitters release in many parts of the brain, resulting in regulatory effects in different neuronal circuits (Perea et al., 2014; Savtchouk & Volterra, 2018; Zorec et al., 2012). Among the wide range of gliotransmitters effects on neurones, glutamate-induced activation of NMDA receptors has been shown to modulate neuronal excitability and synchronize action potential (D'Ascenzo et al., 2007; Parri, Gould, & Crunelli, 2001).

Importantly, modulators of astrocytic $[Ca^{2+}]$ signals are not restricted to neurotransmitters. Changes in protons and mitochondrial depolarization underlie the chemoception role of astrocytes, which actively detect alteration in oxygen, pH and CO_2 levels (Angelova et al., 2015; Gourine et al., 2010). Oxygen sensing by astrocytes involves hypoxia-induced inhibition of mitochondrial respiration, which, through a

succession of signalling events, results in astrocytic Ca^{2+} signalling. Increased intracellular Ca^{2+} concentration triggers vesicular- or connexin hemichannel-mediated ATP release, which in turn acts by activating respiration-involved neuronal circuitry in the brainstem (Angelova et al., 2015; Gourine & Funk, 2017). Alterations in CO_2/H^+ also culminates in increased intracellular Ca^{2+} concentration in brainstem astrocytes in a process mediated by the activity of membrane transporters. This Ca^{2+} signalling induces release of ATP, which acts in the respiratory neuronal network to evoke adaptative increases in breathing (Gourine et al., 2010; Marina et al., 2018; Turovsky et al., 2016).

Thus, in gliotransmission, astrocytes are able to detect neuronal activity and participate directly in its regulation through a neurone-astrocyte bidirectional communication scheme. Some aspects of gliotransmission are nonetheless under debate, which is mainly due to the temporal and spatial complexity of Ca^{2+} signalling in astrocytes and its underlying consequences for neuronal activity (Bazargani & Attwell, 2016; Fiacco & McCarthy, 2018; Savtchouk & Volterra, 2018). In fact, gliotransmission has been suggested to be a complex event, requiring sophisticated tools for better comprehension of this phenomenon (Savtchouk & Volterra, 2018).

1.1.3 Noradrenergic neurones and the Locus Coeruleus

Noradrenaline (NA) in the central nervous system (CNS) is involved in the modulation of many brain functions, including attention and vigilance, arousal, cognition, appetite, sleep-wake cycle, and autonomic outflows (Aston-Jones & Cohen, 2005; Aston-Jones, Rajkowski, & Cohen, 1999; Berridge & Waterhouse, 2003). The vast majority of the NA released in the brain is provided by noradrenergic neurones whose cell bodies are concentrated in a small and bilateral nucleus in the brainstem, the locus coeruleus (LC). The LC is localized in the pons adjacent to the fourth ventricle and it is comprised of a well-delineated and densely packed cluster of approximately 1,600 NA-producing cells in the rodent brain (Robertson, Plummer, De Marchena, & Jensen, 2013; Schwarz & Luo, 2015). LC receives afferent projections from many brain regions, including hypothalamus, brainstem and prefrontal cortex circuits, integrating cognitive, homeostatic and environmental information (Berridge & Waterhouse, 2003; Carter et al., 2010). LC neurones exhibit a widespread, and yet regionally-specialised,

axonal projection system, extensively innervating the forebrain and providing the entire NA supply for the hippocampus (Berridge & Waterhouse, 2003). The extensive projections of LC neurones target different adrenoceptor types in distinguished brain regions, underlying the various regulatory functions attributed to NA (Schwarz & Luo, 2015). Although LC is generally considered a homogenous structure, evidence has long demonstrated that LC neurones exhibit different cell morphology and molecular composition (Holets, 1988; Loughlin, Foote, & Grzanna, 1986; Schwarz & Luo, 2015). Moreover, optogenetic experiments showed that different firing rates displayed by LC noradrenergic neurones affect the specificities of the behaviour seen in mice (Carter et al., 2010; Lonergan et al., 2005; McCall et al., 2015).

NA is mainly released via non-junctional varicosities (synaptic boutons) spread throughout the noradrenergic neurone (O'Donnell, Zeppenfeld, McConnell, Pena, & Nedergaard, 2012). Through diffusion in the extracellular and spinal fluid, NA can target multiple cells over a wide area, evoking coordinated responses from cells within the space of diffusion (Fuxe, Agnati, Marcoli, & Borroto-Escuela, 2015; O'Donnell et al., 2012). Amperometric recordings using carbon fibre microelectrodes revealed that NA is released through exocytosis from axonal varicosities as well as from the soma-dendritic compartments (Chiti & Teschemacher, 2007). Soma-derived NA may act in an autocrine manner, whereas NA released from axonal varicosities have a wider effect throughout the neuraxis (Chiti & Teschemacher, 2007; Kasparov & Teschemacher, 2008).

1.1.4 Interaction between astrocytes and noradrenergic neurones

An increasing body of evidence indicates that astrocytes are the main cell type targeted by noradrenergic volume transmission (Fuxe et al., 2015; Hertz, Chen, Gibbs, Zang, & Peng, 2004; Pankratov & Lalo, 2015). Expression of β-, α1- and α2-adrenoceptors in the astrocytic membrane *in vitro* and *in vivo* in many regions of the brain was described long ago, raising postulations that astrocytes are targets of the central noradrenergic system (Aoki, 1992; Aoki & Pickel, 1992; Hertz et al., 2004; Milner, Lee, Aicher, & Rosin, 1998; Shao & Sutin, 1991; Stone & Ariano, 1989). Nonetheless, the extent and impact of the signalling between astrocytes and noradrenergic neurones are still to be investigated.

In vivo electric stimulation of noradrenergic neurones in the LC as well as indirect LC activation triggered by footshock evoked robust rise in intracellular Ca^{2+} concentration in cortical astrocytes (Bekar et al., 2008). Such responses were sensitive to α-adrenoceptor antagonists as well as to a neuronal toxin (Bekar et al., 2008). NA effects on astrocytes can also be illustrated by a report from Juric and colleagues (2008), which showed that application of NA in cultured astrocytes induces α- and β-adrenoceptors-mediated increase in the expression of brain-derived neurotrophic factor (BDNF), a key regulator of neuronal plasticity (Jurič, Lončar, & Čarman-Kržan, 2008). Moreover, activation of astrocytic β1- or α2-adrenoceptors has been shown to trigger glycogenolysis in astrocytes (Hertz et al., 2015b; Subbarao & Hertz, 1990).

Conversely, little is known about the effects of astrocytes in noradrenergic neuronal activity. In fact, our group was the first to describe a signalling pathway by which astrocytes actively control the central noradrenergic system (Tang et al., 2014). As further described in section 1.4.4, astrocyte-derived L-lactate (LL) binds to a putative Gs-coupled receptor in noradrenergic neurones in the LC, evoking depolarization and NA release (Tang et al., 2014).

1.2 Brain energy metabolism

The energy required for normal brain functioning is remarkably high, accounting for at least 20% of all glucose consumed by the body. Besides, brain energy metabolism is highly dynamic – it must respond to transient and regional energetic demands. It is well-established that glucose is the mandatory fuel of the brain and, therefore, fulfils many critical roles, such as reconstitution of ion gradients across membranes, neurotransmitter and neuromodulator biosynthesis and oxidative stress handling (Dienel, 2018). Moreover, metabolic products including LL also carry signalling functions, closely coupling metabolism with signalling. Nonetheless, the exact metabolic role of glucose and LL in sustaining neuronal activity at the local level is a controversial issue. In this section, the main metabolic pathways involved in brain energy metabolism will be described. The differences in neuronal and astrocytic energetic profile will be also discussed, as well as the controversies behind the cellular responses to energy demand.

1.2.1 Glycolysis

Glycolysis is the transformation of one molecule of glucose into 2 molecules of pyruvate with the concomitant net generation of two molecules of ATP (Berg, Tymoczko, & Stryer, 2002) (Figure 1.1). In the cytosol, a phosphoryl group is transferred from ATP to glucose by the irreversible activity of the enzyme hexokinase. This reaction results in the formation of glucose 6-phosphate (G-6P), a molecule that cannot diffuse through the membrane due to its negative charge. G-6P subsequently undergoes isomerization, which is the rearrangement of atoms in a molecule, which in this case is catalysed by phosphoglucose isomerase, forming fructose 6-phosphate (F-6P). A second phosphorylation reaction then takes place, in which ATP donates a phosphoryl group to F-6P, generating fructose 1,6-biphosphate (F-1,6-BP). This irreversible process is catalysed by phosphofructokinase (PFK), a central enzyme regulating glycolysis rate. The six-carbon molecule F-1,6-BP is subsequently cleaved by the enzyme aldolase into two isomers containing three-carbon units each - glyceraldehyde 3-phosphate (GAP) and dihydroxyacetone phosphate (DHAP). GAP is the only fragment that can proceed through the glycolysis pathway. However, since GAP and DHAP can be readily interconverted through activity of triose phosphate isomerase, DHAP is not wasted in the process of energy generation due to its conversion into GAP. The following steps of glycolysis take place twice to account for the two phosphorylated molecules of GAP formed. While two molecules of ATP have been invested at this point, the final stage of glycolysis is comprised of a sequence of reactions that harvest the energy contained in GAP. Firstly, GAP is oxidized into 1,3-biphosphoglycerate (1,3-BPG) by the enzyme glyceraldehyde 3-phosphate dehydrogenase (GAPDH), which concomitantly reduces the coenzyme nicotinamide adenine dinucleotide (NAD^+) into NADH. Then, phosphoglycerate kinase catalyses the transfer of a phosphoryl group from 1,3-BPG to ADP, forming ATP and 3-phosphoglycerate. The two molecules of ATP formed in this process compensate the 2 molecules of ATP consumed in the initial steps of glycolysis. The enzyme phosphoglycerate mutase subsequently shifts the position of the phosphoryl group in the 3-phosphoglycerate, forming 2- phosphoglycerate, which in turn is dehydrated into phosphoenolpyruvate (PEP) by the enzyme enolase. Finally, PEP donates a phosphoryl group to ADP, an irreversible reaction catalysed by pyruvate kinase,

forming additional ATP and pyruvate. The net reaction of glucose metabolism into pyruvate is:

$$Glucose + 2\ P_i + 2\ ADP + 2\ NAD^+ \rightarrow 2\ Pyruvate + 2\ ATP + 2\ NADH + 2\ H^+ + 2\ H_2O$$

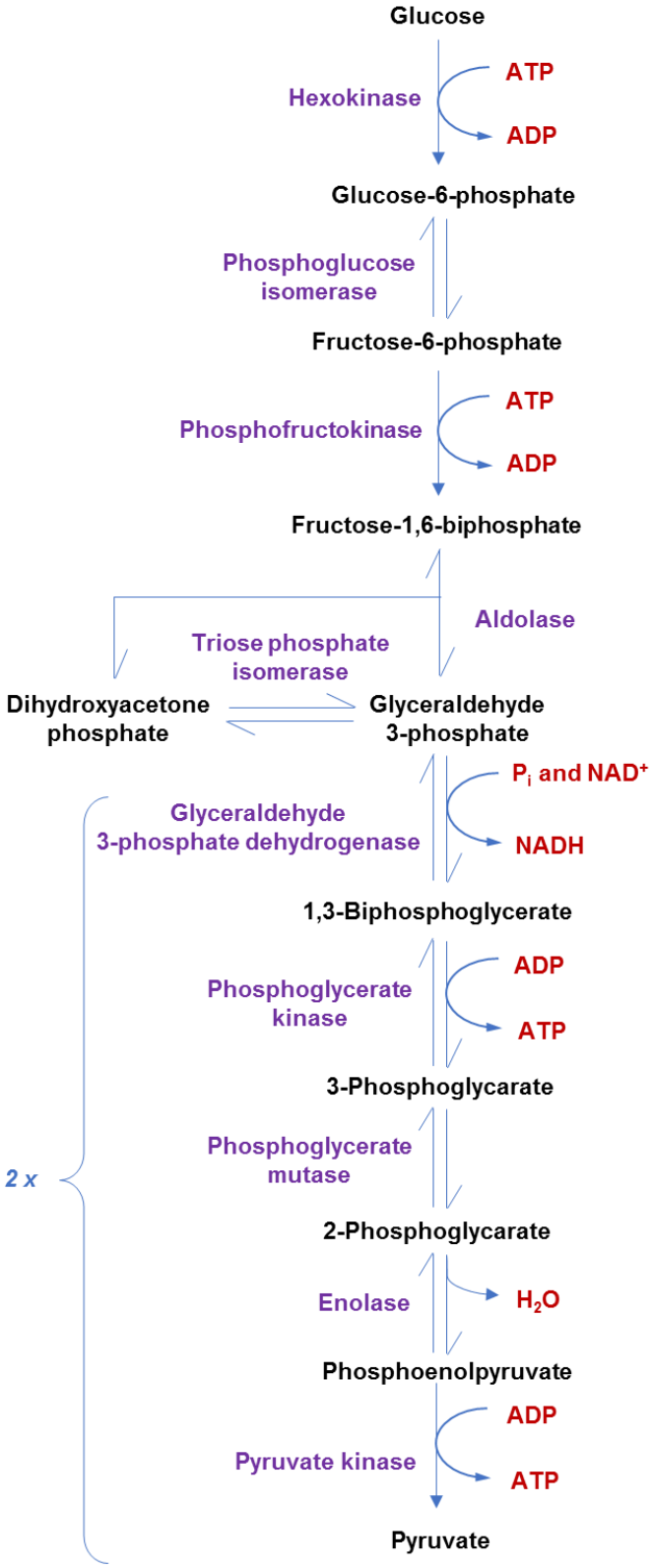

Figure 1.1. Glycolysis pathway. Sequence of reactions driving the metabolism of one molecule of glucose into two molecules of pyruvate with associated net generation of two molecules of ATP. Schematic adapted from Berg et al. (2002).

1.2.2 Fates of Pyruvate

Although synthesis of pyruvate leads to the net production of 2 molecules of ATP, it also generates a redox unbalance due to the reduction of NAD^+ to NADH by dehydrogenation of glyceraldehyde 3-phosphate. Since NAD^+ concentration is limited within the cells, this intermediate electron carrier must be regenerated to maintain the continued operation of glycolysis. Therefore, the final process in glycolysis culminates with the metabolism of pyruvate, which in higher organisms can be either converted into lactate or engaged in the tricarboxylic acid cycle (TCA) and electron-transport chain.

1.2.2.1 TCA cycle and electron transport chain

While only a fraction of the energy of glucose is extracted through glycolysis, much more energy can be released upon complete oxidation of glucose, by means of TCA cycle and electron transport chain. The TCA cycle, which will be briefly discussed here, takes place inside the mitochondria and involves a series of oxidation reactions that breaks carbon compounds into smaller fragments and CO_2 with simultaneous collection of high energy electrons.

The entry point of TCA cycle is the formation of Acetyl CoA, which occurs through irreversible oxidative decarboxylation of pyruvate by the pyruvate dehydrogenase (PDH) complex. Carboxyl groups are lost as CO_2 and the electrons released in this reaction, which resembles many of the enzymatic reactions of the TCA cycle, are transferred to the intermediate electron carrier NAD^+, which in turn, conserves the energy of the oxidation process in the form of reduced NADH (Figure 1.2). Acetyl CoA – a two-carbon acetyl unit – fuses with the four-carbon oxaloacetate, generating the six-carbon TCA (citrate). Citrate undergoes oxidative decarboxylation, yielding a five-carbon compound (α-ketoglutarate) that is also oxidatively decarboxylated to form succinate, a four-carbon molecule. Finally, succinate is enzymatically regenerated into oxaloacetate, which can restart the cycle upon condensation with acetyl CoA. The sequential oxidation of carbon atoms to CO_2 in the TCA cycle releases electrons that are transferred as hydride ions ($:H^-$) to NAD^+ and as hydrogen atoms to flavin adenine dinucleotide (FAD), resulting in the formation of reduced NADH and $FADH_2$,

respectively. At the end of each turn of TCA cycle, three molecules of NADH, one molecule of $FADH_2$, as well as one GTP and two CO_2 are released (Figure 1.2). Importantly, the role of TCA cycle is not restricted to the harvest of energy from carbon compounds. Four- and five-carbon intermediate products of the cycle also act as precursors for a range of biosynthesis pathways, such as the generation of glutamate and aspartate from α-ketoglutarate and oxaloacetate, respectively.

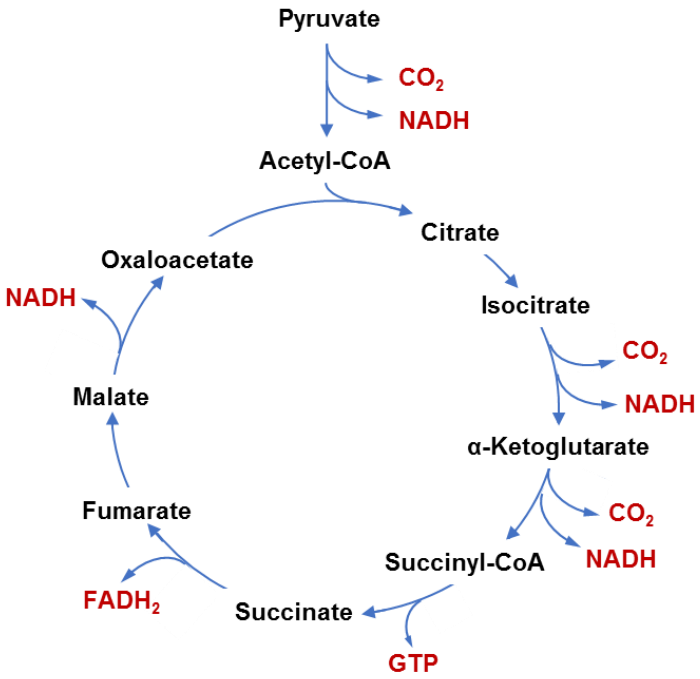

Figure 1.2. Overview of the products generated by each turn of the TCA cycle. In the mitochondria, acetyl-CoA is formed mainly by oxidative decarboxylation of pyruvate formed during glycolysis. The cycle starts with formation of citrate by the inclusion of oxaloacetate to the acetyl group of acetyl-CoA. Through a series of oxidative decarboxylation reactions, carbon elements are fragmented into smaller compounds and CO_2. Electrons released in these reactions are transferred to intermediate electron carriers, forming NADH and $FADH_2$. Schematic adapted from Berg et al. (2002).

The energy collected in the TCA cycle and stored in the intermediate electron carriers is used to generate ATP in the respiratory chain, which comprises of molecular complexes embedded in the inner mitochondrial membrane. Although this process – oxidative phosphorylation – is mechanistically complex (Berg et al., 2002), the concept underpinning is straightforward as briefly outlined here. NADH and $FADH_2$ enter the chain at Complex I and II, respectively, and the electrons are shuttled from

either of these complexes to complex III by the lipid-soluble carrier ubiquinone (Figure 1.3). Cytochrome c carries electrons from complex III to IV, where electrons reduce oxygen to water. Thus, oxygen in mitochondrial respiration is the electron acceptor required to regenerate NAD+ and FAD consumed during glycolysis and TCA cycle. The transfer of electrons through the complexes is based on coupled redox reactions, in which a carrier is reduced and subsequently oxidized by the next carrier in the chain. The electron transport chain acts, therefore, as an electrical wire passing down the electrons through the chain. This process is exergonic, and the energy released is used to pump protons to the intermembrane space, creating a proton gradient across the membrane, also referred as proton-motive force. Finally, in the ATP synthase enzymatic complex, protons flow down the concentration gradient into the mitochondrial matrix, passing the energy required for the formation of ATP from ADP and inorganic phosphate (Pi).

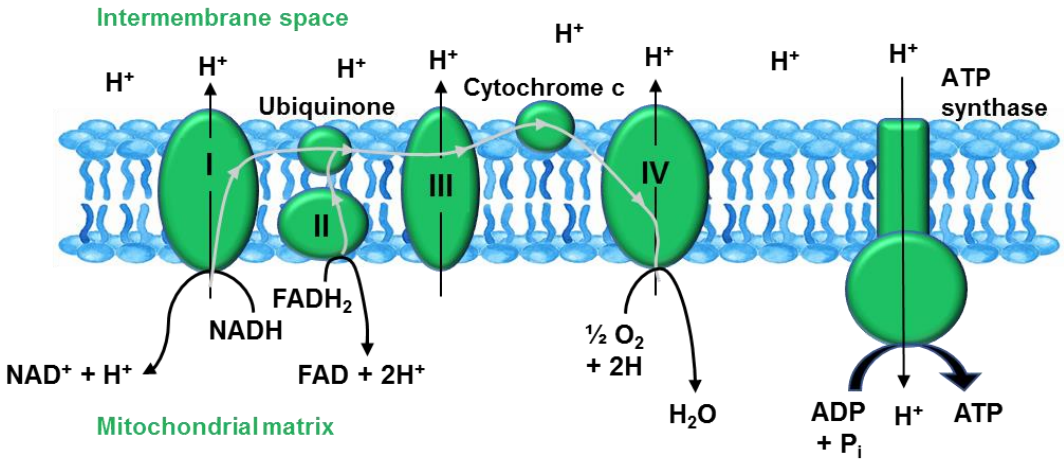

Figure 1.3. Generation of ATP through the respiratory chain. Electrons harvested in the TCA cycle are transferred from NADH and $FADH_2$ to Complex I and II, respectively. Through the loosely membrane-associated carriers Ubiquinone and Cytochrome c, electrons are passed down the respiratory chain (curvy grey line) to complex IV. The energy released in this process is used to drive protons to the intermembrane space, creating a proton gradient across the membrane (proton-motive force). At complex IV, electrons react with oxygen and protons to form water. Finally, the protons held in the intermembrane space pass down through the ATP synthase to the mitochondrial matrix, and the energy release in this process is used to generate ATP from ADP and P_i. Schematic adapted from Benard et al. (2011)

1.2.2.2 L-lactate production

Another fate of pyruvate is its reduction into LL. This reversible reaction is catalysed by the enzyme L-lactate dehydrogenase (LDH) (Figure 1.4) and requires the intermediate electron carrier NAD.

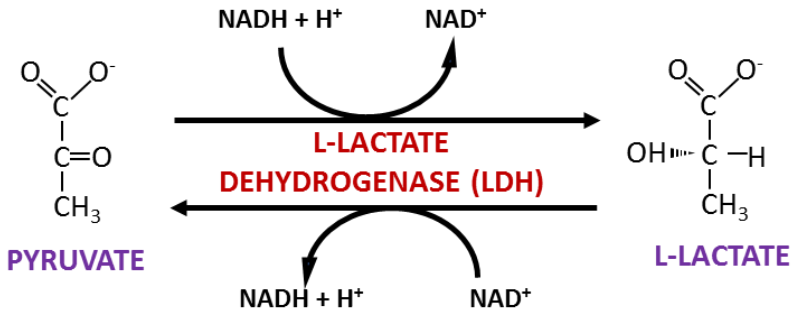

Figure 1.4. Reaction catalysed by the enzyme LDH. Pyruvate is reduced to LL through the activity of the NADH-dependent LDH.

LDH is a tetramer composed of A (also known as M, or 5) and B (also known as H, or 1) subunits. Combination of these subunits in all possible arrangements of four yields five different isoenzymes (Fisenne et al., 1961). Expression of LDH isoenzymes containing B subunits (LDH-B) is enhanced in tissues characterised by intense oxidative metabolism, such as the heart. On the other hand, tissues that often undergo anaerobic metabolism express mainly LDH isoenzymes enriched with A subunits (LDH-A), which is the case of skeletal muscle and liver (Laughton et al., 2000; Markert, Shaklee, & Whitt, 1975). In the brain, the cellular distribution of LDH isoenzymes has been investigated at the gene and protein levels. Previous reports have described enriched or exclusive expression of LDH-B in neurones, while astrocytes express mainly the LDH-A subtype (Bittar, Charnay, Pellerin, Bouras, & Magistretti, 1996; Laughton et al., 2000; O'Brien, Kla, Hopkins, Malecki, & McKenna, 2007). More recent data using single-cell transcriptome analysis indicated twofold increase in LDH-B in astrocytes as compared to neurones, which in turn showed 1.7-fold enhanced LDH-A (Zhang et al., 2014).

This different expression pattern of LDH isoenzymes has been suggested to reflect the metabolic requirements of the tissue or cell population. This is due to the fact that the different subtypes of LDH exhibits different catalytic properties, i.e. Michaelis

constant (Km), which express the substrate concentration at which the reaction reaches half of its maximum value, and the maximum rate of reaction (V_{max}), which is the rate of the reaction when the enzyme is saturated with the substrate. Different values of Km and V_{max} may favour the reaction towards either LL formation (LDH-A) or LL degradation (LDH-B) (Bittar et al., 1996; Swiderek & Paneth, 2011). These observations led to the proposition of a predominant glycolytic profile in astrocytes, which culminates in accentuated LDH-A-mediated production of LL, which in turn is transported to neurones to be converted via LDH-B into pyruvate (Bittar et al., 1996; Pellerin & Magistretti, 2012). Nonetheless, this assertion has been challenged under steady-state conditions (Quistorff & Grunnet, 2011). According to the authors, the fact that the equilibrium constant is still the same in the different isoenzymes, variations in the kinetics properties would not dictate the level of LL concentration in steady-state conditions. Moreover, although non-steady situations may influence the time-course of LL accumulation, the high activity of LDH causes the transitions in net flux of LL to be short-lived (Quistorff & Grunnet, 2011).

1.2.2.3 Control of the cellular redox balance

The variety of coenzymes specialized in electron transport such as NAD, FAD, nicotinamide adenine dinucleotide phosphate (NADP), and flavin mononucleotide (FMN) is very insignificant if compared to the multitude of reactions in a cell that are catalysed by these electron carriers (Nelson & Cox, 2017). NAD, in particular, is essential for metabolism of glucose and LL and the ratio between the reduced and oxidized forms of this coenzymes can dictate the metabolic dynamics within a cell.

The major processes that regulate NADH/NAD^+ ratio in astrocytes and neurones are glycolysis, LDH activity and the malate-aspartate shuttle (MAS) (Díaz-García et al., 2017). Activity of GAPDH enzyme during glycolysis generates NADH, which is recycled to NAD^+ by the conversion of pyruvate to LL (Figure 1.5).

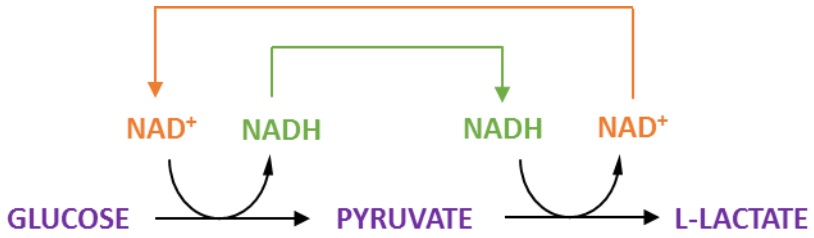

Figure 1.5. Regeneration of NAD in the glycolytic pathway. The electron acceptor NAD^+ is reduced to NADH during glycolysis, whereas LL production causes NADH oxidation to NAD^+. Therefore, conversion of glucose into lactate maintains the redox balance as there is no net change in NAD^+ and NADH. Schematic adapted from Berg, Tymoczko, and Stryer (2002).

Another mechanism to restore the cellular redox balance is the MAS, which consists of a mitochondrial shuttle system composed of a series of enzymes and transporters that carry reducing equivalents from cytosolic NADH to the mitochondria, as NADH is an impermeable molecule to the mitochondrial membrane. Briefly, the cytosolic malate dehydrogenase (MDH) enzyme reduces oxaloacetate to malate, regenerating NAD^+ (Figure 1.6). Malate is then transferred to the mitochondrial matrix via the malate–α-ketoglutarate carrier in exchange for α-ketoglutarate. The mitochondria MDH, which is part of the TCA cycle, oxidizes malate to oxaloacetate, forming NADH that will transfer its electron to oxygen in the respiratory chain. Oxaloacetate is then converted to aspartate by the activity of aspartate aminotransferase, which also converts glutamate to α-ketoglutarate. Aspartate exits the mitochondria by the aspartate-glutamate carrier, which concomitantly carries glutamate and H^+ in opposite directions. In the cytosol, aspartate aminotransferase converts aspartate to oxaloacetate at the same time that it forms glutamate from α-ketoglutarate (McKenna, Waagepetersen, Schousboe, & Sonnewald, 2006).

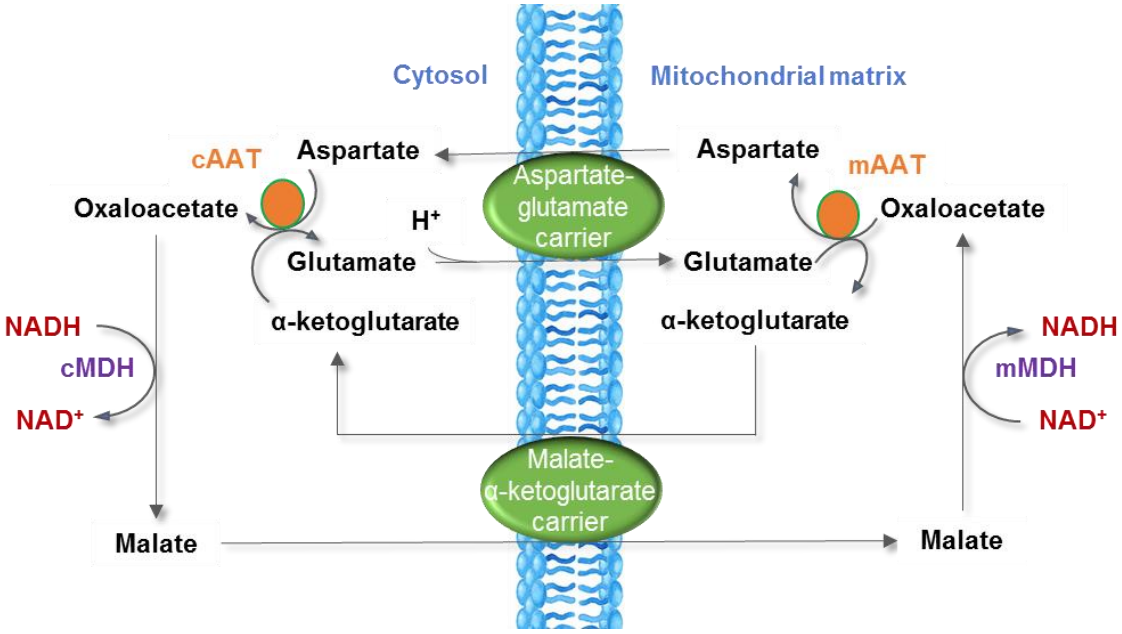

Figure 1.6. Malate-aspartate shuttle. Through a series of enzymatic reactions and transporters, reducing equivalents from NADH are transferred from the cytosol to the mitochondrial matrix. All the components of the shuttle are regenerated, except for the cytosolic proton transported with glutamate in exchange for aspartate. cAAT: cytosolic aspartate aminotransferase; cMDH: cytosolic malate dehydrogenase; mAAT: mitochondrial aspartate aminotransferase; mMDH: mitochondrial malate dehydrogenase. Schematic adapted from McKenna et al. (2006).

Some reports suggest that MAS is the major process regenerating the cytosolic levels of NAD^+ in neurones under resting conditions (Cheeseman & Clark, 1988; McKenna et al., 2006). Recent work investigating the NADH/NAD^+ ratio in stimulated neurones in hippocampal slices indicated that MAS contribution to the cytosolic NADH transients is minor as compared to the activity of LDH (Díaz-García & Yellen, 2019). In astrocytes, MAS activity has been suggested to be remarkably reduced or nearly absent (Ramos et al., 2003).

1.2.3 Glycogen metabolism

Glycogen is comprised of branches of glucose residues assembled around a core protein, forming granules in the cells' cytoplasm with sizes ranging from approximately 10 to 60 nm (Calì et al., 2016). In the brain, glycogen concentration is approximately 100 times lower than the glycogen stores found in the liver and skeletal muscles

(Stryer, 1995). Glycogen granules in the CNS appear almost exclusively in astrocytes, except for a few studies which detected glycogen in neurones – either in moto-neurones or under pathological conditions, ultimately leading to neurodegeneration (Sotelo & Palay, 1968; Vilchez et al., 2007). More recently, evidence using more sensitive assays has suggested that neurones are endowed with enzymes that synthesize and degrade glycogen and, although in small amounts, glycogen is in fact accumulated in these cells (Saez et al., 2014). Interestingly, this study has suggested that neuronal glycogen plays an important role in neuronal survival under hypoxic conditions since absence of glycogen shunt in neurones increased their vulnerability to oxygen deprivation (Saez et al., 2014).

Glycogen is readily metabolised to provide energy substrates to the brain. Its degradation relies on the activity of the enzyme glycogen phosphorylase, which adds P_i to the substrate, yielding glucose 1-phosphate (G-1P) (Table 1.1). The phosphoryl group in the G-1P is then shifted by phosphoglucomutase to form G-6P, a molecule that can engage in the metabolic mainstream. Importantly, generation of G-6P from glycogen is an energetically advantageous process as compared to the glycolytic degradation of glucose since it does not require energy input to phosphorylate the substrate (Berg et al., 2002). Therefore, since incorporation of glycogen-derived G-6P into the glycolysis skips the hexokinase reaction, it yields 3 molecules of ATP, while 2 molecules of ATP are released from glucose-derived G-6P.

Synthesis of glycogen is not the reverse reaction of the degradative pathway (Table 1.1). Addition of a glycosyl residue in the glycogen chain is catalysed by glycogen synthase, which uses as a substrate the uridine diphosphate (UDP)-glucose – the activated form of glucose. UDP-glucose, in turn, is formed from uridine triphosphate (UTP) and G-1P by the activity of UDP-glucose pyrophosphorylase (Berg et al., 2002).

Table 1.1. Biochemical processes mediating glycogen synthesis and degradation Berg et al. (2002).

Process	Key regulatory enzyme	Reaction
Synthesis	Glycogen synthase	$Glycogen_n + UDPglucose \rightarrow glycogen_{n+1} + UDP$
Degradation	Glycogen phosphorylase	$Glycogen_{n+1} + P_i \rightarrow glycogen_n + G1P$

Although glycogen synthesis and degradation are fairly simple biochemical processes, these reactions are tightly regulated by multiple allosteric effectors. Glycogen turnover in astrocytes is regulated by cells' energetic requirements as well as by the concentration of Ca^{2+} and K^+ in the intracellular and extracellular compartments, respectively (Dienel, 2018; Dienel & Cruz, 2016; Hertz et al., 2015b). Moreover, glycogen degradation can be driven by interactions of astrocytic receptors with neurotransmitters, such as serotonin, adenosine, and NA (Hertz et al., 2015b). NA-induced glycogenolysis has been shown to be mediated mainly by β1-adrenoceptor activation and, to a lesser extent, by α2-adrenoceptors (Hertz et al., 2015; Subbarao & Hertz, 1990). Contrarily to the classical view of glycogen as an emergency fuel to the brain, evidence has indicated that glycogen metabolism can take place under adequate conditions of glucose availability and delivery (Swanson, Morton, Sagar, & Sharp, 1992). Indeed, glycogen metabolism has been shown to have an essential role in brain energetics and aerobic glycolysis, which can greatly influence many aspects of brain function (Dienel, 2018; Hertz et al., 2015).

1.2.4 Neuronal and astrocytic energetic profiles

Brain cells exhibit different metabolic profiles. Neuronal metabolism is considered to be highly oxidative, whereas astrocytes are suggested to favour the glycolytic pathway, preferentially converting glucose to LL (Magistretti & Allaman, 2015). These metabolic differences are neither due to a decreased number of mitochondria in astrocytes nor because of defective astrocytic respiration (Lovatt et al., 2007; Magistretti & Allaman, 2015). Instead, differential metabolic profiles are thought to be a result of several factors, including a cell-type specific pattern of gene expression of

enzymes that regulate metabolic fluxes as well as differential organization of the respiratory chain in the mitochondria.

Single-cell transcriptome analysis showed that the glycolytic enzyme 6-phosphofructose-2-kinase/fructose-2,6-bisphosphatase-3 (PFKFB3) is upregulated in astrocytes (Zhang et al., 2014). This enzyme converts F-6P to fructose-2,6-biphosphate, which in turn acts as allosteric activator of PFK-1, stimulating glycolysis (Zhang et al., 2014). Furthermore, subtypes of another key enzyme regulating glycolysis – pyruvate kinase, subtypes PKM1 and PKM2 – are differently expressed in neurones and astrocytes (Zhang et al., 2014). The latter cell type expresses PKM2, which can regulate the glycolytic flux according to the local energy demand. This feature is not present in PKM1 expressed by neurones, which may prevent upregulation of glycolysis in these cells (Zhang et al., 2014). Following glycolysis, the rate-limiting step for pyruvate entry in the TCA cycle is its decarboxylation, catalysed by PDH. In astrocytes, PDH has been shown to be remarkably phosphorylated, which decreases its activity, suggesting reduced flux of pyruvate to mitochondrial respiration as compared to neurones (Halim et al., 2010). At the mitochondrial level, evidence has suggested that complexes of the respiratory chain in neurones are organized into supercomplexes, resulting in more efficient oxidative phosphorylation and decreased production of reactive oxygen species (ROS) (Lopez-Fabuel et al., 2016). On the other hand, complex I in astrocytes is free, which is associated with poor mitochondrial respiration and higher generation of ROS (Lopez-Fabuel et al., 2016). Importantly, LL production is driven by the cell redox state, which has been investigated in mouse hippocampal brain slices using an intracellular redox biosensor (Mongeon, Venkatachalam, & Yellen, 2016). Results indicated that the NADH/NAD^+ ratio in astrocytes in steady-state condition is higher than in neurones, which is consistent with increased astrocytic conversion of glucose to LL (Mongeon et al., 2016). Moreover, a recent *in vivo* study using biosensors for real-time measurement of metabolite dynamics in brain cells of anesthetised mice indicated that astrocytes maintain higher resting levels of LL (Mächler et al., 2016). Other factor previously discussed that may also contribute to the glycolytic profile of astrocytes include the control of glycogen shunt.

Overall, at the cellular level, astrocytes are in fact more equipped to produce LL than neurones. Unequivocal establishment of astrocytes as glycolytic cells arose from

recent observations using mutant mice lacking Complex IV of the electron transport chain in Bergmann glia cells of the cerebellum (Supplie et al., 2017). Surprisingly, respiration-deficient astrocytes were completely viable even 1 year following gene knockout, implying that these cells can rely on glycolysis for energy generation (Supplie et al., 2017).

1.2.5 Aerobic Glycolysis

The net energy provided from the conversion of glucose to pyruvate is 2 ATPs per molecule of glucose, while oxidative phosphorylation releases approximately 32 ATPs. Although LL production seems a coherent pathway for energy generation under hypoxic conditions, cancer cells tend to favour the glycolytic pathway even under adequate oxygen levels. This phenomenon is called Walburg effect and its underlying regulatory mechanisms have only now been elucidated (Vander Heiden & DeBerardinis, 2017; Yellen, 2018). The preferential conversion of glucose to LL in these cells is likely to be driven by an increase in the $NADH/NAD^+$ ratio, which is due to the intense nucleotide production that sustains cell growth (Vander Heiden & DeBerardinis, 2017). Importantly, mitochondrial respiration is not defective in cancer cells. On the contrary, the TCA cycle must take place in order to generate precursors for the synthesis of cell components for the proliferative counterparts (Vander Heiden & DeBerardinis, 2017). In the brain, glucose is thought to be nearly completely oxidized to CO_2 under resting conditions (Dienel, 2012). However, transient neuronal stimulation evokes a Warburg-like effect, also known as aerobic glycolysis. Accordingly, during transient episodes of neuronal activity, there is a disproportionate upregulation of glucose consumption as compared to oxygen utilization, even though the oxygen levels and means of delivery are adequate (Fox, Raichle, Mintun, & Dence, 1988). The actual physiological function of aerobic glycolysis has intrigued many researchers in recent decades. Astrocytes are thought to play an important role in this phenomenon since these cells are key regulators of glycogen turnover and LL can diffuse through the astrocytic gap-junction network (Dienel & Cruz, 2016). Nonetheless, the precursor substrate sustaining neuronal activity and the cellular and molecular mechanism underlying this transient increase in LL production is a long-

lasting controversial topic (Bak & Walls, 2018; Barros & Weber, 2018; Dienel, 2018; Magistretti & Allaman, 2018), and will be further discussed below.

1.2.6 Astrocyte-to-neurone L-lactate shuttle hypothesis

The astrocyte-to-neurone LL shuttle (ANLS) hypothesis has been proposed over two decades ago and provides an explanation for the paradoxical aerobic glycolysis that follows neuronal excitation (Pellerin & Magistretti, 1994). It originated from observations that, in glutamatergic neurotransmission, glutamate released in the synaptic cleft is taken up by closely associated astrocytes through glutamate transporters, which work upon symport with Na^+, in order to restore the basal extracellular levels of glutamate (Figure 1.7). Increased influx of Na^+ into the astrocytic cytosol activates Na^+/K^+ ATPase, which restores Na^+ and K^+ homeostasis at the expense of ATP. Energy utilization triggers glycolysis in astrocytes, in which glucose is non-oxidatively converted into LL via LDH. LL is then shuttled to neurones via monocarboxylate transporters (MCTs), where it is converted to pyruvate by the activity of LDH. Pyruvate in neurones is further metabolized in the TCA cycle for oxidative generation of ATP in the mitochondrial respiratory chain. Concomitantly, glutamine synthetase in astrocytes catalyses the conversion of glutamate into glutamine, which is released to the extracellular space and taken up by neurones to be recycled back to glutamate (Pellerin & Magistretti, 1994; Pellerin & Magistretti, 2012).

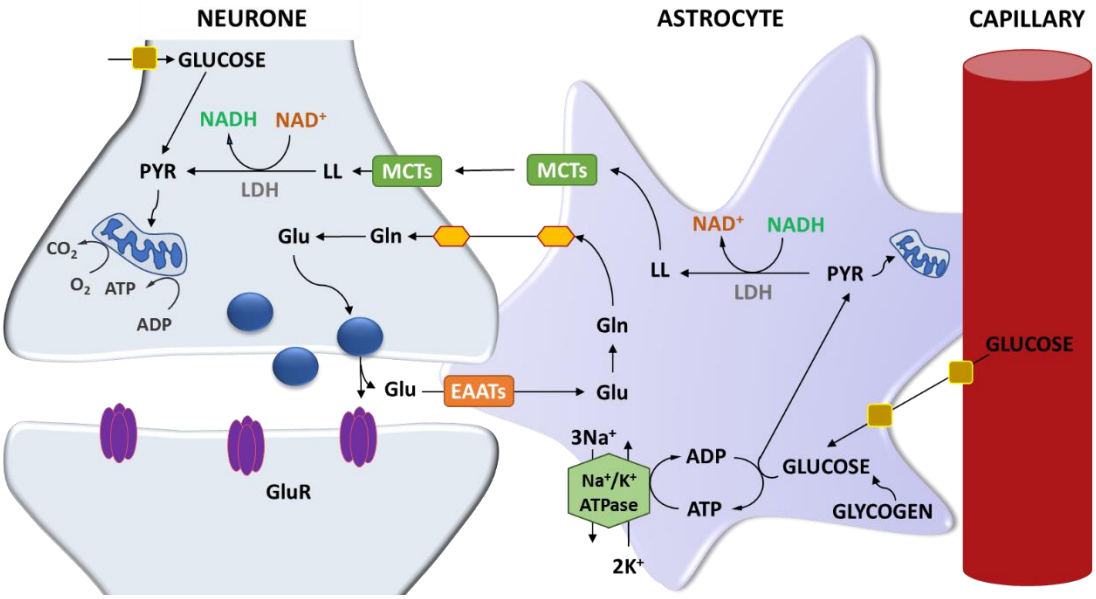

Figure 1.7. LL shuttle from astrocytes to activated neurone. ANLS predicts that glycolysis in astrocytes surrounding active neurones is triggered by the activity of the Na^+/K^+ ATPase, which is activated by the astrocytic uptake of glutamate (Glu) through excitatory amino acid transporters (EAATs). LL produced by glycolysis in astrocytes is then exported to neurones, where it is oxidised to pyruvate to be further used in the production of ATP. Glutamate in astrocytes is converted to glutamine (Gln), which is released and taken up by neurones to be converted to glutamate. GluR: glutamatergic receptors. Schematic adapted from Bélanger, Allaman, and Magistretti (2011).

The ANLS model, which predicts that stimulated neurones use astrocyte-derived LL as a primary energy source, has gained support over the years by reports from several laboratories (Magistretti & Allaman, 2015, 2018; Weber & Barros, 2015). ANLS has expanded beyond glutamatergic neurotransmission, such as in a study showing that K^+ released by excited neurones stimulated astrocyte-derived LL release (Fernández-moncada, Ruminot, Robles-maldonado, Alegría, & Deitmer, 2018; Sotelo-Hitschfeld et al., 2015). Moreover, genetic ablation of specific glycolytic enzymes in *Drosophila melanogaster* resulted in neurodegeneration, suggesting that ANLS is a phylogenetic conserved mechanism (Volkenhoff et al., 2015). Other glia cells – the oligodendrocytes – were also reported to release LL, which was essential for maintenance of adequate axonal function (Saab & Nave, 2017). LL shuttle from astrocytes to neurones has proven to be feasible by various experiments in culture (Magistretti & Allaman, 2018; Pellerin & Magistretti, 2012). In particular, the astrocytic store of glycogen in regions of intense synaptic activity as well as astrocytic control of glycogen shunt, which in turn is stimulated by neurone-derived molecules such as

NA, is in favour of neurone-astrocyte metabolic coupling as predicted by ANLS (Pellerin & Magistretti, 2012).

LL transport from astrocytes to neurones, where LL is subsequently used as an energy source, has been shown to be pivotal for long-term memory formation in the hippocampus (Suzuki et al., 2011). Inhibition of glycogen-derived LL through intrahippocampal injection of the glycogen phosphorylase blocker 1,4-dideoxy-1,4-imino-d-arabinitol (DAB) disrupted long-term potentiation and memory consolidation. On the other hand, memory formation has been rescued when DAB was co-applied with LL. LL also rescued the amnestic effect evoked by downregulation of MCT1 and MCT4 expression, which has been induced by injection of targeted antisense oligonucleotides (Suzuki et al., 2011). According to the study, decreased expression of these transporters culminated in reduction of LL export from astrocytes. Conversely, downregulation of MCT2 expression prevented the rescue effect of LL on memory formation due to impaired LL import to neurones (Suzuki et al., 2011). The specific molecular mechanisms mediating LL effects on long-term memory consolidation has not been elucidated yet. Nonetheless, further research suggested that activation of astrocytic β2-adrenergic receptors in the hippocampus has an essential role in triggering glycogenolysis and LL release that support neuronal molecular changes related to memory consolidation processes (Gao et al., 2016).

1.2.6.1 Controversies and challenges to the hypothesis

The evidence supporting the ANLS is mostly indirect, such as the observations of a preferential glycolytic metabolism of glucose in astrocytes, whereas neurones rely mainly on oxidative phosphorylation (previously discussed in section 1.2.4). One of the cornerstones of the ANLS model is the differential expression of LDH and MCT subtypes in astrocytes and neurones, which, due to differences in kinetics and affinities explained elsewhere in this chapter, would lead to unidirectional LL flux from astrocytes to neurones (Bittar et al., 1996; Pellerin & Magistretti, 2012; Pierre & Pellerin, 2005). However, the equilibrative feature of these enzymes and carriers as well as single-cell transcriptome databases challenge the role of MCTs and LDHs in substantiating the ANLS hypothesis (Bak & Walls, 2018; Dienel, 2012; Yellen, 2018; Zeisel et al., 2015; Zhang et al., 2014).

Although LL shuttle from astrocytes to neurones at rest is feasible due to increased intra-astrocytic basal levels of NADH and LL (Kasparov, 2016; Mächler et al., 2016; Mongeon et al., 2016), ANLS operation during neuronal activation is broadly controversial (Dienel, 2017; Yellen, 2018). Technical limitations in temporal and spatial resolution prevent proper identification of the cell type accountable for stimulation-induced aerobic glycolysis and hinder direct measurement of LL transfer and its metabolic contribution to neuronal energetics.

Many of the arguments against the ANLS are based on theoretical grounds which, for example, question the lack of adequate stoichiometry between the rate of glucose utilization, which is converted to LL, and the rate of oxygen consumption, which is used for energy generation following LL oxidation in neurones (Dienel, 2017). Moreover, the rate of glycolysis induced by treatment with glutamate did not match the rate of LL that is released from astrocytic cultures (Dienel, 2017). Opponents of the ANLS model also point out that glutamate oxidation following its uptake by astrocytes generates energy at higher yield than glycolysis, contributing at least in part for the energetic cost of glutamate uptake (Dienel, 2017, 2018; McKenna, 2013).

A recent study using intracellular biosensors for $NADH/NAD^+$ in acute hippocampal slices of mice showed that stimulation evoked a prolonged rise in neuronal $NADH/NAD^+$ ratio, which was accompanied by an increase in the intracellular concentration of LL (Dıaz-Garcıa et al., 2017). Blockade of MCTs did not prevent stimulation-induced NADH and LL transients in neurones, which is inconsistent with LL import from astrocytes as predicted by ANLS. In fact, the authors reported that inhibition of either MCTs or LDH increased $NADH/NAD^+$ ratio, which not only implies that neurones enhance their own glycolytic rate to meet the acute metabolic demands of stimulation, but also may export LL in order to alleviate NADH accumulation (Dıaz-Garcıa et al., 2017).

In fact, there is no compelling evidence that irrefutably reveals the role of aerobic glycolysis during neuronal stimulation. The expression of glycolytic enzymes close to neuronal synaptic vesicles may indicate that glycolysis plays a role in the acute replenishment of energy in locations where ATP is highly required (Hinckelmann et al., 2016). A speculative interpretation of this process takes into consideration that, in glycolysis, although ATP yield per molecule of glucose is lower than in oxidative

phosphorylation, the rate of ATP production is much faster (Crow, 1982). Therefore, similar to fast-twitch muscle fibres, neurones may use LL as a prompt additional energy source to the costly process of neuronal processing (Yellen, 2018).

1.3 L-lactate transport across membranes

Although much is currently discussed about the source and actions of LL in the brain, the mechanisms by which LL is released from astrocytes and what regulates its release are not well understood. Transmembrane MCTs have been assigned as the main carriers accountable for LL trafficking. As a result, extensive pharmacological and genetic manipulations of MCTs activity and expression have been employed in order to investigate LL metabolism and signalling in the brain. Nonetheless, recent evidence has indicated that LL exchange is not exclusively executed by MCTs. In addition, the main source of LL in the brain, the astrocytes, are endowed with connexins and pannexins able to transport LL across membranes (Karagiannis et al., 2015). Yet, another potential mechanism by which LL can be released from astrocytes is described as an efficient ion-channel that responds to neuronal depolarisation and can be modulated by LL itself (Sotelo-Hitschfeld et al., 2015).

1.3.1 Monocarboxylate transporters

Monocarboxylates such as LL, pyruvate, ketone bodies, acetate, among others, are carried across plasma membranes through a family of proton-linked transporters, the MCTs. MCTs are a family of 14 members that mediate the facilitated diffusion of a monocarboxylate with a proton across the membrane following a concentration gradient. Of note, metabolic processes generate monocarboxylic acids (R-COOH, R referring to the rest), which are nearly completely dissociated to their monocarboxylic anion ($RCOO^-$) at physiological pH (Halestrap, 2011). However, in case of low pH and high undissociated monocarboxylate concentration, a direct diffusion of the monocarboxylic acids across phospholipid bilayers of biological membranes can take place (Poole & Halestrap, 1993). Indeed, free diffusion of undissociated monocarboxylic acids through membrane lipids was believed to be the sole transport pathway of LL, pyruvate and acetate until 1970s. The involvement of a proton-linked

carrier was only demonstrated when transport of LL and pyruvate in erythrocytes was blocked by the inhibitor α-cyano-4-hydroxycinnamate (CHC) (Halestrap, 1976; Halestrap & Denton, 1974; Halestrap, 2011). Since then, extensive research has been carried out in order to characterize MCTs activity, specificity and expression.

MCTs share a common structure that is predicted to contain 12 transmembrane helices with a large cytosolic loop between two of the intermediate helices and the C- and N-termini in the cytoplasm (Poole, Sansom, & Halestrap, 1996). The net cotransport of a monocarboxylate with a proton through MCTs requires that a proton binds to the MCT in the first place, followed by the binding of a monocarboxylate anion (Halestrap, 2011). As a consequence, the carrier experiences a conformational change, translocating the proton and the monocarboxylate across the membrane, with subsequent release of the ligands in the cytosol (Halestrap, 2011) (Figure 1.8A). Since MCT kinetics are the same regardless of the side of the membrane, the direction of monocarboxylate transport (influx or efflux) depends exclusively on the concentration gradient, which is provided by either monocarboxylate or protons (Halestrap, 2011).

Translocation of MCTs binding site across the membrane occurs at faster speed when the substrate is bound to the carrier (Halestrap, 2011). The step limiting the transportation rate is, therefore, the return of the unloaded carrier to the original conformation. Nonetheless, following substrate release from the carrier, another monocarboxylate can bind the newly empty binding side of the MCT, a process called monocarboxylate exchange or trans-acceleration of MCTs (Fishbein, Foellmer, Davis, Fishbein, & Armbrustmacher, 1988; Halestrap, 2011) (Figure 1.8B). Since in this situation the translocation of the carrier to both sides of the membrane occurs at the bound state, monocarboxylate exchange is considered to be notably faster than the net proton-linked cotransport (Halestrap, 2011). Therefore, transport of a monocarboxylate is accelerated by the presence of another monocarboxylate on the opposite side of the membrane (Garcia, Goldstein, Pathak, Anderson, & Brown, 1994). This concept has been recurrently applied in this project as well as in other *in vitro* and *in vivo* studies in order to deplete the cells of LL (Mächler et al., 2016; San Martín et al., 2013). Efflux of LL from astrocytes was achieved by increasing the inward gradient of pyruvate (Figure 1.8B).

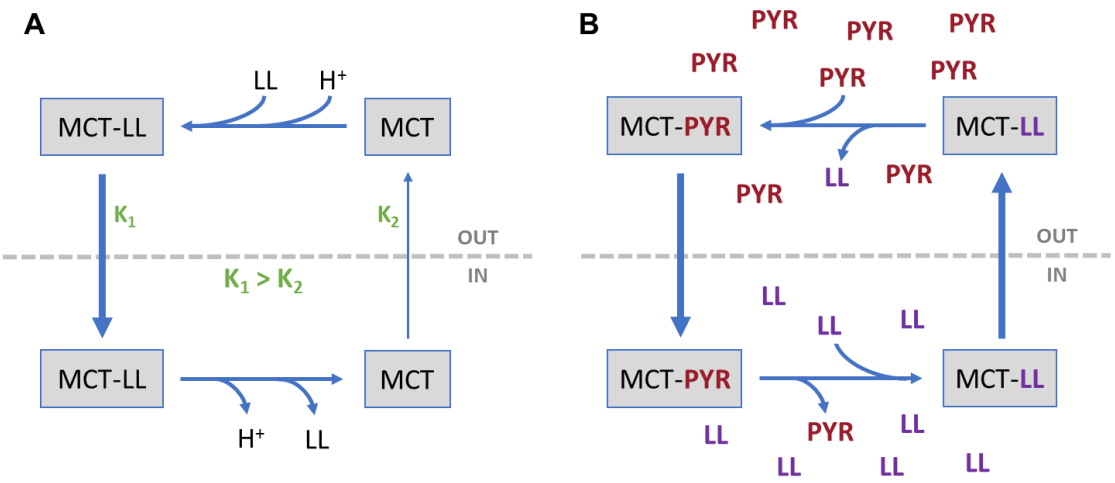

Figure 1.8. Proton-linked transport of monocarboxylates through MCTs. (A) Proton (H+) and LL bind to the MCT evoking a conformational change that translocates the carrier across the membrane. After release of H+ and LL, the conformational change that brings the unbound carrier to the original configuration (K2) is slower as compared to the translocation of the bound MCT across the membrane (K1). **(B)** In this example of monocarboxylate exchange, an inward gradient of pyruvate (PYR) drives MCT-mediated transport of pyruvate to the intracellular compartment. Following PYR release, the inward-facing empty binding sites of MCTs bind to LL, translocating it to the extracellular compartment. This process is called trans-acceleration of MCTs since the carrier is continually in the bound state, where translocation of MCTs is faster (Halestrap, 2011; Mächler et al., 2016).

1.3.1.1 MCTs isoforms and their cell-specific distribution

Although sequence homology studies have so far identified 14 isoforms of MCTs in mammals, only 4 of them have been unequivocally shown to be involved with monocarboxylate transport in humans, i.e. MCT1, MCT2, MCT4, and MCT3 (Halestrap, 2011). Among those, MCT1, MCT2 and MCT4 are expressed in brain cells, while MCT3 is primarily found in the retinal pigment epithelium (Halestrap & Price, 1999; Philp, Yoon, & Grollman, 1998; Pierre & Pellerin, 2005). Even though there is a consensus that distribution of distinct MCT isoforms in the CNS differ regionally and cellularly, employment of different techniques, antibodies and animal species led to controversial results in this regard (Pierre & Pellerin, 2005). The data here presented are mostly based on RNA sequencing studies of acutely isolated brain cells performed by the Barres group (Zhang et al., 2014).

MCT1 is the best described isoform and has been reported to exhibit a wide specificity for short chain monocarboxylates. Km values are 3.5 mmol/L and 1.0 mmol/L for LL and pyruvate, respectively (Table 1.2) (Bröer et al., 1998; Carpenter & Halestrap, 1994). The higher Km for D-lactate (DL) (27.5 mmol/L) indicates that MCT1 is stereoselective for lactate isomers (Carpenter & Halestrap, 1994; Poole, Cranmer, Halestrap, & Levi, 1990). In the brain, MCT1 is expressed at the highest levels in endothelial cells, underpinning their role in the transport of LL between the periphery and the CNS (Bergersen, 2015; Zhang et al., 2014). Astrocytic somata and processes also express MCT1 and, although immunoreactivity studies have mostly failed in confirming this, neurones can also express MCT1, but at lower level as compared to astrocytes (Pierre & Pellerin, 2005; Zhang et al., 2014).

MCT2 is characterized by the higher affinity to monocarboxylates (Bröer et al., 1999; Lin, Vera, Chaganti, & Golde, 1998). Despite the fact that the substrate specificity of MCT2 is similar to MCT1, Km values of most of the ligands are lower for MCT2 as a result of the enhanced affinity (Table 1.2). MCT2 is predominantly expressed in neurones, which has been confirmed by studies using a variety of techniques (Pierre & Pellerin, 2005; Zhang et al., 2014).

MCT4, on the other hand, exhibits very low affinity to monocarboxylates, which results in increased Km values for the majority of the substrates (5- to 100-fold higher than observed for MCT1 – Table 1.2) (Dimmer, Friedrich, Lang, Deitmer, & Bröer, 2000; Manning Fox, Meredith, & Halestrap, 2000). Data on cellular distribution of MCT4 are the most contradictory amongst the MCT isoforms in the brain. Immunoreactivity studies detected expression solely in astrocytes, culminating in many reports considering MCT4 to be specific for these cells (Magistretti & Allaman, 2015; Pierre & Pellerin, 2005; Rafiki, Boulland, Halestrap, Ottersen, & Bergersen, 2003). Nonetheless, analysis of a transcriptome database revealed that neurones also express this carrier and at higher levels as compared to astrocytes (Zhang et al., 2014).

Expression of MCT isoforms has been proposed to be under transcriptional or post-transcriptional regulation in order to meet fluctuations in energetic demands of brain cells (Halestrap & Wilson, 2012). Exposure of cultured cortical neurones to NA, insulin, insulin-like growth factor 1 (IGF-1) and BDNF resulted in upregulation of MCT2

in these cells (Chenal & Pellerin, 2007; Chenal, Pierre, & Pellerin, 2007; Robinet & Pellerin, 2010). Such changes in MCT2 expression have been associated with increased synaptic transmission and neuronal plasticity, which demands an enhanced energy supply (Pellerin & Magistretti, 2012). Although changes in MCT1 expression have been widely demonstrated in skeletal muscles in response to physical activity, denervation and spinal injury, there is no report to the best of my knowledge describing alterations of MCT1 expression levels in brain cells.

Table 1.2. Cell-specific expression of MCT isoforms in brain tissue and their affinity to monocarboxylates that are relevant to this project. Non-available data are expressed as n.a. 80mM acetate did not saturate MCT4. Km values were taken from Halestrap (2011) and Rae et al. (2012).

		Affinity – Km values (mmol/L)			
MCTs	**Expression**	**L-lactate**	**Pyruvate**	**D-lactate**	**Acetate**
MCT1	Endothelial cells, astrocytes and neurones	3.5	1.0	27.5	3.7
MCT2	Neurones	0.7	0.1	n.a.	2.6
MCT4	Astrocytes and neurones	28	153	519	Non-saturable

The majority of the naturally occurring substrates of MCTs are products of metabolic processes and exhibit a range of physiological roles in the CNS. Likewise, the different kinetics and expression profiles of the MCT isoforms in the brain are expected to follow the physiological relevance of their ligands. One of the pillars of the ANLS hypothesis is the fact that expression of the low affinity MCT1 and MCT4 in astrocytes indicates efflux of LL, while expression of the high-affinity MCT2 in neurones suggests influx of LL even at lower concentrations of this compound (Pellerin & Magistretti, 2012). MCTs are, therefore, suitable for shuttling LL from astrocytes to neurones, where it can be oxidized to be used as an energy source according to the ANLS model (Magistretti & Allaman, 2015; Pellerin & Magistretti, 2012). Hypothalamic microinjections of antisense oligodeoxynucleotides to evoke knock-down of MCT2 in neurones and MCT1 or MCT4 presumably in astrocytes have been shown to impair

memory consolidation in rats due to impairment of glycogen-derived LL transport from astrocytes to neurones (Suzuki et al., 2011). Localized application of LL successfully rescued memory formation when either MCT1 or MCT4 was knocked down, but failed to do so with reduced expression of the neuronal MCT2 (Suzuki et al., 2011). Critics of the ANLS hypothesis claim that the evoked reduction of MCTs expression - around 50% for MCTs 1 and 4 and 30% for MCT2 - is unlikely to be sufficient to overcome the high transport capacity of these carriers; also, other LL release mechanisms have not been taken into consideration in the investigation (Dienel, 2017; Dienel & Cruz, 2016).

1.3.2 Connexin hemichannels and pannexins

Whilst MCT activity has been established for a long time as a means for LL trafficking in the CNS, a more recent publication has shown that connexin hemichannels and/or pannexins actively participate in LL efflux from brain cells (Karagiannis et al., 2015). Using amperometric LL sensors to monitor extracellular LL levels in acute brain slices, the authors showed that application of compounds inhibiting pannexin/connexin hemichannels reduced tonic release of LL. On the other hand, application of substances that enhance the open probability of hemichannels led to an increase in LL release from the slices (Karagiannis et al., 2015). Likewise, hypoxia-triggered LL release was significantly reduced following block of connexins. Pannexin and connexin hemichannels have also been shown to play a crucial role in LL release *in vivo*, where blockade of connexin hemichannels reduced LL release triggered by stimulation of Schaffer collateral fibres in the hippocampus (Karagiannis et al., 2015). Further discussion of the role played by connexin hemichannels on LL release will be presented in Chapter 6.

1.3.3 L-Lactate-permeable anion channels

The first preposition of the existence of an astrocytic LL-permeable anion channel arose from the observation that increased extracellular K^+ concentration triggered membrane depolarisation-mediated LL release from astrocytes despite the absence of a favourable gradient of LL and H^+ (Sotelo-Hitschfeld et al., 2015). According to the

authors, *in vitro* application of 9-12 mM of K^+ increased glycolytic rate of astrocytes as indicated by alterations in the intracellular concentration of metabolic compounds. However, in contrast to what it is expected at high glycolytic rate, cytosolic LL levels fell, suggesting K^+-dependent release of LL (Sotelo-Hitschfeld et al., 2015). Moreover, extracellular application of high concentrations of LL enhanced cytosolic LL levels to a lesser extent when it was coapplied with high doses of K^+, indicating that LL efflux from a putative anion channel may outpace influx through MCTs (Sotelo-Hitschfeld et al., 2015). The putative astrocytic LL-permeable anion channel was partially blocked by the nonspecific ion channel inhibitor Cd^{2+}, while the K^+-driven LL release was mimicked by Ba^{2+}, an ion that does not occupy K^+ transporters (Sotelo-Hitschfeld et al., 2015).

The specific anion channel involved in LL release has yet to be identified. Several anion channels have been described so far in astroglia (Kimelberg, MacVicar, & Sontheimer, 2006), including large anion channels that mediate efflux of anionic species that are larger than LL, such as the volume-regulated anion channel (VRAC), which has been shown to play an important role in the efflux of taurine, aspartate and glutamate from astrocytes following cell swelling (Hyzinski-García, Rudkouskaya, & Mongin, 2014; Okada et al., 2019). Although other anions and amino acids may permeate through astrocytic anion channels, most of the research being carried out uses mainly chloride for the biophysical characterisation, preventing further progress in the comprehension of LL-permeable anion channels (Kimelberg et al., 2006).

1.4 L-lactate as a signalling molecule

LL has been increasingly described to carry energy-independent signalling roles that are critical for a range of vital brain functions, including neuronal excitability and plasticity, learning and memory, and angiogenesis. Some of the metabolic-independent LL actions are mediated by changes in the intracellular cAMP levels following LL interaction with either Gs or Gi protein-coupled receptors. Additionally, some of LL effects may be mediated by changes in the intracellular redox state that is controlled by the NAD-dependent and reversible conversion of LL into pyruvate. The latter mechanism requires transport of LL into the cell, while the first relies on extracellular LL-receptor interactions.

LL levels in the brain, which are mainly the result of LL release from astrocytes, respond dynamically to neuronal network activity. Nonetheless, in contrast to wired neurotransmission, LL release and signalling does not rely on vesicular exocytosis in restricted spatial domains. On the contrary, it is more likely that it operates in volume transmission mode and affects a wider area and at expanded timescales (Magistretti & Allaman, 2018). Therefore, sensitivity of the mechanisms involved in LL-mediated signalling should be adequate to detect LL at physiological ranges, rather than the supraphysiological LL levels related to some disease states (Mosienko, Teschemacher, & Kasparov, 2015).

1.4.1 Signalling effects of intracellular L-lactate

LL transported into the neuronal cytosol is oxidized to pyruvate by the activity of the LDH enzyme, leading to the production of NADH and ultimately ATP, which directly modulate the redox and energetic state of the cells, respectively. Intracellular LL, therefore, has been suggested to signal by interfering with cellular redox- and energy-dependent processes (Magistretti & Allaman, 2018).

Yang et al. (2014) have reported a LL-dependent enhancement in the expression of numerous plasticity-related genes in neurones through a mechanism that involves activation of NMDA receptors, which in turn are modulated by changes in the redox state of the cell. Application of 2.5 - 20 mM LL in primary culture of neurones evoked dose-dependent increased expression at both mRNA and protein levels of immediate early genes (IEG) such as Arc, c-Fos, and BDNF. LL also enhanced phosphorylation of the extracellular signal-regulated kinase (Erk1/2), which is involved in NMDA receptor signalling-mediated neuronal plasticity (Yang et al., 2014). Although the precise molecular mechanisms underpinning LL actions on NMDA receptors have not been elucidated, previous research has shown that NMDA-gated currents are amplified by reducing agents (Sullivan et al., 1994). As LL conversion into pyruvate increases NADH/NAD ratio, the authors hypothesized that changes in the neuronal redox state is mediating LL effects on NMDA receptor and IEG expression (Figure 1.9) (Yang et al., 2014). Indeed, extracellular application of NADH mimicked LL-induced expression of IEG, while inhibition of NMDA receptors antagonized this

response. Conversely, exposure of cultured cortical neurones to an oxidizing agent abolished LL-induced increases in IEG expression (Yang et al., 2014).

Another signalling effect of intracellular LL refers to the closure of ATP-sensitive potassium (K_{ATP}) channels due to increased cytosolic ATP/ADP ratio derived from LL metabolism (Parsons & Hirasawa, 2010). Orexin neurones in the perifornical area, which are essential modulators of food intake, have been shown to lose their spontaneous firing activity upon glucose deprivation. These effects could be reversed by a K_{ATP} channel blocker as well as by extracellular addition of LL (Parsons & Hirasawa, 2010). On the other hand, LL application upon MCT blockade failed to prevent the loss of neuronal firing activity under glucose withdrawal. The depolarising effect of LL on orexin neurones has been suggested to be mediated by K_{ATP} channels, which close under enhancement of energy supply (Figure 1.9) (Parsons & Hirasawa, 2010). Although LL-mediated increase in firing rate of orexin neurones is LL dose-dependent (EC_{50} = 2.1mM), other neuronal phenotypes such as arcuate neurones do not show the same sensitivity and activity towards LL (Parsons & Hirasawa, 2010).

Intracellular LL has also been suggested to play an important role in the regulation of sleep-wake cycles (Clasadonte, Scemes, Wang, Boison, & Haydon, 2017). Disruption of astroglial network by knockout of astrocytic Cx43 expression in the brain resulted in wakefulness instability in the active phase as well as extreme sleepiness. Closer investigation of the activity of the wake-promoting orexin neurones in the lateral hypothalamic area revealed reduced excitability and spontaneous firing frequency when Cx43 expression was decreased in astrocytes. A similar inhibitory effect on orexinergic neuronal activity was observed during both glucose deprivation and MCT blocker application. Exogenous LL addition (2.5 mM) or LL dialyses in a single astrocyte (5 mM) could reverse the effect of glucose deprivation on neuronal activity, but failed to do so when MCTs had been blocked, indicating that the excitatory effect of LL relies on its transport into neurones (Clasadonte et al., 2017). Interestingly, application of LL also restored activity to orexin neurones and rescued the disrupted sleep-wake cycle when Cx43 expression was depleted in astrocytes. Therefore, these results suggest that LL transport through the astroglia network and its further delivery to neurones is fundamental to the normal activity of orexin neurones and, consequently, the maintenance of normal wakefulness cycle (Clasadonte et al., 2017).

1.4.2 G protein-coupled receptor 81

LL has been shown to be an endogenous ligand of G protein-coupled receptor 81 (GPR81), also referred as hydroxycarboxylic receptor 1 (HCA1) (Cai et al., 2008; Liu et al., 2009). LL interaction with GPR81 was firstly described in adipose tissues, and resulted in decreased lipolysis rates in adipocytes of mouse, rats and humans (Cai et al., 2008; Liu et al., 2009). GTPγS binding assays suggested that the effect of LL on GPR81 was dose-dependent with an EC_{50} of approximately 1.30 ± 0.32 mM (Cai et al., 2008). DL also stimulated GPR81 activation, but with a higher EC_{50} (3.03 ± 0.21 mM), indicating potential activity as a partial agonist of the receptor (Cai et al., 2008). The EC_{50} value described by Liu and colleagues using GTPγS binding assays was higher than previously described by Cai et al. (2008), ranging from 4 to 7 mM depending on the species (Liu et al., 2009). Reduction in cytosolic cAMP levels following LL-mediated activation of GPR81 confirmed activation of a signalling pathway consistent with a Gi protein-coupled receptor (Figure 1.9) (Cai et al., 2008; Liu et al., 2009).

GPR81 expression in the brain is considerably lower than in adipose tissue and it is predominantly found in the hippocampus, cerebellum, neocortex and in the blood-brain barrier (Lauritzen et al., 2014). At the cellular level, GPR81 is particularly enriched in postsynaptic neuronal membranes and appears at lower level in epithelial cells, whereas very few GPR81-expressing astrocytes can be detected (Lauritzen et al., 2014). Data from Barres lab using single-cell RNA sequencing indicated equally low levels of GPR81 expression in both neurones and astrocytes in the mouse cerebral cortex (Zhang et al., 2014). Neurones in the LC area of the brainstem do not express GPR81 (Mosienko et al., 2018).

GPR81 activation by LL was shown by the Chatton group to reduce excitability of primary cultured neurones, in which activity was monitored by Ca^{2+} imaging (Bozzo, Puyal, & Chatton, 2013). According to that study, LL application decreased Ca^{2+} spiking frequency by approximately 50% in a reversible and dose-dependent manner, with an EC_{50} of about 4.2 mM. This effect was reproduced by the GPR81 agonist 3,5-dyhydroxybenzoic acid, whereas pyruvate did not mimic LL effects on neuronal activity, thus excluding the energetic role of LL in this outcome. On the other hand, LL-mediated decrease in the frequency of Ca^{2+} transients was abolished by the

application of pertussis toxin, an inhibitor of G_i-protein. DL application reduced Ca^{2+} spiking frequency to the same extent as LL (IC_{50} = 4.6 ± 1.2 mM) (Bozzo et al., 2013). More recently, a follow-up study from the same group showed that the reduction in LL-mediated spontaneous Ca^{2+} spiking activity in cortical neurones was absent in GPR81 knockout mice, which exhibited increased neuronal basal activity (de Castro Abrantes et al., 2019). Moreover, activation of GPR81 by LL [5mM] was suggested to occur in presynaptic neurones through inhibition of adenylyl cyclase, followed by reduction of cAMP levels and inactivation of protein kinase A (PKA) (de Castro Abrantes et al., 2019). Since activation of neuronal GPR81 requires supra-physiological levels of LL, it is unlikely that this signalling pathway takes place unless under certain disease conditions such as ischemia and seizures (Mosienko et al., 2015).

A recent *in vivo* study showed that high intensity exercise or subcutaneous LL application (18 mmol/kg, 5 days a week for 7 weeks in an attempt to mimic exercise-induced increase in blood LL in mice) induced GPR81-mediated brain angiogenesis (Morland et al., 2017). Following LL applications, the hippocampus exhibited an enhanced density of blood capillaries and of the expression of vascular endothelial growth factor A (VEGFA). These results were suggested to occur downstream of GPR81 activation in *pia mater*, where the receptor is highly expressed (Morland et al., 2017).

1.4.3 Olfactory L-lactate receptor

LL has been reported to activate a class of Gs protein-coupled receptor, the Olfactory Receptor Family 51 Subfamily E Member 2 (OR51E2). LL-induced activation of OR51E2 raised cAMP levels in a dose-dependent manner with an EC_{50} of 4 mM (Figure 1.9) (Chang, Ortega, Riegler, Madison, & Krasnow, 2015).

Although OR51E2 is implicitly found in the rodent olfactory bulb, expression of this receptor has also been reported in the brain as well as in the periphery (Chang et al., 2015). Indeed, high levels of OR51E2 have been detected in glomus cells of the carotid body, a chemosensory tissue that monitors changes in the composition of the arterial blood (Chang et al., 2015). According to the authors, OR51E2 expression in

the carotid body plays an important role in sensing low oxygen levels. This is because hypoxic conditions are linked with increased concentration of LL, which in turn activates OR51E2, ultimately leading to stimulation of carotid sinus nerve activity (Chang et al., 2015; Torres-Torrelo et al., 2018). Although mRNA analysis indicated that this receptor is also expressed in the brainstem, OR51E2 has not been detected in dissociated noradrenergic neurones in the LC (Mosienko et al., 2018; Yuan et al., 2001).

1.4.4 Putative L-lactate receptor on noradrenergic neurones

Our group has previously demonstrated that LL can act as an excitatory signalling molecule for noradrenergic neurones in the brainstem, an effect that is independent of the caloric value of LL (Marina et al., 2015; Mosienko et al., 2018; Tang et al., 2014). Current-clamp whole-cell recordings demonstrated that both exogenous LL application (0.2-20 mM) and optogenetic stimulation of astrocytes promoted reversible depolarisation and increased action potential firing of LC noradrenergic neurones (Tang et al., 2014). This effect was dose-dependent with an EC_{50} of approximately 680 µM and was avoided by pre-treatment with compounds that prevent LL formation (Tang et al., 2014). Moreover, direct measurements of NA release with fast-scan cyclic-voltammetry showed that LL application as well as optogenetic activation of astrocytes triggered NA release from LC organotypic slices. On the other hand, bath-application of DL (0.001-2mM) almost fully abolished depolarisations in LC neurones evoked by optogenetic activation of astrocytes, and also blocked the stimulatory effect of LL on the release of NA by LC neurones (Tang et al., 2014). The excitatory effect of LL was further shown *in vivo*, where injections of LL into the LC increased arterial blood pressure and evoked an arousal response comparable to the effect of the excitatory transmitter L-glutamate as measured at the level of the cortical electroencephalogram (EEG) (Tang et al., 2014). Pharmacological manipulations showed that the LL effect on noradrenergic neurones is mediated by the activity of adenylate cyclase and protein kinase A, implying the involvement of cAMP as the intracellular second messenger following LL-induced activation of a Gs protein-coupled receptor in noradrenergic neurones (Figure 1.9) (Tang et al., 2014).

When assessing the role of LL in the rostral ventrolateral medulla (RVLM), it was found that bath application of LL in brainstem slices *in vitro* evoked depolarization and elevated rates of action potential firing in C1 neurones (Marina et al., 2015). Moreover, *in vivo* administration of LL on the ventral surface of the medulla oblongata of normotensive rats evoked a profound and sustained increase in the sympathetic nerve activity and arterial blood pressure (Marina et al., 2015). Thus, overexposure of the RVLM to LL may actively contribute to the development and maintenance of hypertension by intensifying the activity of pre-sympathetic C1 bulbospinal vasomotor neurones and consequently the sympathetic tonus (Marina et al., 2015).

The receptor underpinning LL actions in the brainstem (LLRx) has not been identified yet and it does not fit the properties of the receptors that have already been described to be selectively activated by LL. OR51E2, where LL-induced activation also increases cAMP, has not been detected in dissociated noradrenergic neurones in the LC, implying that this receptor may not be accountable for the cAMP-mediated excitatory effects of LL in neurones of the brainstem (Mosienko et al., 2018). Next generation sequencing of isolated noradrenergic neurones in the LC identified expression of a range of orphan G protein-coupled receptors in this region, and their ability to be stimulated following LL application was further tested using an assay that measures cAMP (Mosienko et al., 2018). Amongst the receptors analysed, GPR137 transiently expressed in HEK293 cells displayed a dose-dependent enhancement of intracellular cAMP levels following application of 1-5 mM LL. This response, however, was not blocked by the application of the enantiomer DL (0.4 mM), indicating that GPR137 may not be the proposed LLRx (Mosienko et al., 2018).

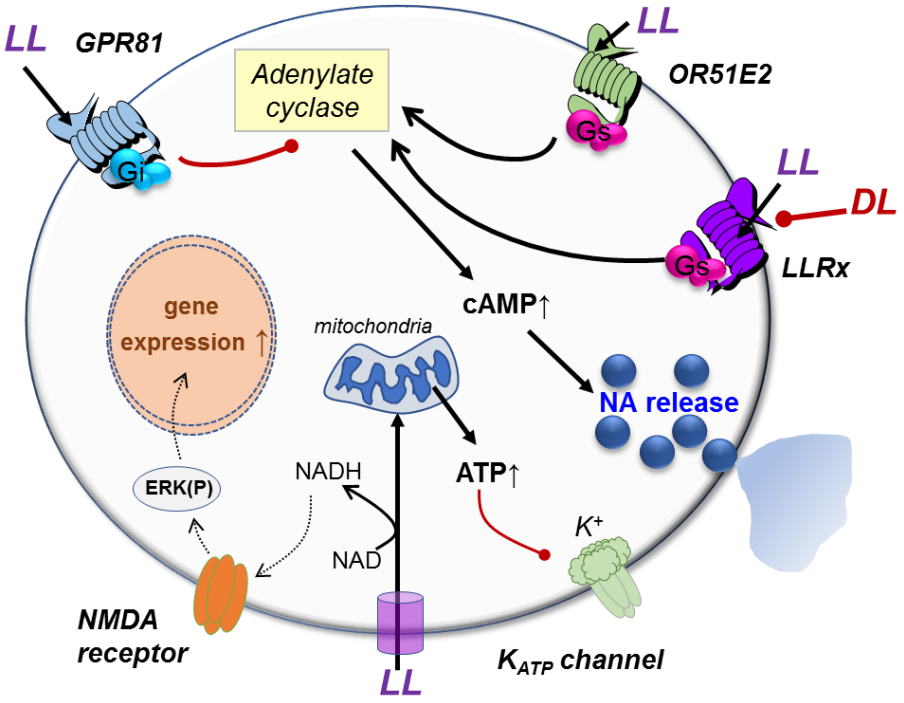

Figure 1.9. LL-mediated signalling pathways in neurones. LL interacts with neuronal Gi- or Gs-coupled receptors leading to inhibition or activation of intracellular cAMP-dependent signalling pathways, with the potential of ultimately, for example, decreasing or inducing neuronal activity and NA release. LL can also be transported into the neuronal cytosol to be metabolised. Products of LL metabolism such as NADH and ATP can modulate gene expression through NMDA receptor or increase neuronal activity by inhibition of K_{ATP} channel, respectively. Schematic adapted from Mosienko et al. (2018).

1.5 Study of LL-mediated astrocyte-neurone signalling

Astrocytes are able to modulate neuronal activity through the release of LL. During periods of high activity, astrocyte-derived LL is thought to act as an additional metabolic supply to neurones. Moreover, LL has signalling roles in the brain and its release can affect a range of vital brain functions, including learning and memory and the central control of respiration and cardiovascular performance. Studying the effects of astrocyte-derived LL in the brain requires tools that limit the long-term release of LL selectively from astrocytes as well as the actions of LL in neurones.

The aim of my PhD project was, therefore, to develop and validate novel genetic tools to selectively limit LL-mediated signalling between astrocytes and neurones *in vitro* and *in vivo*. In order to achieve this goal, the novel molecular tools aimed to targeted

different aspects of astrocyte-derived LL signalling, which included: (I) reduction of intra-astrocytic LL pool; (II) production and release of an antagonist of LL actions in noradrenergic neurones; and (III) reduction of astrocytic LL release. Construction and validation of these tools are presented in the following chapters.

Chapter 2 – Technical approaches to study astrocytic L-lactate dynamics and astrocyte-neurone communication

2.1 Molecular approaches to manipulate brain cells

Neuroscience research over the past decades has benefited from advances in molecular biology. Development of new tools to target specific brain cells with transient or stable expression of transgenes provided the means to address the role of astrocytes in supporting and actively modulating brain function.

A fundamental requirement for specifically studying astrocytes in a physiological setting is the ability to selectively manipulate their activity, independently of the neurones'. This can be achieved by using astrocyte-selective promoters, which restrain transgene expression specifically to astrocytes. Astrocyte-specific promoters can drive the expression of genetically encoded reporters such as fluorescent nanosensors for high-resolution imaging of intracellular astrocytic physiology. To selectively manipulate astrocytic signalling, expression of optogenetic and pharmacogenetic actuators, such as channelrhodopsin and designer receptors exclusively activated by designer drugs (DREADDs), respectively, have been used. Efficient expression of transgenes in astrocytes requires effective gene delivery tools. Apart from transgenic animals, which are restricted to mice in astrocyte research, transgene expression or suppression in subpopulations of mature astrocytes *in vitro* and *in vivo* can be achieved with viral vectors.

My PhD research has been centred around the development of novel molecular tools designed to affect intra-astrocytic levels of LL, with the ultimate goal of expanding the knowledge on astrocytic LL dynamics and astrocyte-to-neurone LL signalling in different physiological contexts. The strategies to target and deliver the expression of these novel LL-limiting tools to astrocytes will be briefly detailed in this chapter. My work included the construction of the tools and performance of a range of physiological tests on LL dynamics and signalling in the brain in order to validate the novel constructs. As also briefly described in this chapter, many of these validation techniques relied on the detection of specific metabolites or messengers, which in turn was performed by genetically-encoded proteins or through enzymatic activity.

2.2 Approaches to selectively target specific brain cells

Comprehending the role of astrocytic signalling in modulating brain function requires specific and effective manipulation of cell types in the brain. In our case, in order to modulate LL production or release specifically in astrocytes, we had to combine the efficient transgene delivery system based on viral vectors with a promoter that targets transgene expression selectively to astrocytes. Achievement of the proposed objective of this project depended, therefore, on the ability of the transgene to be expressed in the target cell at a rate that evokes a physiological response.

2.2.1 Viral vectors

Genetic manipulation of brain cells depends on efficient and controlled gene transfer systems. Taking into account the high capability of viruses to infect mammalian organisms, the development of viral vectors for gene delivery allowed achievement of high transduction efficiency at the same time that viral pathogenicity could be overcome by genetic modifications (Merienne, Douce, Faivre, Déglon, & Bonvento, 2013). Indeed, deletion of parts of the viral genetic material that is linked to the pathogenic viral mechanisms increased the cloning capacity of these vectors, allowing insertion of longer transgenes into the viral genome. Gene transfer through viral vectors is achieved independently of the age of the targeted tissue or organism and, in most of the cases, the genetic material does not require cells to divide to be successfully delivered (Merienne et al., 2013).

The most commonly used viral vectors in neuroscience research are adenoviral vectors (AVVs), adeno-associated viral vectors (AAVs), and lentiviral vectors (LVVs), whose characteristics are further detailed below. AVVs were extensively used in this study as a tool to deliver the novel constructs into primary cultured astrocytes and organotypic brain slices.

2.2.1.1 Adenoviral vectors

Adenoviruses are medium sized non-enveloped viruses containing approximately 36 kb of double-stranded (ds) DNA (Graham & Prevec, 1995). Since adenoviruses are formed only by a protein shell (capsid) and DNA, their infection process relies on interactions between the viral protein fibres with a range of protein receptors expressed in the membrane of the host cell (Merienne et al., 2013; Teschemacher, Paton, & Kasparov, 2005). This fact determines the tropism of different serotypes of adenoviruses to different brain cell types. Indeed, modifications of adenoviral capsids leading to shifting of viral tropism has been utilised in order to select the cellular type to be transduced (Wickham, 2000). Adenovirus infection is initiated by binding of the capsid fibre to the coxsackie adenovirus receptor expressed in the membrane of the target cell (Koizumi, Kawabata, Sakurai, & Watanabe, 2006; Merienne et al., 2013). Following virus-receptor interaction, viral particles are internalized into the host cell through endocytosis. Once uncoated in the cytoplasmic endosomes, viral DNA is transported into the nucleus, where it can be transcribed and replicated (Koizumi et al., 2006). This virus-receptor-based entry mechanism is shared among many types of viruses, while the fate of the viral genetic material once in the host cell varies according to the viral vector employed. AVVs DNA genome, for example, remains episomal in the host cell nucleus. The failure of the transgene to insert into the host genome results in transient expression, which in turn may lead to a quick transgene dilution, particularly in dividing cells (Kasparov et al., 2004). On the other hand, extrachromosomal localization of the transgene decreases the risk of insertional mutagenesis (Merienne et al., 2013).

Although several serotypes of adenoviruses have been identified, only a few of them have been described to infect brain cells. One of the most commonly used adenovirus serotypes for CNS applications is derived from the type 5 serotype, whose genes are divided according to the stage of the replication cycle they are involved in. Thus, early genes, i.e. early region 1 (E1; comprised of E1a and E1b), E2, E3, and E4, are expressed prior to DNA replication, while late genes express after the replication has started (Graham & Prevec, 1995). Incorporation of large transgene fragments into recombinant adenoviruses requires deletion of significant amounts of viral DNA, which is generally acquired by removal of E1 and E3 genes (Graham & Prevec, 1995).

The first gene is involved in viral replication, whereas the latter is a non-essential gene associated with immune evasion. E1 deletion renders a replicating-incompetent virus that can only be propagated in cells that supply E1 gene products, such as the human embryonic kidney 293 (HEK293) cell line (Graham & Prevec, 1995). The increased cloning capacity of replication-defective AVVs allows insertion of more than 7kb fragments, which is completely adequate to accommodate a transgene containing a promoter and 1 or 2 genes (Teschemacher et al., 2005). Although the initial construction of AVVs can take months to materialize, any subsequent amplification is a matter of days and yields high titres of vector particles (approximately 2.5ml per preparation at a concentration ranging from 10^{10} to 10^{12} transducing unit (TU)/ml), which is sufficient material for a substantial series of imaging and electrophysiological experiments (Teschemacher et al., 2005).

2.2.1.2 Lentiviral vectors

A widely used and described LVV is derived from a subclass of retrovirus, the human immunodeficiency virus (HIV)-1. Viral entry into the target cell is initiated by binding of the glycoproteins of the viral envelope with receptors expressed in the cellular membrane. Therefore, as for the other viral vectors, capsid/envelope-receptor interactions dictate the viral tropism, which can be modified through genetic alterations of the viral structure (Kay, Glorioso, & Naldini, 2001). Accordingly, in order to extend the host-range of LVVs, the majority of the original LVVs envelope has been completely substituted by a protein coat from an unrelated virus, a process called pseudotyping. A commonly used foreign envelope is the vesicular stomatitis virus glycoprotein G (VSVG), which broadens LVV tropism by binding with the ubiquitously expressed low-density lipoprotein (LDL) receptor (Amirache et al., 2014).

Regarding the genetic material, LVVs carry a single-stranded (ss) RNA genome of 7 to 11 kb. Once within the host cell, the viral RNA is retro-transcribed into ds DNA, which is incorporated into the host cell genome resulting in stable and long-lasting expression of the transgene (Merienne et al., 2013). Another advantage of LVVs is their high cloning capacity. Since only a small segment of the original HIV genome is retained during the production of the viral vector, LVVs are in theory able to accommodate around 11kb of expression cassette (Coleman et al., 2003).

2.2.1.3 Adeno-associated viral vectors

Adeno-associated viruses are small and non-enveloped particles containing approximately 5 kb of ss DNA (Grimm, 2002). Even though the wild-type viral genome was almost entirely removed, leaving only essential genes for packaging and integration, the cloning capacity of AAVs is rather low due to the short genome length (Grimm, 2002). On the other hand, although AAVs are able to naturally infect human cells, they haven't been linked with any human disease. This non-pathogenic feature of AAVs make them a quite safe tool for gene delivery, especially for gene therapy in the brain (Kay et al., 2001).

Many serotypes of AAVs have been identified so far, each of them displaying a specific tropism towards various types of brain cells. As previously detailed, viral tropism may rely on the expression level of a cell surface receptor that recognizes and binds to the viral capsid, starting the virus entry process. Accordingly, AAV2 infection depends on the expression of both the heparan sulphate proteoglycan receptor and the fibroblast growth factor receptor 1, which results in a predominant tropism for neurones (Merienne et al., 2013). Tropism of AAV5, on the other hand, depends on the level of expression of the platelet-derived growth factor receptor (Merienne et al., 2013). Several AAV variants have been developed by genetic modification of the capsid in order to improve cell specificity.

Once inside cells, AAVs require a helper virus (adenovirus or herpesvirus) to perform their replication cycle (Shin, Yue, & Duan, 2012). Since this infection step is absent during transgene transduction, AAVs remain as extrachromosomal ds episomes, although some reports suggest a possible integration into the host genome (Kay et al., 2001). Different from AVVs, AAVs show long-lasting and stable expression of the transgene, which is believed to be due to the formation of circular intermediates and/or integration into the host genome (Duan et al., 1998; Schnepp, Jensen, Chen, Johnson, & Clark, 2005).

2.2.2 Cell-specific promoters

The CNS is occupied by an extensive range of cell phenotypes, each of them containing an exclusive profile of gene expression. Determination of this spatial and temporal expression pattern of genes is mediated by a regulatory region in the DNA called the promoter. The promoter enables the transcription of a specific gene by binding with the transcription factors needed to transcribe that gene (Nettelbeck, Jérôme, & Müller, 1998). Therefore, the different gene expression profiles amongst cells in a non-homogenous population such as the brain relies on specific promoters and the recruited transcription factors (Betley & Sternson, 2011; Nettelbeck et al., 1998).

In the construction of a transgene, a promoter sequence must be added in the expression cassette so that the endogenous cellular machinery can transcribe the transgene DNA sequence into mRNA. In case the transgene expression is targeted throughout the brain, a promoter of an endogenous ubiquitously expressed gene is employed. On the other hand, if transgene expression needs to be confined to a specific cell type, promoters of genes with restricted expression in this cell type are used to confer specificity to transgene expression. The challenge imposed by the application of cell-type specific promoters is generally their long size in mammals, which may hamper their use with AAVs due to the modest packaging capacity of this gene delivery tool (Betley & Sternson, 2011).

2.2.2.1 EF1α promoter

Human elongation factor-1α (EF1α) is a ubiquitous enzyme that catalyses the nucleotide-binding protein implicated in the elongation of polypeptide chains during protein synthesis on the ribosome (Riis, Suresh, Derventzi, & Clark, 1990). Cellular expression levels of EF1α are considered to be generally high, especially in actively dividing cells (Sanders, Brandsma, Janssen, Dijk, & Möller, 1996). As a consequence, EF1α gene transcription occurs at high rates, rendering this promoter a high activity, being widely regarded as a constitutive promoter (Kasparov et al., 2004).

Although the precise expression pattern of this promoter in brain cells has not been described yet, the crucial housekeeping function of EF1α contributes to its relatively continuous expression in the majority of cell types (Tsuchiya, Yoshiki, Kudo, & Morita, 2002). Utilization of the EF1α promoter to drive green fluorescent protein (GFP) expression in rat cortical primary cultures suggested primarily labelling of neuronal cells (Tsuchiya et al., 2002). In the brainstem, EF1α-driven expression of enhanced GFP (EGFP) targeted neurones as well as some glial cells, suggesting a wide spectrum of cells supporting transgene expression driven by EF1α (Kasparov et al., 2004).

2.2.2.2 CMV promoter

Cytomegalovirus (CMV) immediate-early promoter is widely used to drive gene transcription in a broad range of cell types. Similar to EF1α, CMV promoter is considered to be constitutive, i.e. expressing at high levels in cells on account of the variety of response elements and enhancers associated (Teschemacher et al., 2005). Although function of CMV promoter is affected by regulatory elements of the host cell, the extent by which cellular environmental conditions affect promoter activity still remains unclear (Teschemacher et al., 2005). Activation of the transcription factor cAMP response element-binding (CREB), for instance, leads to increased activity of the CMV promoter (Wheeler & Cooper, 2001). This response is suggested to be due to the 5 cAMP response elements (CRE) present in the CMV promoter, binding of which with CREB results in improved gene transcription (Wheeler & Cooper, 2001). Nonetheless, some cells can silence the promoter following long-term expression of the transgene (Löser, Jennings, Strauss, & Sandig, 1998; Sinclair, Baillie, Bryant, Taylor-Wiedeman, & Sissons, 1992)

2.2.2.3 GFAP promoter

Glial fibrillary acidic protein (GFAP) is an intermediate filament extensively used as an astrocytic marker. GFAP is an essential component of the astrocytic cytoskeleton and is suggested to be the main element responsible for maintaining astrocytic shape and mechanical strength (Middeldorp & Hol, 2011; Wang & Bordey, 2008). Besides

the morphological and structural role of GFAP, changes in its expression levels have been suggested to alter other cellular processes such as migration, motility, and proliferation (McIver, Faideau, & Haydon, 2013; Middeldorp & Hol, 2011). Moreover, reactive changes displayed by astrocytes after CNS injury have been shown to include upregulation of GFAP expression (Middeldorp & Hol, 2011).

Although GFAP-expressing cells have been systematically classified as astrocytes, not all astrocytes express GFAP. Evaluation of GFAP distribution within the CNS indicated that the brainstem expresses the highest level of this protein, while scarce GFAP expression is found in astrocytes residing in the striatum and cortex (Martin & O'Callaghan, 1995). Moreover, reports of GFAP-expressing neural stem cells in the subventricular zone challenged the utility of GFAP as an astrocyte-specific marker (Chojnacki, Mak, & Weiss, 2009; Doetsch, Caillé, Lim, García-Verdugo, & Alvarez-Buylla, 1999; Oberheim et al., 2012). In reality, rather than using genetic and functional profiles for astrocytic characterization, assignment of brain cells as astrocytes has been classically done following phenotypic criteria. This may be due to the paucity of proteins that are selectively and ubiquitously expressed by astrocytes (Oberheim et al., 2012) which, in turn, can be explained by an increasing body of evidence implying that astrocytes are a heterogenous population of cells (Khakh & Deneen, 2019; Matyash & Kettenmann, 2010), a concept that has already been thoroughly demonstrated for neurons.

Nevertheless, GFAP is still a widely accepted astrocytic marker and its regulatory elements are extensively used in the development of promoters that direct transgene transcription specifically to astrocytes (Brenner, Kisseberth, Su, Besnard, & Messing, 1994; Lee, Messing, Su, & Brenner, 2008; Liu, Paton, & Kasparov, 2008). An expression system based on the GFAP promoter (gfa2) was first developed by Brenner et al. (1994). It consisted of a 2.2 kb 5'-flanking fragment of the human GFAP gene that successfully drove transgene expression in astrocytes in transgenic mice (Brenner et al., 1994). In order to optimize transcriptional activity and shorten the size of the GFAP promoter, Lee et al. (2008) developed the variant gfaABC1D, which contained 681 bp and achieved nearly double the activity of gfa2 (Lee et al., 2008). The approach to generate gfaABC1D relied on identification and removal of promoter sequences that hamper astrocyte specificity and decrease transcriptional performance. Yet, another strategy to enhance activity of mammalian promoters is to

employ recombinant transcriptional activators, also referred to as two-step transcriptional amplification (Figure 2.1) (Liu et al., 2006). It relies on the cell-specific promoter driven-expression of both a transgene and a recombinant fusion protein, the latter consisting on a strong artificial transcriptional activator domain and a DNA binding site (Liu et al., 2006). Binding of the transcriptional activator to specific sites introduced into the promoter potentiates transcriptional activity, which consequently improves transgene expression. However, to achieve simultaneous expression of the transgene and the transcriptional activator, inclusion of two copies of the cell-selective promoter were necessary, restricting the employment of viral gene targeting strategies with smaller cloning capacities (Liu et al., 2008). In order to overcome this limitation in the design of a strong astrocyte-selective promoter based on recombinant transcriptional activators, our group has used a bidirectional promoter approach, in which a minimal CMV (mCMV) core promoter (65 bp) was merged upstream and in opposite direction to gfaABC1D promoter (Figure 2.1) (Liu et al., 2008). Expression of GAL4p65, a chimeric transactivator formed from a fragment of the transcriptional activation domain of the murine NF-κBp65 protein fused to the DNA-binding domain of the GAL4 protein from yeast, is driven by the mCMV promoter. GAL4p65 binds to its binding domain (5xGAL4) located 5' to the gfaABC1D promoter, thus enhancing astrocyte-specific transgene expression (Liu et al., 2008).

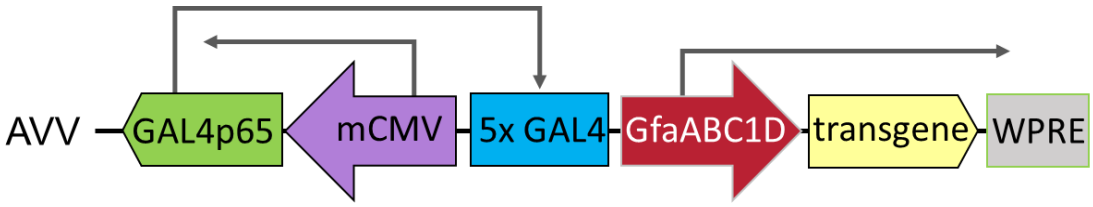

Figure 2.1. Schematic diagram of the synthetic bidirectional astrocyte-specific promoter with enhanced transcriptional activity (sGFAP). Astrocyte-selective promoter with enhanced transcriptional activity, also known as sGFAP, contains a mCMV core promoter upstream in the expression cassette and in opposite direction to drive the synthesis of the strong transcriptional activator GAL4p65. Besides the transcriptional activation domain of the NFκB p65 protein, the chimeric transactivator GAL4p65 also contains the unique binding domain of the GAL4 protein from yeast, which interacts with GAL4 binding sequences in the gfaABC1D promoter. As a result, transcription driven by the sGFAP promoter is enhanced (Liu et al., 2008). A woodchuck hepatitis post-transcriptional regulatory element (WPRE) at the end of the expression cassette further increases transgene expression.

2.2.2.4 PRSx8 promoter

Since neuroscience research has historically centred on neuronal activity, the functional diversity of different neuronal subtypes has long been recognized. Neurones have been systematically categorized into groups based on similarities between gene expression profile, molecular properties, and function, which facilitated the development of subpopulation-restricted gene targeting strategies to manipulate each neuronal type independently. In our group, there is long-standing interest in the study of astrocytic interactions specifically with noradrenergic neurones since we have previously discovered a relevant signalling axis between these two cell types in the rat brainstem (Tang et al., 2014). In order to target transgene expression selectively in noradrenergic neurones, we used a synthetic promoter developed by Hwang et al. (2001), the PRSx8, which carries a noradrenergic-specific *cis*-regulatory element (PRS2) (Hwang et al., 2001). PRS2 has been identified in the human dopamine β-hydroxylase (DBH) promoter and has been described to interact with Phox2a/2b, a transcription factor that is crucial for neuronal differentiation into the noradrenergic phenotype (Hwang et al., 2001; Kasparov et al., 2004). PRSx8 is comprised of 8 binding sites of Phox2a/2b merged with a minimal DBH promoter containing a TATA box and a transcription start site (Hwang et al., 2001). Experiments *in vitro* and *in vivo* using PRSx8 promoter to drive transgene expression through AVV or LVV showed high selectivity and transcriptional activity of the promoter, enabling characterization of NA release and *in vivo* modulation of the cardiovascular system activity (Chiti & Teschemacher, 2007; Duale et al., 2007; Lonergan et al., 2005).

2.3 Approaches to study compound-specific dynamics in the brain

The processes related to brain energy metabolism lead not only to the generation of cellular energy currency which supports appropriate cell function and tissue viability. They also drive the production of metabolites that carry important signalling roles in the brain. Therefore, interfering with LL production, release and signalling as proposed by this research project requires employment of tools able to analyse the fluxes of metabolites within cells and tissues as well as evaluate how these modifications influence certain neurone-astrocyte signalling pathways.

By using experimental approaches that combine a range of compound-specific sensors with real-time imaging techniques and amperometric recordings, it is possible to analyse the effects of transgenic or pharmacological interventions in the glycolytic state of individual astrocytes. Employment of these sensor-based procedures also allows the assessment of how modifications at the cellular level translate into adjustments of the cerebral LL tone and release, as well as into astrocyte-neurone LL signalling. Utilization of intracellular or extracellular biosensors are advantageous at the temporal resolution since they offer real-time recording of specific molecules (Barros et al., 2017). The mechanism of detection includes either a selective binding site or enzyme. Modifications in the concentration of the molecule of interest are detected by changes in either the fluorescence intensity of the sensor or the amount of the product yielded by the enzymatic reaction, respectively.

2.3.1 Genetically-encoded fluorescent nanosensors

Genetically-encoded fluorescent nanosensors are chimeric proteins that mandatorily express two elements: a unique binding site, which confers specificity to a certain compound, fused to one or two fluorescent proteins. The detection domain can be comprised of a bacterial protein or a transcription factor and undergoes conformational change upon binding of the ligand (Barros et al., 2017). Binding and fluorescence are conformationally coupled in the nanosensor, so that a structural change in the binding domain dynamically modifies fluorescence intensity of the fluorophores, which can be detected through microscopy, fluorescence platereader, and fluorescence-activated cell sorting (FACS). Microscopy is undoubtedly the most suitable method to monitor changes in fluorescence intensity since its high resolution allows visualization of single-cells and provides real-time readout of the nanosensor in continuous superfusion conditions (Barros et al., 2017). Conversely, in platereaders, continuous superfusion is impractical and spatial and temporal resolution are reduced. FACS, on the other hand, is not recommended when analysing the metabolic state of cells since metabolic properties can change following cellular detachment that is required to perform this technique (Hung & Yellen, 2014).

Many of the genetically-encoded fluorescent nanosensors are based on Förster Resonance Energy Transfer (FRET), which relies on two fluorescent proteins with

overlapping emission and excitation spectra. If they are in close proximity, i.e. within roughly 10nm, the fluorophore in the higher excited state (donor) transfers energy to the second fluorophore (acceptor) (Jones & Bradshaw, 2019; Sahoo, 2011). As a result, the emission intensity of the donor fluorophore decreases while the emission intensity of the acceptor fluorophore increases. Binding of the ligand to the recognition domain can either bring the two fluorescent molecules closer together or further apart, increasing or decreasing, respectively, the FRET efficiency (Sahoo, 2011). The readout from FRET-based nanosensors is the ratio of the fluorescence emitted by the fluorophores.

2.3.1.1 FRET-based L-lactate nanosensor

A genetically-encoded and FRET-based reporter for LL – Laconic – has been widely used for the determination of intracellular LL dynamics *in vitro* and *in vivo* (Mächler et al., 2016; San Martín et al., 2013). The LL-binding domain of Laconic consists of the bacterial transcriptional factor LldR from *E. coli*, which is defined by two elements: a LL-binding/regulatory domain and a DNA-binding domain (San Martín et al., 2013). The recognition element is attached at one side to the fluorescent protein mTFP and at the other side to the fluorescent protein Venus (Figure 2.2A), with emission peaks at 492 nm and 526 nm, respectively (San Martín et al., 2013). When LL is unbound, mTFP acts as a photon donator to the acceptor Venus upon excitation with the 458nm line of an argon laser. However, binding of LL evokes a conformational change in the biosensor, increasing the distance between the two fluorophores. FRET efficiency then decreases, leading to enhanced ratio of mTFP over Venus (Figure 2.2B). Fluctuations in the intracellular concentration of LL can, therefore, be monitored through the ratio between the fluorescence emitted by mTFP and Venus (San Martín et al., 2013).

Laconic has been described to exhibit high specificity to LL and to be able to detect LL changes over four orders of magnitude (from 1µM to 10mM) with maximum increase in Laconic FRET ratio being around 25% (San Martín et al., 2013).

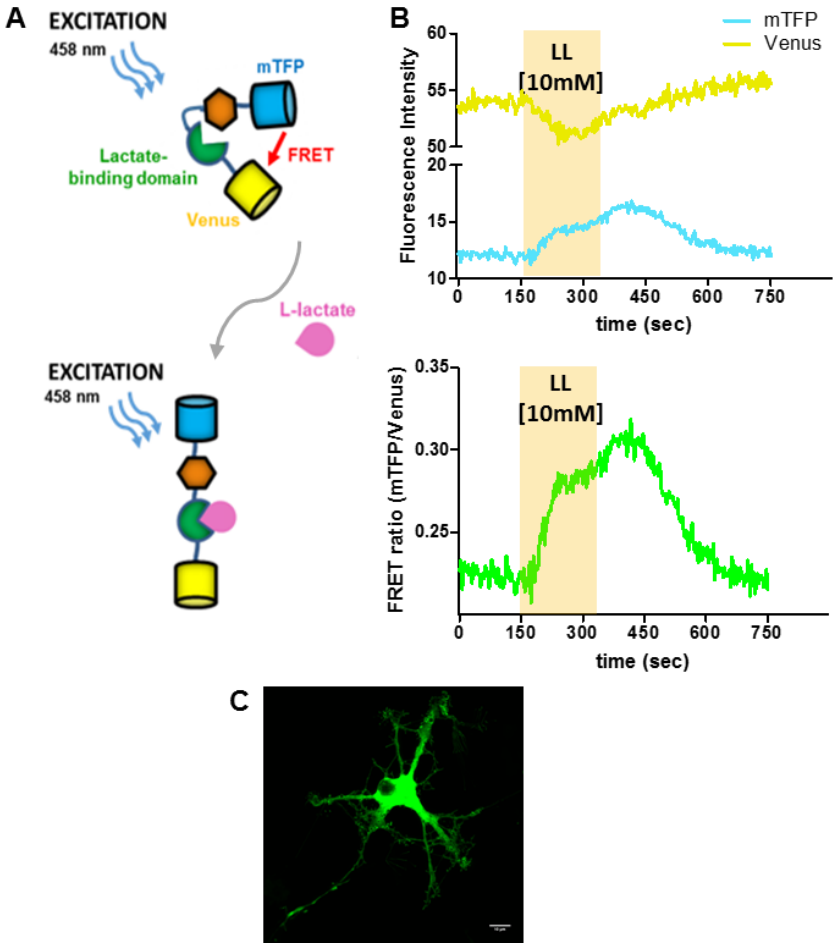

Figure 2.2. Characterization of Laconic. (A) Representative Laconic structure: in the unbound state, proximity between the 2 fluorophores enable the transfer of photons from the donor mTFP to the acceptor Venus. LL binding evokes a conformational change in Laconic, increasing the distance between the two fluorescent proteins, which causes a decrease in FRET efficiency and enhanced ratio of mTFP over Venus. **(B)** Top – representative FRET recordings showing fluorescence intensity of mTFP and Venus in HEK293 cells upon application of 10mM LL. Below – resulting FRET ratio. **(C)** Image of Laconic-transduced cultured astrocyte. Scale bar 10 µm.

2.3.1.2 FRET-based pyruvate nanosensor

Pyruvate is a central molecule in brain energy metabolism. By using the FRET-based pyruvate nanosensor Pyronic, we can estimate intracellular pyruvate levels. The detection domain of Pyronic consists of the transcriptional regulator PdhR from *E. coli*, which coordinates the pyruvate-induced expression of the pyruvate dehydrogenase gene (San Martin et al., 2014). Similar to Laconic, the binding element of the sensor is linked to the fluorescent proteins mTFP and Venus, which act as a photon donor and acceptor, respectively (Figure 2.3A). Upon pyruvate binding, the sensor assumes an open conformation, which decreases the FRET efficiency between the two fluorophores. As a result, the fluorescence intensity emitted by mTFP increases while that in Venus decreases, causing an increased ratio between mTFP and Venus (Figure 2.2B).

Pyronic has been shown to detect pyruvate at concentrations ranging from 10µM to 1mM (San Martin et al., 2014). Moreover, the sensor did not show significant pH-dependence, nor sensitivity to other compounds. The maximum change reported in fluorescent intensity was described as approximately 25% in culture conditions and around 40% *in situ* (San Martin et al., 2014).

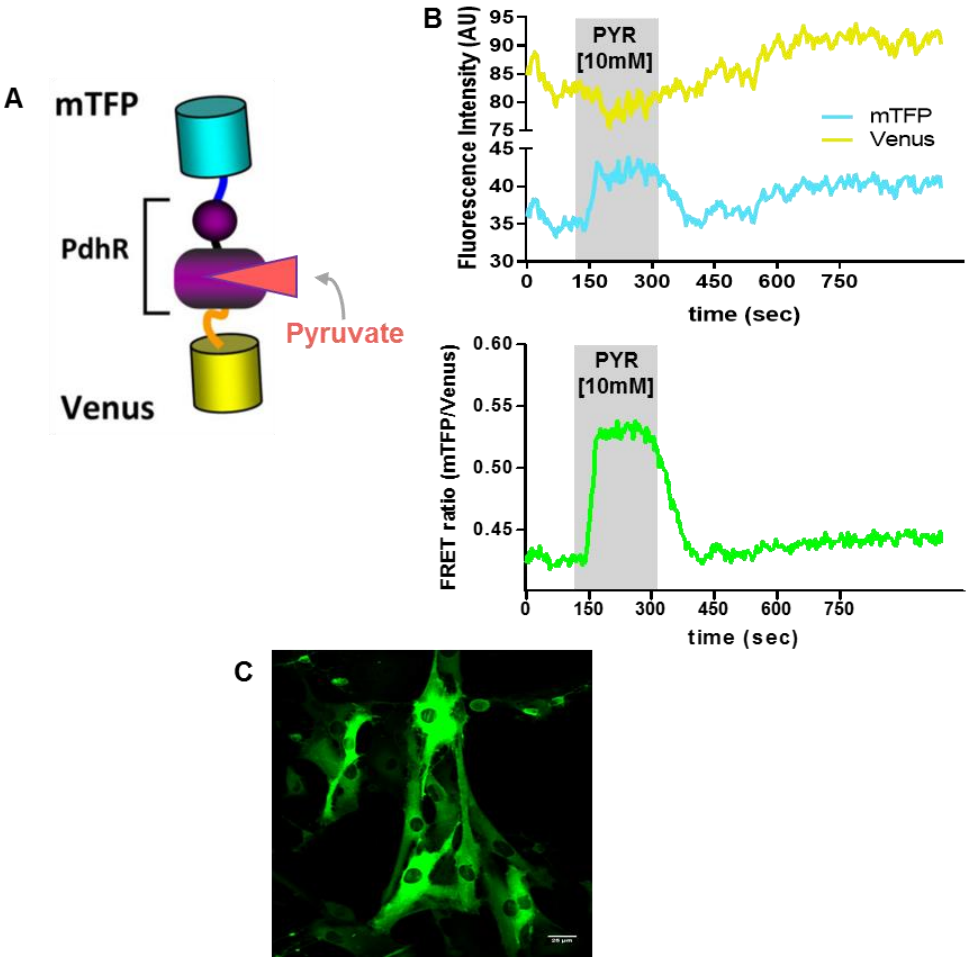

Figure 2.3. Characterization of Pyronic. (A) Representative Pyronic structure at the bound state depicting the binding element of the sensor (PdhR) and the FRET pair of fluorescent proteins – mTFP (photon donor) and Venus (photon acceptor) (San Martin et al., 2014). **(B)** Top – representative FRET recordings showing fluorescence intensity of mTFP and Venus in cultured astrocytes upon extracellular application of 10mM pyruvate. Below – resulting FRET ratio. **(C)** Image of Pyronic-transduced cultured astrocytes. Scale bar 25 µm.

2.3.1.3 Cell-based neurotransmitter fluorescent engineered reporter

NA in the brain is involved in the modulation of various processes, including arousal, attention, anxiety, and nociception (see Chapter 1, section 1.1.3). NA is mostly released in the interstitial space, in the absence of synaptic contact, through vesicles exocytosis from axonal varicosities as well as from soma and dendrites of noradrenergic neurones (Chiti & Teschemacher, 2007; Fuxe et al., 2015; Kasparov & Teschemacher, 2008). Real-time detection of NA release is widely performed through fast-scan cyclic voltammetry, which consists of applying triangular waveform at high scan rate at carbon-fibre microelectrodes, causing the electroactive neurotransmitter to rapidly and repeatedly oxidize and reduce (Ribeiro, Fernandes, Pereira, & Silva, 2016). Although fast-scan cyclic voltammetry offers high temporal resolution, it does not distinguish between compounds with similar electrochemical characteristics, such as NA and dopamine. To overcome this limitation, Muller et al. (2014) developed an imaging-based biosensor technology for detection of specific catecholamines that takes into account that NA and dopamine activate different types of G protein-coupled receptors. The cell-based neurotransmitter fluorescent engineered reporters (CNiFERs) of NA are genetically modified HEK293 cells that constitutively express the α_{1A} adrenoceptor and the FRET-based Ca^{2+} nanosensor TN-XXL (Muller et al., 2014) (Figure 2.4A). The α_{1A} receptor couples to a Gq protein, and its activation triggers a rise in the intracellular Ca^{2+} concentration through the phospholipase C–inositol triphosphate pathway. Upon α_{1A} adrenoceptor activation, an increase in Ca^{2+} level is reflected by a change in the FRET ratio of CFP (photon donor) and Citrine (photon acceptor) of TN-XXL (Mank et al., 2008). CNiFERs, therefore, translate noradrenergic volume transmission into fluorescence signals, which can be quantified through microscopy or plate readers.

In vitro and *in vivo* characterization showed that these CNiFERs are sensitive to nanomolar ranges of NA and do not respond to variable concentrations of other neurotransmitters such as serotonin, dopamine and adenosine (Muller et al., 2014). Our own recordings showed changes in FRET ratio following application of low concentrations of NA, confirming sensitivity of this system (Figure 2.4B). CNiFERs have been used to confirm our findings previously obtained by fast-scan cyclic voltammetry, namely, that LL evokes NA release from LC neurones (Mosienko et al.,

2018; Tang et al., 2014). They were then used to test a wide range of LL analogues for their ability to mimic LL effects on LC neurones, in an attempt to map the binding properties of the putative LL receptor on noradrenergic neurones (Mosienko et al., 2018; Tang et al., 2014).

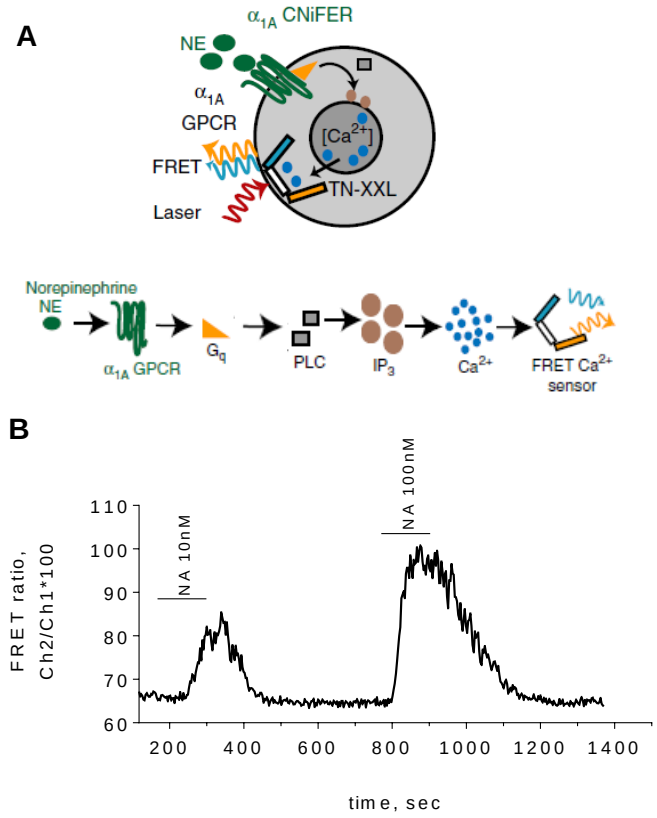

Figure 2.4. Characterization of α1A CNiFERs. (A) Schematic adapted from Muller et al. (2014) showing NA detection using CNiFERs expressing α1A-adrenoceptors and the FRET-based Ca^{2+} sensor TN-XXL. NA binds to the receptor leading to an increase in Ca^{2+}, which can be quantified by TN-XXL FRET signal. **(B)** Representative recordings showing increase in FRET ratio of CNiFERs following application of 10nM and 100nM NA.

2.3.2 Enzyme-based sensors

Electrochemical approaches to detect non-electroactive biomolecules rely on the employment of enzymes that use the analyte of interest as a substrate and drive the formation of an electroactive product (Bucher & Wightman, 2015). The enzyme is immobilized at the tip surface of an electrode and the enzymatic activity, stability and

selectivity while restrained on the electrode will determine the performance of the sensor (Bucher & Wightman, 2015).

The enzyme most employed in sensor-based electrochemical measurements are oxidases, and the electroactive product of their enzymatic reaction is hydrogen peroxide (H_2O_2). In the presence of the electron acceptor O_2 – endogenous oxygen, which is assumed to be available at sufficient concentrations to support the reaction; (Wilson & Johnson, 2008) – the analyte of interest in its reduced form is oxidized, leading to the formation of H_2O_2 as following:

$$SUBSTRATE\ (reduced) + O_2 \rightarrow SUBSTRATE\ (oxidized) + H_2O_2$$

Enzyme-based sensors are often coupled with amperometry. In this case, the sensors are kept at a constant potential that is sufficient to oxidize the electroactive product H_2O_2 and generate a current as following:

$$H_2O_2 \rightarrow O_2 + 2H^+ + 2e^-$$

The resulting current is proportional to the concentration of H_2O_2, and thus of the analyte in the tissue (Wilson & Johnson, 2008). By calibrating the sensor with known amounts of the analyte, current values can be converted into specific quantitative information about analyte concentration in the biological tissue. It is important to highlight, however, that any endogenous electroactive component has a potential to generate a non-specific current. This effect can be minimized by using a second enzyme-free electrode, the readout of which is subtracted from the current generated by the enzyme-based sensor (Bucher & Wightman, 2015). Using a permselective membrane to separate the enzymatic layer from the electrode has also been proven to be an additional useful strategy to decrease interference from endogenous species (Wilson & Johnson, 2008).

Enzyme-based sensors have been widely used for detection of a range of non-electroactive compounds, including LL (Karagiannis et al., 2015), glutamate (Gourine et al., 2008), ATP (Gourine et al., 2010), adenosine (Dale, Pearson, & Frenguelli,

2000), among others. Enzyme-based LL sensors (Sarissa Biomedical, UK) and constant-potential amperometry have been employed in this research project in order to electrochemically detect real-time fluctuations in LL concentration in brainstem organotypic slices under different circumstances. The detection system of LL sensors relies on the enzyme LL oxidase (LOX), which in the presence of O_2 converts LL into pyruvate and H_2O_2 (Figure 2.5). Under a constant potential of +500mV, H_2O_2 is oxidised, generating a current that is proportional to the concentration of LL in the tissue. A second electrode (null) lacking the enzymatic layer is employed to control for non-specific currents.

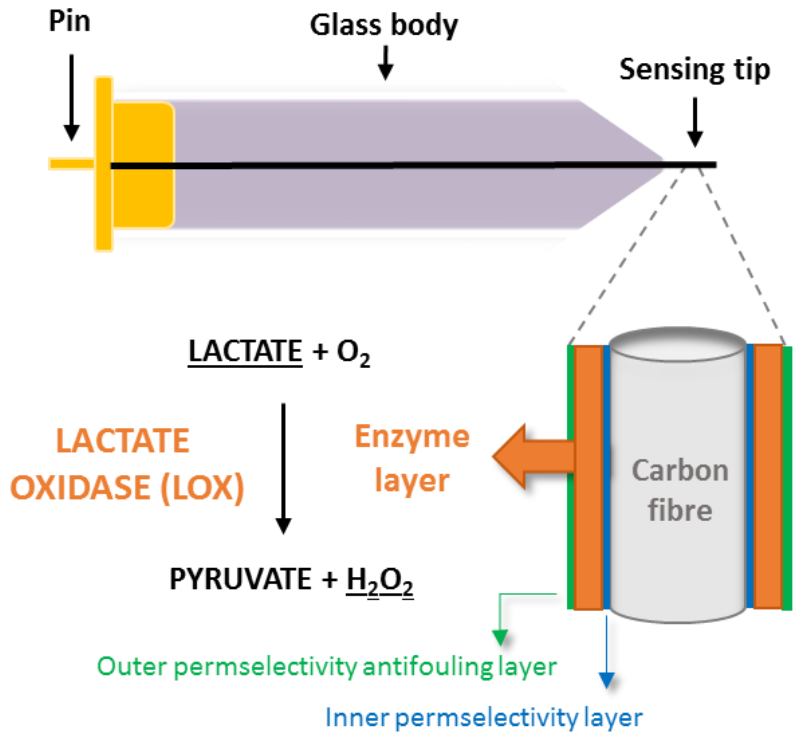

Figure 2.5. Structure of a LL electrode. LL electrode comprises of carbon fibre surrounded by a glass sheath and an uncovered sensing tip. The enzyme LOX around the sensing tip converts LL into H_2O_2, which creates a quantifiable current under a constant potential of +500mV. The electrode incorporates permselective layers as an additional aid to avoid interference from electroactive tissue compounds.

Commercially available LL sensors (Sarissa Biomedical, UK) have a limit of detection of approximately 200nM, which is way below the physiological LL level, and operate at a linear range from 0.5µM to 800µM. Although the majority of our recordings show linearity in the activity of LL sensors, their sensitivity may change over time, which

reiterates the need for consistent re-calibration of the electrodes. Pharmacological agents used in this study were tested for their potential ability to generate non-specific currents through this sensor system. NA (1µM), pyruvate (10mM) and DL (10µM) evoked a negligible current compared to the effect of 10µM LL, confirming specificity of the sensors to LL (Figure 2.6).

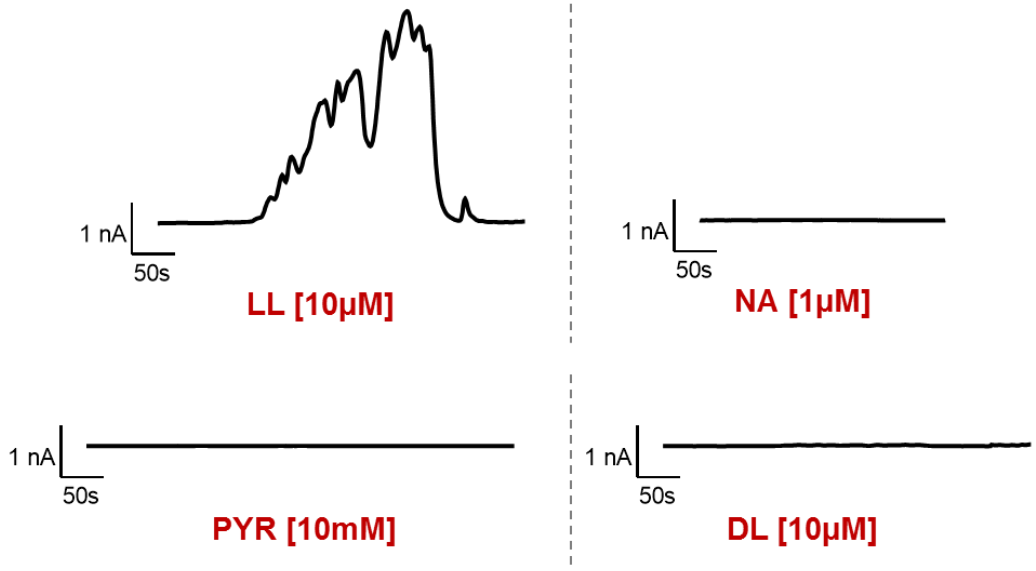

Figure 2.6. Specificity of LL biosensors (Sarissa Biomedical, UK). Traces at the same graphic scale of the current generated by LL electrodes following application of LL (10µM), Na (1µM), pyruvate (PYR, 10mM) and DL (10µM). Compared to LL, current response evoked by the other compounds was insignificant.

In conclusion, the challenge in the investigation of the role of astrocytes in many aspects of brain function is to monitor and manipulate the different cell types independently. The strategies summarized in this chapter allow the delivery of transgene expression in specific brain cells. Moreover, the involvement of astrocytes in brain energy metabolism and the communication between astrocytes and neurones can be investigated using compound-specific sensors to detect in real-time fluctuations in the levels of specific metabolites and messengers.

Chapter 3 – Materials and Methods

This chapter details the approaches used for the design, construction, and validation of the novel molecular tools developed during my PhD project for modulation of LL-mediated astrocyte-to-neurone signalling.

3.1 Molecular cloning

Cloning strategies were designed *in silico* using Vector NTI Software (Invitrogen, USA). DNA sequences of the bacterial enzymes were obtained from Genbank (NCBI), optimized for the mammalian codon preference and made to order by either Life Technologies (USA) or Invitrogen (USA). The open reading frames (ORFs) were incorporated into shuttle vectors for adeno- and lentiviral vectors, i.e. pXCX or pTYF, respectively. Expression cassettes were bicistronic with a red or green fluorescent protein sequence placed downstream of an internal ribosomal entry site (IRES). Different versions also varied according to their promoter - EF1α, CMV, or enhanced GFAP (sGFAP). The recombinant shuttle vectors were propagated in competent bacteria and analysed by diagnostic restriction digestions and partial DNA sequencing (Eurofins MWG, Germany). They were subsequently used for production of viral vectors and/or *in vitro* experimentation.

3.1.1 Restriction enzyme digestion

Construction of a recombinant plasmid requires that both precursor vector backbone and the insert be subjected to restriction digestions with endonucleases so that they exhibit DNA ends suitable for being ligated together. Restriction endonucleases cleave the DNA in specific palindromic sequences, the restriction sites, resulting in analogous blunt or sticky ends in the DNA strands that allow the ligation of the parent vectors. In order to achieve high efficiency restrictive digestion, the DNA and endonucleases were mixed with a suitable bovine serum albumin (BSA)-containing buffer as instructed by the suppliers (New England Biolabs, Promega or Roche). To reach a total volume of 50µl, sterile water was added into the reaction mix, which was briefly and thoroughly mixed and incubated for 45 min at 37°C (or as indicated by the product protocol) in water bath (Table 3.1).

Table 3.1. Standard restriction digestion.

DNA	*1µg*
10X BSA-containing buffer	*5µl*
Restriction enzyme (10,000 units/ml)	*10 units (1µl)*
Sterile water	*Up to 50µl*
Total reaction volume	***50µl***

3.1.2 Blunting DNA sticky ends

In case of lack of compatibility between sticky-ends of vector and insert, a Klenow treatment of DNA was carried out. Klenow consists of a large protein fragment of *Escherichia coli* DNA polymerase I, which retains the 5'→3' polymerase and 3'→5' exonuclease activity but lacks 5'→3' exonuclease activity. Therefore, by filling in 5' overhangs, Klenow forms blunt ends, which are compatible with other blunt-ended DNA fragments and carry a 5' phosphate group that assists with the ligation process. To carry out the Klenow treatment, 1µg of DNA fragment that was purified following restriction digestion was mixed with 2µl of an appropriate filling buffer provided by the supplier (Roche, 11008404001). 1U of Klenow enzyme (Roche, 11008404001) as well as 1mM of deoxynucleotide triphosphate mix (dNTPs, England Biolabs, N0447L) were added into the mixture along with nuclease-free water to make up a total volume of 40µl. The reaction mix was then incubated for 30 min at 37°C and the resulting DNA fragment was again purified using QIAquick PCR Purification Kit (Qiagen, 28104) as described below.

3.1.3 DNA dephosphorylation

In order to avoid re-circularization and subsequent re-ligation of linearized DNA fragments with blunt or compatible ends, alkaline phosphatase from calf intestine (CIAP; Promega, M1821) was used to catalyse the hydrolysis of phosphate groups from the 5'-termini of the plasmid DNA after restriction digestion.

To perform the dephosphorylation reaction, CIAP was firstly diluted in 1x reaction buffer to reach a final concentration of 0.01u/µl. One volume of the diluted CIAP was then mixed with the same volume of 10x reaction buffer and 4 volumes of the digestion reaction mix containing the DNA to be phosphorylated. After 30 min incubation at 37°C in the water bath, another aliquot of one volume of the diluted CIAP was added into the resulting mix, followed by further incubation at 37°C for 30 min. After completion of the dephosphorylation process, DNA was recovered through agarose gel electrophoresis and subsequently purified using QIAquick PCR Purification Kit (Qiagen, 28104).

3.1.4 Polymerase chain reaction

Polymerase chain reaction (PCR) allows amplification of a specific sequence of DNA flanked by sense and antisense oligonucleotide primers that are complementary to the target DNA segment. The procedure requires a thermal cycling protocol that favours different reactions in the synthesis of DNA, i.e. denaturation, annealing, and elongation. PCR also requires nucleotides and DNA polymerase to take place.
Forward and reverse primers were designed using Vector NTI software (Invitrogen, USA) and ordered from Eurofins MWG (Germany). 2.5µl of both forward and reverse primers at a concentration of 10µM were added into the PCR tube (Starlab, I1402-8100) containing 10ng of the template DNA. 1µl of dNTPs [10mM] (New England Biolabs, N0447L) was also included in the PCR mix. Finally, 0.5µl of Phusion High-Fidelity DNA Polymerase and 10µl of 5X Phusion HF Buffer (New England Biolabs, B0518S) were added into the mixture and topped up to a final volume of 50µl by addition of nuclease-free water (Table 3.2).

Table 3.2. Standard components of a PCR.

Components	*Volume*	*Final Concentration*
Forward primer [10μM]	*2.5μl*	*0.5μM*
Reverse primer [10μM]	*2.5μl*	*0.5μM*
Template DNA		*10ng*
dNTPs [10mM]	*1μl*	*200μM*
5X Phusion HF Buffer	*10μl*	*1X*
Phusion HF DNA Polymerase	*0.5μl*	*1unit*
Nuclease-free water	*up to 10μl*	

The PCR tube was then placed into a thermal cycler (G-Storm, UK); the tube lid was heated (110ºC) to prevent condensation of the sample. Initial denaturation at 98ºC for 20s was then performed. At this temperature, hydrogen bonds of the ds DNA template break, yielding 2 complementary ss DNA. The temperature was then lowered and held for 10s to allow annealing of the primers to each strand of the DNA template. Annealing temperature varied according to the primers' Tm, ranging from approximately 45ºC to 72ºC. The extension step was then performed at 72ºC, which is the optimum activity temperature of DNA polymerase, and lasted for 30s per each 1kb of DNA. At this stage, DNA polymerase uses the free dNTPs previously added to the sample to synthetize in 5'-to-3' direction a DNA strand that is complementary to the ss DNA template. This cycle (denaturation, annealing, and extension) was repeated for 25-35 times, yielding exponentially increasing copies of the target DNA sequence. In order to certify that any remaining ss DNA is completed extended, a single extension step of 10s at 72ºC was performed at the end of the PCR.

3.1.5 Annealing of single-stranded oligonucleotides

During construction of a construct to drive the expression of a precursor microRNA (pre-miRNA), complementary ss DNA oligonucleotides were annealed in order to generate a ds DNA insert suitable for ligation with the vector backbone. DNA oligos

were designed using the BLOCK-iT™ RNAi Designer online tool (Invitrogen) and the reagents necessary for the annealing reaction were provided with the BLOCK-iT™ Pol II miR RNAi Expression Vector Kit (Invitrogen, K493600). 5µl of both top and bottom oligo strands at a concentration of 200µM were added into a PCR tube, followed by the addition of 2µl of 10x Oligo Annealing Buffer. To reach a final volume of 20µl, 8µl of DNase/RNase-free water were added into the sample tube, which was subsequently placed in a thermal cycler (G-Storm, UK). After heating the reaction mixture at 95ºC for 4 min, the sample was removed from the thermal cycler and allowed to cool down at RT for 5-10 min. The resulting 50µM of ds oligo mixture underwent serial dilutions to yield a final concentration of 10nM. The sample was then stored at -20ºC until further use for molecular cloning.

3.1.6 DNA purification

Following cloning procedures, contaminants such as primers, nucleotides, enzymes, oil, salts were removed from the DNA sample using the QIAquick PCR Purification Kit (Qiagen, 28104). This procedure is based on the adsorption of the DNA to a silica membrane, which occurs in the presence of high concentration of salts and optimal pH (≤ 7.5).

Firstly, 5 volumes of the high-salt buffer PB containing a pH indicator was added to 1 volume of the DNA sample. In case the colour of the mixture did not turn yellow, the pH was corrected by the addition of 3M sodium acetate, pH 5.0. The sample was then transferred to the QIAquick column placed in a 2ml collection tube. After 30-60s centrifugation, impurities that passed through the column were discarded, while the DNA kept bound to the silica membrane of the column. To wash away salts, 750µl of the ethanol-containing Buffer PE was added to the column, followed by 30-60s centrifugation. The flow-through was discarded and an extra centrifugation step was applied to remove residual PE Buffer. For DNA elution, which is most efficient at low salt concentrations and basic pH, 30µl of nuclease-free water was added to the column. The column was then placed in a clean 1.5ml centrifuge tube and centrifuged for 1 min.

3.1.7 DNA separation by agarose gel electrophoresis

Following restriction digestion that cleaved the DNA plasmid into distinct sized fragments according to the location of the restriction sites in the DNA sequence, agarose gel electrophoresis was carried out for separation and selection of the fragments of interest. In electrophoresis, nucleic acids, which are negatively charged due to their phosphate backbone, migrate to the positively charged anode when loaded in agarose gel placed in an electric field. For the purposes of our cloning strategies, 1% agarose gel has the appropriate molecular sieving property for the movement of the DNA. The speed of DNA migration throughout the gel is proportional to the size of the cut segments and, as a result, the shortest pieces of the plasmid run furthest through the gel.

To carry out this procedure, an agarose gel was freshly prepared using 1% of agarose powder (New England Biologicals, NBS-AG500) suspended in 1X Tris-acetate-EDTA buffer (Sigma, T9650). The mixture was then heated in a microwave until the agarose was completely melted. In order to enable visualization of the DNA after electrophoresis, 0.01% of SafeView Nucleic Acid Stain (NBS Biologicals, NBS-SV1) was added to the solution once the temperature had cooled to about 60°C. This compound binds to the DNA and emits green fluorescence under UV-light. The melted mixture was then poured into a gel casting tray containing a sample comb. Following gel solidification at room temperature (RT), 1 volume of a gel loading dye (Orange G; Sigma, O-3756) was mixed with 4 volumes of DNA sample and subsequently loaded into the wells of the gel. Orange G also contains glycerol, which, due to its high density, eases loading and settlement of the sample at the bottom of the well. For reference purposes, a DNA indicator containing fragments of known size (2-Log DNA Ladder, 0.1-10.0 kb, 1,000µg/ml; New England Biolabs, N3200S) was added in one of the wells and allowed to run in parallel with the samples. The electrophoresis power supply was set to an appropriate voltage and the gel was allowed to run until the samples had migrated a suitable distance. The gel was then placed into a transilluminator and exposed to UV light. A picture was taken for documentation purpose and the fragments of interest were identified by comparison with the DNA marker.

3.1.7.1 DNA recovery after agarose gel electrophoresis

For extraction and purification of the DNA fragments from agarose gel, a QIAquick Gel Extraction Kit (Qiagen, 28704) was used. Like the purification process detailed previously, it relies on the capacity of the DNA to adsorb to a silica membrane in high salt conditions and relatively acidic pH, while the debris can be washed away, followed by DNA elution in nuclease-free water.

Firstly, a sharp and clean scalpel was used to precisely excise the DNA fragment from the agarose gel. The gel slice was placed in a centrifuge tube and 3 volumes of the high-salt and solubilizing buffer QG was added to 1 volume of the DNA-containing gel. The mixture was incubated at 50°C for 10 min in a water bath to allow the gel to dissolve. In case the colour of the mixture turned either orange or violet, 3M sodium acetate (pH 5.0) was added to the mix to correct the pH. The solubilized gel solution was transferred to the silica membrane-containing QIAquick column placed on a provided collection tube. Following 30-60s centrifugation, the flow-through was discarded and additional 500µl of Buffer QG were loaded onto the column to eliminate all traces of agarose from the sample. After 30-60s centrifugation, the flow-though was removed and a washing step was performed in order to eliminate the remaining salts by the addition of 750µl of the ethanol-containing Buffer PE. The column was allowed to stand 2-5 min prior to centrifugation. The resulting flow-through was discarded and the column was centrifuged again to remove all remnants of Buffer PE. Lastly, for DNA elution, the column was placed in a clean centrifuge tube and 30µl of nuclease-free water were added to the centre of the membrane followed by 1 min centrifugation.

3.1.8 DNA ligation

In order to construct a novel recombinant plasmid, the linearized and purified vector and insert fragments were ligated together using the Rapid DNA Ligation Kit (Roche, 11 635 379 001). Ligation of DNA with either sticky or blunt ends relies on the activity of the enzyme T4 DNA ligase, which catalyses the formation of phosphodiester bonds between 5′-phosphate and 3′-hydroxyl groups. An ideal molar ratio of 1:3 (for blunt-end ligations) or 1:5 (for sticky-end ligations) between vector and insert was calculated

prior to the ligation, which took into consideration normalized proportions of mass and length of the DNA fragments as following:

$$\frac{ng\ Vector}{kb\ Vector} = \frac{ng\ Insert}{kb\ Insert} \quad \times \quad \frac{1\ Vector}{3\ or\ 5\ Insert}\ Ratio$$

To proceed with the ligation reaction, appropriate amounts of vector and insert DNA were suspended in 10µl of 2X T4 DNA Ligation Buffer and 2µl of 5X Dilution Buffer in a microcentrifuge tube. The volume of the suspension was topped up to 20µl with double distilled water (dd) water. Lastly, 1µl of T4 DNA Ligase (5U/µl) was added and the ligation reaction mixture was thoroughly but gently mixed and incubated for 20 min at RT. Since success of this step depends on the integrity of each component of the process, appropriate controls were run in parallel with the ligation reaction, such as: 'no insert' (NI), 'no vector' (NV), and 'no ligase' (NL) reactions, in which insert, vector, or the enzyme T4 DNA Ligase, respectively, were lacking. Following DNA ligation, 4µl of the reaction were transformed into competent *E. coli* for propagation.

3.1.9 Transformation of competent cells with plasmid DNA

The recombinant plasmid, which carries a gene conferring resistance to either ampicillin or kanamycin, was propagated in DH5α *E. coli* (Life Technologies, 18265-017). These were made chemically competent to take up plasmid DNA with high transformation efficiency following a heat shock.

DH5α competent cells were thawed on ice, gently suspended and 50µl were mixed with 4µl of each ligation or control reaction mix at 0ºC. This allows the DNA plasmid to bind to the bacterial membrane ready to penetrate the cell. The suspension was then placed in a water bath at 42°C for 45s in order to induce the heat shock, which generates pores in the cell wall allowing the plasmid entry. The cells were subsequently transferred back to ice for 2min in order to stabilise the membranes and trap the DNA plasmid inside, followed by the addition of pre-warmed Luria Bertani (LB) broth (Sigma, L3022). The mixture was then incubated at 37°C for 1 hour with gentle and continuous shaking. This step enables bacterial cells to express the

antibiotic resistance gene from the recombinant plasmid DNA. The bacterial suspension was plated on freshly prepared ampicillin- or kanamycin-containing agar plates to selectively allow the propagation of *E. coli* colonies carrying the correct plasmid. Following overnight incubation at 37°C, agar plates were checked for the presence of bacterial colonies. A single bacterial colony was picked and inoculated into antibiotic-containing LB broth.

3.1.10 Isolation of plasmid DNA

In order to recover amplified plasmid DNA from *E. coli*, small (Miniprep) or large-scale (Midiprep) purification from bacterial suspension was carried out.

3.1.10.1 Miniprep

The rapid and small-scale method called miniprep was carried out to isolate the recombinant plasmid from the host bacterial cells with the ultimate goal of verifying if they carry the correct DNA of interest. Miniprep allows analyses of the DNA sequence before scaling up the plasmid preparation.

Single bacterial colonies were picked from the agar plate and inoculated into LB broth containing either ampicillin (Sigma, A9518) (100µg/ml) or kanamycin (from *Streptomyces kanamyceticus*, 10mg/ml; Sigma, K0129), depending on the resistance expressed by the plasmid of interest. Following overnight incubation at 37°C under constant agitation, 1.5ml of the bacterial suspension were transferred to a microcentrifuge tube and pelleted for 2 min. Using the GenElute Plasmid Miniprep Kit (Sigma, PLN350), the plasmid DNA was isolated as following:

- **Bacterial cells resuspension:** The pellet was drained and thoroughly resuspended by pipetting up and down 200µl of the RNase A-containing Resuspension Solution.

- **Cell lysis:** To break the bacterial membrane, 200µl of the alkaline Lysis Solution was added to the resuspension solution, which was gently mixed until the colour and texture became clear and viscous.

- **Neutralization:** After 5 min, the cell debris was precipitated by the addition of 350µl of the Neutralization/Binding Solution. The reaction tube was then gently inverted 4-6 times, followed by centrifugation at maximum speed, which resulted in the accumulation of cell debris at the bottom of the tube. The plasmid-containing supernatant was transferred to a binding column placed in a provided collection tube. After centrifugation for 1 min, the flow-through was discarded. In order to maximize DNA binding to the silica membrane, 500µl of the Column Preparation Solution had been previously added to the column, followed by centrifugation and discard of the flow-through liquid.

- **Washing:** Two different types of washing solutions were used at this stage to completely remove any residual salts and impurities left in the column. Firstly, 500µl of the Optional Wash Solution were added to the column, followed by the addition of 750µl of the ethanol-containing Wash Solution. In each step, the column was centrifuged and the flow-through was discarded. In order to entirely remove residues of ethanol that may affect DNA quality, another column centrifugation was carried out.

- **DNA elution:** 50µl of water were added in the centre of the column, which was transferred to a clean microcentrifuge tube and centrifuged for 1 min. The DNA plasmid present in the eluate was subsequently used for diagnostic restriction digestion and stored at -20°C.

3.1.10.2 Midiprep

To scale up plasmid production, 200µl of the suspension of bacteria containing the right plasmid were transferred to a conical flask containing 200ml of LB broth mixed with the suitable antibiotic (ampicillin or kanamycin). The bacterial culture was allowed to grow overnight under constant shaking at 37°C. In order to pellet the cells, a centrifugation (4000 rpm for 15 min at 4°C) was carried out and the plasmid DNA in the resulting pellet was isolated using NucleoBond Xtra Midi Plus Kit (Macherey-Nagel, NZ74041250) as following:

- **Bacterial cells resuspension:** 8ml of the RNase A-containing Buffer RES was added to the drained pellet and pipetted up and down to completely resuspend the cells.

- **Cell lysis:** 8ml of Buffer LYS was added, mixed and incubated for 5min at RT. This step relies on the sodium hydroxide/sodium dodecyl sulphate (SDS) activity, which denatures proteins and chromosomal DNA.

- **Neutralization:** To neutralize the lysate, 8ml of the potassium-containing Buffer NEU was added to the suspension and mixed by inverting the tube 3 times. This caused precipitation of SDS as potassium dodecyl sulphate (KDS), which pulled down proteins, chromosomal DNA, and other cell impurities.

- **Column and filter equilibration and loading:** A provided filter inserted into the NucleoBond Xtra Column was first equilibrated with the addition of 12ml of Buffer EQU in the perimeter of the filter and allowed to empty by gravity flow. The lysate was then loaded onto the pre-wet filter column. The filter retained the cell debris, while the plasmid DNA bound to the column silica membrane.

- **Washing:** In order to transfer any residual lysate from the filter to the column, 5ml of Buffer EQU was applied in the rim of the filter, which was subsequently discarded. Although RNA and proteins are not supposed to bind to the silica membrane due to the high salt concentration of the lysate, an additional washing step was carried out to eliminate all traces of impurities. In this stage, 8ml of Buffer WASH was added throughout the surface of the column.

- **DNA elution:** 5ml of pre-heated Buffer ELU was used to elute the plasmid DNA, which was collected in a Bijou sample container. The alkaline buffer used in this process neutralizes the positive charges of the resin, releasing the DNA plasmid from the column membrane.

- **DNA precipitation:** 3.5ml of RT isopropanol was added to the DNA eluate, which was subsequently vortexed and incubated for 2min at RT.

- **Washing and drying:** The precipitation mixture was transferred into a 5ml syringe whose outlet had been attached to a NucleoBond Finalizer. The plunger was slowly pressed down and the resulting flow-through was discarded. The DNA plasmid bound to the finalizer's silica membrane was washed by loading the syringe with 2ml of 70% ethanol (Sigma, 32221), which was carefully pressed through the finalizer. The flow-through was discarded and the membrane was dried by passing air through the finalizer.

- **DNA reconstitution:** For elution of the highly pure plasmid DNA, NucleoBond Finalizer was attached to the outlet of a 1ml syringe, which was placed over a microcentrifuge tube. The syringe was loaded with 800µl of Buffer TRIS (5mM Tris/HCl, pH 8.5) and the plunger was slowly pressed down. The resulting eluate was transferred back to the syringe and pressed down again through the membrane into the same collection tube in order to maximize DNA yield.

3.1.10.2.1 Ethanol precipitation

The plasmid DNA was further concentrated and purified using an ethanol precipitation protocol. Since DNA is a highly hydrophilic molecule, a salt was used to neutralize the negatively charged DNA backbone, which decreased solubility of the molecule in water. Ethanol was applied to increase the force of attraction between cations from the salt and the DNA backbone, causing it to drop out of the solution especially after centrifugation steps.

To carry out ethanol precipitation, 1 volume of DNA eluate was initially centrifuged for 2 min, followed by the addition of 2.5 volumes of 100% cold ethanol (Sigma, 32221) and 0.1 volume of 3M sodium acetate. The mixture was then stored in the freezer (-20°C) for at least 10 min and later centrifuged for 5 min. The supernatant was carefully discarded, and 2.5 volumes of 70% cold ethanol were added to the DNA pellet. The sample was subsequently kept in the freezer (-20°C) for 5 min, followed by 5 min centrifugation. The supernatant was again gently discarded, and the resulting DNA pellet was allowed to dry at RT until no trace of ethanol could be seen in the collection tube. To resuspend the DNA pellet, 100-300µl of nuclease-free water were added to

the sample, which was subsequently incubated in the water bath at 37°C for 1 hour. The DNA plasmid prep was stored in the freezer (-20°C) until further use.

A sample of the isolated and purified plasmid was submitted for diagnostic restriction digestions and sent for sequencing (by Eurofins MWG, Germany). If the restriction digestion patterns obtained by electrophoresis and the DNA sequence were both as predicted by the vector map, the DNA plasmid was further used for cloning or production of viral vectors, or transfection of cell lines or primary cultures of astrocytes, as appropriate.

3.1.11 DNA quantification

DNA yield and purity were determined with a spectrophotometer, which exposes the DNA sample to UV light and measures the resulting absorbance through a photodetector. Nucleic acids in DNA most strongly absorb UV light at 260nm, while RNA and proteins most strongly absorb light at 280nm. The final DNA concentration is calculated from a reference absorbance of 1 corresponding to 50µg/ml of ds DNA. Light absorbed by the sample is directly proportional to the concentration of DNA. Regarding assessment of DNA purity, the absorbance read at 260nm is divided by the absorbance detected at 280nm. A 260/280 ratio of 1.8 is considered a highly pure plasmid DNA sample. Lower values indicate protein contamination, while higher numbers imply RNA presence in the sample.

The spectrophotometer (NanoDrop ND-1000, Thermo Scientific) was firstly cleaned by pipetting 2µl of water onto the lower measurement pedestal. Water was wiped off from both upper and lower pedestals after an initial spectral measurement, and the same procedure was repeated in order to calibrate the equipment. Since water is the solvent used to dissolve DNA, the latter reading was set as the blank in the operating software on a computer. After wiping the water off the spectrophotometer, 2µl of the DNA sample was loaded into the lower pedestal and the resulting reading taken as the DNA concentration in the sample.

3.2 Adenoviral vector production

For the production of AVVs, the shuttle plasmid (pXCX) carrying the expression cassette of interest has to spontaneously recombine with the helper plasmid (pBHG10), which contains the majority of the adenovirus serotype 5 genome cloned in a bacterial plasmid. The external plasmid DNA must contain overlapping sequences with the left-end adenovirus genome, including the packaging system necessary to generate infectious viral vectors, which has been deleted in the helper plasmid (Bett, Haddara, Prevec, & Graham, 1994). Moreover, replication of the viral genome is defective due to deletion of E1 gene in pBHG10. Thus, viral propagation can only take place in HEK293 cells as they express and supply the E1 gene products (Graham & Prevec, 1995).

3.2.1 Co-transfection

All the recombinant plasmids constructed throughout my PhD project were directed to AVV production, in order to enable or maximize the transduction efficiency and transgene delivery to mammalian astrocytes, particularly *in vitro*.

For the co-transfection step, 5µg of shuttle vector and 5µg of helper plasmid pBGH10 were combined in a microcentrifuge tube containing 400µl of serum- and antibiotic-free Dulbecco's Modified Eagle Medium (DMEM, high glucose, with GlutaMAX; Invitrogen, 61965-059). 20µl of FuGENE® transfection reagent (Promega, E2691) were added to the mixture and briefly vortexed. Following 5min incubation at RT, the transfection mix was added to a T25 flask (Corning, 3289) containing 60-70% confluent HEK293 cells. The cells were kept in the incubator at 37°C in 5% CO_2 and a partial replacement of culture media was performed when its colour turned orange/yellow, indicating acidification. When cytopathic effect (CPE) was observed (Figure 3.1), crude viral suspension was harvested and frozen at -20°C to lyse the cells and release the AVV.

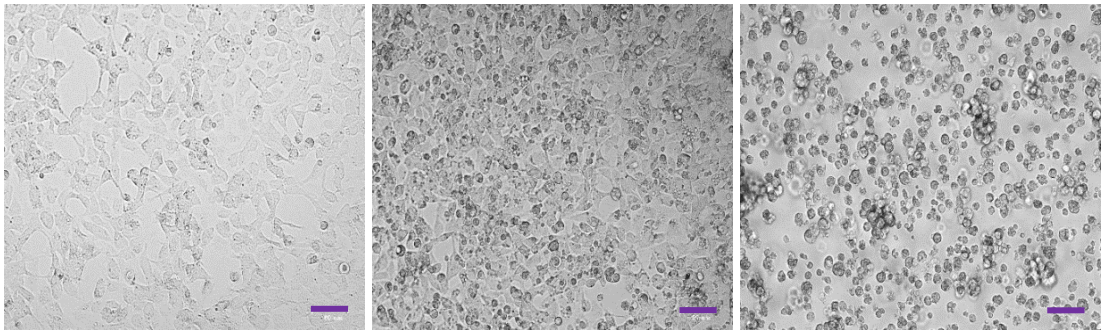

Figure 3.1. Progressive impact of AVV replication in HEK293 cells, leading to CPE. From left to right, images show the AVV production from the co-transfection stage until the cells lose adherence and exhibit swollen and rounded shape indicating CPE. Scale bars 60µm.

3.2.2 Re-infections

The crude cell suspension was defrosted and subsequently centrifuged for 5 min. 500µl of the virus-containing supernatant was added to a new T25 flask with 60-70% confluent HEK293 cells, while the remaining supernatant was returned to the freezer. The cells were again left in the incubator until CPE was observed, carrying out partial media exchange when necessary. The crude cell suspension was collected and the same procedure – freezing, centrifugation, HEK293 cells re-infection, CPE, viral suspension collection and freezing – was performed. Following co-transfection, cells normally take around 7-11 days to exhibit CPE. Once cells start displaying CPE within 2-3 days after re-infection, 1ml of the collected crude viral suspension is used to re-infect a new batch of HEK293 cells in T75 flasks (75 cm^2 Rectangular Canted Neck Cell Culture Flasks with Vent Cap; Corning, 430641) to proceed with the AVV bulking-up process.

3.2.3 Bulking-up

When CPE was observed in HEK293 cells in a T75 flask, the crude cell suspension was harvested, frozen, and subsequently used to re-infect 10 T150 flasks (150cm^2 Rectangular Canted Neck Cell Culture Flasks with Vent Cap; Corning, 430641) containing 70-80% confluent HEK293 cells (1ml of the crude viral suspension was added to each flask). After observing CPE, rounded and swollen HEK293 cells were transferred to a falcon tube (Greiner Bio-One, 227261) and concentrated by

centrifugation. The supernatant was discarded, and the resulting pellet was resuspended with 2.5ml of 0.1M tris-HCl (Sigma, T-5941) pH 8.0. To lyse the cells and release the virus particles, the crude cell suspension was frozen and kept at -20°C until further use.

3.2.4 Purification

In order to purify the AVV suspension for use in *in vitro* experimentation, any residual contaminants had to be cleared. This involved a series of sonification and ultracentrifugation cycles as well as desalination and filtration as following:

- **Sonification:** The suspension containing the infected cells was defrosted and kept on ice. To disrupt the cells, a sonificator probe (Vibra-Cell Ultrasonic Processor; Sonics, USA) was placed in direct contact with the cell pellet and 4 sonification cycles were performed lasting 45s each. At the end of each cycle, the virus-containing falcon tube was transferred to an ice-filled box for 1 min to cool down the sample. The viral suspension was then centrifuged at 3000 rpm at 4°C for 10 min. The clear AVV-containing supernatant was set aside while the pellet formed by the cell debris was discarded.

- **1st ultracentrifugation:** To enable virus collection from the supernatant, a Cesium Chloride (CsCl; Invitrogen, 15507-023) density gradient ultracentrifugation was carried out. 1 volume of the virus suspension and 0.6 volume of saturated CsCl diluted in 0.1M Tris-HCl pH 8.0 were transferred to a Sorvall UCF tube, which was topped up with 0.6 volume of saturated CsCl. The tube was then sealed and placed into buckets in the rotor (Sorvall TV-865B). The same procedure was repeated for the balance tube, which contained comparable volume and weight. The samples were then centrifuged at 55,000 rpm, overnight, at 15°C, to form a band of AVV within the CsCl gradient.

- **2nd ultracentrifugation:** The AVV-containing tube was pierced with a needle (21gx1.5”) attached to a 5ml syringe, which was used to extract up to 5ml of the band. A second needle was used to pierce the top of the tube and

compensate for the negative pressure due to AVV band collection. The AVV suspension was then transferred to a new Sorvall UCF tube, whose volume was topped up with CsCl diluted in 0.1M Tris-HCl. Both AVV-containing tube and balance tube were then centrifuged at 55,000 rpm for 4 hours at 15°C.

- **Desalination:** Prior to the end of the 2nd ultracentrifugation step, a PD-10 desalting column (GE Healthcare, 17-0851-01) was equilibrated by allowing 25ml of 10mM Tris/$MgCl_2$ (pH7.5) (Qbiogene, MGCL0500) to flow through it. Following centrifugation, a volume of up to 3ml of AVV band was extracted using a needle attached to a syringe as described before and transferred to the desalting column. This was followed by the addition of 0.5ml of 10mM Tris/$MgCl_2$ (pH 7.5) to the column, which was allowed to empty by gravity flow. For elution of the desalted AVV, 2.5ml of 10mM tris/$MgCl_2$ (pH 7.5) were applied to the column and the eluate was collected in a tube.

- **Filtration:** The AVV-containing tube was transferred to a laminar flow hood, in which it was sterile filtered using a 0.22µm sterile syringe filter (13 mm diameter, Millipore, SLGP033RS). The purified AVV was then aliquoted in sterile microcentrifuge tubes (20µl per tube) and stored at -80°C until further use.

3.2.5 Titration

Titration of the newly produced AVV was performed by staining for the adenovirus hexon protein, following a protocol adapted from Bewig and Schmidt (2000):

- **Cell infection:** 10-fold serial dilutions (10^{-2}, 10^{-3}, 10^{-4}, 10^{-5}, 10^{-6}, 10^{-7}, 10^{-8}) of the harvested AVV suspension were prepared in DMEM, 100µl of each was added to different wells of a 12-well plate (Greiner Bio-One, 665180) containing 70% confluent HEK293 cells. The plate was kept in the incubator at 37°C in 5% CO_2 for 48h to allow infected cells to express hexon proteins. Media was then aspired, and cells were fixed by gently adding 1ml of ice-cold 100% methanol (Fisher, 67-56-1) to each well. The plate was stored in the freezer -20°C for 10 min, followed by removal of the fixative compound and

rinsing 3 times with phosphate buffered saline (PBS; Fisher Scientific, BR0014G) containing 1% BSA (Sigma, A9647).

- **Immunostaining:** 500µl of 1000x diluted anti-adenovirus hexon protein (goat anti Adenovirus; Biodesign, B65140G) were added to each well of the plate, which was subsequently incubated at 37°C with constant gentle shaking. The first antibody was removed, and the wells were then rinsed 3 times with PBS containing 1% BSA. 500µl of 500x diluted secondary horseradish peroxidase (HRP)-conjugated antibody (rabbit anti-goat; Zymed, 81-1620) were applied to each well, followed by incubation at 37°C for 1h. The antibody was then removed, and the wells were washed 3 times with PBS containing 1% BSA. All antibody dilutions were performed using PBS + 1% BSA as diluent.

- **3,3-Diaminobenzidine (DAB) reaction:** The DAB reaction mix was freshly prepared by adding one tablet of DAB (0.7 mg/mL; Sigma, D4293) to an aluminium-foil-wrapped tube containing 15ml of distilled water. Following dissolution, a tablet of urea hydrogen peroxide (2 mg/mL; Sigma, U1380) was added to the mix, which was hand-shaken several times until the tablets added dissolved into the mixture. 500µl of the DAB mix were then added to each well and the reaction was evaluated under a microscope. As soon as a dark product appeared, the reaction was stopped by the addition of excess PBS, which was later exchanged by 1ml of fresh PBS. Stained cells were then counted in 5 fields of view at appropriate dilutions and the AVV titre was calculated as TU/ml as following:

$$\frac{Average\ stained\ cells\ per\ field\ X\ Fields\ per\ well^{*}}{Volume\ of\ virus\ (ml) X\ Dilution\ factor}$$

$$* Fields\ per\ well = 157$$

3.3 Lentivirus vector production

HIV-derived and VSVG glycoprotein-pseudotyped LVVs were produced as described in Hewinson, Paton, and Kasparov (2013). Generation of LVVs relies on the co-transfection of multiple recombinant plasmids that encode the elements necessary for

viral packaging into a packaging cell line, followed by various concentration and purification steps. The helper plasmids comprised of: (i) the packaging vector (pNHP), which provides the HIV-1 genome for expression of the genes required for vector assembly; (ii) the envelop vector (VSVG), which encodes VSVG envelope for viral pseudotyping; (iii) a vector encoding tat gene, which is the transcriptional enhancer of HIV-1; and (iv) the shuttle plasmid (pTYF) carrying the expression cassette of interest. The packaging cell line used was Lenti-X 293T cells (Clonthech, 362180), which express the SV40 large T antigen, allowing replication of plasmids carrying the SV40 origin of replication.

3.3.1 Co-transfection

Lenti-X 293T cells were seeded onto two T150 flask and incubated at 37°C in 5% CO_2 until they reached approximately 50% confluence. 30µg of pNHP, 12µg of pHEF-VSVG, 2.5µg of pCEP4-tat, and 15µg of the pTYF shuttle vector were added into a Bijou sample container containing 1.8ml of serum- and antibiotic-free DMEM culture media. 120µl of TurboFect transfection reagent (Thermo Scientific, R0533) were added to the transfection mix, which was incubated for 20min at RT. The transfection mix was then transferred to a falcon tube containing 22ml of culture media and gently mixed. The media of the two T150 flasks seeded with Lenti-X 293T cells was discarded and the content of the falcon tube was divided into the two T150 flasks, which were overnight incubated at 37°C in 5% CO_2.

3.3.2 Media harvest

Approximately 30 hours after transfection, the culture media covering the Lenti-X 293T cells in the two T150 flasks was collected and transferred to a falcon tube, which was centrifuged at 2000 rpm for 5 min. The supernatant was then transferred to a new falcon tube placed on ice, which was subsequently stored at 4°C. 12ml of fresh culture media was added into each T150 flasks containing the Lenti-X 293T cells. Following approximately 18 hours of incubation at 37°C in 5% CO_2, the media was again collected, centrifuged and the supernatant was combined with the media previously harvested.

3.3.3 Purification

In order to remove cell debris, the media was filtered through a 0.45µm polyethersulfone membrane vacuum filter (Thermo Scientific, TKV-246-013T) and subsequently transferred to ultracone thin wall ultracentrifuge tube (Seton Scientific, 5067) placed on ice. 1ml of cold and sterile 20% sucrose (Fisher Scientific, S/8600/53) in PBS was carefully added into the bottom of the ultracone tube, which was placed in an ultracentrifuge alongside a balance tube containing comparable volume and weight. Following 20,500 centrifugation at 4°C for 2 hours, the supernatant was aspirated off and 25µl of sterile cold PBS were carefully added to the pellet. The tube was then placed back on ice and maintained in the fridge at 4°C overnight. In the next morning, the viral suspension was aliquoted in microcentrifuge tubes and stored at -80°C until further use.

3.3.4 Titration

Determination of LVV titres was performed using an enzyme-linked immunosorbent assay (ELISA) and the Lenti-X p24 Rapid Titre Kit (Clontech, 632200), which measures the core protein p24 of a HIV-1-based LVV. The assay relies on the binding of p24 in the lentiviral sample to anti-HIV-1 p24 capture antibody present in the wells of a supplied microtitre plate.

Firstly, p24 positive control (10ng/ml) was diluted in PBS in order to create concentration points ranging from 0 to 200pg/ml. LVV samples were diluted 1,000,000 and 10,000,000 times in PBS. 20µl of Lysis Buffer was dispensed in each well. 200µl of each standard curve as well as the LVV sample and PBS were added in duplicates to the wells containing the Lysis Buffer. The microplate was covered to prevent evaporation and incubated for 1 hour at 37ºC. The content was then removed, and the wells were manually washed by addition of 275µl of 1x Wash Buffer in each well. The washing solution was aspirated off, and 100µl of the Anti-p24 biotin conjugated antibody was added per well. Following 1 hour incubation at 37ºC, the antibody was removed and the wells were washed as previously described. 100µl of Streptavidin-HRP conjugate was then dispensed to each well and the microplate was incubated for 30min at RT. The conjugate was aspirated off, followed by a washing step.

Protected from light, 100µl of Substrate Solution was quickly added to each well. Following incubation at RT for 20min, the reaction was blocked by the addition of 100µl of Stop Solution, which changed the colour of the solution from blue to yellow. The absorbance values were read at 450nm in a microplate reader. The absorbance values of the PBS/blank duplicates were averaged and used to subtract the background of each standard dilution and sample. The standard curve was then constructed and used to convert the absorbance values of the sample into p24 concentration (pg/ml). Importantly, the values of the LVV samples were corrected for the dilution factor of the samples. Conversion of p24/ml values to lentiviral particle (LP)/ml was performed considering that 1 LP contains $8x10^{-5}$ pg of p24, whereas the conversion of LP/ml values took into account that 1 TU corresponds to 148 LP.

3.4 Dissociated cell culture

Experiments involving cell lines, dissociated culture of rat astrocytes, and organotypic brainstem slices were conducted under aseptic conditions in a laminar flow hood. Cultures were kept in an incubator at 37ºC in 5% CO_2 and regularly fed with appropriate growth medium.

3.4.1 Handling and subculturing

Primary cultured astrocytes and HEK293 cells were cultured in complete growth media (Table 3.3).

Table 3.3. Components of complete growth media.

DMEM (high glucose, with GlutaMAX; Invitrogen, 61965-059)	*89%*
Foetal Bovine Serum (FBS, Invitrogen, 10108-165)	*10%*
Penicillin-Streptomycin (Pen/Strep, 10,000 U/mL, Invitrogen, 15140-122)	*1%*

Cultured cells were maintained in either T25 or T75 flasks until they exhibited 100% confluence, when the old media was discarded, and cells were gently rinsed in DMEM. To detach cells from the substrate, trypsin (Trypsin, 0.05% (1X) with EDTA; Invitrogen, 25300-054) was added to the flask, which was subsequently placed in the incubator at 37°C for 3 min. Trypsin is a protease that acts by cleaving the extracellular matrix, inducing dissociation of the cell monolayer. Following incubation, complete media was added to the flask since serum deactivates trypsin activity. The cell suspension was then collected and centrifuged at 2000 rpm for 5 min. The formed pellet was resuspended in complete media and the cells were either plated on glass coverslips or in multi-well plates for further experimentation, or used to inoculate a new flask. Since primary cultures of astrocytes show a lower growth rate, a media exchange was gently carried out before cells reached confluence to a continuous supply of nutritive growth media.

3.4.1.1 Cell counting and plating

In some experiments, the number of cells in the suspension had to be precisely determined before plating. In these cases, an optically transparent chamber of known depth engraved with a grid of known area (haemocytometer) was used and cells were counted under a microscope.

A volume of the suspension containing dissociated cells was diluted in DMEM sufficiently to prevent the cells from overlapping in the chamber. 10µl of this suspension was transferred by capillarity action to the haemocytometer chamber (Neubauer/ Marienfeld, Germany), which had been previously covered with a glass coverslip. Cells located in the 4 outer squares were counted using a handheld cell counter. Considering the chamber depth beneath the coverslip as 0.1mm and the

area of each square as 1mm^2, the final cell density per 0.1mm^3 (or 10^{-4}ml) in the original suspension was calculated as following:

$$Concentration\ of\ cells\ (cells/ml) = \frac{Number\ of\ cells\ counted}{Number\ of\ squares}\ X\ Dilution\ factor\ X\ 10^4$$

Following determination of cells concentration, 500µl of cell suspension containing 10^5 cells were plated onto each well of a 24-well plate (Greiner Bio-One, 662160), while 100µl of cell suspension containing from 1x10^4 to 7x10^4 cells were plated onto each well of a 96-well plate (Greiner Bio-One, 655083).

3.4.2 HEK293 cell line

HEK293 cell line originated from the transfection of human embryonic kidney cells with part of the AVV 5 DNA. HEK293 cells are extensively used in biomedical research due to their fast growth and propensity for transfection. They were used in this project for AVVs production as well as for the initial stages of the validation process of the novel molecular tools.

3.4.2.1 Cell line transfection

DNA was delivered to HEK293 cells by TransIT-293 transfection reagent (Mirus, MIR 2700), which provides high transfection efficiency, low toxicity, as well as a straightforward protocol. 18-24h prior to transfection, HEK293 cells were seeded onto either a 24- or a 96-well plate at a concentration that results in 80-90% cell density at the time of transfection. To allow formation of DNA complexes, up to 1.5µg/µl of the DNA of interest was added to a microcentrifuge tube containing the appropriate amount of Opti-MEM I (Reduced-Serum Medium, Life Technologies, 31985070), followed by the addition of TransIT-293 reagent. The quantity of the elements used in the complex formation step depended on the culture well size (Table 3.4). Following 15 min of incubation at RT, the DNA complex mixture was dispensed into the culture

wells (9.4µl/well for a 96-well plate and 52µl/well for a 24-well plate). The plate was then incubated at 37ºC in 5% CO_2 for 48-72 hours and subsequently used for experimentation.

Table 3.4. Elements of DNA transfection using TransIT-293 transfection reagent.

Culture vessel	*96-well plate*	*24-well plate*
Complete growth medium	*100µl*	*500 µl*
Opti-MEM I	*9µl*	*50µl*
DNA (1µg/µl) stock	*0.1µl*	*0.5µl*
TransIT-293 reagent	*0.3µl*	*1.5µl*
Total per well	***9.4µl***	***52µl***

3.4.3 Primary culture of rat astrocytes

To obtain primary dissociated cultured rat astrocytes, protocols adapted from Marriott, Hirst & Ljungberg (1995) were adopted as detailed here. Neonates Wistar rats were used in the procedure in accordance with the schedule 1 of the UK Home Office (Scientific Procedures) Act (1986). All the procedures of the glial preparation were performed under aseptic conditions. Sterilisation of tools and instruments was ensured by either autoclaving or UV treatment. Two fresh solutions were prepared preceding the prep: DNase I solution, which contained 3mg/ml of BSA (Sigma, A3294) and 0.04mg/ml of Deoxyribonuclease I (DNase I, from bovine pancreas; Sigma, D5025) diluted in 40ml of Hank's Balanced Salt Solution (HBSS; Invitrogen, 14175-129); and Trypsin solution, which was prepared by transferring 15ml of the DNase I solution to a new falcon tube and adding 0.25mg/ml of trypsin (from bovine pancreas; Sigma, T9935).

Wistar rat P2 pup was overdosed with isoflurane 5% (Isoflurane-Vet, Merial Animal Health Ltd), followed by exsanguination through decapitation using sharp scissors. The head was then transferred to a well of a 6-well plate (Greiner Bio-One, 657160) containing cold HBSS in a laminar flow hood. After placing the head in a petri dish (60mm x 15mm; Corning, 430166), the skin was removed, and the skull was exposed,

followed by extraction of the brain tissue. Excess of brain cortex was eliminated, while the remaining tissue containing part of the midbrain and the brainstem was crudely cross-chopped and immersed in the trypsin solution for 15min under gentle and constant agitation. Trypsination was terminated by the addition of 15ml of complete culture media, followed by centrifugation at 2000rpm for 5min. The supernatant was discarded, and the pellet formed was resuspended in 10ml of the solution DNase I. The cell suspension was allowed to settle down, and the debris-free supernatant was collected and reserved in a new falcon tube. Another 10ml of the solution DNase I was used to resuspend and triturate the remaining tissue, and the resulting debris-free supernatant was combined with the previous collection. The same procedure was repeated using the remaining 5ml of the solution DNase I. The collected suspension was then filtered with a 40µm cell strainer (Falcon, 352340), and subsequently centrifuged at 2000rpm for 5min. The supernatant was discarded, and complete growth media was used to resuspend the pellet. The cell suspension was then transferred to a T75 flask and incubated at 37°C in 5% CO_2 for 7 days, allowing the glia culture to grow, and astrocytes to attach to the substrate. To eliminate microglia and oligodendrocytes from the primary culture, flasks were gently shaken overnight at 37°C in a temperature-controlled chamber. The culture media containing non-astrocytic cells was discarded and the primary astrocytes attached to the flask's wall were subcultured as previously described. The primary cultured rat astrocytes were kept in the incubator at 37°C in 5% CO_2 until further use and subcultured whenever needed up to 21-25 days after prep.

3.4.3.1 Primary culture transduction with AVVs

DNA delivery to primary cultures such as rat astrocytes yields higher transduction efficiency using AVVs when compared to transfection reagents. Multiplicity of infection (MOI), which in an overly simplistic description is the ratio of the number of viral particles to the number of cells targeted in a culture, was optimised to avoid cytotoxic effects while achieving a high transduction efficiency. Cultured astrocytes were transduced with a range of titres of AVVs and astrocyte morphology and density were daily examined for signs of deterioration. Once an appropriate MOI was established for each AVV, it was kept constant for all experiments during this project.

3.4.3.2 Determination of astrocyte viability

The novel molecular tools developed in this project have the potential to affect the viability of cells in which they are expressed, either by compromising their metabolic state or by formation of potentially harmful by-products. Cell viability tests were performed in order to quantify any cytotoxic effects of astrocytic transduction with AVVs, in order to optimise transduction titres.

3.4.3.2.1 Trypan Blue exclusion assay

Trypan blue is an impermeable dye which can only penetrate damaged membranes of either dying or dead cells. It is, therefore, a dye exclusion assay that distinguishes between live and dead cells. Primary astrocytes were plated in a 96-well plate at a concentration of $3x10^4$ cells/100µl and transduced with the appropriate AVV at various MOIs as previously described. Following 2-3 days of incubation at 37ºC in 5% CO_2, the complete media was aspirated from the wells, which were subsequently rinsed with 100µl of DMEM in order to remove any remaining serum. 40µl of trypsin were then dispensed into each well and the plate was transferred to the incubator. After 3min incubation at 37ºC, 40µl of complete media were added to the cell suspension to terminate trypsin action, followed by the addition of 80µl of sterile-filtered trypan blue solution 0.4% (Sigma, T8154). 10µl of the resulting suspension solution containing dye-stained cells were transferred to a haemocytometer chamber, which was subsequently placed on a microscope stage for cells counting purposes. Cells showing blue colour were counted as unviable, while non-stained cells were considered to be alive. The total number of blue and unstained cells was determined, and cell viability was calculated as following:

$$\%\ cell\ viability\ = \frac{number\ of\ unstained\ (living) cells}{total\ cell\ number} \times 100$$

3.4.3.2.2 XTT cell viability assay

The XTT assay infers cell viability by detecting the metabolic activity of the cell. It relies on the action of dehydrogenase enzymes present in functional mitochondria to reduce the yellow tetrazolium salt XTT to a highly coloured formazan dye (Figure 3.2), which is soluble in aqueous solution and can be quantified by measuring the sample absorbance at wavelength 450nm. Tetrazolium salt XTT is negatively charged and does not easily penetrate the cell membrane (Berridge, Herst, & Tan, 2005). The assay requires, therefore, addition of an intermediate electron acceptor, which crosses the membrane and picks up electrons in the cytosol of viable cells. Once exited from these cells, the intermediate electron acceptor donates its electrons for the conversion of tetrazolium salt XTT into the soluble and coloured formazan product (Berridge et al., 2005). Since dehydrogenase mitochondrial enzymes are inactivated shortly following cell death, the amount of formazan produced is proportional to the viability of the cells in the sample.

Figure 3.2. Reduction of XTT tetrazolium salt into formazan. Dehydrogenase enzymes in viable cells reduce the slightly yellow XTT tetrazolium salt into the bright orange and soluble dye formazan. Since this reaction relies on the performance of enzymes that are active only in viable cells, formazan absorbance at wavelength 450nm is proportional to the amount of viable cells in the sample.

To perform this assay, primary astrocytes were plated in 96-well plate at a density of $3x10^4$ cells/100µl. Various quantities of the appropriate AVVs were added to the complete media containing astrocytes in order to achieve a range of different MOIs. The plate was kept in the incubator at 37ºC in 5% CO_2 for 2-3 days to allow the gene to be delivered and properly expressed by the cells. Prior to the experiment, reagents from the XTT cell viability kit (Cell Signalling Technology, 9095) were defrosted and checked for absence of precipitation. A fresh detection solution was prepared by adding in a microcentrifuge tube 1 volume of the electron coupling solution, which

increases efficiency of the reduction reaction, and 50 volumes of the XTT reagent. 50µl of the detection solution was then transferred to each well of the 96-well plate, which contained astrocytes seeded in 100µl/well of complete growth media. The reaction of formazan formation was allowed to proceed for 2 hours, during which time the plate was kept in the incubator at 37ºC. 100µl of the supernatant were then transferred to a new 96-well plate and the sample's absorbance was read at 450nm using a microplate reader (Tecan Infinite M200 PRO, Labtech).

3.5 Organotypic cultured brainstem slices

Preparation of organotypic brainstem slice cultures followed the protocol previously described by Teschemacher, Paton, and Kasparov (2005). The procedure was performed under sterile conditions and all tools used were previously autoclaved or treated with UV light. Male Wistar rat P7-8 pups were used in the procedure in accordance with the schedule 1 of the UK Home Office (Scientific Procedures) Act (1986). The animals were overdosed with isoflurane 5% (Isoflurane-Vet, Merial Animal Health Ltd), followed by exsanguination through decapitation using sharp scissors. The rat's brain was then transferred to a laminar flow hood, where the caudal part of cerebellum and the entire brainstem were isolated and bathed in a cold dissection medium containing HBSS enriched with 20 mM glucose (Fisher Chemical, G/0500/60), 10 mM $MgCl_2$ (Fluka, 63020), 1 mM HEPES (Sigma, H3375-250G), 1 mM kynurenic acid (Sigma, K3375-1G), 0.5% phenol red (Sigma, P0290), 100 U/ml penicillin and 0.1 mg/ml streptomycin (Sigma, P4333). To function as a supporting base for the brainstem, the cerebellum was glued with cyanoacrylate adhesive (Loctite) onto a vibratome stage, which was mounted onto the platform of the vibrating microtome 7000 (Campden Instruments, UK) in a bath filled with cold dissection medium. 200µm-thick coronal slices were cut at the level of the locus coeruleus (LC). Using a rubber bulb attached to the tip of a 1ml pipette, each section was carefully transferred to a 24-well plate containing ice-cold dissection medium. LC slices were deposited onto organotypic culture inserts (Millicell-CM, Millipore) placed in a six-well plate filled with 1ml/well of the Optimem+ plating media, which is comprised of 49% of Opti-MEM Reduced Serum Medium (GlutaMAX Supplement, Life Technologies, 51985026), 25% of HBSS, 25% of FBS, 1% Penicillin/Streptomycin (Sigma, P4333)

and 25mM glucose. Slices were kept at the interface between media and the humidified and carbonated air in an incubator (37ºC, 5% CO_2). Plating media was exchanged twice a week.

3.5.1 Transduction of organotypic slice cultures

Since cultured organotypic slices comprise a more integrated preparation that allows ideal viral gene transfer and high-resolution imaging (Teschemacher et al., 2005), slice cultures were transduced with AVVs for further experimental applications. Transduction of organotypic cultured slices occurred immediately following the slice prep, when AVVs were directly added into the plating media. In case the slices had to be transduced with different AVVs that targeted distinct cell populations, the neuronal-driven AVV was handled as just described and the slices were kept in the incubator for 24-40h. Following incubation time, the old media was discarded and a fresh plating media containing the astrocyte-targeting AVV was dispensed into the wells. After 3 days, the old media was removed from the wells and replaced with fresh plating media. Slices were used for experimentation from the 7th day after the preparation, allowing for fully established expression of the transgene cassette.

3.6 Immunofluorescence

In order to detect expression and distribution of certain proteins throughout the brain tissue or in primary cultured astrocytes, an immunofluorescence (IF) protocol was carried out. This widely used technique relies on specific antibodies to target antigens with fluorophores, which can be visualized under a fluorescent microscope. Indirect IF, as adopted in this study, requires a primary antibody that recognises and binds specifically to the target molecule, as well as a secondary antibody, which is conjugated to a fluorophore and binds to the primary antibody. The following steps were applied to IF in primary cultured astrocytes seeded in glass coverslips placed into a 24-well plate, as well as organotypic brainstem slices in membrane inserts placed into a 6 well-plate:

- **Tissue preparation:** The samples were rinsed 3 times in PBS for 5min, followed by fixation with paraformaldehyde 4% (Sigma, 441244) for 15min at RT. Excess of the fixative compound was removed with a washing step - 3 times 5min rinse in PBS. Organotypic brain slices were excised from the culture membrane and placed on a microscope slide (22x50mm, VWR, 631-0137). Using a pen with hydrophobic content (Pink PAP Pen Mini, Zytomed Systems, ZUC065), a circle around the samples was drawn so that the solutions would be pooled in a small droplet.

- **Permeabilization and blocking:** A solution containing 0.3% Triton X-100 (Sigma, T8787) in PBS (PBST) and 10% serum (from the species the secondary antibody was raised in) was added to the sample, which was incubated at RT for 1 hour. Triton X-100 is a detergent that improves access of antibodies to intracellular targets. Serum was used to block nonspecific binding sites in the tissue sample that can be targeted by the secondary antibody. Following incubation, samples were washed in PBS for 5 min 3 times.

- **Immunostaining:** Primary antibody mix, which contained appropriate amounts of the primary antibody diluted in PBST and 1% serum, was dispensed into the samples and incubated overnight at 4ºC. The primary antibody used in this study was anti-red fluorescent protein (RFP, Rockland, 600-401-379). Samples were subsequently rinsed in PBS for 5min 3 times. A secondary antibody mix was prepared by adding 2 drops/ml of Alexa Fluor 488 (Life Technologies, R37116) or Alexa Fluor 594 (Life Technologies, R37117) to PBST and 1% serum. The secondary antibodies were directed against the species in which the primary antibody was raised in. The mix was then dispensed into the samples and incubated for 1h at RT protected from light, followed by a washing step with PBS.

- **Mounting:** The samples were placed on the top of an adhesion microscope slide and coverslipped with Mowiol 4-88 (Sigma, 81381) for imaging.

3.7 Quantitative fluorometric determination of L- and D-lactate

The successful expression and activity of the novel constructs in cell lines and primary cultured astrocytes was tested through a fluorometric enzymatic assay for detection of LL (EnzyFluo L-Lactate Assay Kit, BioAssay Systems, EFLLC-100) and DL (EnzyFluo D-Lactate Assay Kit, BioAssay Systems, EFDLC-100). These commercial assays measure the concentration of LL or DL based on their oxidation by LDH or DLDH, respectively, which builds up NADH as by-product. NADH is used by diaphorase to reduce a probe to a fluorescent product (Figure 3.3A). The fluorescence intensity, which can be detected using a microplate reader, is proportional to the concentration of either LL or DL in the sample.

HEK293 cells were transfected with 0.5-1.5µg/µl of the novel recombinant plasmids under the control of either CMV or EF1α promoters using TransIT-293 as previously described. Primary cultured astrocytes were transduced with AVVs under the control of a sGFAP promoter as described above. Following 2-3 days in the incubator, in order to allow for transgene expression to proceed, media were aspirated, and cells were rinsed in serum- and antibiotic-free DMEM, followed by the addition of 300µl of DMEM per well. The plate was then transferred to the incubator, where HEK293 cells were kept for 2h, while an incubation time of 6h was adopted for astrocytes. DMEM was harvested and samples which were used to determine DL levels underwent deproteination using a 10 kDa spin filter (Microcon-10kDa Centrifugal Filter Unit with Ultracel-10 membrane, Merk, MRCPRT010). As recommended by the manufacturer, this step was necessary to deplete any potential activity of endogenous LDH enzyme that may interfere with DL measurements. The following steps were applied for determination of both DL and LL. Samples were diluted 3 to 10 times with distilled water and 50µl of the final diluted sample were transferred into a black 96-well plate (Greiner Bio-One, 655077). To generate a standard curve that allowed translation of fluorescence intensity onto LL or DL concentration, the provided 20mM LL or DL Standard was diluted in DMEM to yield 4 different concentrations in a curve ranging from 0µM-250µM for LL assay and 0µM-40µM for DL assay (Figure 3.3B and C, respectively). 50µl of each LL or DL dilution for the standard curve was transferred into the black 96-well plate. For each sample and standard curve well, a reagent mix comprised of 40µL of assay buffer, 1µL of enzyme A (lactate dehydrogenase), 1µL of enzyme B (diaphorase), 10µl of NAD solution, and 5µl of probe was freshly prepared

and quickly added to the wells. The plate was then tapped gently to mix and incubated for 60 min at RT protected from light. Following incubation, fluorescence was measured in a microplate reader using wavelength 530nm for excitation and 585nm for emission. The concentration of LL or DL in each sample was determined by comparison to a calibration curve as follows:

$$[Lactate](\mu M) = \frac{F_{sample} - F_{blank}}{Slope} \times n$$

where F_{sample} and F_{blank} represent the fluorescence intensity values of the sample and 0µM LL or DL, respectively. Slope is the slope of the standard curve and n is the dilution factor.

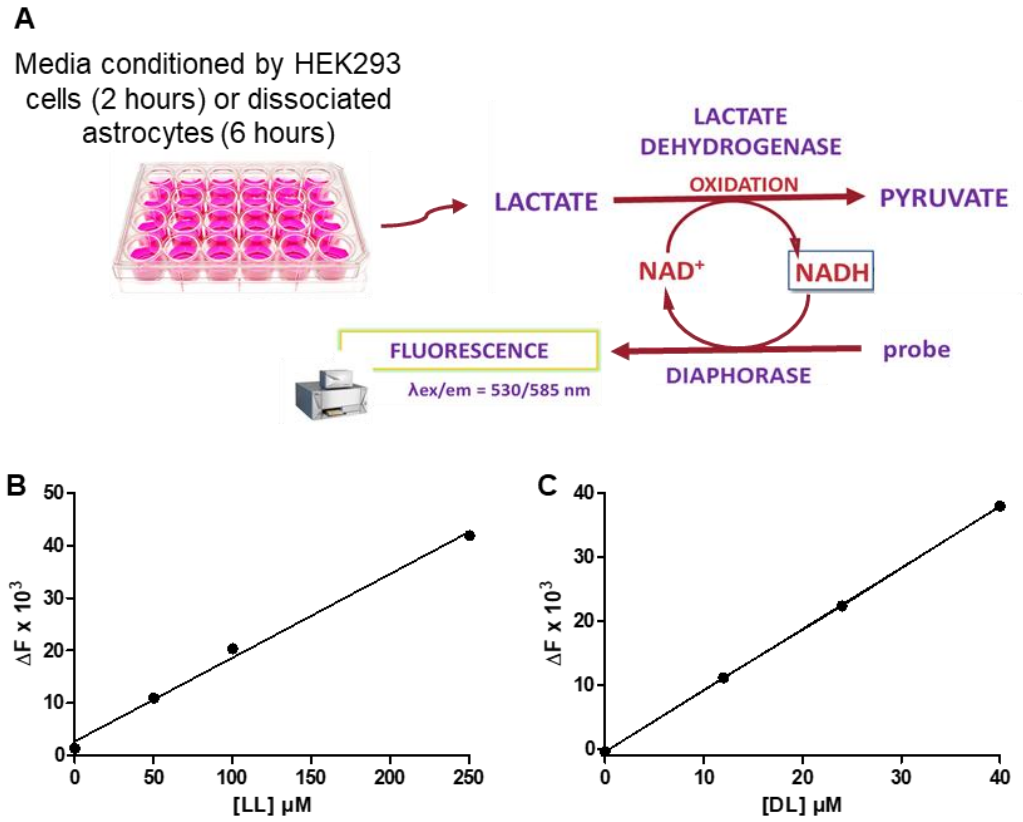

Figure 3.3. Determination of LL and DL concentration in media conditioned by transfected HEK293 cells and transduced astrocytes. (A) Lactate oxidation reaction catalysed by lactate dehydrogenase results in the formation of NADH, which is used by diaphorase to reduce a probe of the EnzyFluo LL or DL Assay Kit into a highly fluorescent product. The fluorescence intensity measured by a microplate

reader is proportional to the concentration of LL or DL in the sample. **(B)** Example of a LL standard curve from a single assay in culture media (slope = 0.160, R^2 = 0.99). **(C)** Example of a DL standard curve from a single assay in culture media (slope = 0.957, R^2 = 1).

3.8 L-lactate amperometry

Real-time determination of LL levels in organotypic brainstem slices was performed using amperometric enzymatic LL biosensors (Sarissa Biomedical, UK, SBS-LAC-05-50). The potential at the electrode surface was controlled by a potentiostat (Duo-Stat ME200+) and the signal detected was further processed and analysed using a 1401 interface and Spike 2 software (Cambridge Electronic Design, UK). In order to minimize the effects of any non-specific electroactive interference, a null sensor (Sarissa Biomedical, UK, SBI-NUL-05-50) lacking the enzymatic layer was used as a control in the amperometric recordings in conjunction with the LL biosensor in a dual recording configuration scheme (Figure 3.4A). Both electrodes were placed in contact with the surface of the slice and the null sensor currents were automatically subtracted from the LL biosensor currents using Spike 2 software. An $Ag/AgCl_2$ reference electrode was connected to the potentiostat and acted as an earth.

For recordings, slices transduced with appropriate AVVs were removed from the incubator, excised from the membrane, and transferred to the recording chamber of the amperometry set up, which was continuously superfused with HEPES-buffered solution (HBS) (Table 3.5) at a rate of 2.5 ml/min. To immobilise the slice under the flow in the chamber, a small horse-shoe-shaped weight holding nylon threads was placed on top of the slice. Null and LL biosensor were removed from the storage pot kept in the fridge at 4ºC in HBS and immediately connected to the electrode holders, which were attached to micromanipulators mounted on magnetic bases. Electrodes were then rapidly placed under the flow in the chamber since dryness of electrodes can compromise their sensitivity. Prior to the recordings, electrodes were allowed to stabilize their baseline for at least 30 min and the current was set to zero in order to remove any background noise. With the aid of a stereomicroscope (GSZ 2, Germany), null and LL biosensors were inserted into a region of the slice containing transduced noradrenergic neurones. Electrodes were then allowed to settle until the LL tone was reached, during which period the current generated by the LL biosensor remained

fairly constant. Drugs were delivered to the chamber using an infusion pump at a rate of 3ml/hour. To calibrate the electrodes, known amounts of LL were applied in the chamber at the beginning and at the end of each recording. The values were averaged and used to convert the biosensor currents to LL concentration (Figure 3.4B). All pharmacological substances used in this experiment were first tested for their ability to be detected by the LL biosensor system, which confirmed the electrodes to be selectively sensitive to LL only.

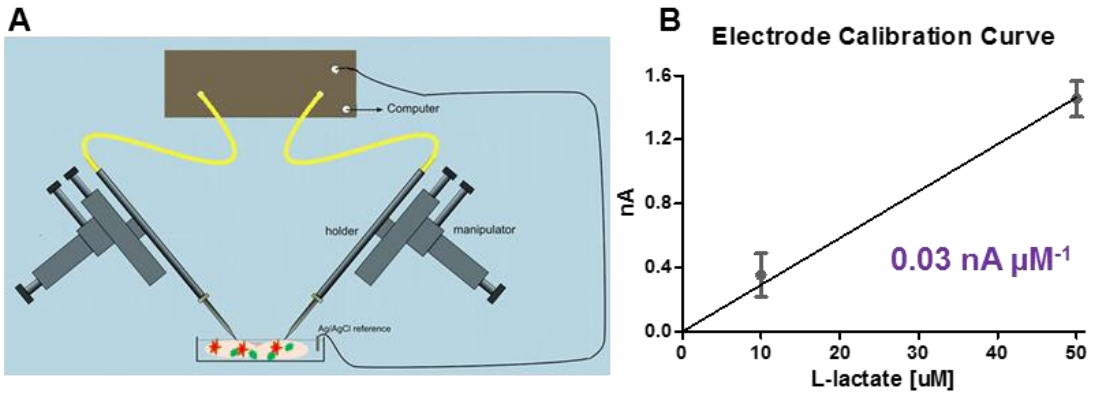

Figure 3.4. Measurement of extracellular LL levels with LL sensors and constant-potential amperometry. (A) Schematic depicting the amperometric setup for recordings with LL sensors. LL and null sensors were placed in direct contact with the tissue in a chamber under constant flow. A constant voltage of +500mV *vs* AgCl/Ag reference was applied and controlled through a potentiostat (brown box in the figure). **(B)** Example of a calibration curve of a LL electrode determined while off-slice.

Table 3.5. Chemical constituents of HBS. For preparation of 1 litre of the buffer, 25ml of each 40x concentrated stock solution were added to a beaker and the volume was topped up with ddH_2O. The pH of the final solution was adjusted to 7.4.

COMPONENT	CONCENTRATION (mM)
NaCl	137
KCl	3 or 5.4
$NAHCO_3$	4.2
$CaCl_2$	1.67
$MgSO_4$	0.8
KH_2PO_4	0.44
Na_2HPO_4	0.34
HEPES (free acid)	10
D-glucose	2 or 5.5

3.9 Confocal imaging

Confocal images from live dissociated astrocytes and organotypic brain slices were obtained using upright Leica SP1 and SP5 confocal laser scanning microscopes with 10x, 25x or 40x water immersion objective lenses. For imaging experiments, primary cultured astrocytes were seeded onto sterile glass coverslips, which were directly placed into a recording chamber mounted on the confocal microscope (Figure 3.5). Organotypic slices, on the other hand, were excised from the membrane using a sterile scalpel and instantly transferred to the recording chamber. The chamber temperature was kept at 32.5 ± 1ºC and the coverslips were continuously superfused with HBS (Table 3.5) with pH 7.4 at a rate of 2.5 ml/min. An infusion pump coupled to the chamber was used to deliver drugs for experimentation at a rate of 3ml/hour. The pair of fluorophores used in the FRET imaging experiments were excited with the 458nm line of an Argon ion laser. Cyan fluorescent protein (CFP) emission was detected at wavelength 465-500nm, while yellow fluorescent protein (YFP) emission was collected at wavelength 515-595nm. Other variants of GFP were excited with 488nm line of the Argon ion laser and the red fluorescent protein tdTomato was excited with 561nm of yellow laser. Leica Software in time-lapse mode was employed to record the fluorescence intensity dynamics over time, such as in FRET imaging experiments. In these cases, 512x512 resolution images were taken every 3 or 4 seconds in xyt mode. Images were quantitatively analysed using the quantifying tool of Leica software and the data were exported to Excel and GraphPad Prism software for further statistical analyses. Note that once the ideal pinhole and photomultiplier tube (PMT) were defined for each of the fluorophores of the FRET sensors, these parameters were kept the same throughout the study.

In order to obtain high resolution confocal images, 1024x1024 resolution stack images were obtained in xyz series, in which approximately 4 images per confocal plane were averaged adopting a z-step of <1µm.

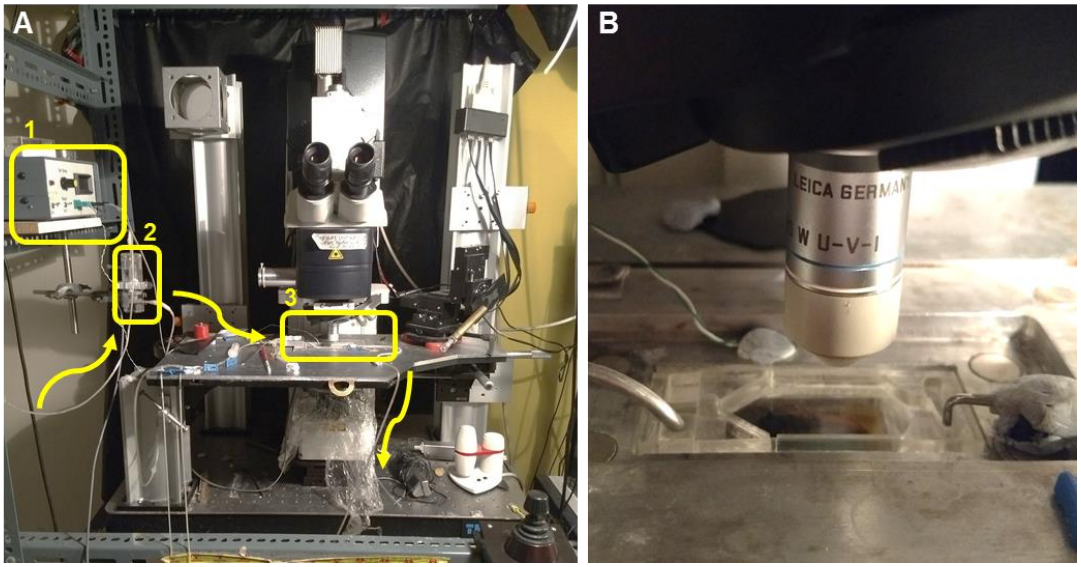

Figure 3.5. Imaging setup in an upright SP5 confocal. (A) Leica SP5 confocal with integrated imaging stage, which contains: 1 – heating device; 2 – perfusion cylinder; 3 – recording chamber. Arrows show the direction of HBS flow through polyethylene tubing. **(B)** Magnified image of the chamber where astrocytes seeded on coverslips and brainstem cultured slices were placed for imaging under continuous superfusion with HBS using water immersion objective lenses.

3.9.1 Imaging of Laconic and Pyronic

Primary cultured astrocytes at a concentration of $2x10^5$ cells/ml were seeded onto collagenised (Sigma, C3867) and sterile 13mm glass coverslips placed into a 24-well plate. AVVs driving the expression of the FRET sensors Laconic or Pyronic (AVV-CMV-Laconic or AVV-CMV-Pyronic, respectively) were directly added to the culture media at the time of plating. Wherever appropriate, co-transduction with the novel molecular tools was performed at the same time. Following 2-3 days incubation at 37ºC in 5% CO_2, coverslips were transferred to the recording chamber and images were taken as described above. At the end of the recordings, cells in the field of view were selected as region of interest and the fluorescence intensity of the two FRET fluorophores was computed by the Leica software over time. For analysis, the FRET ratio (mTFP/Venus) was calculated and the average ratio between 0 to 150 seconds was set as the baseline. The FRET ratio at each time point was then divided by the average baseline value for normalization purpose.

4.9.2 Imaging of CNiFERs

CNiFERs (see Chapter 2, section 2.3.1.3) were employed in order to evaluate the effect of the LL-limiting tools on LL-induced NA release (Mosienko et al., 2018; Muller et al., 2014). Organotypic brainstem slices containing the LC were transduced with AVV-PRSx8-eGFP in order to visualize noradrenergic neurones. Co-transduction with AVVs carrying the expression of the LL-limiting tools to astrocytes were performed whenever appropriate. Release of NA was recorded following a protocol previously described in Mosienko et al. (2018). One day prior to the recordings, 25µl of CNiFERs resuspended in Optimem^{+} plating media at a concentration of 4x10^{5} cells/ml were plated on top of each cultured slice (Figure 3.6). Following overnight incubation at 37ºC in 5% CO_2, the slices were excised from the membrane and placed in the recording chamber of the SP5 confocal microscope, which was continuously superfused with HBS (Table 3.5). Each slice received a first application of 2mM LL (Sigma, L1750) to evoke NA release from LC neurones (Tang et al., 2014), followed by a second application of pyruvate 10mM (Alfa Aesar, A11148). At the end of the recordings, changes in CNiFERs FRET ratio (Citrine/CFP) over time were calculated and NA release was quantified by analysing the area under the FRET emission curve. NA released by the pyruvate-induced LL release was normalised to the response triggered by the application of LL 2mM in each cultured slice. Statistical significance was assessed using paired Student's t-test, which compared the response from the application of LL 2mM to the response evoked by the application of pyruvate 10mM.

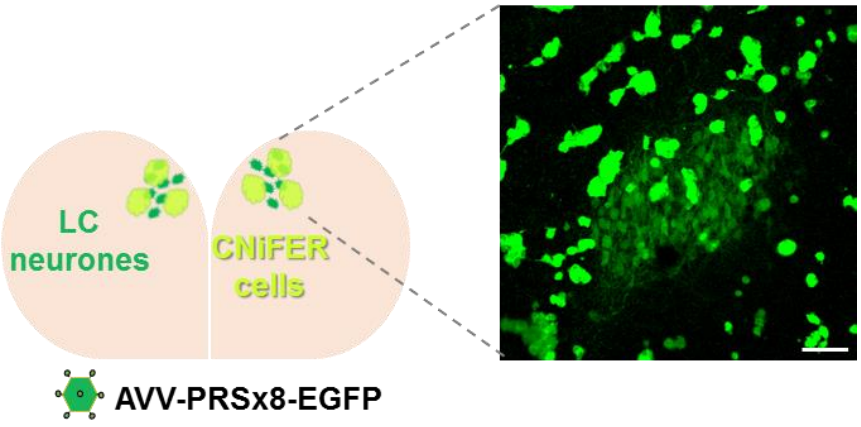

Figure 3.6. Measurement of NA release with the cell-based neurotransmitter fluorescent engineered reporter (CNiFER) system. Schematic of NA-sensitive CNiFERs cells seeded on a cultured brainstem slice preparation containing noradrenergic neurones transduced with AVV-PRSx8-EGFP. Inset is a confocal

image stack. Scale bar 100µm. Note that even though both noradrenergic neurones and CNiFERs express green fluorescence, their depth in the tissue and shape make it straightforward to distinguish between these 2 cells types.

3.10 Statistical analyses

Data were compared using One-way ANOVA followed by Bonferroni's Multiple Comparison post hoc test, or Student's t-test paired or unpaired as indicated. Calibration curves were analysed by linear regression. Values are presented as average ± standard deviation and plotted in box and whisker diagrams. The edges of the boxes illustrate the upper and lower quartile values, the central horizontal line defines the median, the central plus sign represents the mean, and whiskers indicate the minimum and maximum range of the data. Statistical tests were performed using GraphPad Prism 5 and 8. Statistical difference of $p<0.05$ between the experimental groups was considered significant.

Chapter 4 – Interfering with L-lactate signalling through intra-astrocytic L-lactate breakdown

4.1 Metabolic and signalling functions of astrocytic L-lactate

Understanding the metabolic and signalling interactions between neurones and astrocytes requires the employment of tools that monitor and/or modulate their intrinsic physiological activity. Although pharmacological approaches have been long available and are unquestionably valuable for neuroscience research, their effects are generally transitory. Comprehension of the role of an endogenous compound in the modulation of aspects of brain function requires, therefore, genetic tools that change its dynamics in specific brain cells long-term. LL, in particular, which in the brain is considered to be derived mainly from astrocytes, has attracted increasing attention due to its signalling roles and the consequent implications in many brain activities. Moreover, LL levels respond dynamically to neuronal activity and metabolic needs and may act as an additional energy supply to neurones during periods of high activity. Nonetheless, research in this field lacks the means to selectively manipulate astrocyte-derived LL for further investigation of its actions in the brain.

In order to explore how astrocytic LL supply contributes to central network function, we have developed molecular tools to reduce LL pool size selectively in astrocytes. These tools aim to chronically limit the effects of astrocyte-derived LL by restricting the availability of this compound in the brain, rather than directly interfering with astrocytic LL production and release. For this purpose, we have identified bacterial enzymes that use LL as a substrate for irreversible reactions. We postulated that, once expressed specifically in astrocytes, enzymatic activity may decrease LL concentration in these cells and, consequently, constitutive and reactive LL release to the extracellular space and its action on neuronal cells.

This chapter will explore the construction and *in vitro* validation of novel molecular tools based on bacterial enzymes to decrease LL concentration specifically in astrocytes. Preliminary results on the effects of one of these novel tools *in vivo* in collaboration with Professor Mikhail Pletnikov at Johns Hopkins University and Dr. Valentina Mosienko at University of Exeter will also be briefly described in this chapter.

4.2 L-lactate breakdown by bacterial enzymes

In order to thrive under conditions of limited oxygen, microorganisms have developed fermentation for generation of energy, in which glucose is metabolised to pyruvate that can be further processed to either LL or ethanol (Berg et al., 2002). This high capacity of bacteria to handle LL led us to search in these microorganisms for enzymes that are specialized in breaking down LL irreversibly. We have identified 2 different bacterial enzymes that catalyse reactions using LL as substrate: L-lactate oxidase (LOX; E.C. 1.1.3.15) and L-lactate 2-monooxygenase (LMO; 1.13.12.4). Although these enzymes are expressed in many bacteria, we selected the species whose activity of LOX and LMO were better described: *Aerococcus viridans* for LOX and *Mycobacterium smegmatis* for LMO.

These two microbial enzymes, once adapted to mammalian codon preference, were expressed selectively in astrocytes in order to inhibit astrocyte-derived LL effects in the brain.

4.2.1 L-lactate oxidase

LOX from the bacterium *Aerococcus viridans* has been widely employed in the production of biosensors, which are used to detect and quantify LL concentration for a range of purposes, including clinical diagnoses, food quality control, and sports medicine (Hiraka et al., 2018).

LOX is a flavoenzyme that catalyses the FMN-dependent oxidation of LL. Molecular oxygen is used in the oxidation reaction, which yields pyruvate and hydrogen peroxide as products (Figure 4.1). An intermediate species is formed between the oxidized and reduced forms of LOX, indicating that the reaction process does not occur in one step (Maeda-Yorita et al., 1995). Indeed, LOX firstly catalyses the oxidation of LL into pyruvate by reducing FMN, which in turn is reoxidized by molecular oxygen. The latter compound functions as an electron acceptor, which culminates in the production of hydrogen peroxide (Maeda-Yorita et al., 1995). It is important to note that pyruvate is released very rapidly from the reduced enzyme-pyruvate complex, a feature that accounts for the fast reaction kinetics of LOX (Maeda-Yorita et al., 1995). Structural

analysis revealed that LOX is a tetramer enzyme that reacts specifically with the L-isomer of lactate (Umena et al., 2006). Although DL can also bind to the active site of LOX, the opposite chirality of this molecule is not ideally accommodated by the enzyme and, as a consequence, it does not trigger the enzymatic reaction. Therefore, DL may act as a LOX inhibitor (Furuichi et al., 2008).

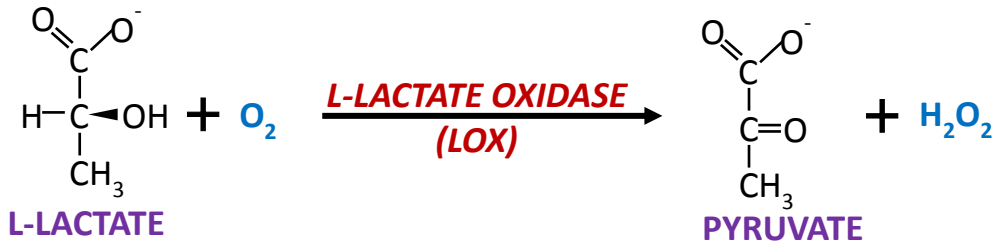

Figure 4.1. Reaction catalysed by LOX. Using molecular oxygen as co-substrate, LL is oxidized by LOX, generating pyruvate and hydrogen peroxide.

De Bari et al. (2010) suggested the existence of a putative flavin-dependent LOX in the intermembrane space of purified rat liver mitochondria. According to the study, addition of LL to peroxisome-free mitochondrial samples evoked oxygen consumption as well as production of pyruvate and hydrogen peroxide in a 1:1 stoichiometry (de Bari et al., 2010). The authors also suggested that the process was independent of the respiratory chain since application of respiration inhibitors did not disrupt hydrogen peroxide generation (de Bari et al., 2010). Nonetheless, taking into consideration that a LOX sequence has not been identified yet in the mitochondrial genome and little is known about the enzymatic properties of the putative mammalian LOX, we decided to base our strategy for breaking down astrocytic LL on the well-established microbial LOX.

4.2.2 L-lactate 2-monooxygenase

Another bacterial enzyme which breaks down LL in an irreversible manner is LMO, which catalyses the FMN-dependent oxidation reaction of LL into acetate, carbon dioxide and water (Figure 4.2).

Figure 4.2. Reaction catalysed by LMO. Using molecular oxygen as co-substrate, oxidation of LL by LMO irreversibly generates acetate, carbon dioxide and water.

The LMO enzymatic reaction shares many properties with that of LOX, including the oxidation of LL at the expense of flavin cofactor reduction. Accordingly, LL oxidation in the first half-reaction of LMO forms the reduced enzyme-pyruvate complex (Maeda-Yorita et al., 1995). However, in contrast with LOX, the intermediate species in the LMO reaction is highly stable, which makes the pyruvate dissociation from the reduced enzyme complex a markedly slower process (Maeda-Yorita et al., 1995). Due to this higher kinetic stability, the reaction of the reduced enzyme-pyruvate complex with the co-substrate molecular oxygen culminates in pyruvate decarboxylation (Maeda-Yorita et al., 1995). The differences between the overall reactions catalysed by LOX and LMO relies, therefore, on the stability of a common intermediate species. While oxidation of LL by LOX is a very fast reaction, LMO catalyses the dissociation of LL approximately 7000-fold slower than LOX (Maeda-Yorita et al., 1995).

4.3 Construction of LOX- and LMO-carrying recombinant plasmids

Expression of enzymes of microbial origin in mammalian astrocytes required adaptation of the DNA sequence to mammalian codon usage. This is because different organisms are biased towards employment of particular codons over others

for the same amino acid. Therefore, to improve the yield of gene expression, the bacterial DNA sequence was optimised for the codon that is more frequently used by mammals (human or rodent). Codon optimization was performed by the company the enzymes sequences were ordered from (Invitrogen, USA, for both LOX and LMO) using provided amino acid sequence input.

Different regulatory elements were included in the expression cassettes, depending on the cell type targeted for gene expression. For some applications, a transcriptionally enhanced fragment of GFAP (sGFAP) promoter was employed in order to selectively drive expression of the enzymes in astrocytes (Liu et al., 2008). For gene transcription in a wider range of cell types, e.g. HEK293 cells, the CMV promoter was used. To enable visualization of the transgene-expressing cells, a sequence of inert fluorescent protein – either EGFP or tdTomato – was also included in the expression cassette, 3' of an internal ribosome entry site (IRES). The IRES element enables translation initiation, allowing independent translation of the microbial enzyme and the fluorescent protein, while, at the same time, both ORFs are regulated by the same promoter.

Once constructed, the recombinant plasmids or AVVs driving the expression of either LMO or LOX were used for transfection or transduction of a mammalian cell line, primary cultured astrocytes, or organotypic brainstem slices for testing purposes.

4.3.1 pCMV-LOX-IRES-EGFP

The mammalianised ORF sequence of LOX from A*erococcus viridans*, preceded by a Kozak sequence, was first cloned under the control of the promiscuous promoter CMV to form the recombinant plasmid pCMV-LOX-IRES-EGFP. The CMV promoter was required in the initial stages of this project to test if the enzyme was functionally active in the mammalian cell line HEK293, swapping to sGFAP promoter for astrocyte-selective expression and proceeding with the time-consuming process of AVV production. The LOX sequence was received in a pMA-T vector backbone and subjected to a double-digestion with the restriction enzymes *BglII* & *PstI* so that the DNA fragment of the gene of interest received sticky ends, allowing its ligation with the vector DNA sequence. In this case, the plasmid used as vector backbone was

pCMV-GPR4-IRES-EGFP, for which restriction digestion with the enzymes *BglII* & *PstI* resulted in the removal of GPR4 sequence from the cassette and made it suitable to be replaced by LOX. Subsequent ligation of 5.0kb DNA fragment of the vector backbone with 1.1kb DNA fragment from the insert formed the recombinant plasmid pCMV-LOX-IRES-EGFP (Figure 4.3A). Assessment of the plasmid sequence through diagnostic digests with *BstBI* as well as *SalI* & *NheI* confirmed a correct outcome (Figure 4.3B), which was further proven by sequencing (Eurofins MWG) using the following primers: CMV forward (ATGGGCGGTAGGCGTGTA) and IRES reverse (CCAAGTCAGTGGCTGCAC). *In silico* alignment of the DNA sequence of the novel recombinant plasmid using Vector NTI showed the expected outcome.

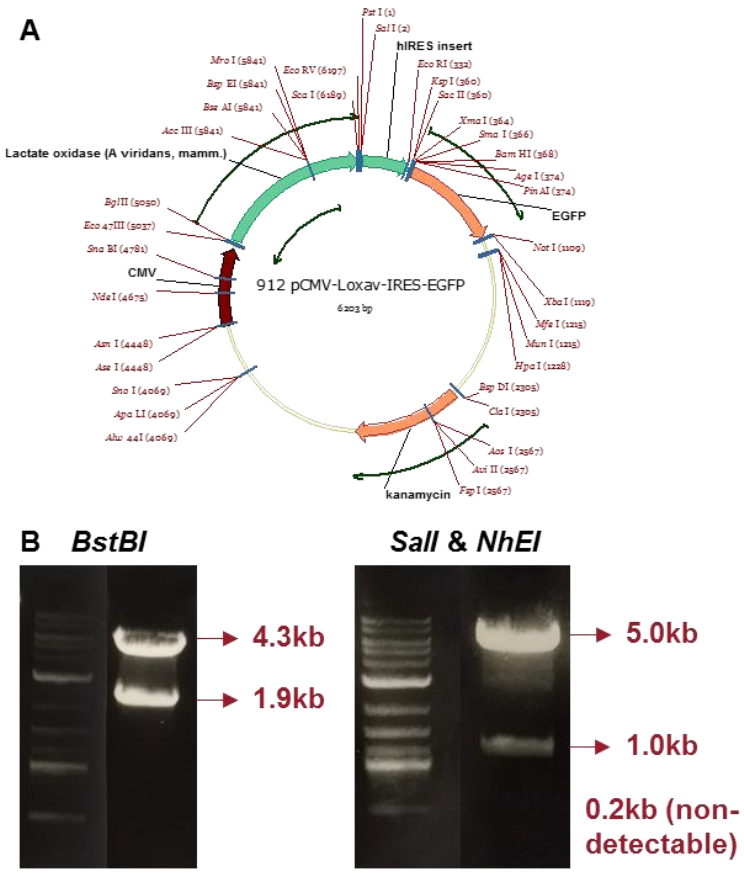

Figure 4.3. Construction of pCMV-LOX-IRES-EGFP. (A) Vector map of the recombinant plasmid carrying LOX (Loxav) and EGFP under the control of a CMV promoter. **(B)** Gel electrophoresis image of the diagnostic restriction digestion with BstBI and SalI & NotI and the yielded bands, which confirmed the correct outcome.

4.3.2 pXCX-sGFAP-LOX-IRES-tdTomato

Another variant of LOX recombinant plasmid containing sGFAP as the astrocyte-selective promoter and tdTomato as a RFP was cloned into a pXCX adenoviral vector shuttle plasmid (Bett et al., 1994). Changing from EGFP to RFP was necessary to avoid interference with emission spectrum of FRET sensors. Among the RFPs available, TdTomato was employed because it has been shown to exhibit increased stability and fluorescence intensity (Shaner, Patterson, & Davidson, 2011). LOX and IRES sequence were isolated from the newly constructed pCMV-LOX-IRES-EGFP by restriction digestion with the enzymes *BstBI* & *AgeI*, generating an insert fragment of 1.5kb. The same restriction digestion was carried out on pXCX-sGFAP-DLDH-IRES-tdTomato, which resulted in an 11.4kb vector backbone fragment. Ligation of both vector and insert created the recombinant plasmid pXCX-sGFAP-LOX-IRES-tdTomato (Figure 4.4A), which underwent diagnostic restriction digestion with the enzyme *EcoRV* (Figure 4.4B) and subsequent sequencing (Eurofins MWG) using specific primers to IRES (IRES forward: CCACTCATCTTATAGCTTTC, and IRES reverse: CCAAGTCAGTGGCTGCAC) and a forward GFAP primer (ATGGGTGAGGGGAGAGCT). The pattern of bands from the restriction digestion matched the one predicted by the sequence of the recombinant plasmid.

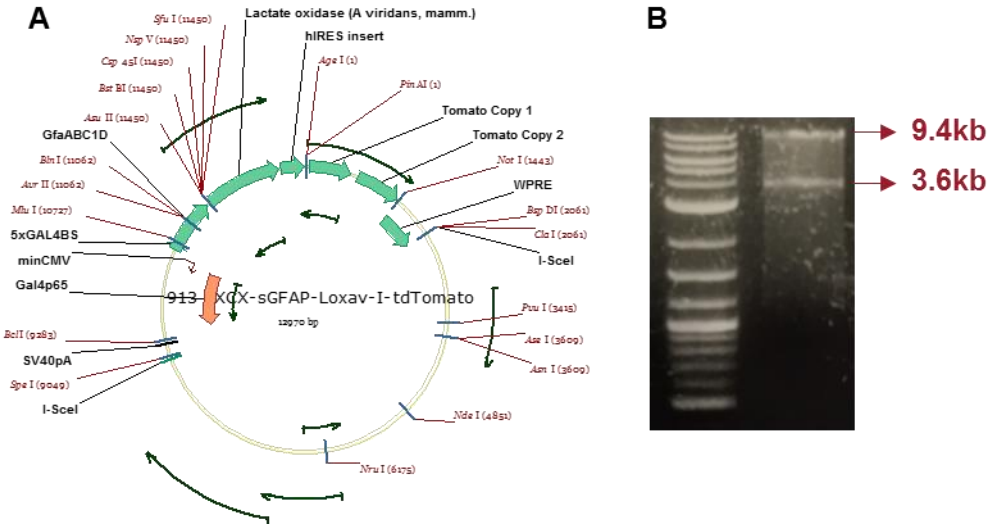

Figure 4.4. Construction of pXCX-sGFAP-LOX-IRES-tdTomato. (A) Vector map of the recombinant plasmid carrying LOX (Loxav) and tdTomato under the control of a sGFAP promoter. **(B)** Gel electrophoresis image of the diagnostic restriction digestion with *EcoRV* was consistent with the correct outcome.

4.3.3 pCMV-LMO-IRES-EGFP

To generate a construct driving the expression of LMO, similar cloning strategies as used to produce LOX recombinant plasmids were employed. Firstly, the mammalianised ORF sequence of LMO from *Mycobacterium smegmatis* on a pMA-T vector backbone as well as the precursor vector backbone pCMV-IRES-eGFP were double-digested with the endonucleases BglII & PstI to generate sticky ends in their DNA sequence. The 1.2kb and 5.0kb resultant fragments of insert and vector, respectively, were ligated together to form the novel recombinant plasmid pCMV-LMO-IRES-EGFP (Figure 4.5A). In order to analyse the clone, diagnostic restriction digestions with the enzymes XhoI & NotI, XhoI & NotI and PvuII were performed, yielding the expected bands (Figure 4.5B). Moreover, the partial DNA sequence using specific primers for CMV promoter (forward: ATGGGCGGTAGGCGTGTA) and IRES (reverse: CCAAGTCAGTGGCTGCAC) aligned with the expected sequence.

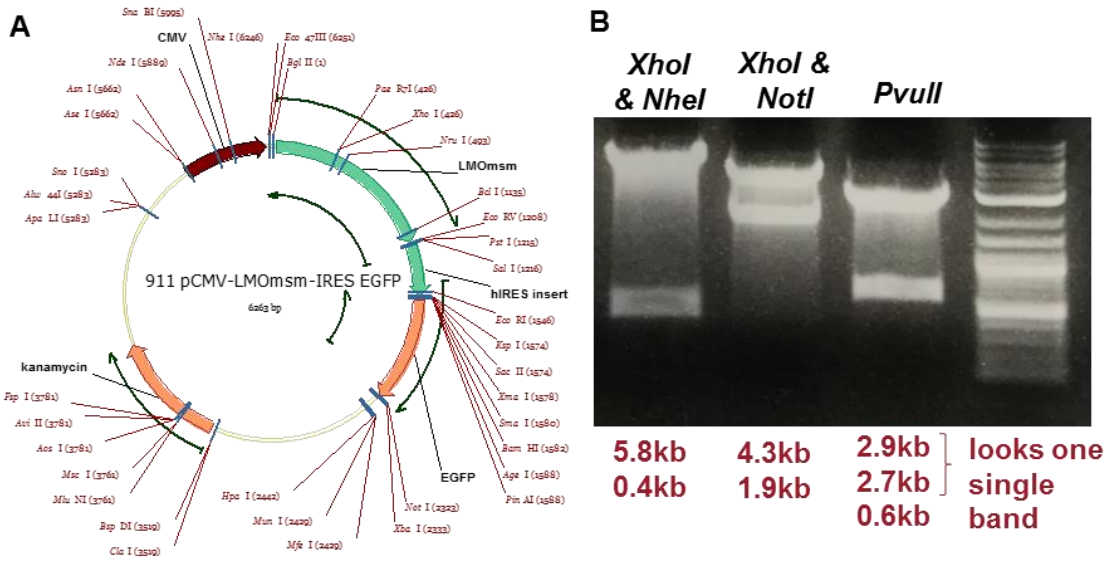

Figure 4.5. Construction of pCMV-LMO-IRES-EGFP. (A) Vector map of the recombinant plasmid carrying LMO (LMOmsm) and EGFP under the control of a CMV promoter. **(B)** Gel electrophoresis image of the diagnostic restriction digestion with *XhoI* & *NotI*, *XhoI* & *NotI* and PvuII yielded the predicted bands, confirming the correct outcome.

4.3.4 pXCX-sGFAP-LMO-IRES-tdTomato

To generate a recombinant plasmid driving the expression of LMO and tdTomato specifically in astrocytes, both LMO and IRES sequences were isolated from pCMV-LMOmsm-IRES-EGFP through restriction digestion with the enzymes *BstBI* & *AgeI*, yielding an insert fragment of 1.6kb. For the vector backbone, pXCX-sGFAP-DLDH-I-tdTomato was digested with the same restriction enzymes as the insert, which yielded a fragment of 11.4kb. Vector and insert fragments were ligated together, generating the recombinant plasmid pXCX-sGFAP-LMO-IRES-tdTomato (Figure 4.6A). Based on the digestion pattern using the endonucleases *SalI* and *EcoRV*, the clone sequence was found accurate (Figure 4.6B). The recombinant plasmid was also partially sequenced by Eurofins MWG using specific primers to IRES (forward: CCACTCATCTTATAGCTTTC, and reverse: CCAAGTCAGTGGCTGCAC) and to GFAP promoter (forward: ATGGGTGAGGGGAGAGCT).

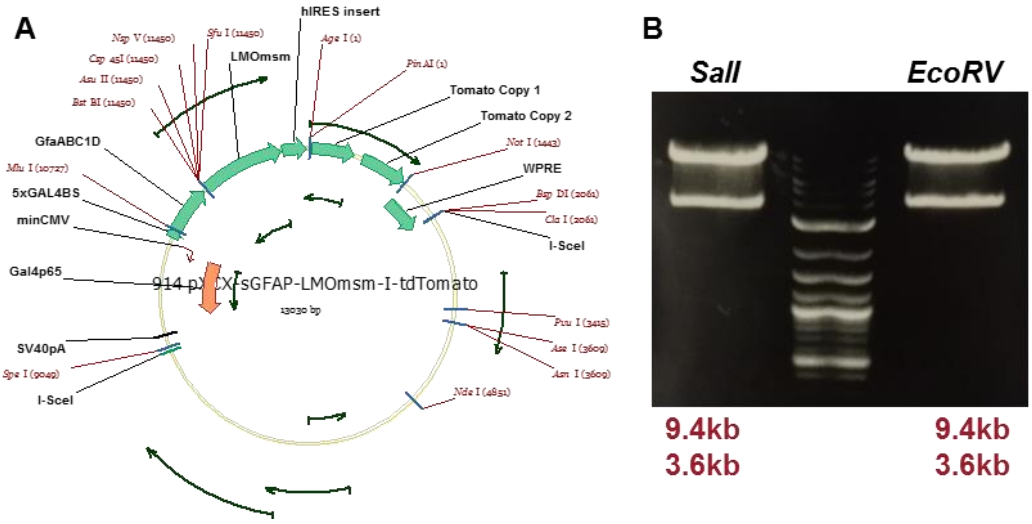

Figure 4.6. Construction of pXCX-sGFAP-LMO-IRES-tdTomato. (A) Vector map of the recombinant plasmid carrying LMO (LMOmsm) and tdTomato under the control of a sGFAP promoter. **(B)** Gel electrophoresis image of the diagnostic restriction digestion with *SalI* and *EcoRV* yielded bands which confirmed the correct outcome.

4.4 Functional validation of LOX and LMO expression *in vitro*

In order to functionally validate the novel constructs, recombinant plasmids or AVVs carrying the expression cassettes for LOX or LMO were transfected or transduced into a mammalian cell line, primary cultured astrocytes and organotypic brain slices. A range of functional tests *in vitro* were then carried out in order to assess the capacity of these bacterial enzyme-based molecular tools for viable expression and functional activity in mammalian cells. Once the basic functionality was confirmed, validation experiments also elucidated metabolic and signalling effects of the decreased astrocytic LL pool that resulted from expression of the LL catabolic enzymes.

4.4.1 LOX and LMO of bacterial origin are expressed in mammalian cells

Activity of the promoters used to drive the expression of the bacterial enzymes was assessed through the expression of the reporter gene. Transfection of HEK293 cell line with 1.0 µg/µl of pCMV-LOX-IRES-EGFP or pCMV-LMO-IRES-EGFP resulted in adequate levels of green expression when examined under an epifluorescence microscope (Figure 4.7), indicating that these cassettes can be successfully expressed in mammalian cells.

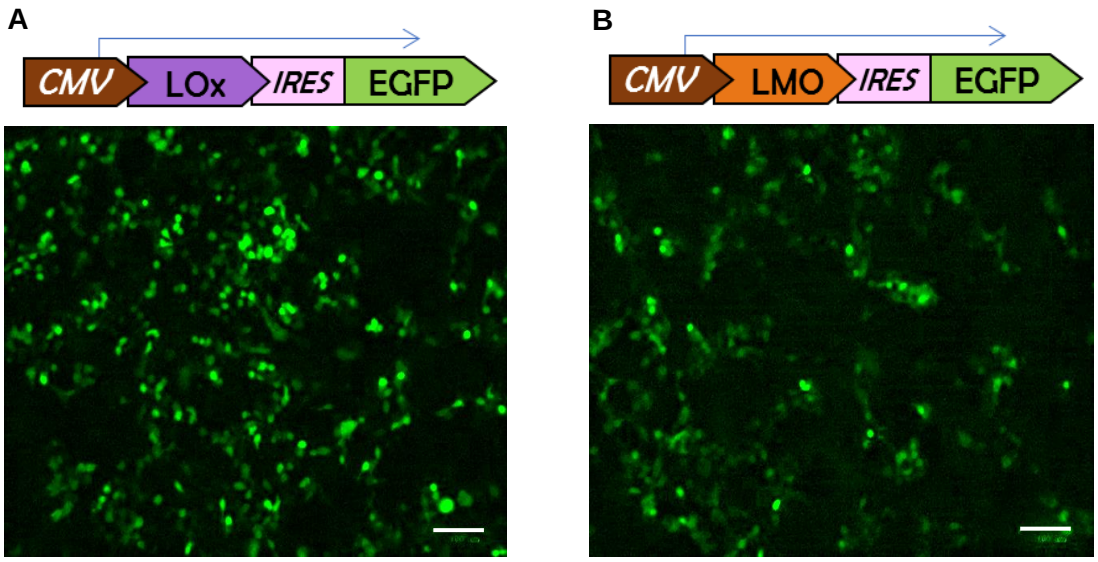

Figure 4.7. LOX- and LMO-transfected HEK293 cells express the reporter gene EGFP. (A) Domain structure of the cassette for expression of LOX in cell lines. Below: HEK293 cells expressing the construct. **(B)** Domain structure of the cassette for

expression of LMO in cell lines. Below: HEK293 cells expressing the construct. Scale bars: 100µm.

On the other hand, primary dissociated cultured astrocytes or astrocytes in organotypic brainstem slices either did not exhibit any detectable red fluorescence or exhibited it at very low levels when transduced with AVV-sGFAP-LOX-IRES-tdTomato or AVV-sGFAP-LMO-IRES-tdTomato. Considering that researchers have consistently reported lower expression levels of the ORF downstream of the IRES element (Jang et al., 1988; Kaufman, Davies, Wasley, & Michnick, 1991), which in our case is the fluorescent protein, we performed immunohistochemistry staining using RFP antigen in an attempt to amplify any tdTomato signal. Results confirmed tdTomato expression in astrocytes in both primary culture and organotypic brain slices transduced with AVV-sGFAP-LOX-IRES-tdTomato (Figure 4.8) and AVV-sGFAP-LMO-IRES-tdTomato (Figure 4.9).

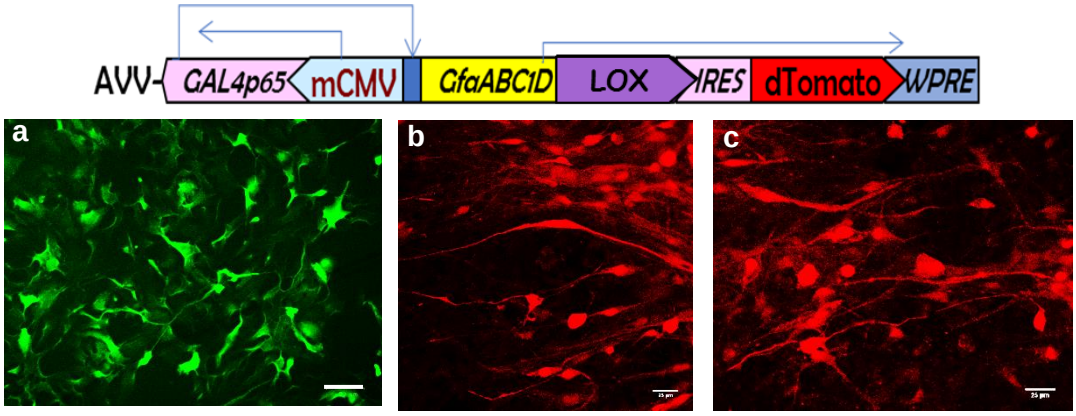

Figure 4.8. LOX-transduced astrocytes express the reporter gene tdTomato. Domain structure of the cassette for expression of LOX in astrocytes through AVV. Below: Confocal stacks showing **(a)** dissociated astrocytes, scale bar 80µm; and **(b and c)** astrocytes in organotypic slice culture expressing the construct, scale bar 25µm. Signal of the reporter gene has been amplified by anti-RFP staining with Alexa 488 (green) for dissociated astrocytes and Alexa 594 (red) for astrocytes in organotypic slice culture.

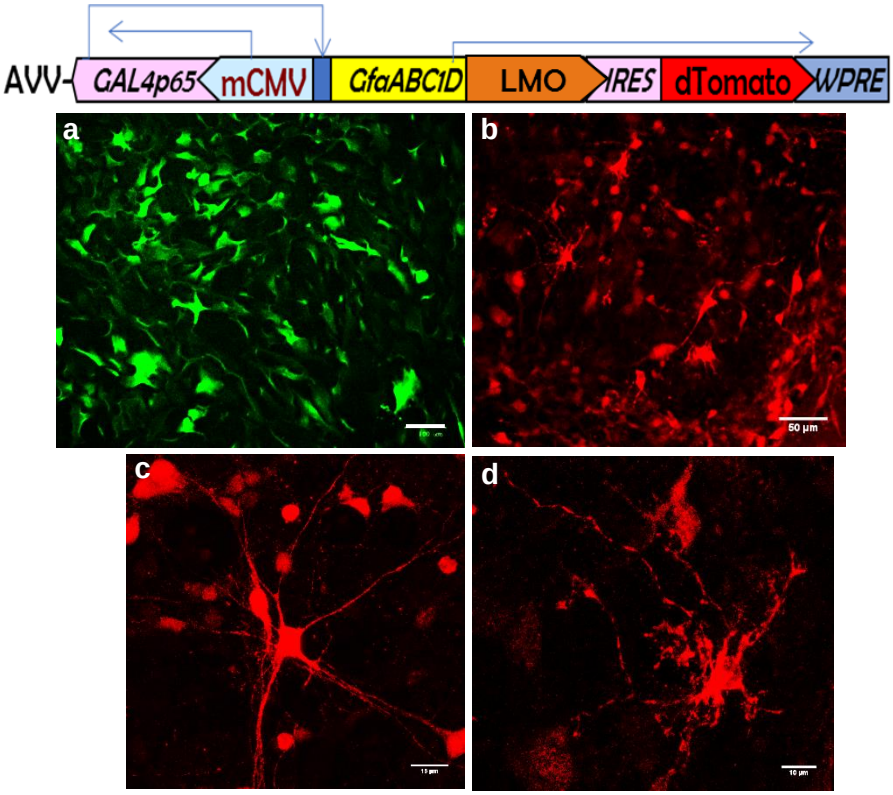

Figure 4.9. LMO-transduced astrocytes express the reporter gene tdTomato. Domain structure of the cassette for expression of LMO in astrocytes through AVV. Bellow: Confocal stacks showing **(a)** dissociated astrocytes, scale bar 100µm; and **(b, c and d)** astrocytes in organotypic slice culture expressing the construct, scale bar 50µm, 15µm, and 10µm, respectively. Signal of the reporter gene has been amplified

by anti-RFP staining with Alexa 488 (green) for dissociated astrocytes and Alexa 594 (red) for astrocytes in organotypic slice culture.

4.4.2 Analysis of astrocytic viability following expression of LOX and LMO

Expression of foreign gene products, interference with astrocytic metabolic pathways, as well as by-products of the enzymatic processes can potentially lead to harmful consequences for cells. Since it was the aim of this project to develop tools for use in physiological contexts *in vitro* and *in vivo*, it was important to establish and avoid potential toxicity of the constructs. A range of MOIs of AVV-sGFAP-LOX-IRES-tdTomato and AVV-sGFAP-LMO-IRES-tdTomato were used to transduce primary cultured astrocytes, whose morphology and density were daily examined for signs of deterioration. Visual assessment by microscope did not reveal any anatomically distinguishable abnormalities in the cells at lower MOIs. Viability assays were performed in order to determine the range of safe MOIs to be used in future functional experiments.

Cell death was assessed through Trypan Blue exclusion assay, which, as previously described, consists of an impermeable blue dye that can only cross cellular membranes that are damaged as a result of cell death (for details, see Chapter 3, section 3.4.3.2.1). Viability of cultured primary astrocytes was tested 3 days following transduction with AVV-sGFAP-LOX-IRES-tdTomato and AVV-sGFAP-LMO-IRES-tdTomato. Two control conditions were used: non-transduced astrocytic cultures and cultures transduced with the control vector AVV-sGFAP-EGFP, which drives the expression of the well tolerated green fluorescent protein. The Trypan Blue assay indicated that AVV transduction per se, in the range of MOIs used, did not change viability of astrocytes (Figure 4.10). Moreover, comparison of the percentage of viable astrocytes expressing the control AVV with astrocytes transduced with either AVV-sGFAP-LOX-IRES-tdTomato or AVV-sGFAP-LMO-IRES-tdTomato at MOI 15 confirmed absence of any significant effect on cell viability under these conditions. However, transduction of astrocytes with AVV-sGFAP-LOX-IRES-tdTomato and AVV-sGFAP-LMO-IRES-tdTomato at MOI 50 resulted in a substantial decrease in the percentage of viable astrocytes, as compared to astrocytes transduced with the same MOI of AVV-sGFAP-EGFP (Figure 4.10).

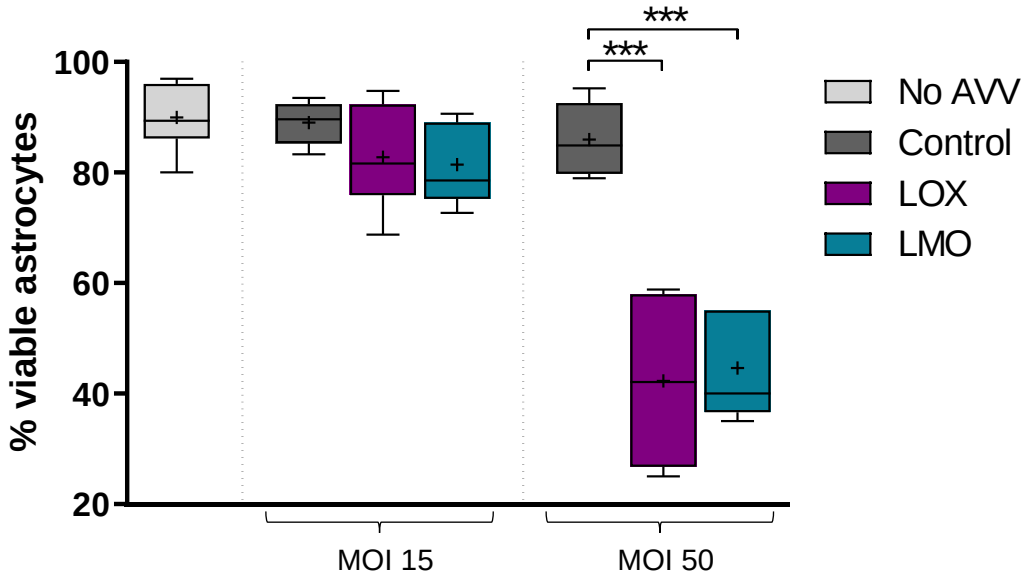

Figure 4.10. Effect of LOX and LMO expression on the viability of primary cultured astrocytes as measured with Trypan Blue exclusion assay. Non-transduced astrocytes (no AVV) and astrocytes transduced with AVV-sGFAP-EGFP (Control), AVV-sGFAP-LOX-IRES-tdTomato (LOX) or AVV-sGFAP-LMO-IRES-tdTomato (LMO) at MOIs 15 and 50 were compared with regard to the % of viable cells. No changes were observed between no AVV (90.0±5.9%, n=6) and Control at all MOIs tested (15: 89.0±3.9%, n=5; 50: 86.0±6.6%, n=6). LOX and LMO at MOI 15 did not evoke significant astrocytic cell death (82.8±9.4%, n=6, and 81.4±7.4%, n= 5, respectively) as compared with Control. LOX and LMO at MOI 50 significantly decreased the % of viable astrocytes (42.3±15.7%, n=5, and 44.6±9.6%, n=5, respectively) as compared to Control. ANOVA (Bonferroni's Multiple Comparison Test) was used to compare: **1)** against No AVV the effects of MOIs 15 and 50: Non-significant (ns) - $p>0.05$ (MOI 15 and MOI 50); **2)** against Control the effects of LOX and LMO at MOIs 15 and 50. **MOI 15:** ns - $p>0.05$ (LOX and LMO); **MOI 50:** *** - $p\leq0.0001$ (LOX and LMO). Data pooled from independent experiments.

Although Trypan Blue exclusion assay is one of the simplest and most routinely employed procedures to assess cell viability, it has limited sensitivity for detecting early damage to cell function. Therefore, in addition, we used the more sensitive XTT cell viability assay, which takes into consideration that viable cells express dehydrogenase enzymes, which reduce XTT tetrazolium salt to the bright and soluble product formazan, as detailed in chapter 3, section 3.4.3.2.2. These enzymes are inactivated shortly after cell death, decreasing the absorbance readout from the formazan product. Results from XTT assay confirmed that employment of AVV as a gene delivery tool did not cause cell damage at the MOIs tested (Figure 4.11).

Astrocytic viability was only significantly decreased with transduction of AVV-sGFAP-LMO-IRES-tdTomato at MOI 50 (Figure 4.11).

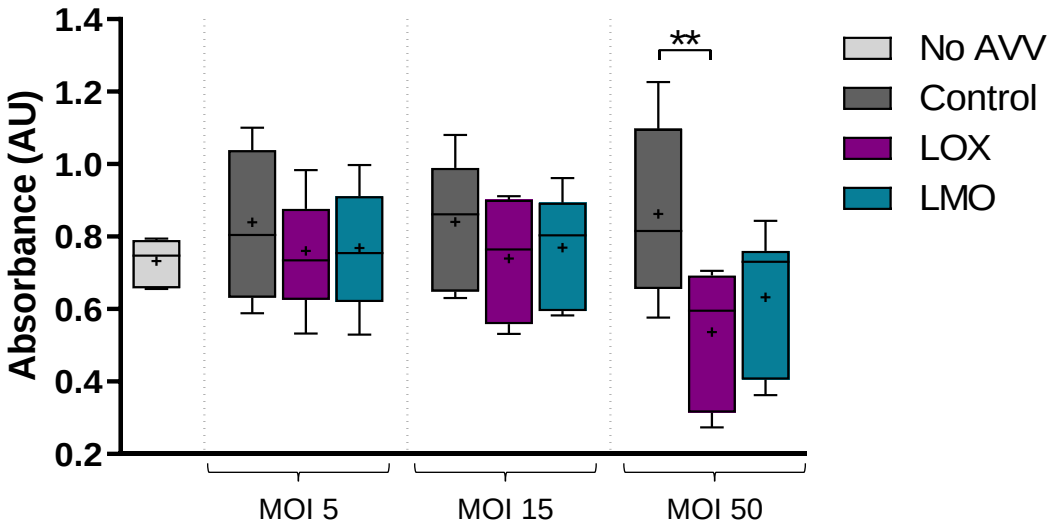

Figure 4.11. Effect of LOX and LMO expression on the viability of primary cultured astrocytes as measured with XTT assay. Non-transduced astrocytes (no AVV) and astrocytes transduced with AVV-sGFAP-EGFP (Control), AVV-sGFAP-LOX-IRES-tdTomato (LOX) or AVV-sGFAP-LMO-IRES-tdTomato (LMO) at MOIs 5, 15 and 50 were compared with regard to the cell viability. No changes were observed between No AVV (0.73±0.06AU) and Control at all MOIs tested (5: 0.84±0.20AU; 15: 0.84±0.17AU; 50: 0.86±0.23AU). LOX and LMO at MOIs 5 and 15 did not alter cell viability (LOX - MOI 5: 0.76±0.15AU, MOI 15: 0.74±0.16AU; LMO - MOI 5: 0.77±0.16AU, MOI 15: 0.77±0.15AU) as compared with Control. At MOI 50, LOX decreased cell viability (0.54±0.18AU), while LMO showed a trend towards a cytotoxic effect (0.63±0.19AU). ANOVA (Bonferroni's Multiple Comparison Test) was used to compare: **1)** against No AVV the effects of Control at MOIs 5, 15 and 50: ns - $p>0.05$; **2)** against Control the effects of LOX and LMO at MOIs 5, 15 and 50. **MOI 5 and MOI 15:** ns - $p>0.05$ (LOX and LMO); **MOI 50:** ** - $p<0.01$ (LOX), ns - $p>0.05$ (LMO). N=6 (No AVV) and N=9 (Control, LOX and LMO). Data pooled from independent measurements.

Since both viability assays revealed that transduction of cultured astrocytes with AVV-sGFAP-LMO-IRES-tdTomato and AVV-sGFAP-LOX-IRES-tdTomato at MOI 15 was safe, all the functional experiments carried out to validate these novel constructs were performed at MOI 15.

4.4.3 LOX or LMO expression reduces constitutive L-lactate release from HEK293 cells and primary cultured astrocytes

The effect of the expression of the novel molecular tools on constitutive LL release was tested in HEK293 cells and primary cultures of dissociated rat astrocytes. LL accumulation in culture media was determined using a fluorimetric assay (Chapter 3, section 3.7). Following 2 hours of incubation, HEK293 cells transfected with 1µg/µl of either pCMV-LOX-IRES-EGFP or pCMV-LMO-IRES-EGFP released 33.2% and 31.6%, respectively, less LL to the extracellular space as compared to HEK293 cells transfected with 1µg/µl of the control vector pCMV-IRES-EGFP (Figure 4.12A). Media conditioned for 6 hours by dissociated astrocytes transduced with either AVV-sGFAP-LOX-IRES-tdTomato or AVV-sGFAP-LMO-IRES-tdTomato showed significantly decreased LL levels, to 88.8% and 87.3%, respectively, as compared to AVV-sGFAP-EGFP-transduced astrocytes (Figure 4.12B).

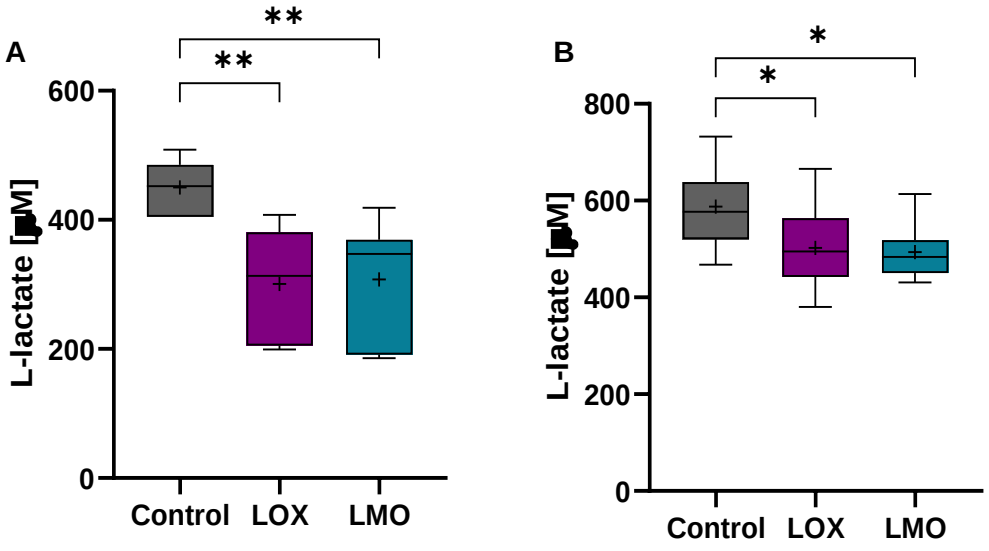

Figure 4.12. LOX and LMO expression in HEK293 cells and cultured astrocytes decrease constitutive release of LL. (A) Media conditioned for 2 hours by HEK293 cells transfected with 1µg/µl of pCMV-LOX-IRES-EGFP or pCMV-LMO-IRES-EGFP contained lower LL levels (LOX, 300.6±84.2µM, n=9; and LMO, 307.6±91.4µM, n=9, respectively) than media conditioned for the same period by HEK293 cells transfected with pCMV-IRES-EGFP (Control, 450.1±41.5µM, n=6). **(B)** Media conditioned for 6 hours by primary cultured astrocytes transduced with AVV-sGFAP-LOX-IRES-tdTomato or AVV-sGFAP-LMO-IRES-tdTomato presented reduced concentration of LL (LOX, 502.4±90.8µM, n=9; and LMO, 493.5±58.1µM, n=8, respectively) as compared to media conditioned for the same period by astrocytes expressing AVV-sGFAP-EGFP (Control, 587.4±84.1µM, n=17). ANOVA (Bonferroni's

Multiple Comparison Test) was used to compare against Control the effect of LOX and LMO expression on LL concentration in the culture media (* - $p<0.05$, ** - $p<0.01$).

4.4.4 LOX or LMO expression decreases forced L-lactate release from primary cultured astrocytes

Estimation of intracellular LL levels in astrocytes was performed by depletion of the cytosolic LL stock through trans-acceleration of MCTs. As detailed in Chapter 1, section 1.3.1, trans-acceleration relies on the application of an inward gradient of pyruvate (10mM) to trigger MCT-mediated extrusion of LL from the intracellular pool. Intracellular levels of LL were monitored with the FRET sensor Laconic 2-3 days following transduction of primary dissociated astrocytes with AVV-CMV-Laconic alone or in combination with either AVV-sGFAP-LOX-IRES-tdTomato or AVV-sGFAP-LMO-IRES-tdTomato.

As expected, bath application of pyruvate [10mM] evoked a substantial drop in the intracellular concentration of LL in primary cultured astrocytes (Figure 4.13A). By measuring the intracellular LL dynamics with Laconic and the relative drop in LL levels following its depletion by application of pyruvate [10mM], we estimated the initial resting levels of LL in astrocytes. Trans-acceleration-induced LL depletion was significantly decreased in LOX- and LMO-expressing astrocytes as compared to control cells (Figure 4.13B). This reduced decrease in LL release is in agreement with lower LL resting levels in these cells.

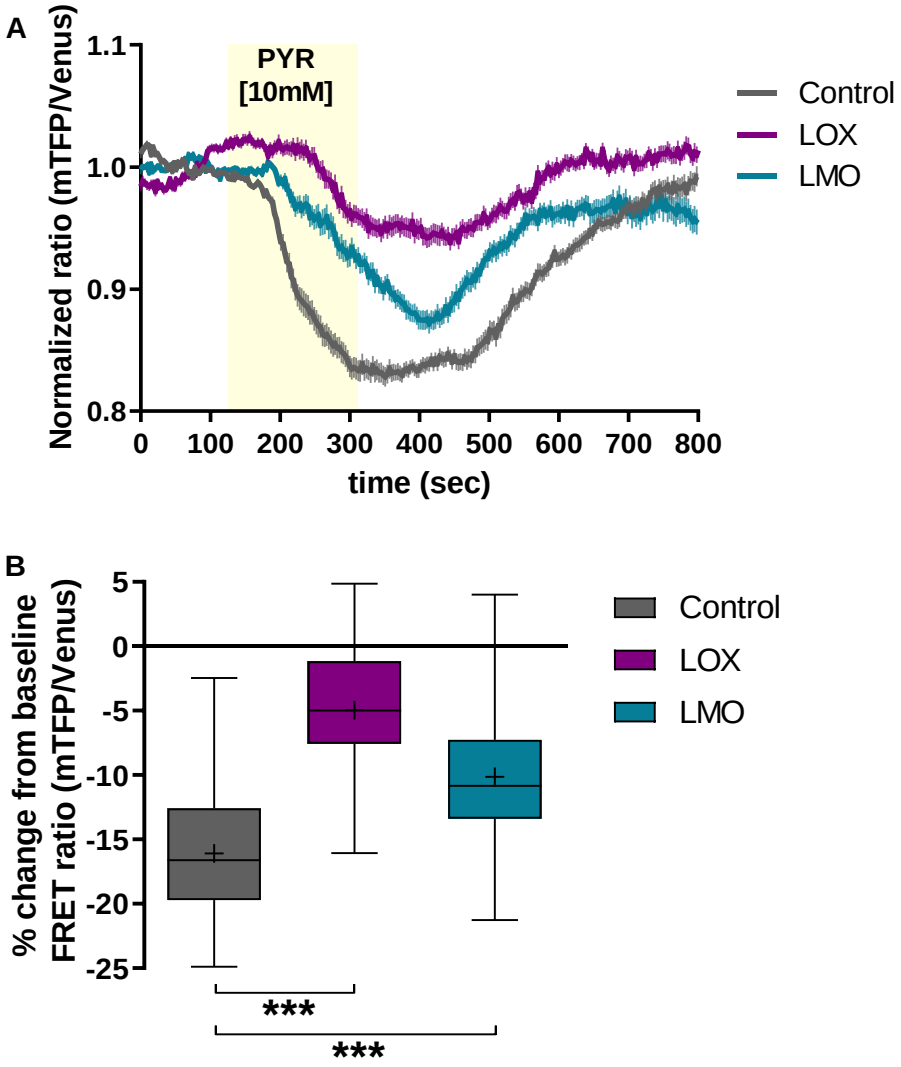

Figure 4.13. Forced LL release is decreased in LOX- and LMO-expressing astrocytes. (A) Estimation of cytosolic LL release using Laconic and a trans-acceleration protocol showed modest LL release from LOX- and LMO-expressing astrocyte as compared to the substantial intracellular LL drop in control cells following application of pyruvate [10mM]. Trace represents average Laconic FRET ratio of astrocytes expressing AVV-CMV-Laconic alone (Control, n=62) or in combination with either AVV-sGFAP-LOX-IRES-tdTomato (LOX, n=53) or AVV-sGFAP-LMO-IRES-tdTomato (LMO, n=52). Data pooled from 7 (Control) and 6 (LOX and LMO) independent experiments. Shaded regions around the trace represents SEM. **(B)** Pooled data for the average Laconic FRET ratio from 300 to 500 seconds to the extrusion of LL with pyruvate [10mM] as compared with the baseline (Control: -16.1±5.1%; LOX: -5.0±4.9%, LMO: -10.1±5.0%). ANOVA (Bonferroni's Multiple Comparison Test) was used to compare against Control the effect of LOX and LMO expression on Laconic FRET ratio (*** - $p<0.0001$).

4.4.5 Expression of LOX or LMO changes the handling of metabolites by astrocytes

Production and/or release of LL from astrocytes can be triggered by a range of stimuli. Since LL that has been newly produced can be almost simultaneously released from astrocytes, the intracellular LL dynamics reflect the sum of both, glycolytic flux and LL release. We, therefore, blocked the efflux of LL through MCT1, the major extrusion route in astrocytes, in order to reveal potential effects of LOX or LMO expression on the glycolytic state of primary cultured astrocytes. 2-3 days following AVV transduction, MCT1 was inhibited with AR-C155858 [1µM] and intracellular LL and pyruvate accumulation was monitored with the FRET sensors Laconic and Pyronic, respectively.

Blockade of MCT1 increased intracellular concentration of LL, indicating that this carrier is essential for constitutive release of LL (Figure 4.14). The level of intracellular LL accumulation upon MCT1 blockade reached a plateau. To investigate whether this plateau corresponds to the saturation of the FRET sensor LACONIC, LL [10mM] was co-applied. Interestingly, LL penetrated the cell probably via MCT4 or other less characterized pathways and evoked a further increase in Laconic FRET ratio (Figure 4.14).

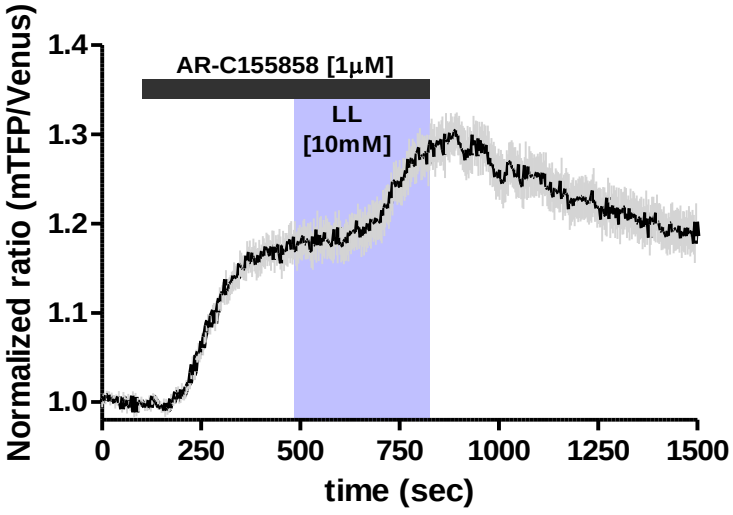

Figure 4.14. MCT1 is essential for constitutive release of LL. Time course of the average Laconic FRET ratio upon application of the MCT1 inhibitor AR-C155858 [1µM] (from 100s to 820s) and LL [10mM] (from 480s to 820s) in primary cultured astrocytes expressing AVV-CMV-Laconic. The plateau in LL level which developed

following AR-C155858 application was not due to reporter saturation. Data pooled from 13 astrocytes from a single recording. Shaded regions around the trace represents SEM.

Once MCT1 had been checked for its ability to block constitutive LL release, we then investigated the rate of LL accumulation in primary cultured astrocytes upon blockade of MCT1 with AR-C1555858 [1µM] in LOX- and LMO-expressing astrocytes. We employed a linear least-square fitting approach to stablish the line of best fit and slopes relative to the linear part of the rising slope, which reflects the rate of LL production (280-600s in Control, 200-550s in LOX, and 330-650s in LMO) (Figure 4.15A).The rates of LL accumulation in LOX- or LMO-expressing astrocytes were not significantly different from that in control astrocytes, although LMO-expressing astrocytes showed a slight trend towards a decreased LL accumulation rate (Figure 4.15B).

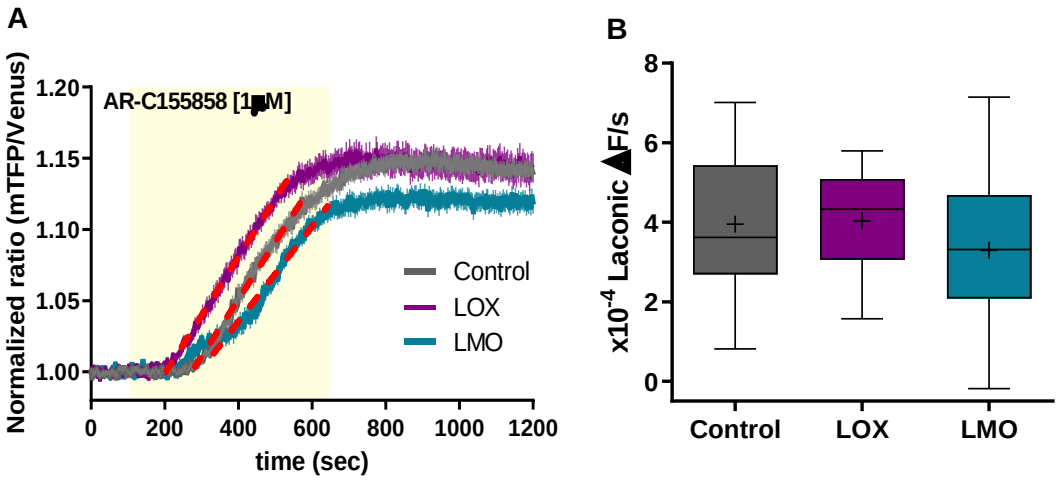

Figure 4.15. LOX- or LMO-expression does not change the rate of LL accumulation in astrocytes. (A) Time course of the average Laconic FRET ratio upon MCT1 inhibition with AR-C155858 [1µM] in primary cultured astrocytes transduced with AVV-CMV-Laconic alone (Control, n=59) or in combination with either AVV-sGFAP-LOX-IRES-tdTomato (LOX, n=37) or AVV-sGFAP-LMO-IRES-tdTomato (LMO, n=46). The dotted red lines are the slopes of LL accumulation fitted by linear regression. Data pooled from 3 independent experiments. Shaded regions around the trace represents SEM. **(B)** Pooled data for the rate of LL production suggested no significant difference in astrocytes expressing LOX (4.0±1.2 $x10^{-4}$ ΔF/s) and LMO (3.3±1.9 $x10^{-4}$ ΔF/s) as compared to control astrocytes (3.9±1.5 $x10^{-4}$ ΔF/s). ANOVA

(Bonferroni's Multiple Comparison Test) was used to compare against Control the effect of LOX and LMO expression on the rate of LL accumulation. ns – p>0.05.

On the other hand, analysis of the time course of Pyronic FRET ratio upon MCT1 blockade with AR-C155858 [1µM] suggested that the rate of pyruvate build-up in the astrocytic cytosol was reduced in both LOX- and LMO-expressing astrocytes as compared to control astrocytes (Figure 4.16). The line of best fit and slopes were calculated using linear least-square fitting method for the linear part of the curve that characterizes the rate of pyruvate build-up (370-620s in Control, and 300-900s in LOX and LMO).

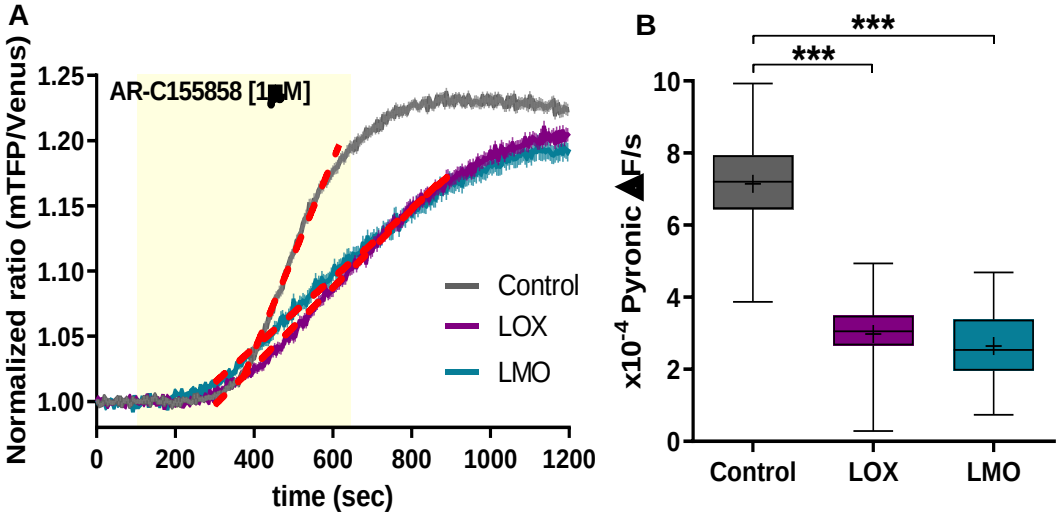

Figure 4.16. LOX- and LMO-expressing astrocytes display decreased rate of pyruvate accumulation. (A) Time course of the average Pyronic FRET ratio upon MCT1 inhibition with AR-C155858 [1µM] in primary cultured astrocytes transduced with AVV-CMV-Pyronic alone (Control, n=53) or in combination with either AVV-sGFAP-LOX-IRES-tdTomato (LOX, n=77) or AVV-sGFAP-LMO-IRES-tdTomato (LMO, n=69).The dotted red lines are the slopes of pyruvate accumulation fitted by linear regression. Data pooled from 3 independent experiments. Shaded regions around the trace represents SEM. **(B)** Pooled data for the rate of pyruvate production suggested reduced rate in LOX (2.9±0.8 $x10^{-4}$ ΔF/s) and LMO (2.6±0.9 $x10^{-4}$ ΔF/s) astrocytes as compared to control astrocytes (7.1±1.2 $x10^{-4}$ ΔF/s). ANOVA (Bonferroni's Multiple Comparison Test) was used to compare against Control the effect of LOX and LMO expression on the rate of LL accumulation. *** - p<0.0001.

4.4.6 Astrocytic expression of LOX or LMO decreases L-lactate tone of organotypic brainstem slices

The effects of the novel genetically-encoded enzymatic tools on LL metabolism and signalling was further investigated using rat organotypic brainstem slices, which provide a more complex and intact context of interactions between astrocytes and neurones. For experimentation in slice culture, we focused on a noradrenergic centre in the brainstem, i.e. the LC, since our group has previously shown that astrocyte-derived LL plays an important excitatory role in neurones residing in this region (Tang et al., 2014). Organotypic brainstem slices containing LC were transduced with either AVV-sGFAP-LOX-IRES-tdTomato or AVV-sGFAP-LMO-IRES-tdTomato to drive expression of LOX or LMO, respectively, specifically to astrocytes. In order to locate noradrenergic neurones in the tissue, the slices were co-transduced with an AVV carrying the expression cassette for EGFP under the control of the PRSx8 promoter (AVV-PRSx8-EGFP) (Figure 4.17). Slices were used for experimentation 8-11 days following AVV transduction.

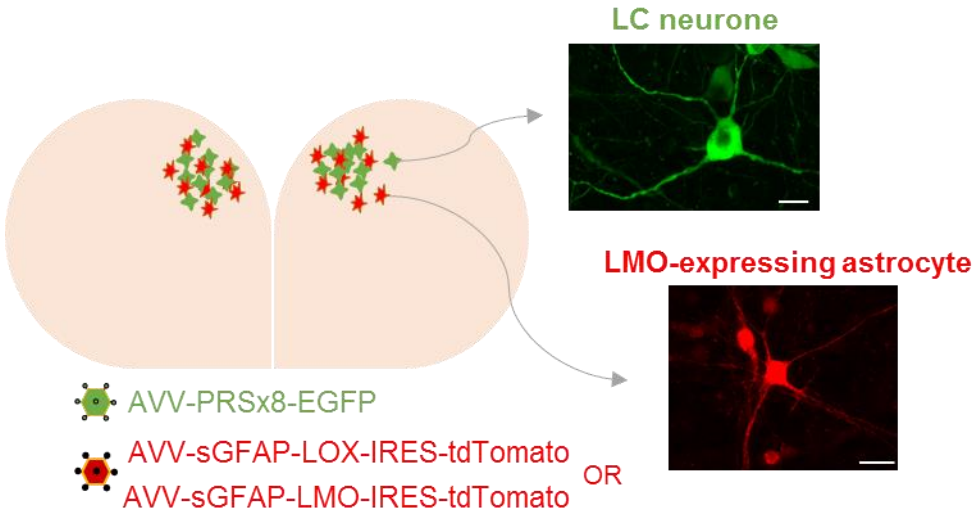

Figure 4.17. Transduction of AVVs in neurones and astrocytes for experimentation in organotypic brainstem slices. Noradrenergic neurones in organotypic brainstem slices containing the LC were transduced with AVV-PRSx8-EGFP (top confocal stack image, scale bar 25µm), whereas astrocytes in the same slice were transduced with either AVV-sGFAP-LOX-IRES-tdTomato or AVV-sGFAP-LMO-IRES-tdTomato (bottom confocal stack image, scale bar 15µm).

The impact of astrocytic expression of LOX or LMO on LL dynamics in organotypic brainstem slices was assessed using LL amperometry, as detailed in Chapter 3, section 3.8. The active LL biosensor was placed in direct contact with the surface of the LC region in an organotypic slice previously transduced with AVV-PRSx8-EGFP and either AVV-sGFAP-LOX-IRES-tdTomato or AVV-sGFAP-LMO-IRES-tdTomato. The null sensor was placed in the adjacent side of the LC to account for non-specific currents. Conversion of current values to LL concentration was performed through interpolation with a calibration curve that was generated by application of known amounts of LL to the tissue chamber at the beginning and end of each recording.

Initial contact of the LL biosensor with the surface of the slice results in a current spike thought, in part, to represent a mechanical artefact, which declines to a constant level, reflecting the constitutive LL release or the extracellular LL tone (Figure 4.18A). Transduction of organotypic brainstem slices with AVV-sGFAP-LOX-IRES-tdTomato or AVV-sGFAP-LMO-IRES-tdTomato resulted in a significantly decreased LL tone as compared to slices containing non-transduced astrocytes (Figure 4.18B).

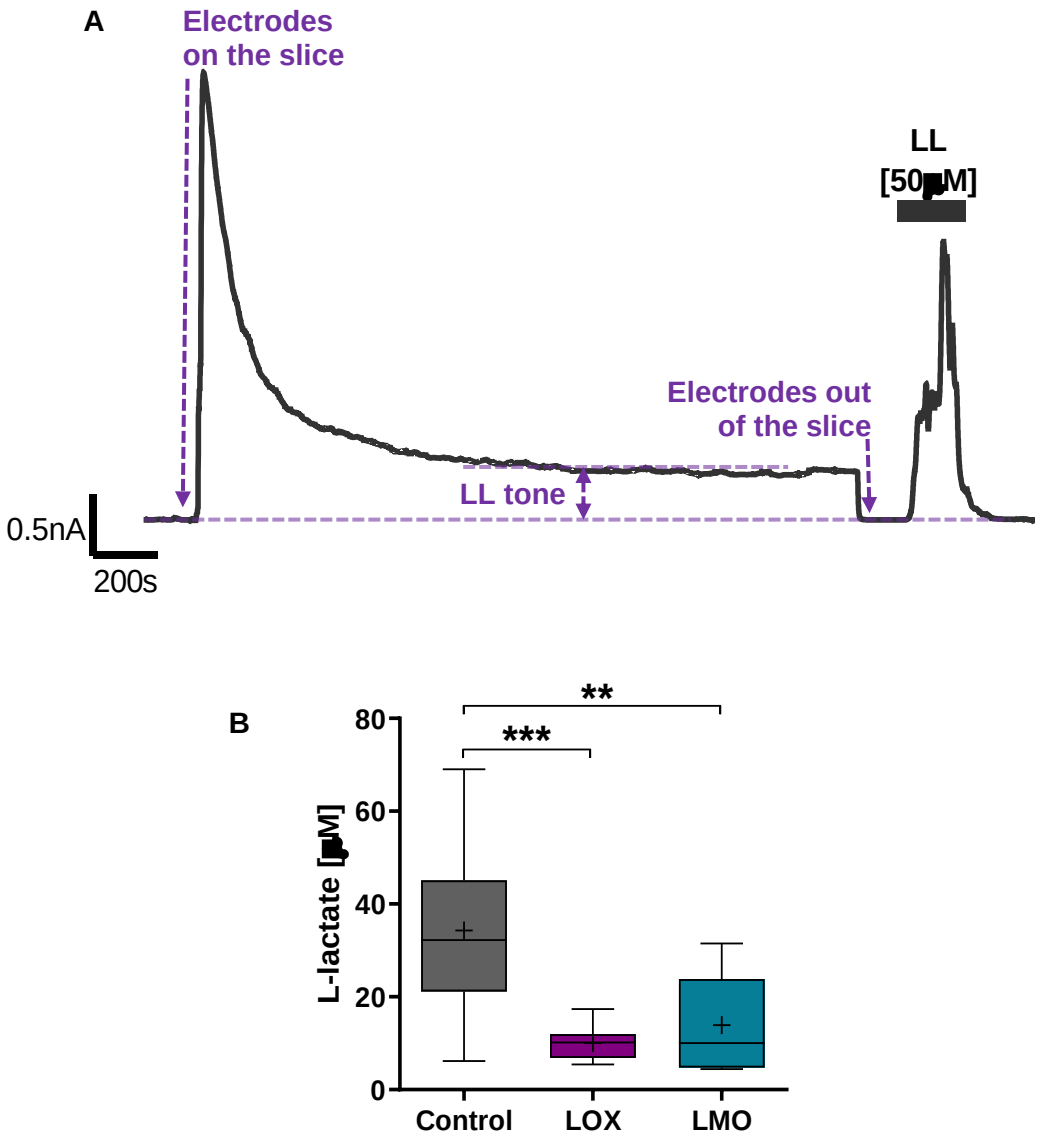

Figure 4.18. Reduced extracellular LL tone in organotypic brainstem slices expressing LOX and LMO. A) Amperometric recording of contact and stabilisation of the enzyme-based LL electrode with the surface of the LC in an organotypic brainstem slice. The LL tone was determined once steady-state had been reached, and converted into LL concentration using a calibration curve. **(B)** Pooled data for the extracellular LL tone of organotypic brainstem slices transduced with AVV-PRSx8-EGFP alone (Control, n=14) or in combination with either AVV-sGFAP-LOX-IRES-tdTomato (LOX, n=12) or AVV-sGFAP-LMO-IRES-tdTomato (LMO, n=9) showed significant reduction in LOX (10.0±3.7µM) and LMO (13.9±10.3µM) slices as compared to control (34.3±18.1µM). ANOVA (Bonferroni's Multiple Comparison Test) was used to compare against Control the effect of LOX and LMO expression on LL tone (*** - $p<0.0001$; ** - $p<0.001$).

4.4.7 LOX or LMO expression in astrocytes reduces forced L-lactate release from organotypic brainstem slices

Organotypic brainstem slices transduced with AVV-sGFAP-LOX-IRES-tdTomato or AVV-sGFAP-LMO-IRES-tdTomato were exposed to high doses of pyruvate short-term, in order to trigger LL release from brain cells through trans-acceleration of MCTs. Amperometric recordings using LL biosensors confirmed that pyruvate [10mM] evoked an immediate and distinct peak in the extracellular concentration of LL in all slices recorded (Figure 4.19A). The net amplitude of trans-acceleration-driven LL release (trans-acceleration amplitude) was reduced in organotypic brainstem slices containing LOX-expressing astrocytes (Figure 4.19B), which may be in accordance with the decreased LL tone in these cells as previously demonstrated. In contrast, although organotypic brainstem slices expressing LMO also exhibited a reduced LL tone, the trans-acceleration amplitude following pyruvate [10mM] application was not significantly different from the control.

Pyruvate-driven LL release is followed by a transient decrease in LL tone, reaching a minimum that may reflect the depletion of LL stock within the tissue (depletion amplitude, Figure 4.19A). LL is then produced intracellularly and released to the extracellular space at a reduced rate until intracellular LL stocks are restored to the baseline level and the initial tone is re-established. The amplitude of LL depletion triggered by application of pyruvate [10mM] was reduced in organotypic brainstem slices containing LOX- and LMO-expressing astrocytes as compared to control slices (Figure 4.19C).

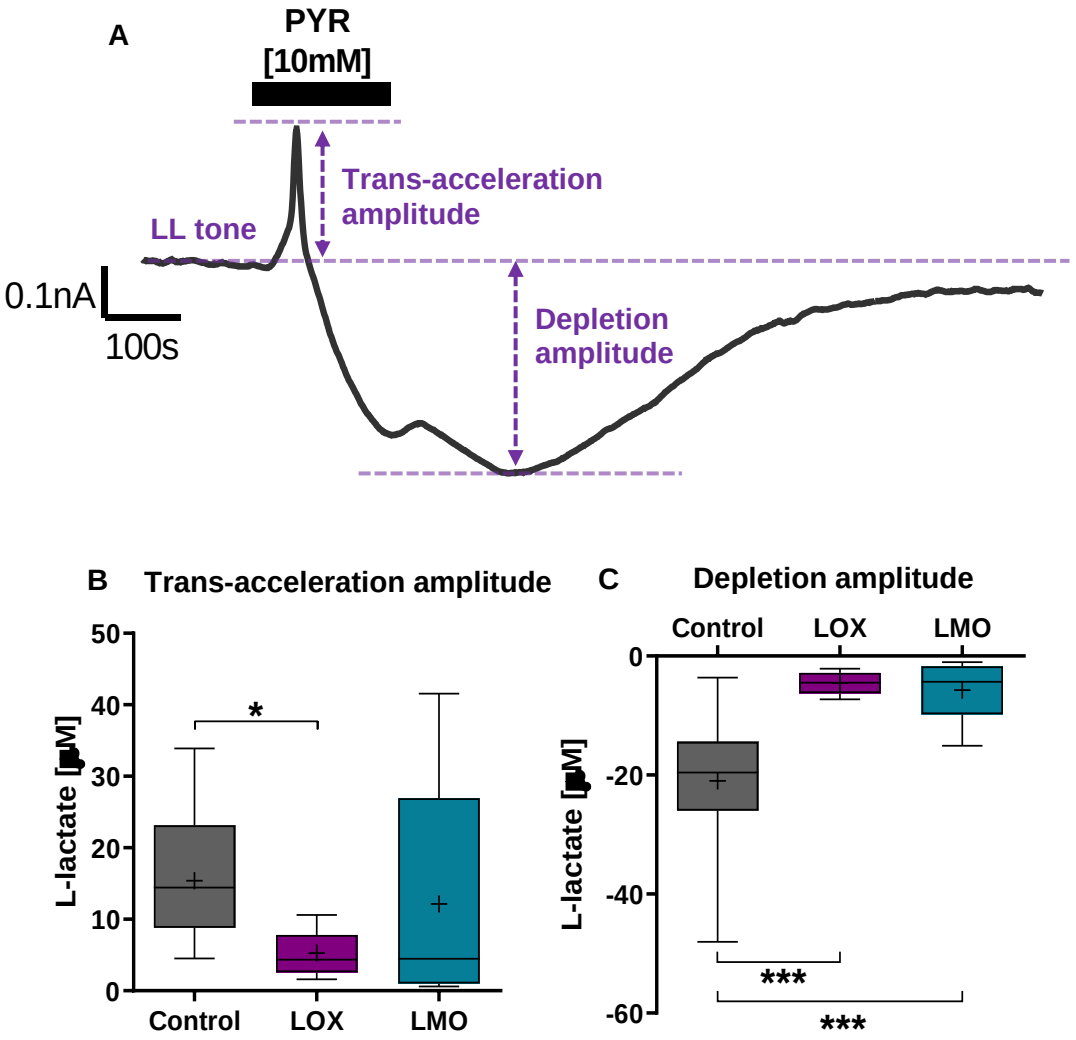

Figure 4.19. Astrocytic expression of LOX in organotypic brainstem slices reduces pyruvate-driven LL release. (A) LL amperometric recording depicting fluctuations in the current following application of pyruvate [10mM]. LL biosensor was placed in the LC region of the brainstem organotypic slice. The current generated is proportional to the extracellular LL concentration. **(B**) Pooled data for the trans-acceleration amplitude following pyruvate [10mM] application in organotypic brainstem slices transduced with AVV-PRSx8-EGFP alone (Control, n=11) or in combination with either AVV-sGFAP-LOX-IRES-tdTomato (LOX, n=12) or AVV-sGFAP-LMO-IRES-tdTomato (LMO, n=8). LOX slices exhibited significant decrease in the amplitude of pyruvate-driven LL release (5.3±3.1µM) as compared to control slices (15.4±8.5µM), while no significant change was observed in LMO slices (12.4±15.5µM). **(C)** Pooled data for LL depletion amplitude following pyruvate [10mM] application in organotypic brainstem slices transduced with AVV-PRSx8-EGFP alone (Control, n=11) or in combination with either AVV-sGFAP-LOX-IRES-tdTomato (LOX, n=12) or AVV-sGFAP-LMO-IRES-tdTomato (LMO, n=8). Both LOX (-4.5±1.7µM) and LMO (-5.7±5.0µM) slices showed significant reduction as compared to control slices (-21.0±11.4µM). ANOVA (Bonferroni's Multiple Comparison Test) was used to

compare against Control the effect of LOX and LMO expression on LL trans-acceleration and depletion amplitude (* - p<0.05; *** - p<0.001).

4.4.8 Release of noradrenaline from neurones in organotypic LC is decreased in slices containing astrocytes transduced with LOX

Among the multiple metabolic and signalling effects of astrocyte-derived LL in the brain, our group is particularly interested in the mechanisms underpinning LL-driven NA release in the brainstem. Since our results so far indicated that astrocyte-specific expression of the bacterial enzymes LOX and LMO modifies LL handling in primary cultured astrocytes and reduces LL tone and release from organotypic brainstem slices, we decided to investigate the extent by which these alterations interfere with LL-triggered NA release from neurones in the LC.

In order to measure NA release from organotypic brainstem slices transduced with either AVV-sGFAP-LOX-IRES-tdTomato or AVV-sGFAP-LMO-IRES-tdTomato, CNiFERs were seeded on top of the slices prior to image recordings. As previously described in Chapter 2, section 2.3.1.3, CNiFERs are genetically engineered HEK293 cells that detect NA through changes in the FRET ratio of the Ca^{2+} indicator TN-XXL. Increase in intracellular Ca^{+2} concentration is caused by NA-mediated activation of α1 adrenoreceptors expressed in the membrane of the CNiFERs (Mosienko et al., 2018; Muller et al., 2014). In order to visually identify the LC region, organotypic slices were also transduced with AVV-PRSx8-EGFP to label noradrenergic neurones with EGFP. To test the ability of LL to stimulate NA release from noradrenergic neurones, each slice received a first application of 2mM of LL (Figure 4.20). The next step was to induce LL release from the intra-astrocytic reservoir and evaluate if endogenous LL-driven NA release is statistically different from the NA released through exogenous application of LL. LL export from astrocytes was triggered by application of pyruvate [10mM], which creates an outward LL gradient by trans-acceleration of MCTs. NA released in response to the application of LL [2mM] was then compared with the response evoked by the application of pyruvate [10mM] in each slice.

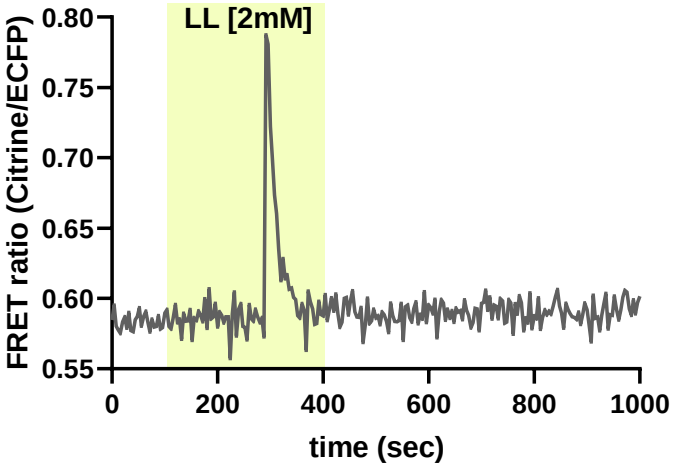

Figure 4.20. Effect of LL in the release on NA from noradrenergic neurones. Representative FRET trace of a single CNiFER seeded on top of a LC organotypic slice following application of 2mM LL.

Results indicated that application of LL [2mM] and pyruvate [10mM] had a comparable effect on NA release in both control and LMO slices (Figure 4.21). Since pyruvate, at least up to 2mM, has been previously reported to be ineffective in prompting release of NA from LC neurones (Tang et al., 2014), and pyruvate [10mM] had no effect on isolated CNiFERs (V. Mosienko, personal communication), the pyruvate effect on NA release observed here is best explained by trans-acceleration-driven LL release from the slice tissue. LOX-expressing slices, on the other hand, showed reduced NA release following application of pyruvate [10mM] as compared to the NA released following addition of exogenous LL [2mM].

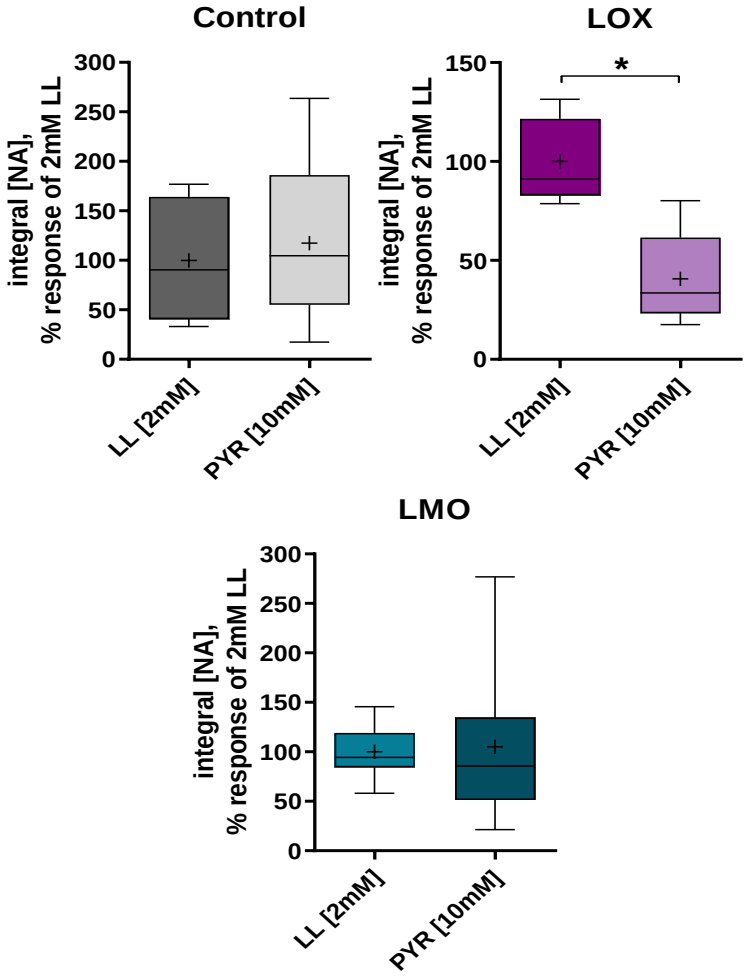

Figure 4.21. LC organotypic slices containing LOX-expressing astrocytes show decreased release of NA. Pooled data for the area under the curve (integral [NA]) of CNiFERs FRET ratio (ECFP/Citrine) following application of LL [2mM] and pyruvate [10mM] in organotypic brainstem slices expressing AVV-PRSx8-EGFP alone (Control, n=5) or in combination with either AVV-sGFAP-LOX-IRES-tdTomato (LOX, n=5) or AVV-sGFAP-LMO-IRES-tdTomato (LMO, n=10). In LOX slices, NA release triggered by pyruvate-driven LL extrusion was reduced as compared to the response from the application of exogenous LL (100.0±21.3% in LL [2mM] *vs.* 40.6±23.9% in PYR [10mM]; * - $p<0.05$). Control and LMO slices did not show significant difference on NA released following application of LL [2mM] and pyruvate [10mM] (Control: 100.0±62.8% in LL [2mM] *vs.* 117.4±89.7% in PYR [10mM], ns - $p=0.80$; LMO: 100.0±27.0% in LL [2mM] *vs.* 105.1±82.4% in PYR [10mM], ns - $p=0.54$). Student's paired t-test.

4.5 Functional validation of LOX expression *in vivo*

The LOX construct is currently being tested *in vivo* by Professor Mikhail Pletnikov at Johns Hopkins University. For this purpose, the AVV shuttle plasmid backbone (pXCX) from the LOX construct was swapped with the LVV shuttle backbone (pTYF), forming pTYF-sGFAP-LOX-IRES-tdTomato, which was then directed towards LVV production. LVV-sGFAP-IRES-tdTomato or LVV-sGFAP-LOX-IRES-tdTomato were bilaterally injected in the hippocampus of mice and expression of the reporter gene in cells with clear astrocytic morphology was confirmed (Figure 4.22). A range of behavioural tests are still ongoing.

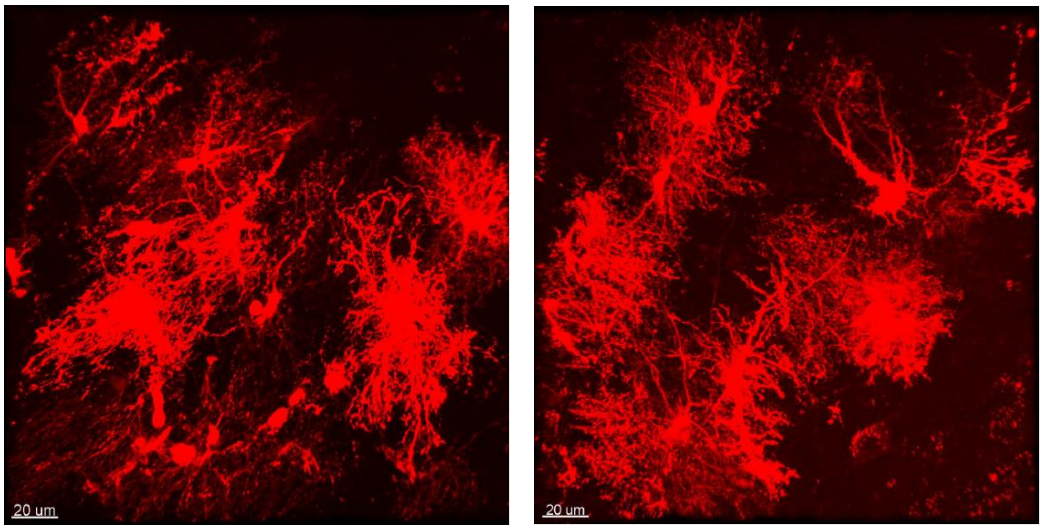

Figure 4.22. *In vivo* expression of tdTomato following transduction with LVV-sGFAP-IRES-tdTomato of astrocytes in the hippocampus. Representative images of hippocampal astrocytes kindly provided by M. Pletnikov. Scale bar 20µm.

The effect of the expression of LOX *in vivo* is also being tested with Dr. Valentina Mosienko at University of Exeter. LVV-sGFAP-IRES-tdTomato or LVV-sGFAP-LOX-IRES-tdTomato were bilaterally injected into the amygdala of mice (AP -1.5mm, ML ±3.4mm, DV -4.0mm and 3.6mm; 200nl, 3-8x10^{10} TU/ml). In order to assure adequate gene expression, behaviour experiments were carried out 4 weeks following surgery. Mice were firstly exposed to 6 hours of restraint stress and, 24 hours later, were subjected to the elevated plus maze test. Mice were then sacrificed, and the brain tissue was collected, processed, and stained with anti-RFP antibody. Analysis of cell

morphology indicated that the majority of cells expressing the construct are astrocytes (Figure 4.23A). Evaluation of mouse behaviour in the elevated plus maze revealed that expression of LOX in the amygdala decreased the number of entries to the open arm, suggesting increased sensitivity to stress displayed as elevated anxiety (Figure 4.23B). Importantly, the total number of entries in the arm was similar between control and LOX mice, which indicates that the overall motor activity was not affected by LOX expression (Figure 4.23C).

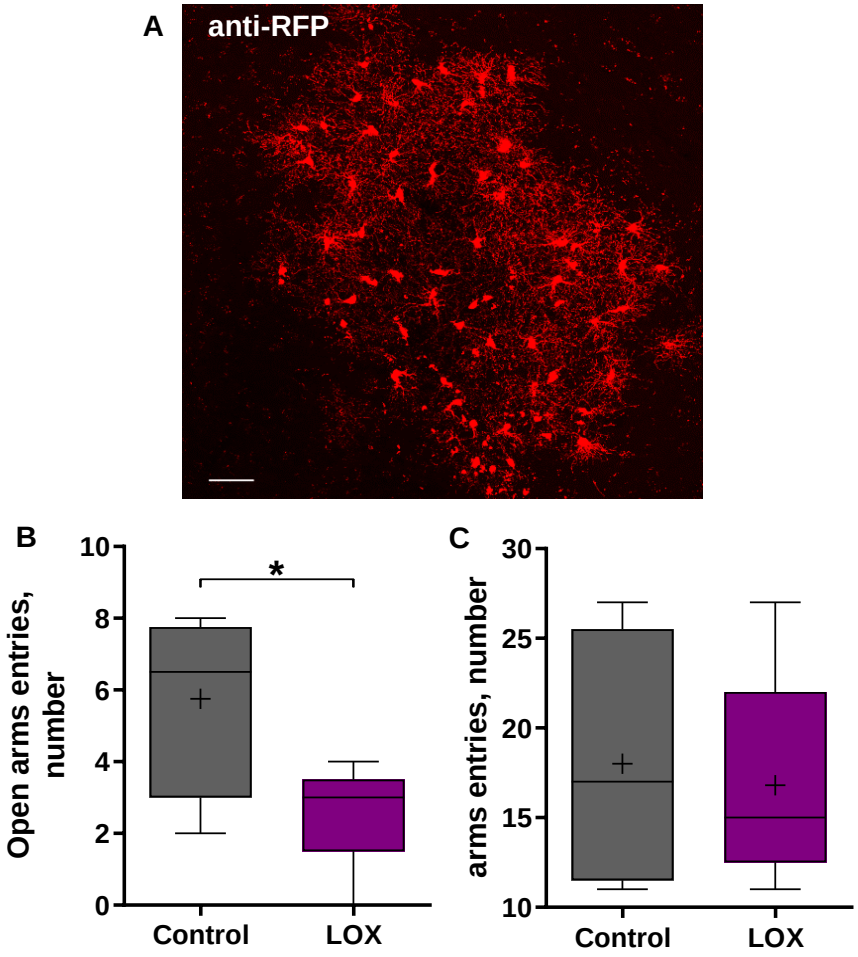

Figure 4.23. *In vivo* expression of LOX in astrocytes in the amygdala of mice enhances anxiety-like behaviour. Mice were subjected to bilateral injection of either LVV-sGFAP-IRES-tdTomato (Control, n=4) or LVV-sGFAP-LOX-IRES-tdTomato (LOX, n=5) into the amygdala. Behavioural and histological analysis were performed 4 weeks following surgery. **(A)** Representative confocal stack of pTYF-sGFAP-LOX-IRES-tdTomato expression in the amygdala *in vivo*. Signal of the reporter gene was amplified by anti-RFP staining. Scale bar 50µm. **(B)** Preliminary results on the effects of LOX expression on the number of entries to the open arm of the elevated plus

maze. **(C)** Overall motor activity in the elevated plus maze test of control and LOX mice. * - $p<0.05$, Student's unpaired t-test.

4.6 Discussion of LOX and LMO effects

The main aim of this project was to develop and validate novel molecular tools to investigate the LL-mediated metabolic coupling and signalling between astrocytes and neurones. Rather than directly interfere with astrocytic LL production and release, which are still subject of study and debate, we have developed molecular tools that aim to limit LL effects by restricting the availability of this compound in the brain. The genetically-engineered molecular tools created in this project degrade LL specifically in astrocytes and, consequently, reduce the constitutive and reactive LL release as tested *in vitro*.

The innovation behind these tools was to take advantage of the high capacity of bacteria to metabolize LL. We have identified two bacterial enzymes that irreversibly degrade LL: LOX and LMO, whose activities are better described in *Aerococcus viridans* and *Mycobacterium smegmatis*, respectively. The ORF sequence of these enzymes was adapted to the mammalian codon usage and cloned under a sGFAP promoter to drive their expression selectively to astrocytes. Then, we needed to determine if the enzymes of microbial origin can be in fact expressed in mammalian cells and, if so, whether they are enzymatically active. A combination of specific assays using dissociated astrocytes or organotypic brainstem slices were performed in order to address these questions and validate the functional effects of these novel constructs when expressed in rat astrocytes.

The first evidence of functional activity of the bacterial enzymes came from assessment of LL content in media conditioned by HEK293 cells and dissociated astrocytes expressing LOX or LMO. In both cell types, concentration of LL in the media decreased, indicating a reduced constitutive release of LL. The level of reduction in LL tone was more profound in HEK293 cells than in dissociated astrocytes, which may be due to the high glycolytic profile of astrocytes (see Chapter 1, section 1.2.4), particularly under the given conditions of an elevated glucose content (25mM) of the culture media used for these experiments. That the rate of LL

production may be higher in astrocytes than in HEK293 cells is suggested by the increased LL levels in the astrocyte-conditioned media as compared to HEK293 cell media (see Figure 4.12), and this difference may be expected to partially mask the LL breakdown through the activity of LOX and LMO in astrocytes. Constitutive LL release was also decreased in organotypic brainstem slices containing astrocytes transduced with LOX and LMO, as measured with LL amperometry.

The next step in the validation process was to determine the effects of astrocytic expression of LOX and LMO on the amount of LL that can be released upon acute stimulation. To force maximal LL extrusion from primary dissociated astrocytes and organotypic brainstem slices, we employed trans-acceleration of MCTs by bath application of pyruvate [10mM]. This approach, which in a simplistic explanation relies on exchanging cytosolic LL for pyruvate, has been established by others as a means to deplete cells of LL (Mächler et al., 2016; San Martín et al., 2013). Although trans-acceleration of MCTs has been recurrently used *in vitro* and *in vivo* to force LL release, cellular overload with pyruvate could be thought to result in LDH-mediated conversion of pyruvate to LL, increasing cytosolic LL concentration rather than reducing it by trans-acceleration. However, astrocytes were constantly superfused with a solution low in glucose (2mM) in order to limit generation of NADH through glycolysis, which is an essential component of LDH reaction. Therefore, in this case, activity of LDH may be limited by the availability of NADH in spite of the excess of pyruvate applied (Hung, Albeck, Tantama, & Yellen, 2011; San Martín et al., 2013; Yuzheng Zhao et al., 2011).

Upon pyruvate application, intracellular levels of LL in astrocytes were monitored with the FRET sensor Laconic, whereas LL extracellular concentration in organotypic brainstem slices was monitored with LL amperometry. In dissociated astrocytes, trans-acceleration-driven LL release was substantially decreased when cells were expressing LOX or LMO. In organotypic brainstem slices, trans-acceleration-driven LL release was only significantly decreased with LOX expression, while slices expressing LMO exhibited large variability in their response to trans-acceleration, resulting in no significant effect overall. It is nonetheless important to keep in mind that intracellular recordings with the biosensor Laconic were performed in primary astrocytic culture where only the cells expressing the constructs were analysed. LL amperometry, on the other hand, was carried out in a more intact preparation in which

neurones and other glia cells that did not express the enzymes were present but that would also have contributed to the trans-acceleration-induced LL release. Moreover, LOX and LMO enzymes exhibit different kinetic properties, with LOX breaking down LL approximately 7000-fold faster rate than LMO (Maeda-Yorita et al., 1995). This raises the possibility that the LL production stimulated by the trans-acceleration-evoked pyruvate load in the cell contributed to the LL peak detected with amperometry, and that only LOX as the faster catabolic enzyme affected the LL transient. Combined, Laconic and amperometric recordings imply that besides decreasing LL tone, astrocytic expression of the bacterial enzymes also reduces the amount of LL released upon stimulation – an outcome that is more pronounced with LOX expression than LMO.

Importantly, validation experiments carried out in this project were performed within the safe range of MOIs for the AVVs carrying the expression cassettes for LOX or LMO. Through evaluation of astrocytic viability with different assays, we established the ideal MOI by which AVV transduction and the expression of LOX and LMO did not lead to harmful consequences for cells, avoiding any potential intrinsic toxicity of the constructs.

Once the basic functionality of the novel genetically-encoded bacterial enzyme tools was confirmed, we then examined their effects on the astrocytic metabolism. At steady-state level, an enzymatic reaction is at equilibrium, i.e. there is no net change in the concentration of both substrate and product (Nelson & Cox, 2017). Equilibrium of a reaction does not mean that concentration of substrate and product are equal. In the case of LDH-mediated LL production, many factors contribute to the equilibrium of the reaction at steady-state, such as the glycolytic rate and, consequently, the $NADH/NAD^+$ ratio, as well as LL release and oxidative phosphorylation. In order to evaluate the rate of LL production and pyruvate accumulation in dissociated astrocytes expressing LOX or LMO, we blocked monocarboxylate extrusion to disturb the reaction equilibrium so that we could evaluate the reaction rate. MCT1 was blocked with AR-C155858, which can inhibit MCT1 at nanomolar range, but is ineffective against MCT4 (Ovens, Davies, Wilson, Murray, & Halestrap, 2010). Since the AR-C155858 binding site on MCT1 is located intracellularly in the C-terminal domain (Ovens et al., 2010), a latency response was observed following application of the blocker. AR-C155858 increased intracellular levels of both LL and pyruvate,

implying an important role of MCT1 in controlling the steady-state levels of these monocarboxylates. Increase in cytosolic LL reached a plateau, suggesting that a new thermodynamic equilibrium was established. In this situation, other LL carriers such as MCT4, or pannexins and connexin hemichannels may be playing a role in keeping the steady-state LL, albeit at a higher level. As for the accumulation of pyruvate upon MCT1 blockade, it has not been tested if the plateau of the curve reflects the saturation of the sensor Pyronic and, therefore, conclusions in this regard cannot be drawn. Evaluation of the rate of LL production showed no change in LOX- and LMO-expressing astrocytes, suggesting that LDH remains highly active under these conditions. Nonetheless, expression of the bacterial enzymes substantially decreased the rate of pyruvate accumulation. The following factors may be involved in this response:

(i) Activity of LOX decreases cytosolic levels of LL, used as substrate, and it is expected to increase the concentration of the reaction product pyruvate (Figure 4.24A). However, pyruvate accumulates at a slower rate in LOX-expressing astrocytes. In fact, the rate of pyruvate accumulation in astrocytes expressing LOX is similar to LMO, which does not produce pyruvate (Figure 4.24B).

(ii) In a scenario of reduced intracellular LL concentration due to LOX or LMO expression, LDH reaction is expected to be shifted towards LL formation. LL generated, on the other hand, is constantly degraded by the bacterial enzymes. Therefore, there is a sink driving LL formation – which may explain the decreased rate of pyruvate accumulation in astrocytes expressing LMO or LOX.

(iii) Formation of pyruvate through LOX activity does not replenish NADH, which is required for LDH-mediated conversion of pyruvate to LL (Figure 4.24A). Since the LDH-mediated LL production, however, seems to be unaffected by LOX, availability of NADH does not appear to be a limiting factor under these conditions and within this range of reactions.

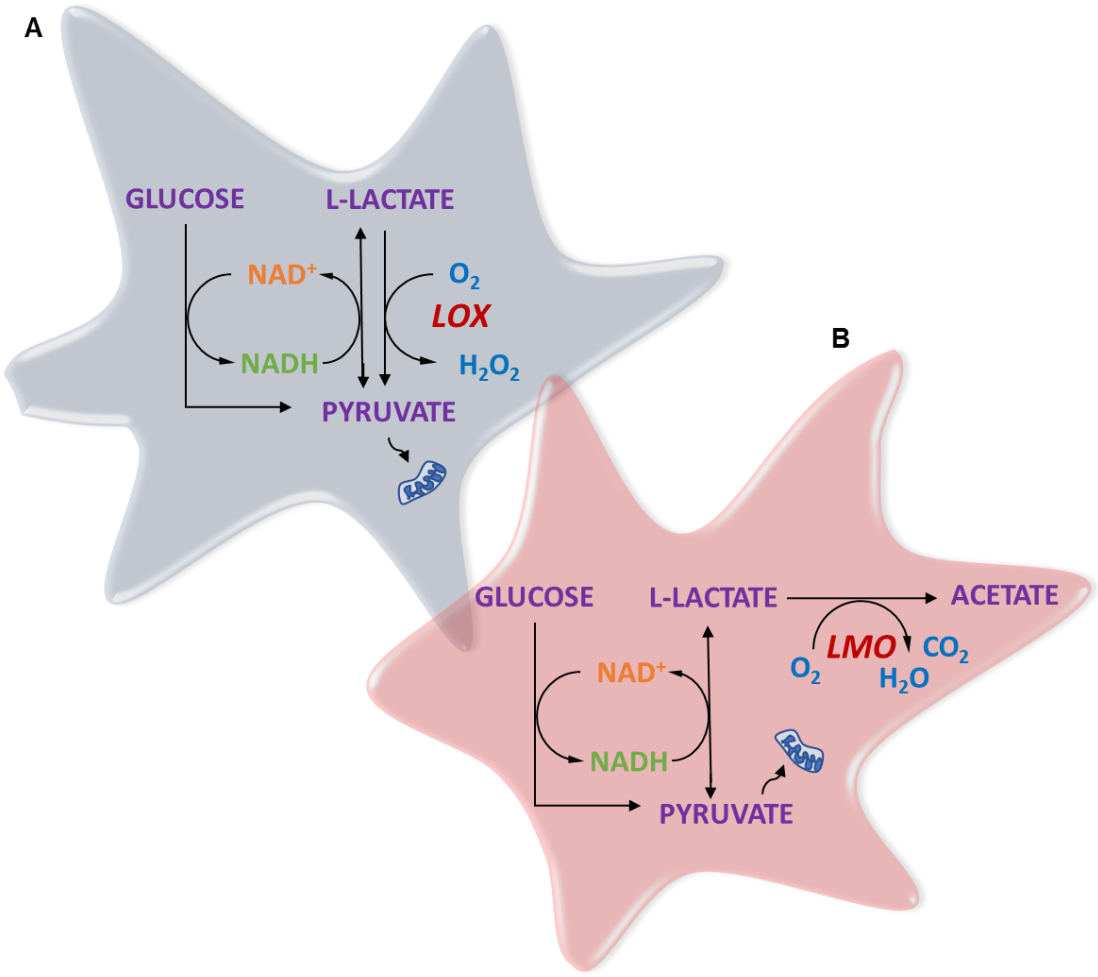

Figure 4.24. Overview of LL metabolism in astrocytes expressing the novel LL-limiting tools. LL generated through glycolysis is degraded into **(A)** pyruvate and hydrogen peroxide in LOX-expressing astrocyte and **(B)** acetate, carbon dioxide, and water in LMO-expressing astrocytes.

In fact, cell metabolism is tightly regulated and changes in one pathway may be accompanied by many regulatory changes in other pathways. Through analysis of the rate of LL and pyruvate accumulation, we can infer that astrocytes expressing the bacterial enzymes undergo metabolic changes, but it was not possible to identify the specific nature of those changes based on the analysis of the metabolites LL and pyruvate alone, and by the method employed (blockade of MCT1).

In order to investigate whether the decreased intracellular LL pool and release that results from the expression of LL catabolic enzymes affects astrocytes-to-neurone LL signalling, we evaluated LL-induced release of NA from LC neurones in slices

containing astrocytes expressing LOX or LMO. Comparison of NA released from bath application of LL [2mM] with NA released from trans-acceleration-driven LL extrusion implied that astrocytic expression of LOX decreases LL-induced NA release. This result is consistent with a decreased constitutive and forced LL release from slices expressing LOX in astrocytes. In contrast, astrocytic expression of LMO had no effect on the NA released from organotypic LC slices, which is also consistent with unchanged trans-acceleration driven LL release from organotypic brainstem slices as measured with LL amperometry.

H_2O_2 is the by-product of LOX activity and, as a ROS, has the potential to oxidize cellular components such as DNA, protein, and membrane lipids, causing a number of deleterious events in the cell. ROS are naturally produced by cells, mainly as a result of aerobic metabolism, when electrons passing down the mitochondrial respiratory chain reduce oxygen prematurely and incompletely, generating superoxide radicals (Nelson & Cox, 2017). Astrocytes are reported to exhibit several fold higher production of ROS than neurones (Lopez-Fabuel et al., 2016). However, astrocytes can efficiently handle oxidative stress as they express high levels of antioxidant scavengers and enzymes that avoid ROS-mediated cellular damage (Dringen, Kussmaul, Gutterer, Hirrlinger, & Hamprecht, 1999; Fernandez-Fernandez, Almeida, & Bolaños, 2012; Sagara, Miura, & Bannai, 1993). Detoxification of H_2O_2 takes place through a series of mechanisms, which mostly require glutathione (GSH) as cofactor (Fernandez-Fernandez et al., 2012). Glucose metabolism, for example, largely contributes to antioxidant processes since it regenerates NADPH(H^+) through the phosphate-pentose pathway (PPP). NADPH(H^+), in turn, mediated by GSH, transfers its reducing equivalents to H_2O_2, forming H_2O (Nelson & Cox, 2017). Astrocytes have been shown to exhibit a high GSH content, which can also be exported to neurones, as well as a robust capacity for GSH-dependent detoxification processes (Bolaños, 2016; Dringen, Brandmann, Hohnholt, & Blumrich, 2015). Therefore, taking into account the high capacity of astrocytes to handle oxidative stress, astrocytes are likely to support LOX expression at the MOI used.

Acetate is the breakdown product of LL with LMO activity. In the brain, acetate is described to accumulate mainly in astrocytes, where it is degraded by the enzyme acetyl-CoA synthetase to acetyl-CoA, which engages the TCA cycle and increases its activity (Waniewski & Martin, 1998; Zielke, Zielke, & Baab, 2009). In fact, acetate has

been shown to be an additional metabolic substrate during periods of brain activation (Dienel & Cruz, 2006). Oxidation of acetate is widely reported to occur in cancer cells, which require metabolic adaptations in order to overcome limited nutrient availability and the high biosynthesis demand of growth (Lin, Zhang, & Lin, 2018; Liu et al., 2018; Qiu et al., 2019). The additional acetate produced by LMO is, therefore, likely to simply be absorbed into oxidative phosphorylation.

In conclusion, this chapter describes the construction and validation of innovative molecular tools based on enzymes of microbial origin to break down LL and study its functions in the brain. Tests *in vitro* showed that the LL-processing enzymes are active when expressed in astrocytes and modify LL dynamics and action in the brain. Successful expression in astrocytes *in vivo* suggested that these tools show potential to be employed to study the roles of astrocytic LL in the brain.

Chapter 5 – Interfering with L-lactate signalling through D-lactate release

5.1 D-lactate-sensitive signalling through astrocytic L-lactate in cardio-respiratory regulation

Despite the multifactorial and complex pathophysiology of cardiorespiratory diseases, there is a consensus that increased activity of the sympathetic nervous system has a profound impact on the development and progression of hypertension and heart failure (Kasparov & Teschemacher, 2008). Presympathetic neuronal circuits in the hypothalamus and brainstem receive inputs from the periphery and from different regions of the CNS, which are translated into tonic descending sympathetic drive (Kasparov & Teschemacher, 2008; Marina, Teschemacher, Kasparov, & Gourine, 2016). Dysregulation of this system may result in enhanced sympathoexcitation, which is detrimental to the maintenance, for instance, of healthy arterial blood pressure.

Increasing experimental evidence shows that astrocytes closely associated with sympathoexcitatory or respiratory neural networks can directly influence synaptic neurotransmission and neuronal activity, and are strongly involved in the modulation of the sympathetic nervous system (Gourine et al., 2010; Marina et al., 2015, 2016; Tang et al., 2014). Astrocyte-derived LL has been shown to activate a putative Gs-coupled LL receptor (LLRx) in noradrenergic neurones in the LC, inducing depolarisation and NA release (See Chapter 1, section 1.4.4) (Mosienko et al., 2018; Tang et al., 2014). Moreover, excitability of C1 neurones has also been shown to be modulated by ventral brainstem astrocytes via the release of LL, which triggered depolarization and increased action potential firing rate (Marina et al., 2015). Although the nature of the proposed LL receptor, LLRx, has yet to be identified, Tang et al. (2014) have reported that DL blocks the activation of this receptor and the effect of LL on noradrenergic neurones (Tang et al., 2014). Application of DL to brainstem slices almost fully abolished NA release and neuronal depolarization induced by astrocyte-derived LL in the LC (Tang et al., 2014). This inhibitory response led us to propose that increasing the DL/LL ratio in astrocytes may represent an effective tool to interfere with LL-mediated signalling, and potentially attenuate excessive sympathoexcitation. Therefore, in order to better understand LL-mediated signalling in the brainstem and in order to attempt to counteract sympathoexcitation induced by

astrocyte-derived LL, we designed and constructed a molecular tool to selectively induce astrocytes to produce and release DL.

This chapter will explore DL production and handling in mammals and bacteria, as well as the design, construction and *in vitro* validation of a novel molecular tool based on bacterial enzyme to produce DL specifically in astrocytes.

5.1.1 D-lactate source in mammalian cells

DL is the laevorotary compound of the chiral molecule lactate. Under physiological conditions in mammals, DL is formed by the methylglyoxal pathway in the nanomolar range (Ewaschuk, Naylor, & Zello, 2005). The glyoxalase system consists of a 2-step reaction catalysed by the ubiquitously expressed enzymes glyoxalase I and II, which convert methylglyoxal into DL via the intermediate S-lactoylglutathione (Figure 5.1). Methylglyoxal is an inevitable by-product of fatty acid, amino acid, and glucose metabolism and must be removed from the cells due to its highly reactive and cytotoxic nature (Ewaschuk et al., 2005). In the mouse brain, glyoxalase enzymes have been shown to be expressed at higher levels in primary astrocytes, which also exhibited higher DL levels as compared to neurones (Belanger et al., 2011).

In addition to the glyoxalase system, another proposed mechanism of DL production in mammalian tissues is a putative mammalian DL dehydrogenase (EC 1.1.2.4), which catalyses the reversible conversion of pyruvate to DL using ferricytochrome c as co-substrate and FAD as coenzyme (de Bari, Atlante, Guaragnella, Principato, & Passarella, 2002; Flick & Konieczny, 2002) (Figure 5.1). Analysis of the expression of the putative mammalian DL dehydrogenase indicated its presence mainly in the kidney and liver, and at lower rates in the brain, heart, and skeletal muscle. At the cellular level, mammalian DLDH is localized in the inner face of the inner mitochondrial membrane (de Bari, Moro, & Passarella, 2013; Flick & Konieczny, 2002).

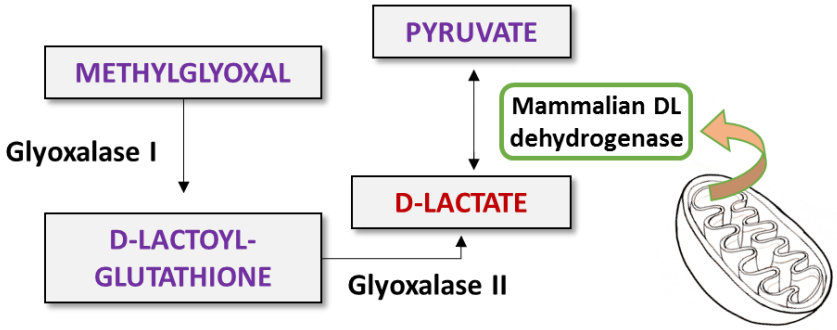

Figure 5.1. Pathways for DL production in mammals. DL can be endogenously formed in mammals through the glyoxalase system, which detoxify cells of methylglyoxal by its conversion into DL, as well as through the activity of a putative mammalian DL dehydrogenase, which converts pyruvate into DL in the inner face of the inner mitochondrial membrane.

DL concentration in mammals is kept at low levels in healthy subjects unless a disease state has been established. Subclinical elevation of DL concentration can be detected in diabetic rats, whose blood have doubled the amount of DL compared with healthy subjects (Kondoh, Kawase, Kawakami, & Ohmori, 1992). In this case, DL has been suggested to be produced from methylglyoxal, which in turn has been generated by the ketone metabolism (Christopher, Broussard, Fallin, Drost, & Peterson, 1995).

Unfortunately, the processes used by mammals to produce DL endogenously cannot be employed as strategies for the development of molecular tools to induce astrocytic DL production. Increasing activity of the glyoxalase system may be a delicate approach since it involves the formation of methylglyoxal, a highly reactive and toxic compound. It may also be complex to design a strategy to effectively overexpress the putative mammalian DL dehydrogenase in astrocytes due to the lack of research describing its activity and function. Moreover, the human DL dehydrogenase is a transmembrane enzyme which reaction requires mitochondrial elements to take place. Therefore, besides the challenge of delivering the enzyme expression to the position it is initially found in the cells – at the inner face of the inner mitochondrial membrane – the enzymatic reaction may be limited, resulting in low DL production (de Bari et al., 2013).

5.1.1.1 D-lactate transport

DL produced outside the CNS can reach the cerebral tissue from the bloodstream. The transport of DL is mediated by the gradient-driven MCT1 and MCT4, although with relatively lower binding affinities when compared with other monocarboxylates (Halestrap, 2011). MCT1 is present in endothelial cells of the blood brain barrier as well as in astrocytes and neurones and translocate DL with a Km of 27.5 mmol/L (Halestrap, 2011). MCT4 in astrocytes has been shown to carry DL with a Km of 519 mmol/L (see Table 1.2) (Halestrap, 2011).

5.1.2 D-lactate source in bacteria

DL plays an important role in energy metabolism in bacteria. Through fermentation, a wide and heterogenous group of bacteria, the lactic acid bacteria, can efficiently convert glucose into LL and/or DL. Lactobacilli are widely employed in food, pharmaceutical and chemical industries. Bacterial production of LL and DL is catalysed by LDH and D-lactate dehydrogenase (DLDH; EC 1.1.1.28 – Figure 5.2), respectively, which are both stereospecific NAD-dependent enzymes.

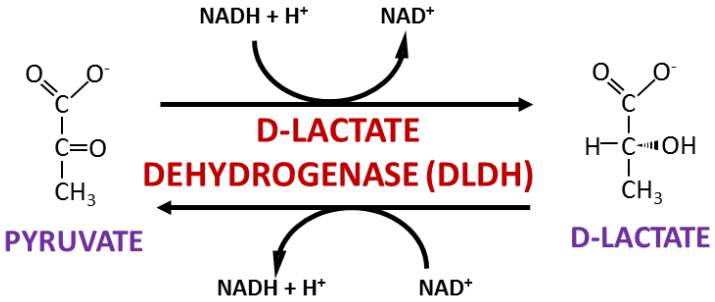

Figure 5.2. Reaction catalysed by DLDH. DLDH utilizes the coenzyme NADH to reversibly reduce pyruvate to DL.

The ratio of LL and DL production varies according to the bacteria specie and strain (Huang, You, & Liu, 2017). In *Lactobacillus delbrueckii* subspecies *bulgaricus (L. bulgaricus)*, for example, DL is the most produced stereoisomer, accounting for over 85% of the total lactic acid generated by lactose fermentation (Manome, Okada, Uchimura, & Komagata, 1998). *L. bulgaricus* is worldwide used for yogurt production. When evaluated at amino acid level, the DLDH gene from *L. bulgaricus* was found to

be positively selected, most likely due a persisting domestication process (Zhang, Gong, Wang, Zhang, & Tian, 2015).

Lactic acid bacteria are part of the human gastrointestinal microbiota. A rare metabolic condition, the short-bowel syndrome (SBS), has been associated with D-lactic acidosis in humans, in which serum DL rises ≥ 3 mmol/L (Uribarri, Oh, & Carroll, 1998). In subjects whose intestines are shorter, carbohydrate digestion is incomplete and non-metabolized sugars can reach the colon. As a consequence, pH at the colonic lumen decreases due to the elevated microbial production of organic acids. Acid environment favours overgrowth of lactic acid bacteria, which culminates in the increased production of LL and DL. While LL can be efficiently metabolized, the metabolism and excretion capacity of DL by humans are limited, leading to the accumulation of this compound in the blood (Ewaschuk et al., 2005). Clinical manifestations of D-lactic acidosis include neurological dysfunction such as irritability, hallucinations, abusive behaviours, among others (Uribarri et al., 1998). Other conditions in humans such as infection, ischemia, traumatic shock, and diarrhoea evoke bacteria-mediated increase in blood DL levels, but at concentrations that do not result in D-lactate acidosis (<1mmol/L) (Ewaschuk et al., 2005).

Even though some bacteria do not express DLDH, DL can still be produced due to the activity of DL-lactate racemase, which converts LL into its enantiomer DL (Figure 5.3) (Ferain et al., 1996; Ferain, Garmyn, Bernard, Hols, & Delcour, 1994). Characterization of lactate racemization activity showed that transformation of LL into DL is controlled by the LL/DL ratio in the sense that the presence of LL induces racemisation, while DL has the opposite effect (Goffin et al., 2005). DL-racemase is a nickel-dependent enzyme whose activity depends on the expression of 4 and 6 genes organized in two separate operons (Desguin et al., 2014).

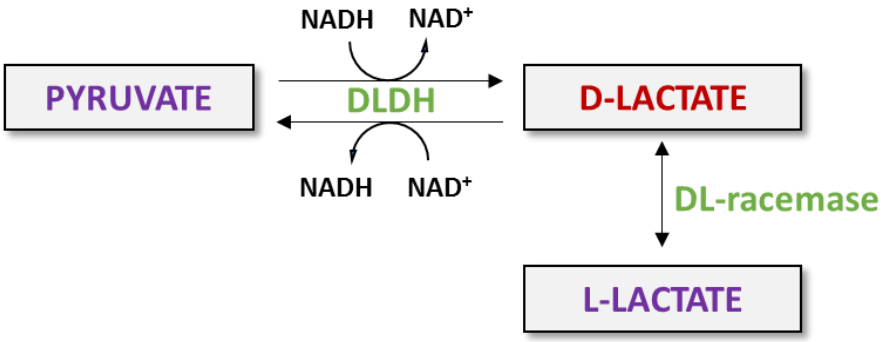

Figure 5.3. Pathways for DL production in bacteria. DL is produced by bacteria though the activity of the enzymes DLDH and DL-racemase, the latter catalysing the direct transformation of LL to DL.

Although expression of DL-racemase seems an attractive approach for producing DL while decreasing LL levels, expression of this enzyme would have been too complex and its activity requires nickel as cofactor, which rendered this strategy unrealistic. On the other hand, activity of bacterial DLDH, which has been extensively described due to its broad industrial utilization, seems feasible once expressed in astrocytes. These cells naturally provide the precursor pyruvate through glycolysis and are equipped with the transport machinery necessary for DL extrusion. Therefore, we chose to express DLDH from *L. bulgaricus* in astrocytes, based on its high efficiency in converting pyruvate into DL.

5.2 Construction of DLDH-carrying plasmids

Since DLDH activity has been well described in *L. bulgaricus*, we used its ORF sequence for the design of molecular cloning strategies. The sequence was optimised to the mammalian codon usage by Life Technologies (USA) using the amino acid sequence provided by us. Several recombinant plasmids containing the mammalianised DNA sequence of DLDH were constructed in this project in order to accommodate the different experimental approaches employed. Accordingly, plasmids were cloned into either adenoviral (pXCX) or lentiviral (pTYF) shuttle plasmids under the control of either ubiquitous (EF1α) or astrocyte-specific (sGFAP) promoters. Recombinant plasmids also differed in the fluorescent protein they carried – EGFP or tdTomato – in order to avoid any interference with imaging recordings

performed. An IRES element was included in the bi-cistronic vector for independent translation of DLDH and the reporter gene.

Following construction, DLDH-carrying recombinant plasmids were used for transfection of HEK293 cells or directed to the production of viral vectors to be further employed for transduction of primary cultured astrocytes and organotypic brainstem slices.

5.2.1 pTYF-EF1α-DLDH-IRES-EGFP

The mammalianised ORF sequence of DLDH was isolated from the original pMA-T vector backbone and cloned into a pTYF shuttle vector driving the expression of EGFP under the control of the ubiquitous EF1α promoter. IRES was added between DLDH and EGFP to allow these two genes to be separately translated, forming pTYF-EF1α-DLDH-IRES-EGFP. For molecular construction of the recombinant plasmid, pTYF-EF1α-SOD1-IRES-EGFP and pMA-T-DLDH were double-digested with the restriction enzymes *NheI* & *SalI*. The SOD1 sequence was excised from the vector cassette, resulting in a 9.8kb vector fragment that was subsequently ligated together with the 1kb insert fragment of DLDH (Figure 5.4A). Diagnostic digestions were carried out on pTYF-EF1α-DLDH-IRES-EGFP using *NheI* & *SalI*, which confirmed an accurate outcome (Figure 5.4B). The construct was also partially sequenced by Eurofins MWG with specific primers for the pTYF backbone (pTYF forward: GGGTTTATTACAGGGACAGCAG, and pTYF reverse: AGTGGCTAAGATCTACAGCTGCCTTG), EF1-α forward (ATTATGGAGGACGCGGCGCT), and reverse GFP (CCGTTTACGTCGCCGTC). The DNA sequence output was aligned *in silico* using Vector NTI, which confirmed the correct sequence.

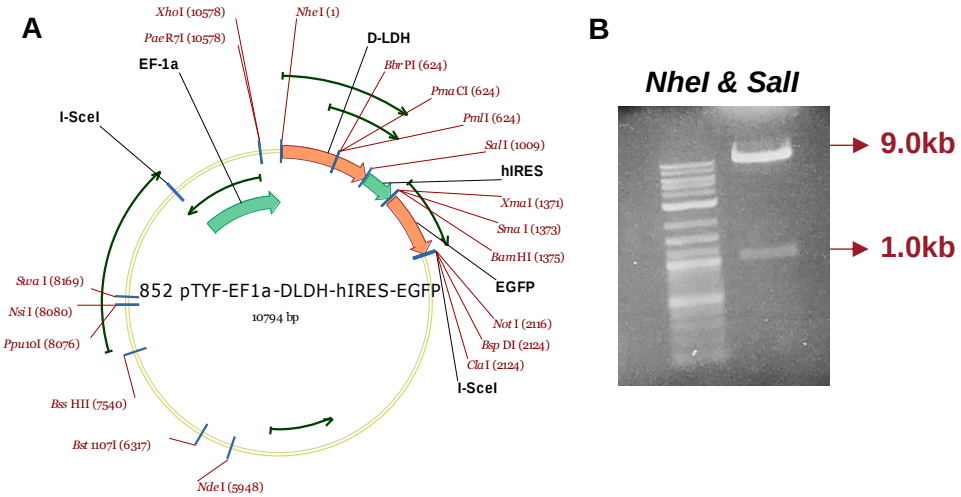

Figure 5.4. Construction of pTYF-EF1α-DLDH-IRES-EGFP. (A) Vector map of the recombinant plasmid carrying DLDH and EGFP under the control of an EF1α promoter. **(B)** Gel electrophoresis image of the diagnostic restriction digestion with *NheI & SalI* and the resulting bands, which confirmed the successful cloning procedure.

5.2.2 pTYF-EF1a-DLDH-IRES-tdTomato

Another variant of DLDH-carrying recombinant plasmid driving the co-expression of tdTomato was created in order to allow FRET imaging with cyan and yellow fluorescent proteins in DLDH-expressing cells. For this cloning strategy, both pTYF-EF1α-DLDH-IRES-EGFP and pXCX-PRS-tdTomato were double-digested with the restriction enzymes *BamHI & NotI*. The resultant fragments of 10kb of the vector pTYF-EF1α-DLDH-IRES and 1.5kb of the insert tdTomato were ligated together, creating pTYF-EF1a-DLDH-IRES-tdTomato (Figure 5.5A). The pattern of DNA fragments from diagnostic digestion of the recombinant plasmid using the restriction enzymes *BamHI & NotI* matched the expected bands (Figure 5.5B). Sequencing of pTYF-EF1a-DLDH-IRES-tdTomato with EF1-α and pTYF primers (ATTATGGAGGACGCGGCGCT and AGTGGCTAAGATCTACAGCTGCCTTG, respectively) by Eurofins MWG also confirmed the correct outcome.

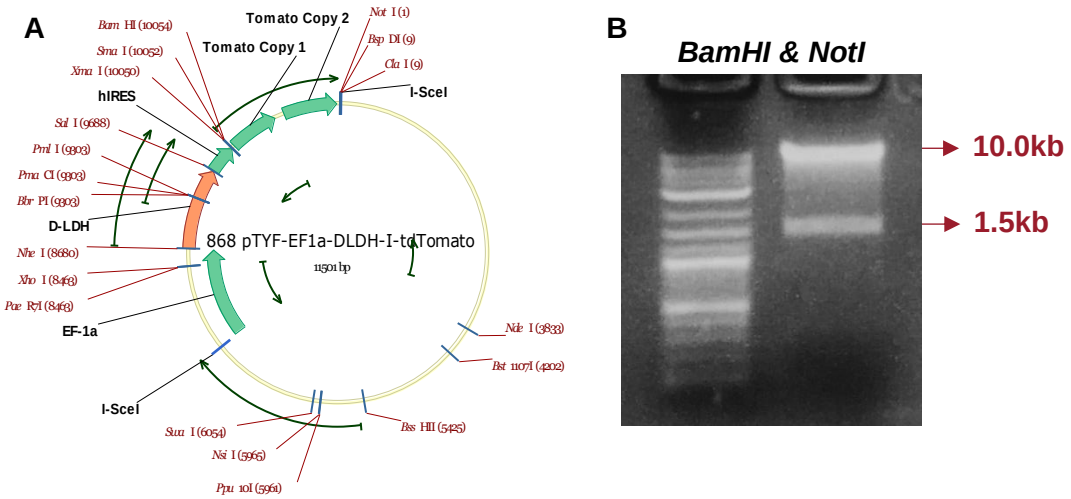

Figure 5.5. Construction of pTYF-EF1α-DLDH-IRES-tdTomato. (A) Vector map of the recombinant plasmid carrying DLDH and tdTomato under the control of an EF1α promoter. **(B)** Gel electrophoresis image of the diagnostic restriction digestion with *BamHI* & *NotI* and the resulting bands, which confirmed the correct outcome.

5.2.3 pXCX-sGFAP-DLDH-IRES-EGFP

To create a recombinant cassette to drive the expression of DLDH specifically in astrocytes, the DLDH ORF sequence was cloned into a pXCX-shuttle backbone under the control of sGFAP promoter. In order to construct pXCX-sGFAP-DLDH-IRES-EGFP, pXCX-sGFAP-tdTomato was digested with the restriction enzyme *AgeI*, while pTYF-EF1a-DLDH-IRES-EGFP was digested with *NheI*. Both plasmids were then submitted to a Klenow treatment in order to generate blunt DNA ends. A second restriction digestion with the enzyme *NotI* was performed, which resulted in a 10.4kb vector fragment and a 2.1kb insert fragment containing the coding sequences of DLDH, IRES and EGFP. Vector backbone and insert were ligated together, forming the recombinant plasmid pXCX-sGFAP-DLDH-IRES-EGFP (Figure 5.6A). Diagnostic restriction digestion was carried out using *SalI*, which yielded the expected bands (Figure 5.6B). The new construct was sequenced by Eurofins MWG with a reverse pXCX primer (ACCTTCCAGGGTCAAGGAAG) and a primer for GFAP (ATGGGTGAGGGGAGAGCT). Following *in silico* alignment of the DNA sequence, the new shuttle vector was considered to be correct.

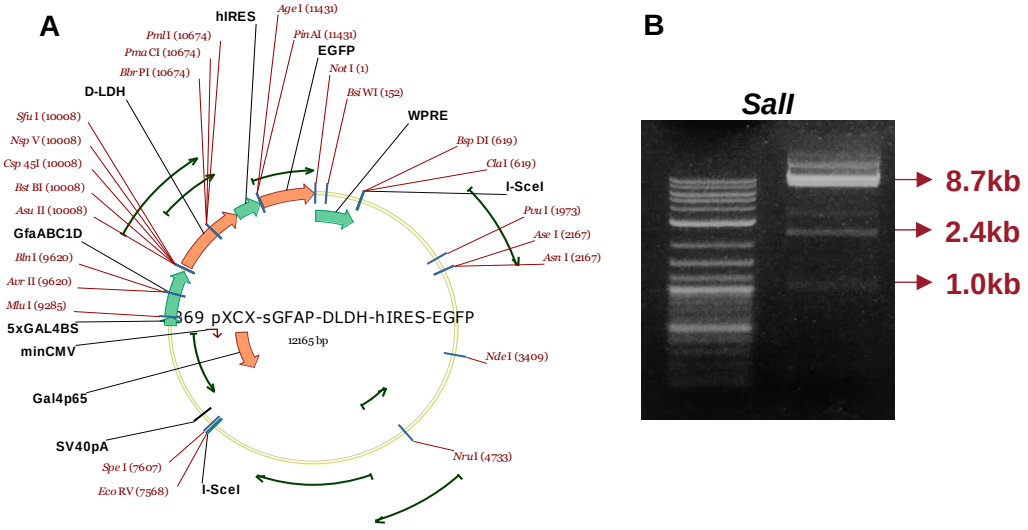

Figure 5.6. Construction of pXCX-sGFAP-DLDH-IRES-EGFP. (A) Vector map of the recombinant plasmid carrying DLDH and EGFP under the control of sGFAP promoter. **(B)** Gel electrophoresis image of the diagnostic restriction digestion with *SalI* yielded the correct pattern of bands.

5.2.4 pXCX-sGFAP-DLDH-IRES-tdTomato

This cloning strategy created a red fluorescent variant of the novel recombinant plasmid driving the expression of DLDH in astrocytes. For the construction of pXCX-sGFAP-DLDH-IRES-tdTomato, EGFP sequence from pXCX-sGFAP-DLDH-IRES-EGFP was swapped for the tdTomato isolated from pXCX-PRS-tdTomato by restriction digestion using the enzymes *AgeI* & *NotI*. 11.4kb and 1.4kb of vector and insert fragment, respectively, were ligated together, resulting in the recombinant plasmid pXCX-sGFAP-DLDH-IRES-tdTomato (Figure 5.7A). For diagnostic purpose, pXCX-sGFAP-DLDH-IRES-tdTomato was digested with the restriction enzymes *AgeI* & *NotI* and the bands in the electrophoresis agarose gel were found to be as expected (Figure 5.7B) The recombinant plasmid was then partially sequenced by MWG Eurofins using specific primers to IRES (IRES forward: CCACTCATCTTATAGCTTTC, and IRES reverse: CCAAGTCAGTGGCTGCAC) and a reverse pXCX primer (ACCTTCCAGGGTCAAGGAAG). Following *in silico* alignment of the DNA, the sequence was confirmed as correct.

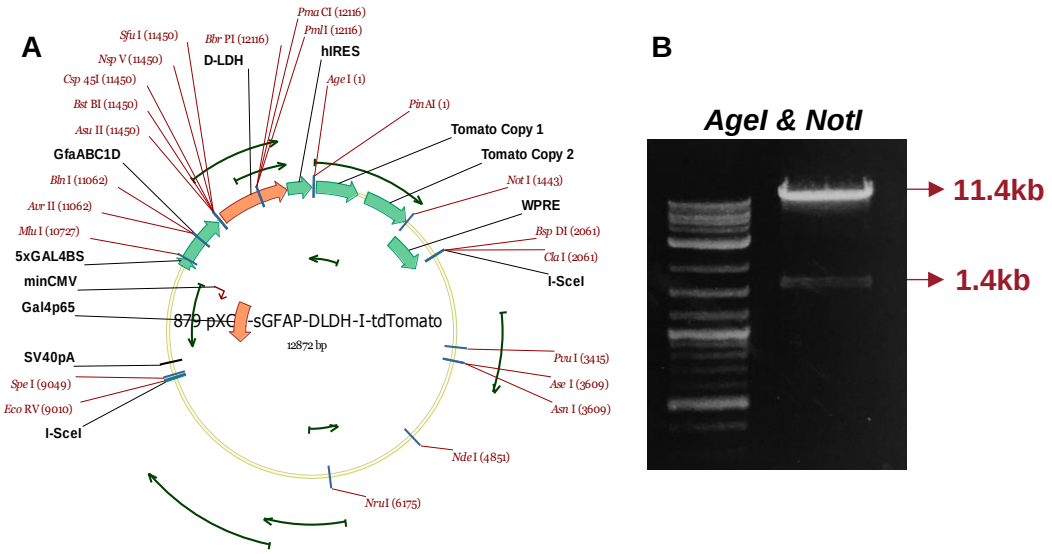

Figure 5.7. Construction of pXCX-sGFAP-DLDH-IRES-tdTomato. (A) Vector map of the recombinant AVV shuttle plasmid carrying DLDH and tdTomato under the control of sGFAP promoter. **(B)** Gel electrophoresis image of the diagnostic restriction digestion with *AgeI* & *NotI* and the resulting bands, which confirmed the correct outcome.

5.3 Functional validation of DLDH expression *in vitro*

DLDH-carrying recombinant plasmids containing the EF1α promoter were used for transfection of HEK293 cells. On the other hand, pXCX-sGFAP-DLDH-IRES-EGFP and pXCX-sGFAP-DLDH-IRES-tdTomato were used for generation of AVVs for astrocyte-specific expression of DLDH in rat primary dissociated astrocytic cultures and organotypic brain slices. Expression and activity of DLDH in mammalian cells was determined *in vitro* with a range of specific functional assays. Once DL production in DLDH-expressing cells had been confirmed, its effects on intracellular LL pool as well as LL signalling were analysed.

5.3.1 DLDH of bacterial origin is expressed in mammalian cells

The ability of the novel DLDH-containing expression cassette to be transcribed in HEK293 cells was initially assessed by monitoring the expression of the reporter gene. Evaluation of EGFP fluorescence in HEK293 cells following transfection with 1.5μg/μl of pTYF-EF1α-DLDH-IRES-EGFP suggested that this construct was, in

principle, expressed in mammalian cells (Figure 5.8), although it does not as such confirm that the microbial enzyme is in fact active.

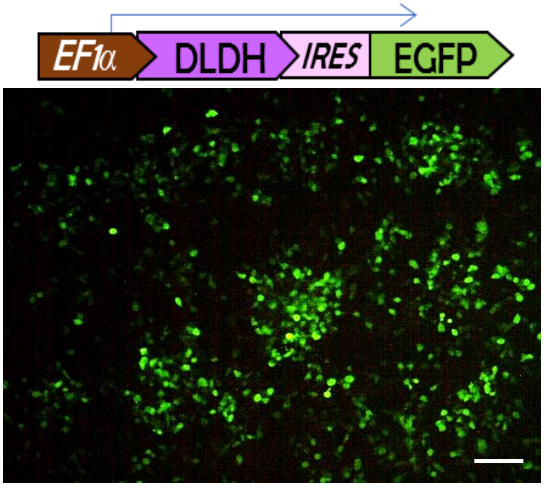

Figure 5.8. DLDH-transfected HEK293 cells express the reporter gene EGFP. Domain structure of the cassette for expression of DLDH in cell lines. The bi-cistronic vector carries the expression of DLDH and EGFP under the control of EF1α promoter. Below: Fluorescence microscopy image of HEK293 cells transfected with 1.5µg/µl of the construct. Scale bar is 100µm.

Transduction of cultured primary astrocytes as well as astrocytes in organotypic brainstem slices with AVV-sGFAP-DLDH-IRES-tdTomato resulted in tdTomato expression being detected only in some scattered astrocytes. In order to amplify the signal of the reporter gene, anti-RFP staining was carried out, which confirmed wide-spread astrocytic expression of the red fluorescent protein in both primary culture and organotypic brain slices (Figure 5.9).

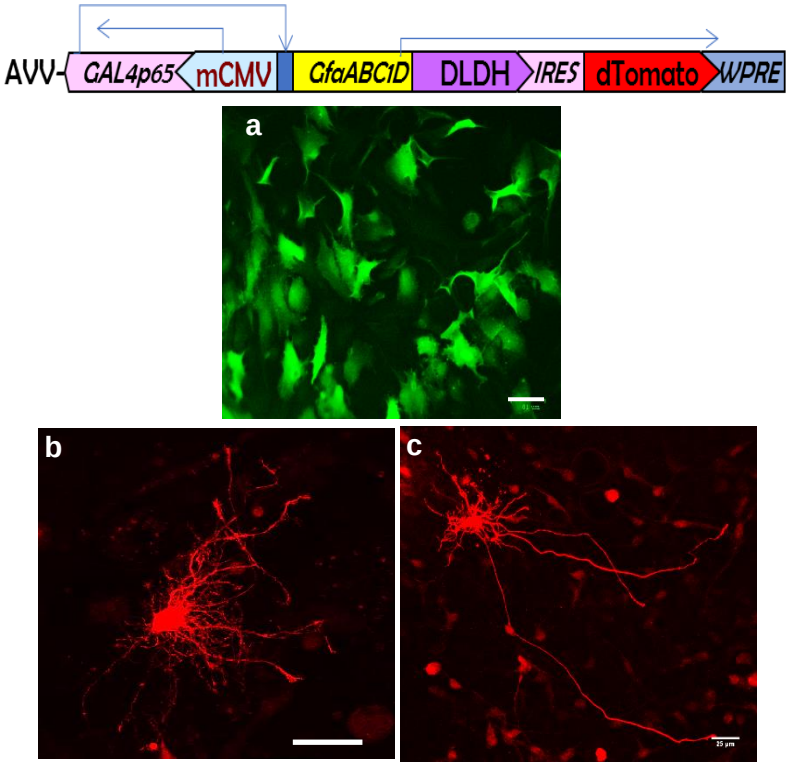

Figure 5.9. DLDH-transduced astrocytes express the reporter gene tdTomato. Domain structure of the cassette for expression of DLDH through AVV. Below: Confocal image stacks showing **(a)** dissociated astrocytes, scale bar 60µm; and **(b and c)** astrocytes in organotypic slice culture expressing the construct, scale bars 25µm. Signal of the reporter gene has been amplified by anti-RFP staining with Alexa 488 (green) for dissociated astrocytes and Alexa 594 (red) for astrocytes in organotypic slice culture.

5.3.2 Astrocytic DLDH expression has no detrimental impact on cell viability

Any potential toxicity that expression of the foreign enzyme and its enzymatic product can cause to astrocytes was assessed with cell viability assays. Establishment of a safe range of MOI of AVV used for astrocytic DLDH transduction was essential so that all the validation experiments could be performed within a physiological context.

Cell death 3 days following transduction of primary cultured astrocytes with different MOIs of AVV-sGFAP-DLDH-IRES-tdTomato was assessed with Trypan Blue exclusion assay. As described in the previous chapter, AVV-sGFAP-EGFP was used as a control since it drives the expression of a well-established inert protein. Results from Trypan Blue assay showed that the percentage of viable astrocytes transduced

with AVV-sGFAP-DLDH-IRES-tdTomato was not significantly different from control astrocytes at MOIs 15 and 50 (Figure 5.10).

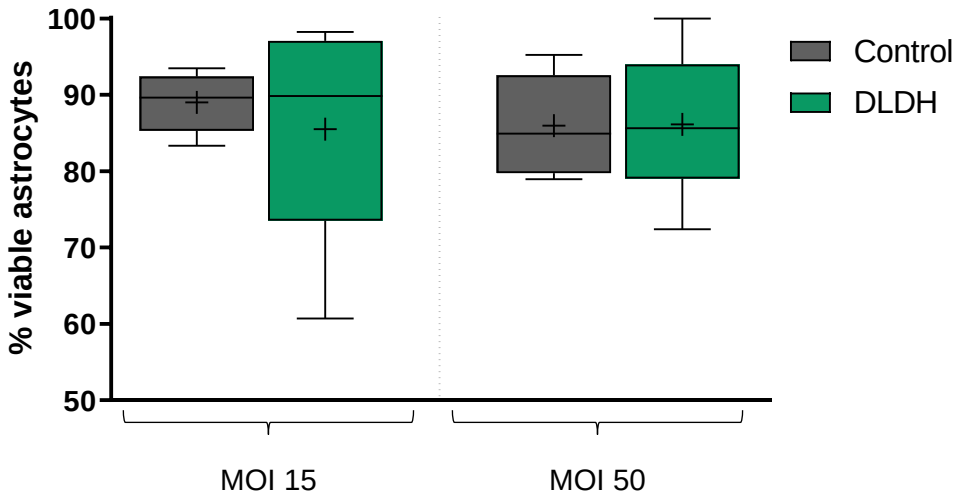

Figure 5.10. DLDH expression does not affect the viability of primary cultured astrocytes as measured with Trypan Blue exclusion assay. Comparison of the % of viable astrocytes transduced with AVV-sGFAP-EGFP (Control) and AVV-sGFAP-DLDH-IRES-tdTomato (DLDH) showed no significant difference at MOI 15 (Control: 89.0±3.9%, n=5; *vs.* DLDH: 85.5±14.5%, n=6) and MOI 50 (Control: 86.0±6.6%, n=6; *vs.* DLDH: 86.1±9.8%, n=6). ns – $p>0.05$, Student's unpaired t-test.

In addition, we performed a more sensitive assessment of cell damage using the XTT assay. Similar to Trypan Blue, the XTT assay also measures cell death. However, as it relies on the activity of endogenous enzymes that are inactivated soon after cell death, this assay is able to detect earlier changes in cell viability. Comparison between primary cultured astrocytes transduced with AVV-sGFAP-EGFP and astrocytes transduced with AVV-sGFAP-DLDH-IRES-tdTomato revealed no significant change in cell viability at all MOIs tested (Figure 5.11).

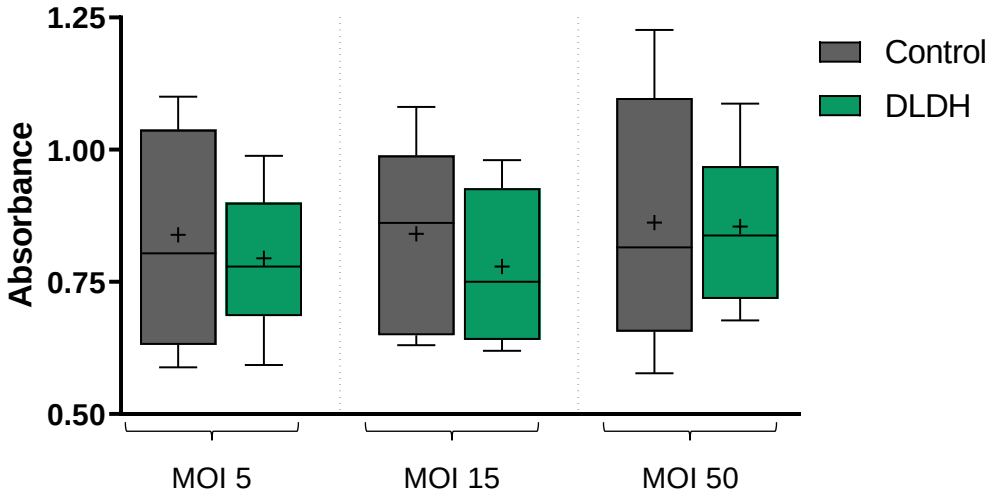

Figure 5.11. DLDH expression does not affect the viability of primary cultured astrocytes as measured with XTT assay. Absorbance readout is proportional to cell viability. Comparison of the viability of astrocytes transduced with AVV-sGFAP-EGFP (Control) and AVV-sGFAP-DLDH-IRES-tdTomato (DLDH) showed no significant difference at MOI 5 (Control: 0.84±0.20, n=9; *vs.* DLDH: 0.79±0.13, n=9), MOI 15 (Control: 0.84±0.17, n=9; *vs.* DLDH: 0.78±0.14, n=9), and MOI 50 (Control: 0.86±0.23, n=9; *vs.* DLDH: 0.85±0.14, n=9). ns – p>0.05, Student's unpaired t-test.

5.3.3 Mammalian cells expressing DLDH constitutively release D-lactate

Whether transduction of DLDH constructs in mammalian cells translates into functional production of DL was determined through a fluorometric DL assay, as detailed in Chapter 3, section 3.7. DL levels in culture media conditioned for 2 hours by HEK293 cells transfected with 0.5 µg/µl of pTYF-EF1α-DLDH-IRES-EGFP showed a 6.5-fold increase in DL concentration, whereas transfection with 1.5 µg/µl of the same recombinant plasmid resulted in a 25.8-fold rise in the constitutive DL release as compared to non-transfected HEK293 cells (Figure 5.12).

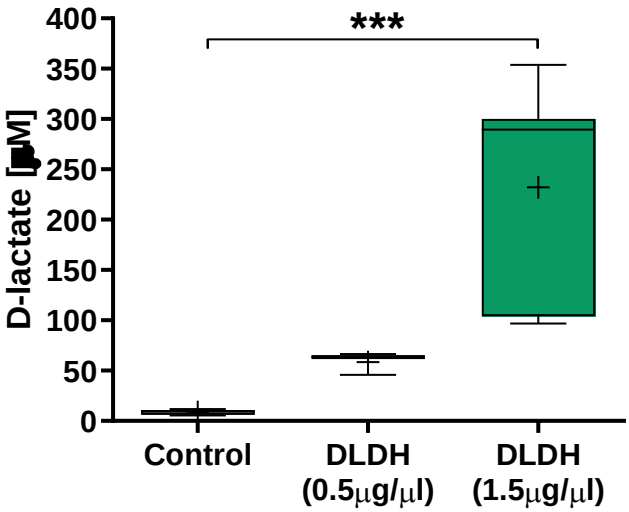

Figure 5.12. DLDH expression increases constitutive release of DL from HEK293 cells. DL concentration in media from HEK293 cells transfected with pTYF-EF1α-DLDH-IRES-EGFP is increased (0.5µg/µl: 58.6±11.1µM, n=3; 1.5µg/µl: 232.2±101.6µM, n=9, respectively) as compared to non-transfected HEK293 cells (Control, 9.0±2.4µM, n=9). ANOVA (Bonferroni's Multiple Comparison Test) was used to compare against control the effects of **1)** DLDH (0.5µg/µl): ns - $p>0.05$; and **2)** DLDH (1.5µg/µl): *** - $p<0.0001$.

The concentration of DL was also quantified in culture media exposed for 6 hours to primary cultured astrocytes transduced with AVV-sGFAP-DLDH-IRES-tdTomato. Compared to non-transduced astrocytes, DLDH-expressing cells exhibited a significant 2.6-fold increase in DL constitutively released to the extracellular space (Figure 5.13). Combined, these results imply that DLDH is enzymatically operational in mammalian cells, which can actively release DL.

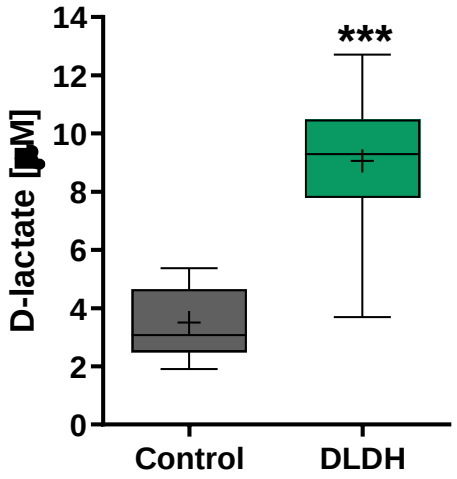

Figure 5.13. Primary cultured astrocytes expressing DLDH increase constitutive release of DL. DL levels in media conditioned for 6 hours by primary cultured astrocytes transduced with AVV-sGFAP-DLDH-IRES-tdTomato (DLDH) is increased (DLDH, 9.1±2.2μM, n=13) as compared to non-transduced astrocytes (Control, 3.5±1.2μM, n=11). *** - p<0.0001, Student's unpaired t-test.

5.3.4 DLDH expression decreases constitutive release of L-lactate from HEK293 cells but not from astrocytes

Although the strategy of targeting DLDH expression in astrocytes was initially designed to interfere with LL signalling through DL production rather than by altering LL levels, DLDH activity consumes pyruvate and NADH, which are also required for LDH reaction. Therefore, to test any potential interference of DLDH expression with LL generation, we measured constitutive release of LL with a quantitative fluorometric assay (Chapter 3, section 3.7).

In HEK293 cells transfected with 1μg/μl of pTYF-EF1α-DLDH-IRES-EGFP, the concentration of LL in culture media following 2 hours of incubation was slightly but significantly reduced as compared to HEK293 cells transfected with the control vector pCMV-IRES-EGFP (Figure 5.14A). On the other hand, astrocytes transduced with AVV-sGFAP-DLDH-IRES-tdTomato show no difference on the amount of LL released to the culture media following 6 hours incubation as compared to astrocytes expressing the control AVV-sGFAP-EGFP (Figure 5.14B).

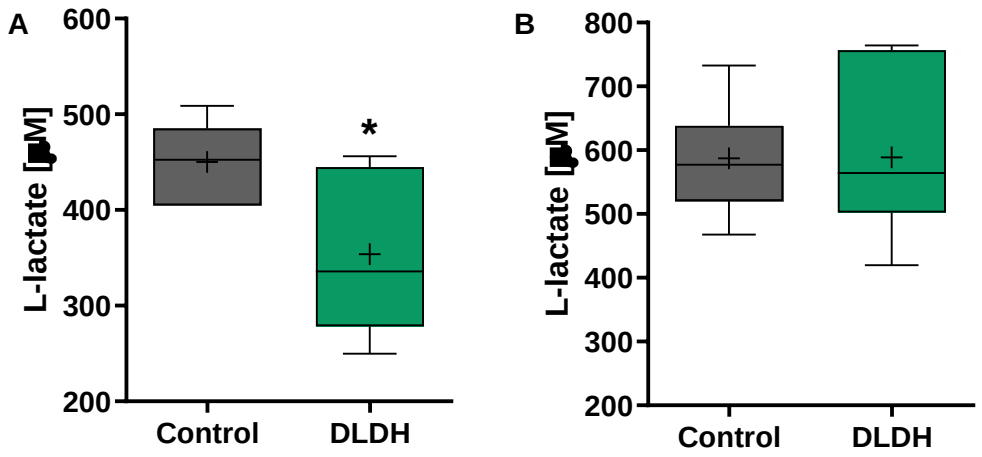

Figure 5.14. Constitutive release of LL is reduced in DLDH-expressing HEK293 cells and unchanged in astrocytes expressing DLDH. (A) Media from HEK293 cells transfected with 1µg/µl of pTYF-EF1α-DLDH-IRES-EGFP exhibited lower LL concentration (DLDH, 353.8±79.7µM, n=9) than media from HEK293 cells transfected with 1µg/µl of pCMV-IRES-EGFP (Control, 450.1±41.5µM, n=6). **(B)** LL level is not significantly different in media from primary cultured astrocytes transduced with AVV-sGFAP-EGFP (Control, 587.4±84.1µM, n=17) and AVV-sGFAP-DLDH-IRES-tdTomato (DLDH, 588.6±118.6µM, n=11). * - $p<0.05$, Student's unpaired t-test.

5.3.5 Expression of DLDH reduces forced L-lactate release from primary cultured astrocytes

To estimate the levels of LL released from DLDH-expressing primary cultured astrocytes upon an acute stimulation, we applied high doses of pyruvate (10mM) while cytosolic LL levels were monitored with the FRET sensor Laconic 2-3 days following astrocytic transduction with AVV-CMV-Laconic and AVV-sGFAP-DLDH-IRES-tdTomato. Pyruvate-driven trans-acceleration of MCTs leads to the extrusion of intracellular LL as discussed in previous chapters.

In DLDH-expressing primary cultured astrocytes, pyruvate [10mM] caused a reduced decrease in cytosolic LL levels as compared to the amount of trans-acceleration-driven LL released from control astrocytes (Figure 5.15).

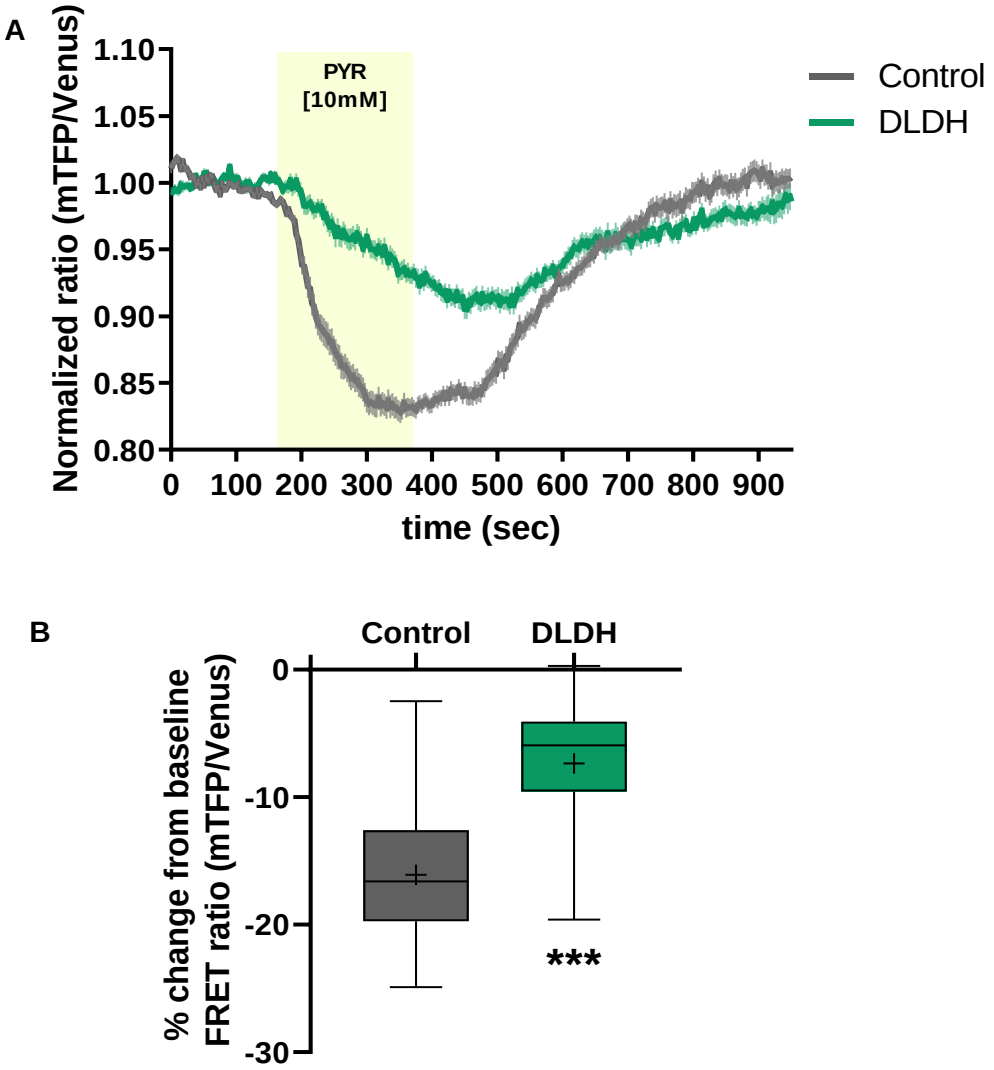

Figure 5.15. Forced LL release is decreased in astrocytes expressing DLDH enzyme. (A) Estimation of relative cytosolic LL levels using Laconic and a trans-acceleration protocol showed reduced intracellular LL in DLDH-expressing astrocytes as compared to the substantial drop in LL concentration in control cells following application of pyruvate [10mM]. Trace represents average Laconic FRET ratio of astrocytes expressing AVV-CMV-Laconic alone (Control, n=62) or in combination with AVV-sGFAP-DLDH-IRES-tdTomato (DLDH, n=56). Data pooled from 7 independent experiments. Shaded regions around the trace represents SEM. **(B)** Pooled data for the average Laconic FRET ratio from 300 to 500 seconds to the extrusion of LL with pyruvate [10mM] as compared with the baseline (Control: -16.1±5.1%; DLDH: -7.4±4.6%). *** - p<0.0001, Student's unpaired t-test.

3.5.6 Astrocytic expression of DLDH does not affect L-lactate dynamics in organotypic brainstem slices

Amperometric measurements with LL electrodes were performed in organotypic brainstem slices in order to investigate if alterations detected in DLDH-transduced primary cultured astrocytes translate into changes in LL dynamics in a more complex and intact brain tissue preparation. Since the signalling role of astrocyte-derived LL in noradrenergic neurones and the antagonistic effect of DL in these cells have been previously shown in the LC (Tang et al., 2014), brainstem slices were cut at the LC level and transduced with AVV-PRSx8-EGFP to guide the insertion of LL electrodes precisely into this noradrenergic region. Organotypic slices were also transduced with AVV-sGFAP-DLDH-IRES-tdTomato to target DLDH expression specifically to astrocytes.

Contact of the LL electrode with the surface of the organotypic brainstem slice generated a constant and steady current, which corresponds to the tonic LL efflux from the tissue. Comparison of LL tone of slices containing astrocytes expressing DLDH with slices whose astrocytes have not undergone transduction suggested that DLDH expression does not significantly modify the extracellular LL tone (Figure 5.16).

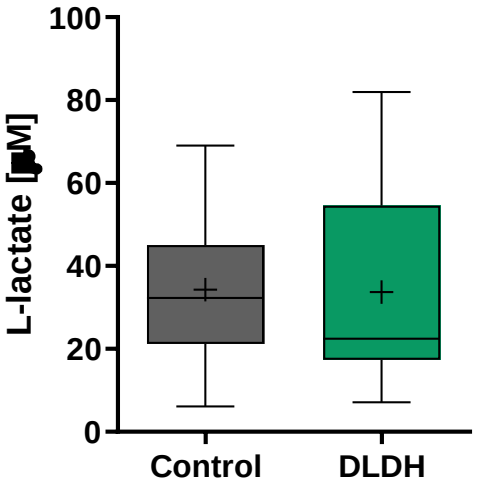

Figure 5.16. Expression of DLDH in astrocytes does not interfere with LL tone of organotypic brainstem slices. Pooled data for the extracellular LL tone of organotypic brainstem slices transduced with AVV-PRSx8-EGFP alone (Control, n=14) or in combination with AVV-sGFAP-DHDH-IRES-tdTomato (DLDH, n=13)

showed no significant effect of astrocytic DLDH expression on LL (Control: 34.3±18.1µM; DLDH: 33.7±23.6µM) as measured with LL amperometry. ns – p>0.05, Student's unpaired t-test.

Real-time analysis of extracellular LL concentration with amperometric LL biosensors was also employed to quantify the amount of LL released from organotypic brainstem slices following application of pyruvate. Due to the trans-acceleration of MCTs, extracellular levels of LL increased rapidly after superfusion of the slice culture with 10mM of pyruvate. The amplitude of trans-acceleration-driven LL release was not significantly different in organotypic brainstem slices containing astrocytes transduced with DLDH as compared with control slices (Figure 5.17A). Accordingly, the amplitude of LL depletion that takes place in the slice following the trans-acceleration protocol was similar in both control and DLDH slices (Figure 5.17B).

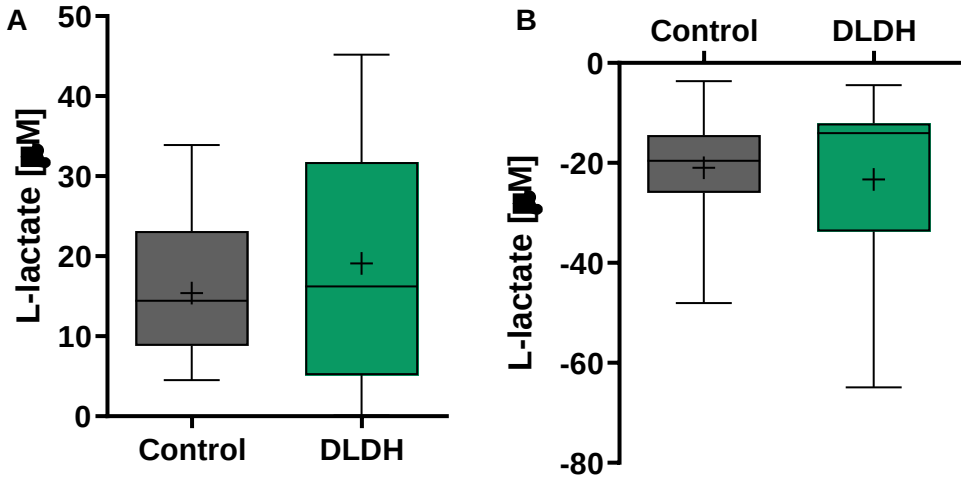

Figure 5.17. DLDH expression in astrocytes does not affect pyruvate-driven LL release from organotypic brainstem slices. A) Pooled data for the amplitude of trans-acceleration-driven LL released from organotypic brainstem slices showed no significant difference between control (15.4±8.5µM, n=11) and DLDH (19.1±15.7µM, n=12). **(B)** Pooled data for the amplitude of LL depletion following cessation of pyruvate application showed absence of significant changes in DLDH slices (-23.3±18.6µM, n=12) as compared to control (-21.0±11.4µM, n=11). ns – p>0.05, Student's unpaired t-test.

5.3.7 DLDH expression decreases the rate of pyruvate accumulation in primary cultured astrocytes

Since DLDH enzymatic activity culminates in the reduction of pyruvate to DL, intracellular pyruvate levels are likely to be affected. To gain insight into intracellular pyruvate handling in cultured astrocytes expressing DLDH, we employed the FRET sensor Pyronic and blocked pyruvate extrusion with the MCT1 inhibitor AR-C155858 (Figure 5.18A). As previously described (Chapter 1, section 1.3.1.1), MCT1 has a high affinity to pyruvate and its blockade allows analysis of the dynamics of intracellular pyruvate build-up.

Monitoring of pyruvate levels with Pyronic showed that upon MCT1 blockade with AR-C155858, astrocytes expressing DLDH significantly decrease the rate of pyruvate accumulation (Figure 5.18B). The line of best fit and slopes were calculated using linear least-square fitting for the linear part of the curve that characterizes the rate of pyruvate build-up (370-620s in Control, and 300-800s in DLDH).

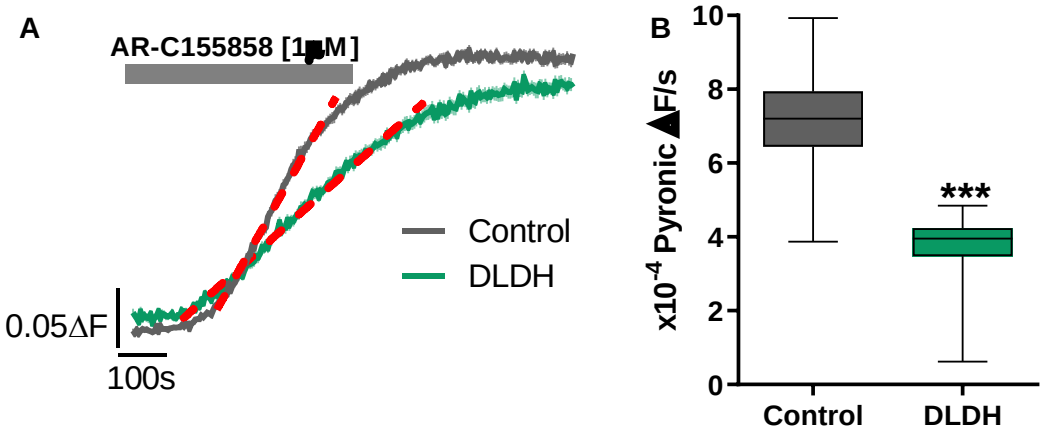

Figure 5.18. DLDH-expressing astrocytes exhibit reduced rate of pyruvate accumulation. (A) Time course of the average Pyronic FRET ratio upon MCT1 inhibition with AR-C155858 [1µM] in primary cultured astrocytes transduced with AVV-CMV-Pyronic alone (Control, n=53) or in combination with AVV-sGFAP-DLDH-IRES-tdTomato (DLDH, n=58). The dotted red lines are the slopes of pyruvate accumulation fitted by linear regression. Data pooled from 3 independent experiments. Shaded regions around the trace represents SEM. **(B)** Pooled data for the rate of pyruvate build-up indicated decreased rate in DLDH astrocytes (3.7±0.9

$x10^{-4}$ ΔF/s) as compared to control cells (7.1±1.2 $x10^{-4}$ ΔF/s). *** - $p<0.0001$, Student's unpaired t-test.

5.3.8 Release of noradrenaline from neurones in organotypic LC slices is unaffected by astrocytic expression of DLDH

To test if DL production through expression of DLDH in astrocytes limits LL-mediated NA release, CNiFERs were seeded on top of organotypic LC slices transduced with AVV-sGFAP-DLDH-IRES-tdTomato and/or AVV-PRSx8-EGFP. The first AVV targets DLDH expression specifically to astrocytes, whereas the latter drives EGFP expression to noradrenergic neurones for visualization purposes. NA release was monitored through changes in FRET ratio of CNiFERs (see Chapter 2, section 2.3.1.3). The ability of LL to trigger NA release from LC neurones was firstly verified through application of LL [2mM] in each slice, which later received a second application of pyruvate [10mM]. Addition of high dose of pyruvate into the recording chamber was necessary to force LL extrusion from the slice pool through trans-acceleration of MCTs. The response of NA released following application of pyruvate was then compared with the response from the application of LL in each slice.

Evaluation of NA release in control organotypic slices revealed that both exogenous and endogenous LL (pyruvate-driven LL extrusion) triggered similar levels of NA release (Figure 5.19). Similar pattern of response was also observed in organotypic brainstem slices transduced with DLDH, indicating that astrocytic expression of DLDH did not affect NA release by LC neurones under these conditions (Figure 5.19).

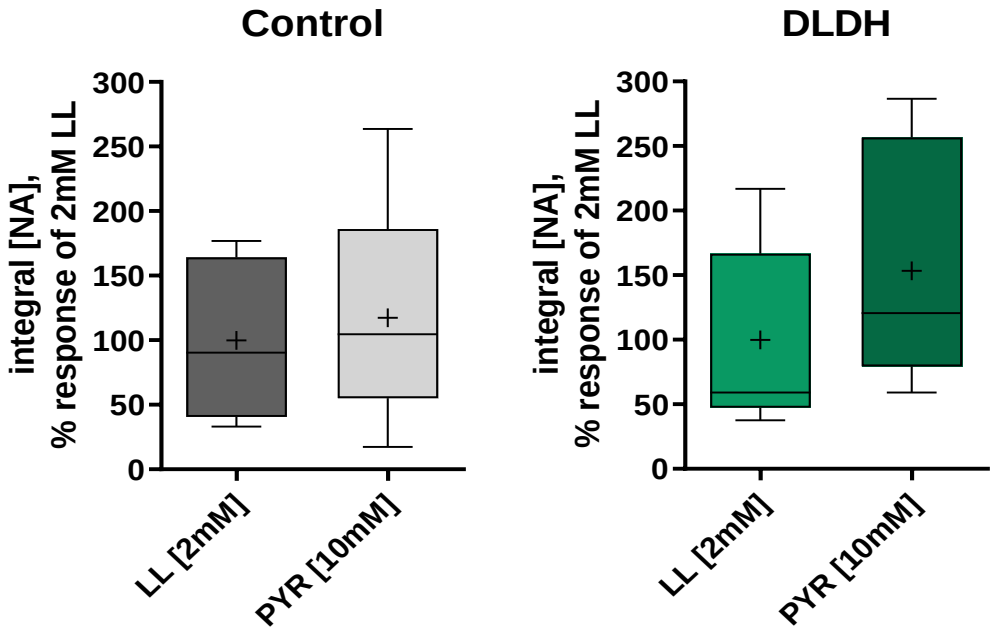

Figure 5.19. Astrocytic expression of DLDH in organotypic brainstem slices does not affect NA release. Pooled data for the area under the curve (integral [NA]) of CNiFERs FRET ratio (ECFP/Citrine) following application of LL [2mM] and pyruvate [10mM] in organotypic brainstem slices expressing AVV-PRSx8-EGFP alone (Control, n=5) or in combination with AVV-sGFAP-DLDH-IRES-tdTomato (DLDH, n=8). Control and DLDH slices did not show any significant difference in NA released following application of LL [2mM] and pyruvate [10mM] (Control: 100.0±62.8% in LL [2mM] *vs.* 117.4±89.7% in PYR [10mM], ns – p>0.05; DLDH: 100.0±70.6% in LL [2mM] *vs.* 153.4±90.3% in PYR [10mM], ns – p>0.05). Student's paired t-test.

5.4 Discussion of DLDH effects

An increasing body of evidence suggests that astrocytes in the brainstem regulate the activity of presympathetic neurons and, consequently, play a pivotal role in the control of the sympathetic drive (Marina et al., 2018). One of the signalling mechanisms underlying communication between astrocytes and neurones in the brainstem is proposed to involve the release of astrocyte-derived LL, which acts through a Gs-coupled receptor in noradrenergic neurones to induce NA release and neuronal depolarization (Tang et al., 2014). Since these effects are blocked by DL, we developed a novel molecular tool to prompt astrocytes to produce and release DL in an attempt to counteract LL-induced neuronal activation.

Although DL is naturally generated in mammals, the pathways for DL production either requires transmembrane expression in the mitochondria of an enzyme the existence of which is still under scrutiny or involve highly cytotoxic compounds. Moreover, it was necessary to create a mechanism for DL degradation since its accumulation in the CNS is associated with varied neuronal disorders (Uribarri et al., 1998). Therefore, as for the molecular tools to break down LL, we took advantage of the diverse metabolism of microorganisms. Lactic acid bacteria, for example *L. bulgaricus*, express DLDH that efficiently converts pyruvate into DL in a reversible reaction, providing a mechanism for DL generation and degradation. Through conversion of the bacterial DLDH ORF sequence to that of mammals, we created a molecular tool to deliver microbial DLDH expression specifically to astrocytes. Evaluation of the cytotoxicity caused by DLDH expression demonstrated that this construct does not have harmful consequences for cells.

The most striking evidence that DLDH is enzymatically active in mammalian cells came from the determination of DL concentration in media collected from seeding cells transfected with DLDH-carrying constructs. The high content of DL in the media after only a few hours of incubation indicated that cells are producing DL and are endowed with the means to release it to the extracellular space. Constitutive release of DL was considerably higher from HEK293 cells than from astrocytes (approximately 232µM in HEK293 cells against 9µM in astrocytes). This difference may be a matter of transfection rate since HEK293 cells are generally considered to be more efficiently transfected.

Validation of the novel DLDH-based molecular tool was challenging due to the lack of means to directly measure intra-astrocytic and extracellular DL dynamics. Since DL is an allegedly non-metabolizable substrate, not much interest has been given to the development of technologies for DL measurement in different biological contexts. Therefore, most of the *in vitro* validation experiments performed here assessed the indirect effects of DLDH expression. LL dynamics were particularly worthy of investigation since DLDH and LDH reactions are analogous with respect to the substrate and coenzymes utilized and, therefore, DLDH activity may indirectly interfere with LL generation.

Analysis of the constitutive LL release from cells expressing the novel molecular tool showed reduction only in HEK293 cells, whereas tonic release from astrocytes expressing DLDH was unchanged. On the other hand, trans-acceleration driven LL release was significantly reduced in dissociated astrocytes, implying a decreased LL reserve available upon acute stimulation. These contrasting results between constitutive and reactive release of LL hampered any conclusions on LL handling by astrocytes expressing DLDH. Therefore, in order to better elucidate LL dynamics in a region of physiological relevance for the study of LL/DL signalling, we employed LL amperometric recordings in the LC area of organotypic brainstem slices. Analysis of LL tone as well as trans-acceleration driven LL release in slices indicated that astrocytic DLDH expression does not interfere with these parameters. Combined, these data indicate that production of DL does not affect LL dynamics.

We also evaluated the rate of intracellular pyruvate accumulation in primary cultured astrocytes upon MCT1-mediated blockade of monocarboxylate extrusion, which was slowed down when astrocytes expressed DLDH. The most likely reason for this is that pyruvate may be driven towards DL production in DLDH-expressing astrocytes, decreasing its rate of accumulation in the cytosol. However, care should be taken when drawing this conclusion since pyruvate metabolism is complex and involves other pathways and regulatory mechanisms that were not evaluated in this study.

Finally, the effect of DLDH expression in astrocytes in the brainstem on NA release from LC neurones was analysed using CNiFERs. FRET imaging indicated that NA released upon bath application of LL [2mM] was similar to the NA released from the application of pyruvate [10mM], which forces LL extrusion from all cells in the slice which express MCTs. Although these results suggest that the initial aim of reducing LL-induced activation of noradrenergic neurones through DLDH expression was not achieved, we have to consider that the methodological approach of trans-acceleration with pyruvate may not entirely reflect LL release triggered by physiological stimuli. Moreover, since DL has lower affinity for MCTs than LL, the DL efflux evoked by trans-acceleration may not have been sufficient to block LLRx.

Therefore, an unresolved issue in the *in vitro* validation of the DLDH-based molecular tool is the question whether the levels of DLDH expression and DL production achieved were sufficient to block LL action at LLRx. Due to the lack of tools available

for measurements, constitutive release of DL has only been evaluated in HEK293 cells and primary astrocytes. If considering the baseline release of DL from dissociated astrocytes, even though it is only about 9µM, DL has been described to be able to antagonize the excitatory action of LL when applied at concentrations 10 to 100 times lower than LL (Tang et al., 2014). In fact, concentration as low as 1µM of DL was able to slightly shift to the right the LL dose-response curve to NA release (Tang et al., 2014). In conclusion, two major factors may be playing a role in the non-existent reduction in LL-induced NA release from LC neurones in slices containing DLDH-expressing astrocytes: non-physiological procedure to evoke DL efflux and/or uncertain intra-astrocytic DL concentrations.

In summary, this chapter describes the development and *in vitro* validation of a novel molecular tool to induce astrocytic production and release of DL by the expression of the DLDH enzyme, which is originally found in bacteria. DLDH expression in mammalian cells successfully leads to the production of DL and can be potentially applied in the study of mechanisms that are DL-sensitive. Our laboratory is currently working on vectors to improve expression levels of DLDH in astrocytes *in vivo*.

Chapter 6 – Interfering with L-lactate release through connexin 43 hemichannel knock-down

6.1 Connexins and the transport of L-lactate in astrocytes

Connexin hemichannels have been suggested to actively participate in LL release from brain cells *in vitro* and *in vivo* (Karagiannis et al., 2015). Although neither the brain source of LL nor the connexin subtype involved in this response have been investigated, we proposed that the major glycolytic cells in the brain – astrocytes – through the activity of the main connexin expressed in these cells – connexin 43 (Cx43) – may play a significant role in this effect. In order to uncover the actual function of Cx43 in the regulation of astrocytic LL pool sizes and signalling, we developed a molecular tool to decrease Cx43 expression selectively in astrocytes. As further detailed in this section, cell-to-cell LL transport through Cx43-forming gap junctions has already been described. However, whether astrocytic Cx43 hemichannels in astrocytes are contributing to the release of LL to the extracellular space remains to be explored.

6.1.1 Connexins and their expression pattern in astrocytes

Connexins consists of four transmembrane domains with one cytoplasmic and two extracellular loops and both N- and C-terminals in the intracellular space (Delvaeye, Vandenabeele, Bultynck, Leybaert, & Krysko, 2018) (Figure 6.1). When assembled, connexins allow cellular communication by two means: (i) intracellular-extracellular exchange through hemichannels, also known as connexons, which are formed by the aggregation of six connexins; (ii) cell-to-cell communication through gap junctions, which are assembled when a hemichannel from one cell docks to another from a neighbouring cell.

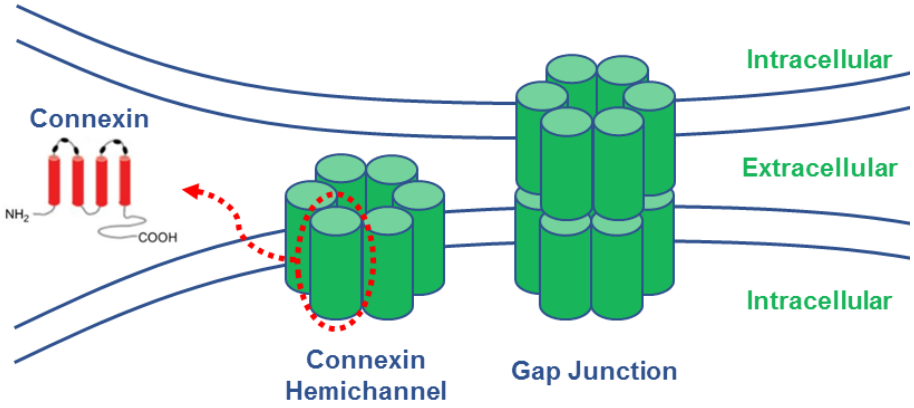

Figure 6.1. Molecular structure of connexins. Aggregation of six connexin subunits forms a connexin hemichannel, which allows exchange between intracellular and extracellular compartments. Docking of a connexin hemichannel to another from the adjacent cell forms a gap junction, which provides an intercellular passageway between both cells. Schematic adapted from Delvaeye et al. (2018).

In the central nervous system, 11 different connexin types can be found in rodents out of 20 family members described so far in mice and 21 in humans (Esseltine & Laird, 2016). Astrocytic and neuronal expression of connexins fluctuate according to the brain area and period of development (Zhao, Xin, He, & Hu, 2018). Astrocytes have been shown to predominantly express Cx43, although astrocytes localized in the grey matter mainly express connexin 30, whereas connexin 26 expression is restricted to astrocytes in subcortical areas (Dermietzel, Hertberg, Kessler, & Spray, 1991; Nagy, Patel, Ochalski, & Stelmack, 1999; Verkhratsky & Nedergaard, 2018). Neurones, on the other hand, do not express Cx43. Instead, these cells have been described to express connexin 36 mostly during the earlier stages of postnatal maturation, and connexins 57 and 45 in both adult and developing rat brain (Condorelli, Trovato-Salinaro, Mudò, Mirone, & Belluardo, 2003).

6.1.2 L-lactate transport through astrocytic gap junctions

While the capacity of non-junctional hemichannels to release compounds to the extracellular space was still under debate, the functional role of astrocytic gap junctions was already established and included the ability to deliver metabolites, including LL, throughout the brain (Harris, 2007; Hofer & Dermietzel, 1998;

Tabernero, Giaume, & Medina, 1996). Roauch et al. (2008) showed that gap junctions play an important role in the astrocyte-neurone metabolic coupling. Their evidence suggested that glutamatergic synaptic activity evoked energetic demand-driven diffusion of metabolites through astrocytic gap-junctions. In this case, glucose initially taken up by astrocytes is metabolized into LL which, in turn, can traffic through astrocytic gap junction networks to sustain the high energy demand of excitatory synaptic transmission (Rouach et al., 2008). The physiological role of LL trafficking through astrocytic gap-junctions was further investigated in mice where Cx43 was specifically knocked out in astrocytes (Clasadonte et al., 2017). This study showed that blocking the trafficking of LL through the astrocytic gap-junction network led to impairment in the sleep-wake cycle due to deficiency in energy supply to the wake-promoting orexin neurones in the lateral hypothalamus (Clasadonte et al., 2017). Although not specifically investigated in the study, a role of astrocytic hemichannels in mediating LL release to the extracellular space was not excluded.

Although gap junctions can be assembled from different hemichannel types (heterotypic channel) and connect distinct groups of cells (heterocellular gap junctions), evidence from freeze–fracture replica immunogold labelling and light microscopic immunocytochemistry experiments has not demonstrated the existence of functional coupling between astrocytes and neurones via gap junctions (Nagy, Dudek, & Rash, 2004; Rash, Yasumura, Dudek, & Nagy, 2001). Indeed, as shown by dye-coupling experiments, the majority of brain cells coupled to astrocytes via gap junctions are astrocytes, which implies that signalling molecules or metabolites mediating astrocyte-to-neurone communication are mainly released to the extracellular space (Giaume, Koulakoff, Roux, Holcman, & Rouach, 2010). However, the possibility of gap junctions linking astrocytes to neurones, even if rare, should not be excluded.

6.1.3 L-lactate transport through astrocytic hemichannels

Experimental evidence has shown that connexin hemichannels in astrocytes play a crucial role in the modulation of brain activity *in vivo* (Karagiannis et al., 2015; Stehberg et al., 2012). Microinjection into the basolateral amygdala of TAT-Cx43L2 peptide, which blocks the opening of Cx43 hemichannels without affecting astrocytic

gap junctional interactions, affected fear memory consolidation (Stehberg et al., 2012). On the other hand, when a mixture of gliotransmitters that included LL among others was co-infused with the blocking peptide, the learning capacity was rescued (Stehberg et al., 2012). Evidence that specifically LL is released via functional connexin hemichannels was recently confirmed by a study that used LL biosensors to monitor in real time the fluctuations in LL concentration in different regions of the brain (Karagiannis et al., 2015). Reduction of extracellular Ca^{2+} in order to enhance open probability of hemichannels resulted in increased LL release from brainstem, hippocampus, and cortex acute slices from adult rats. This response was reduced by pharmacological manipulations that inhibit connexin hemichannels, while blockade of MCTs had no impact on the tonic release of LL (Karagiannis et al., 2015). Interestingly, this mechanism of LL release was also recruited during hypoxic conditions *in vitro* as well as in periods of intense neuronal activity *in vivo* (Karagiannis et al., 2015).

Considering astrocytes as a LL reservoir cell and taking into account that LL can be released through connexin hemichannels, the challenge will be now to define the precise mechanisms regulating their open probability to LL. Connexin hemichannels are known to release molecules under well-defined circumstances and are generally found in their closed/inactive state under physiological resting conditions (Giaume, Leybaert, Naus, & Sáez, 2013). Several experimental conditions have been described to activate connexin hemichannels in astrocytes, including reduction of extracellular Ca^{2+} concentration, robust depolarisation, metabolic inhibition, and pro-inflammatory treatments (Contreras et al., 2002; Hofer & Dermietzel, 1998; Karagiannis et al., 2015; Retamal et al., 2007)

Therefore, in an attempt to better comprehend the role played by connexin hemichannels in the astrocytic release of LL, we have designed and constructed a tool based on RNA interference (RNAi) to decrease expression of Cx43 selectively in astrocytes.

6.2 RNAi as a strategy for knock-down of specific proteins in specific cell types

RNAi is a phylogenetically conserved mechanism to decrease expression of a specific gene which works via small RNAs that exhibit sequence complementarity to the target mRNA. The underlying molecular pathway behind this gene silencing phenomenon has become clear following a study from Fire and Mello labs using the nematode *C. elegans*, in which injection of dsRNA reduced expression of the corresponding gene (Fire et al., 1998). Similar RNA suppression pathways have been subsequently described in distinct genetic systems such as protozoa, plants, fungi, and animals (Leung & Whittaker, 2005; Tijsterman, Ketting, & Plasterk, 2002). Since dsRNA can be introduced by replicating viruses or integrated transposons, RNAi is thought to be part of an endogenous defence scheme, which may explain its highly evolutionary conserved nature (Tijsterman et al., 2002). Importantly, dsRNA can also originate from transcription of specific genome sequences that encode the so-called microRNAs (miRNAs), which contribute to cellular regulation of gene expression.

The cellular mechanisms underpinning RNAi triggered by endogenous miRNA involve several steps (Figure 6.2) (Bartel, 2009; Gebert & MacRae, 2019; Ying, Chang, & Lin, 2008). Firstly, primary precursor miRNA (pri-miRNA) is transcribed from the genome mainly through the activity of RNA polymerase type II (Pol-II), forming a hairpin-containing transcript (Gebert & MacRae, 2019; Ha & Kim, 2014). Pri-miRNA is then cleaved by the Microprocessor complex, formed by the RNase III enzyme Drosha and the DGCR8 protein, which results in a ~60-70 nucleotide (nt)-long precursor miRNA (pre-miRNA). Pre-miRNA is then carried from the nucleus to the cytoplasm by Ran-GTP and the receptor Exportin-5, where it is further cleaved by another RNase III enzyme known as Dicer. This process yields the mature miRNA, which consists of an RNA duplex composed of 18-25 nt in a hairpin structure with 2-nt overhang at the 3' end and a 5' phosphate (Bartel, 2004; Gebert & MacRae, 2019; Ying et al., 2008). Finally, one strand of the miRNA (guide strand) is incorporated into the protein Argonaute, forming the RNA-induced silencing complex, whereas the other strand (passenger strand) is discarded and degraded. miRNA drives Argonaute to the target sites generally located in the 3' untranslated region (UTR) of target mRNAs, where the complex binds, leading to repression of translation and degradation of targeted mRNAs (Gebert & MacRae, 2019).

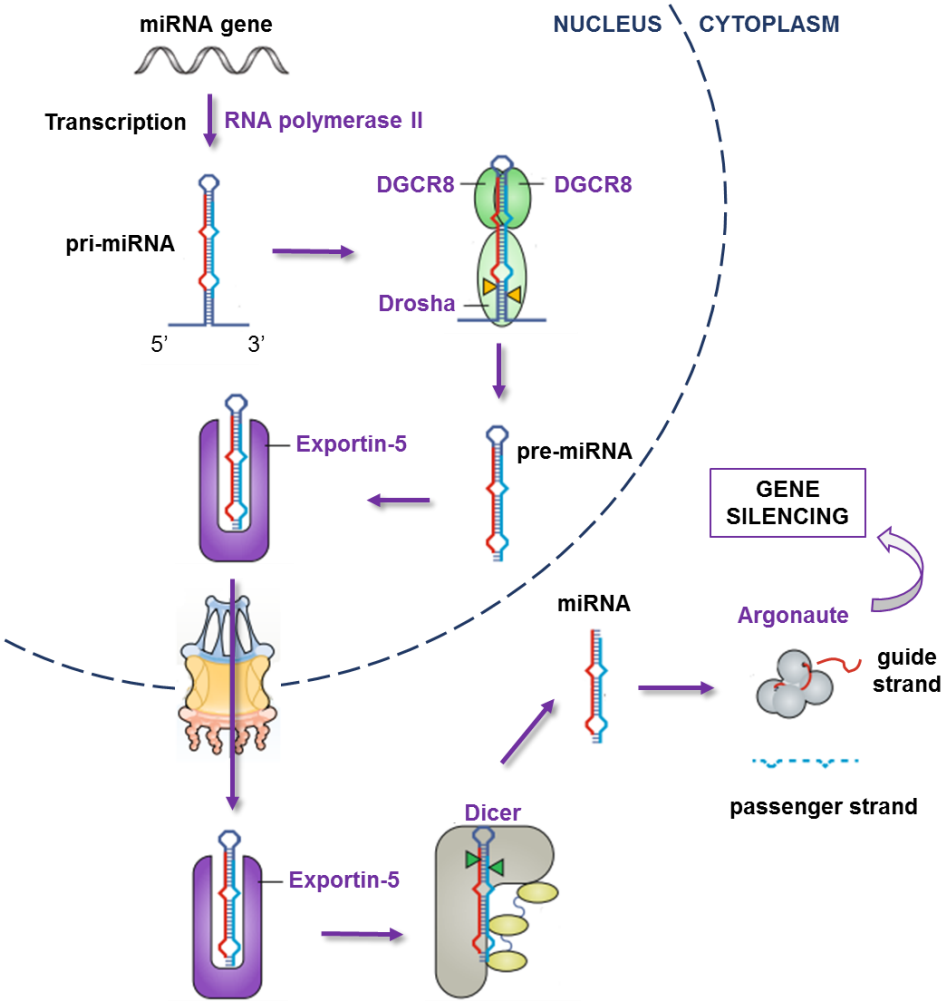

Figure 6.2. Schematics of the miRNA biogenesis and RNAi mechanisms. The multistep process of miRNA biogenesis starts in the nucleus with transcription to pri-miRNA, which is further processed in the nucleus as well as in the cytoplasm to yield the mature miRNA comprised of approximately 22 nt. The guide strand of the miRNA is then loaded into Argonaute, which guides the miRNA-Argonaute silencing complex to bind to the target mRNA, resulting in gene silencing. Figure adapted from Gebert and MacRae (2019).

6.2.1 Knock-down of Cx43 using miRNA

In order to knock-down Cx43 expression in astrocytes, we designed a vector that drives the expression of engineered miRNAs targeting Cx43 gene under RNA Pol II promoter. Cloning of the expression cassette was performed using BLOCK-iT™ Pol II miR RNAi Expression Vector Kit with EmGFP (Invitrogen, K493600). This system leads to the construction of an expression clone encoding one or more pre-miRNA sequences, preceded by a Pol II compatible promoter and a fluorescent reporter ORF.

Due to murine mir-155-derived regions flanking the pre-miRNA sequences, these are subsequently cleaved by the cytoplasmic enzyme Dicer, yielding the mature miRNA. Design of the guide RNA sequences was carried out according to the optimisation algorithm provided by Invitrogen (see below). In order to enhance the degree of gene knock-down, three guide sequences targeting different parts of the Cx43 mRNA were linked together. This approach resembles the natural organisation of miRNA templates which can be found in clusters in the genome and are transcribed as a single and long primary transcript (Ambros, 2004; Gebert & MacRae, 2019; Ha & Kim, 2014).

6.2.1.1 Design of pre-miRNA sequence

Design of pre-miRNAs is a critical step in gene silencing by RNAi. Using BLOCK-iT™ RNAi Designer online tool, complementary ssDNA oligonucleotides were designed and later annealed in order to generate a dsDNA. For proper assembly of the pre-miRNA structure, the top strand of the oligonucleotide carried from 5' to 3' end the following features:

- TGCT nt derived from miR-155, which supplies 5' overhang compatible for ligation with the vector.
- 5'G followed by 21-nt antisense sequence of the target gene, which will form the mature miRNA sequence. Once transcribed, the mature miRNA will target the gene of interest and, therefore, it must be antisense to the target mRNA.
- 19 nt derived from miR-155, which will compose the terminal loop of the pre-miRNA.
- Nucleotides 1-8 and 11-21 of the sense sequence of the target gene. Removal of nucleotides 9 and 10 was designed in order to increase knock-down efficacy by creating a short internal loop in the structure of the mature miRNA.
- CAGG derived from miR-155, which is also compatible with the vector and it is required for directional cloning.

The bottom oligonucleotide strand comprised of the reverse sequence of the top strand, except for the 5' TGCT, which was swapped to CCTG to create a 5' overhang.

Submitting the nucleotide sequence of Cx43 (Gap junction alpha-1 protein – Gja1) from *rattus norvegicus* to the BLOCK-iT™ RNAi Designer online tool generated a range of miRNAs ranked according to their knock-down probability. We selected 3 sequences exhibiting the greatest likelihood of knock-down success, which were rearranged to include the required features detailed below (Table 6.1).

Table 6.1. Sequence of the oligonucleotides encoding the pre-miRNA targeting Cx43 mRNA. The table depicts the location of the target sequence in the Cx43 mRNA as well as the sequence of the top and bottom strands from 5' to 3' end. Nucleotides comprising the linker are in purple, the mature miRNA sequence is in green, the sequence forming the external loop is shown in blue and the 1-8 and 11-21 nucleotides of the 21-mer target is in red.

Start	Oligo type	Oligo sequence
273	Top Strand	TGCTGTGAATATGAAGAGCACTGACAGTTTTGGCCACTGACTGACTGTCAGTGCTTCATATTCA
	Bottom Strand	CCTGTGAATATGAAGCACTGACAGTCAGTCAGTGGCCAAAACTGTCAGTGCTCTTCATATTCAC
559	Top Strand	TGCTGTTCAGGTGCATCTCCACGTTGGTTTTGGCCACTGACTGACCAACGTGGATGCACCTGAA
	Bottom Strand	CCTGTTCAGGTGCATCCACGTTGGTCAGTCAGTGGCCAAAACCAACGTGGAGATGCACCTGAAC
707	Top Strand	TGCTGATAGATGTACCACTGGATGAGGTTTTGGCCACTGACTGACCTCATCCAGGTACATCTAT
	Bottom Strand	CCTGATAGATGTACCTGGATGAGGTCAGTCAGTGGCCAAAACCTCATCCAGTGGTACATCTATC

6.2.1.2 Construction of Cx43 knock-down expression vectors

First, complementary top and bottom strand oligonucleotides were annealed in order to generate ds oligos. Each ds oligo was then cloned into the linearized pcDNA™6.2-GW/EmGFPmiR, which is the backbone vector provided by the supplier (Invitrogen). pcDNA™6.2-GW/EmGFPmiR is driven by a CMV promoter and contains a sequence coding Emerald Green Fluorescent Protein (EmGFP) for tracking of vector expression. Moreover, pcDNA™6.2-GW/EmGFPmiR is endowed with 4-nt 5'

overhangs derived from miR-155 sequences, which are compatible for directional ligation with the ds oligo inserts. By ligation of the linearized vector with each ds oligo, 3 recombinant plasmids were generated: pcDN6.2-GW/EmGFP-miR155-Gja1-273, pcDN6.2-GW/EmGFP-miR155-Gja1-559, and pcDN6.2-GW/EmGFP-miR155-Gja1-707. Assessment of the plasmid sequence through diagnostic restriction digestions with the enzymes *SalI* & *XhoI* confirmed a correct outcome. The samples were also sequenced (Eurofins MWG) using EmGFP forward primer (GGCATGGACGAGCTGTACAA) and miRNA reverse primer (TCTAGATCAACCACTTTGT), which exhibited the expected outcome following *in silico* alignment using Vector NTI.

6.2.1.2.1 pcDN6.2-GW/EmGFP-miR155-Gja1-RNAi

In order to target co-cistronic expression of the 3 pre-miRNAs for simultaneous transcription in one single structure, pre-miRNAs sequences derived from the novel recombinant plasmids were linked together in one construct. Firstly, pcDN6.2-GW/EmGFP-miR155-Gja1-273 was double-digested with the endonucleases *BglII* & *XhoI*, producing a vector backbone of 5.7kb. Pre-miRNA 559 was then isolated from the recombinant plasmid pcDN6.2-GW/EmGFP-miR155-Gja1-559 through restriction digestion with the enzymes *BamHI* & *XhoI*, generating an insert fragment of approximately 150bp. Vector and insert were then ligated together to form pcDN6.2-GW/EmGFP-miR155-Gja1-273-559 (Figure 6.3, step 1). Of note, *BglII* and *BamHI* restriction endonucleases produce compatible overhangs, enabling ligation between 2 DNA fragments. The novel recombinant plasmid containing 2 pre-miRNA sequences (273 and 559) underwent diagnostic restriction digestion with *SalI* & *XhoI*, which yielded the expected bands. Sequencing using EmGFP forward primer (GGCATGGACGAGCTGTACAA) and subsequent alignment with the vector map confirmed the construct to be correct.

Since the pattern of restriction sites in the expression cassette is regenerated after addition of a pre-miRNA sequence (Figure 6.3), linking of the third pre-miRNA followed the same cloning strategy as described above. Accordingly, pre-miRNA 707 was extracted from pcDN6.2-GW/EmGFP-miR155-Gja1-707 by *BamHI* & *XhoI* digest, yielding a DNA insert fragment of approximately 150bp. The vector backbone

containing the pre-miRNAs 273 and 559 – pcDN6.2-GW/EmGFP-miR155-Gja1-273-559 – was double-digested with the enzymes *BglII* & *XhoI,* resulting in a 6.0kb vector fragment. Ligation of both vector and insert created the recombinant plasmid pcDN6.2-GW/EmGFP-miR155-Gja1-RNAi (Figure 6.3, step 2), which contained sequence encoding three pre-miRNAs (273, 559, and 707). Successful cloning was confirmed by diagnostic restriction digestion with the enzymes *SalI* & *XhoI* and sequencing using specific primers to EmGFP (forward: GGCATGGACGAGCTGTACAA) and miRNA (reverse: TCTAGATCAACCACTTTGT).

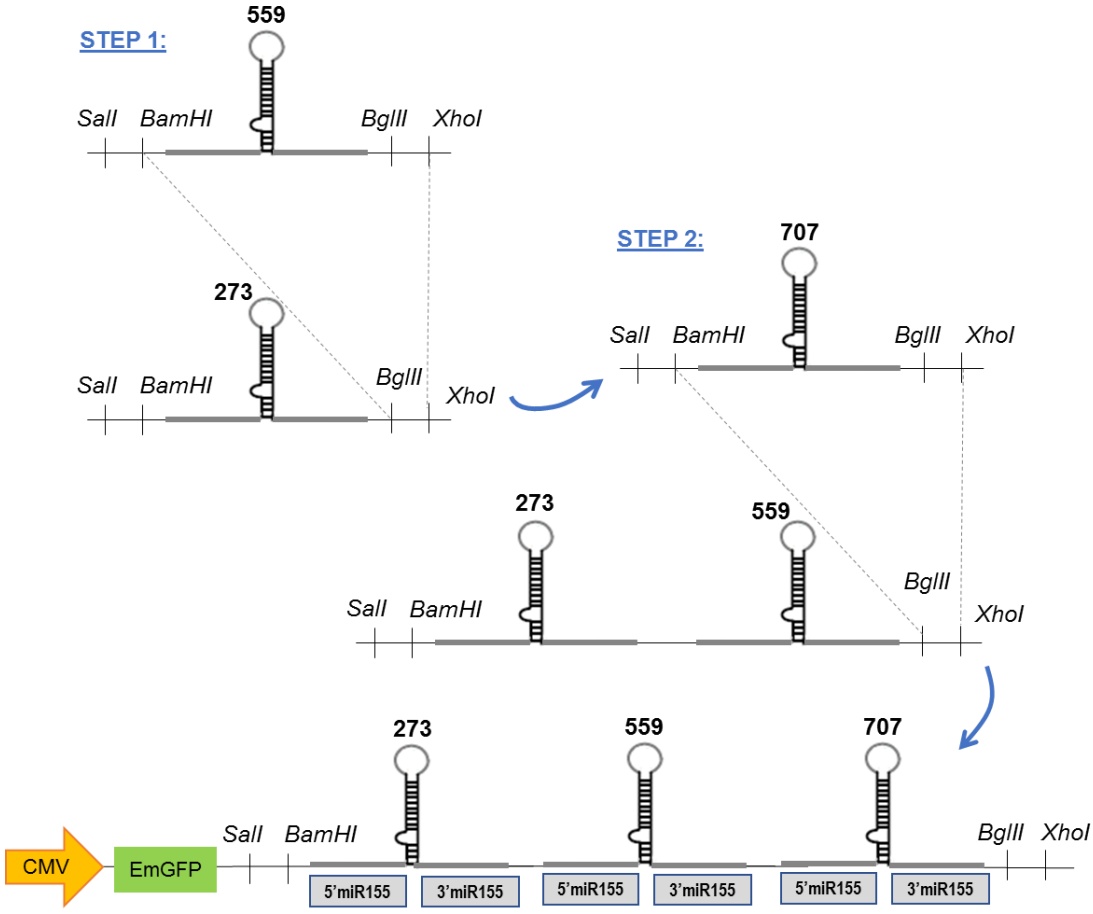

Figure 6.3. Construction of an expression cassette for co-cistronic expression of three miRNAs targeting different regions of mRNA transcribed from the Cx43 gene (Gja1). Other constituents of the expression cassette such as CMV promoter, EmGFP and miR155 flanking regions were only depicted in the last construct of the figure to simplify the schematic representation. Linking of multiple pre-miRNAs in one single construct was based on performing digestions at restriction sites that produce

compatible cohesive ends and are lost or regenerated, respectively, following vector and insert ligation.

6.2.1.2.2 pXCX-sGFAP-EmGFP-miR-Gja1-RNAi

In order to create a recombinant plasmid that drives the expression of Cx43-targeting miRNAs specifically into astrocytes, the sequence encoding EmGFP followed by the three pre-miRNAs from pcDN6.2-GW/EmGFP-miR155-Gja1-RNAi was transferred to a pXCX-shuttle backbone under the control of a sGFAP promoter. For this purpose, pXCX-sGFAP-tdTomato was double-digested with the restriction endonucleases *AgeI* & *NotI*, which resulted in the removal of tdTomato sequence and formation of a 10.0kb vector backbone. EmGFP and pre-miRNAs sequences were then amplified by PCR using pcDN6.2-GW/EmGFP-miR155-Gja1-RNAi as a template and forward Gja1 *AgeI* primer (CATACCGGTGCTAACTAGAGAACCCACTG), adding an *AgeI* restriction site, and the reverse Gja1 *NotI* primer (TTGCGGCCGCGTACAAGAAAGCTGGGTC), adding a *NotI* restriction site to the amplicon of 1.3kb, EmGFP-miR155-Gja1-RNAi. The PCR product was then ligated with the vector fragment, generating the recombinant plasmid pXCX-sGFAP-EmGFP-miR-Gja1-RNAi (Figure 6.4A). Diagnostic restriction digestions were carried out using the enzymes *SalI* and *BglII*, which confirmed an accurate outcome. Sequencing by Eurofins MWG with specific primers for the pXCX backbone (reverse, ACCTTCCAGGGTCAAGGAAG) and a primer for the GFAP promoter (forward, ATGGGTGAGGGGAGAGCT) confirmed the DNA sequence of the new shuttle vector.

6.2.1.2.3 pXCX-sGFAP-EmGFP-miR-control

BLOCK-iT™ Pol II miR RNAi Expression Vector kit (Invitrogen, K493600) also provides a plasmid carrying an insert able to form a hairpin structure that is further processed into mature miRNA. However, the miRNA formed does not target any known vertebrate gene, acting as a control for RNAi analysis. The control miRNA plasmid was transferred to a pXCX-shuttle backbone using similar strategy as previously described. The vector fragment of 10.0kb derived from restrictive digestion

of pXCX-sGFAP-tdTomato with *AgeI* & *NotI* was ligated together with a 1.1kb amplicon, which had been generated through PCR of pcDNA™6.2-GW/miR-control using the primers Gja1 *AgeI* and Gja1 *NotI* (CATACCGGTGCTAACTAGAGAACCCACTG and TTGCGGCCGCGTACAAGAAAGCTGGGTC, respectively) (Figure 6.4B). The novel recombinant plasmid pXCX-sGFAP-EmGFP-miR-control was submitted to diagnostic restriction digestions with *SalI* and *BglII*, which yielded the expected bands. Sequencing with reverse pXCX backbone and forward GFAP promoter primers (ACCTTCCAGGGTCAAGGAAG and ATGGGTGAGGGGAGAGCT, respectively) also confirmed a correct outcome.

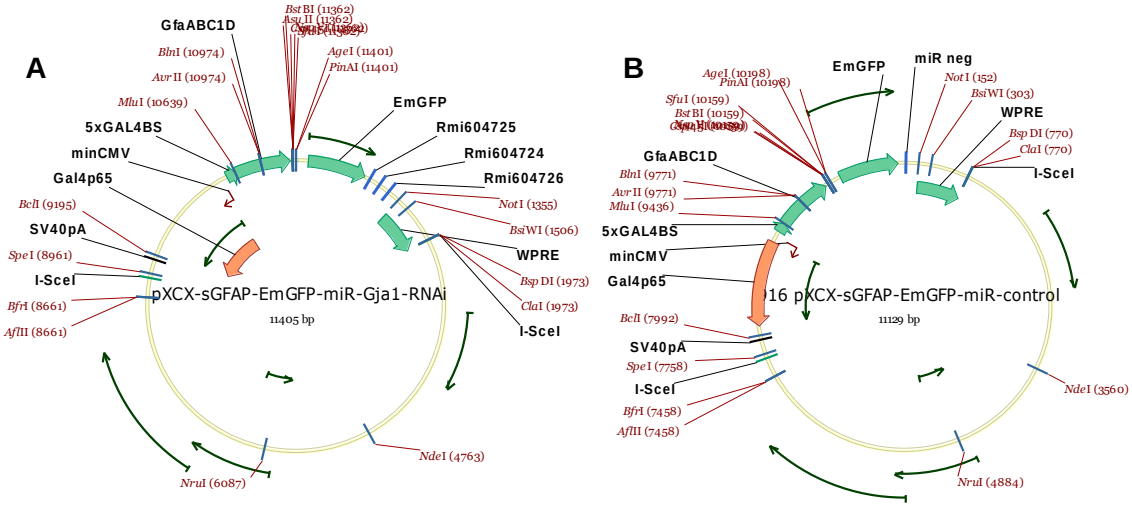

Figure 6.4. Construction of pXCX-sGFAP-EmGFP-miR-Gja1-RNAi and pXCX-sGFAP-EmGFP-miR-control. (A) Vector map of the recombinant plasmid carrying the expression of three pre-miRNAs targeting Cx43 gene under the control of a sGFAP promoter. **(B)** Vector map of the recombinant plasmid carrying the expression of a pre-miRNA that produces a non-functional miRNA under the control of a sGFAP promoter.

6.3 In vitro evaluation of knock-down efficacy of miRNA targeting Cx43 in astrocytes

The recombinant plasmid driving the expression of miRNAs targeting Cx43 knock-down selectively in astrocytes was directed to the production of AVV, which was subsequently used for transduction of primary cultured astrocytes as well as

astrocytes in organotypic brain slices. Successful expression of the reporter gene EmGFP was confirmed by fluorescence imaging (Figure 6.5).

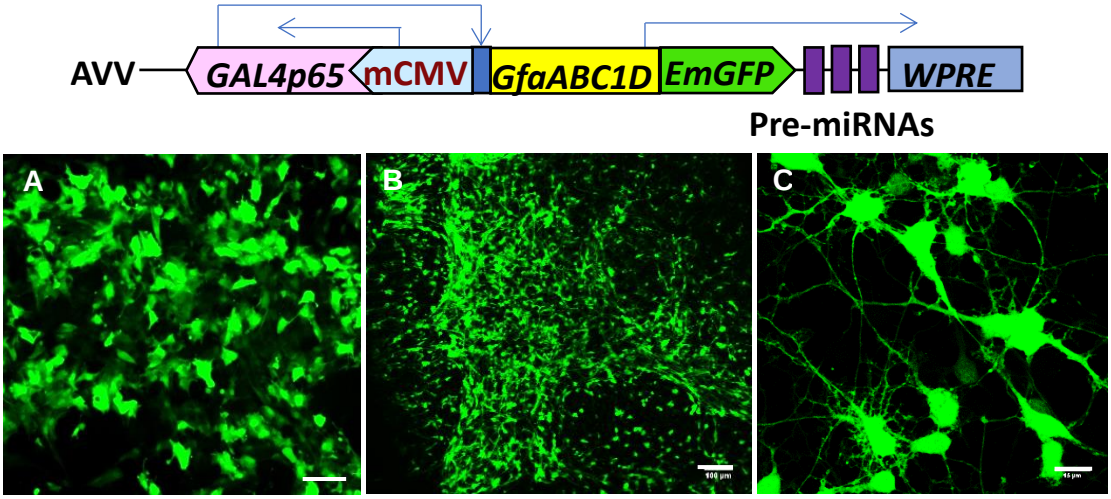

Figure 6.5. Astrocytes transduced with AVV-sGFAP-EmGFP-miR-Gja1-RNAi express the reporter gene EmGFP. Domain structure of the cassette for co-cistronic expression of three different pre-miRNAs targeting Cx43 gene in astrocytes. Below: Fluorescent images of dissociated astrocytes (**A**, scale bar 100µm) and astrocytes in organotypic slice culture (**B** and **C**, scales bar 100µm and 15µm, respectively) expressing the construct.

The ability of AVV-sGFAP-EmGFP-miR-Gja1-RNAi to knock-down Cx43 expression in astrocytes was quantitatively evaluated at the protein level with western blot, which was performed by Dr. Iliana Barrera using anti-Cx43 (Abcam, ab11370, 1:5000 dilution) and anti-actin (Sigma, C6198, 1:5000 dilution) antibodies and equal amount of protein loading (10µg/ml).

Non-transduced (No-AVV) primary cultured astrocytes as well as astrocytes transduced with either AVV-sGFAP-EmGFP-miR-control (Control miR) or AVV-sGFAP-EmGFP-miR-Gja1-RNAi (Cx43 miR) at MOI 100 were harvested 3 days after plating and transduction. Cx43 immunopositive bands were detected at approximately 43kDa, which is the molecular mass predicted for the protein. Western blot analysis suggested that 3 days of AVV transduction did not change the level of Cx43 expression in Cx43 miR primary astrocytes (Figure 6.6). Preliminary results on astrocytes with increased time of incubation with the AVVs driving the expression of

the constructs suggested a slight increase in the knock-down rate of Cx43 expression (Figure 6.6).

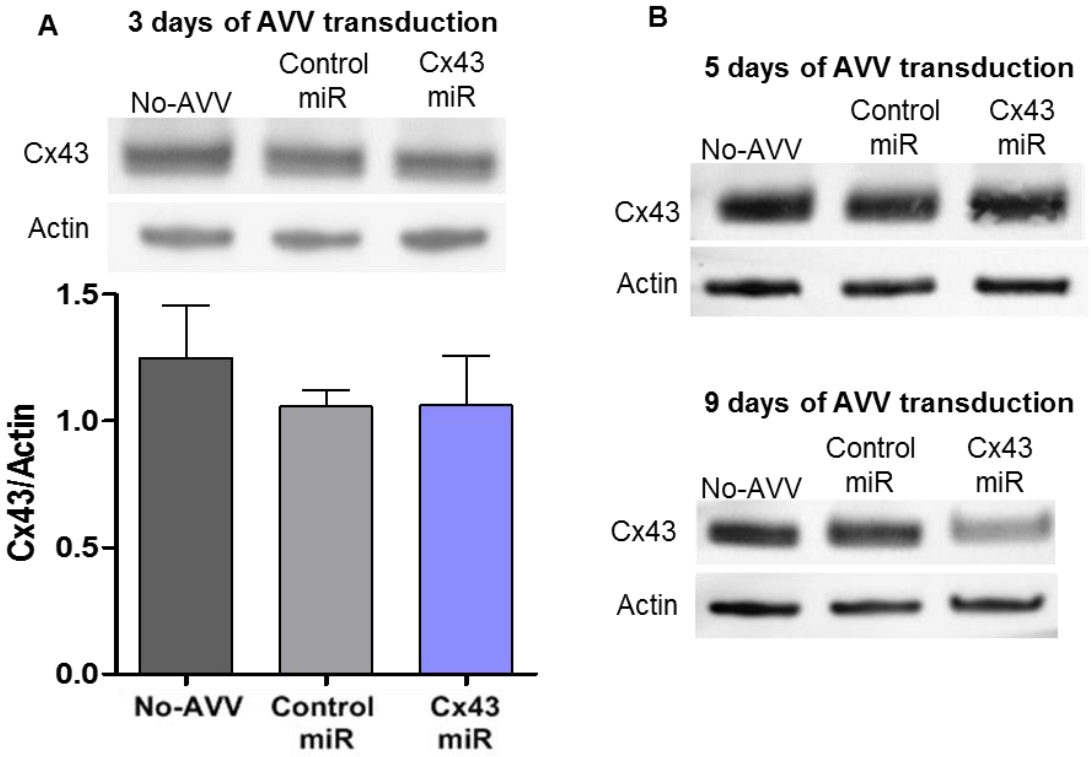

Figure 6.6. Effect of RNAi-mediated Cx43 knock-down strategy in the expression of Cx43 in primary cultured astrocytes. (A) Western blot analysis of Cx43 immunoreactivity in non-transduced primary cultured astrocytes (No-AVV, 1.25±0.36, n=3) and astrocytes transduced with AVV-sGFAP-EmGFP-miR-control (Control miR, 1.06±0.11, n=3) or AVV-sGFAP-EmGFP-miR-Gja1-RNAi (Cx43 miR, 1.06±0.34, n=3) following 3 days of AVV incubation. Error bars represent SEM. **(B)** Western blots of astrocytes following 5 and 9 days of AVV transduction.

6.4 Discussion of the knock-down of Cx43 in astrocytes

The role of connexin hemichannels in the release of LL in the brain has just recently been demonstrated (Karagiannis et al., 2015). In order to further investigate the specificities of this transport mechanism, we developed a molecular tool based on RNAi to selectively decrease Cx43 expression in astrocytes.

RNAi is a post-transcriptional gene silencing tool that has been widely used for the study of gene function. It has emerged as an alternative approach to the costly and

time-consuming process of creation of knockout animals. RNAi-mediated gene knock-down allows the generation of loss-of-function phenotypes without removal of the target gene, preventing, for example, developmental tissue malformations (Iacobas, Iacobas, Urban-Maldonado, Scemes, & Spray, 2008). Cx43 knockout mice die shortly after birth, which has been associated with abnormal heart function (Reaume et al., 2006). Moreover, widespread transcriptomic modification of the target gene in knockout mice may trigger genetic compensation, masking the effects of the missing gene (El-Brolosy & Stainier, 2017). Nonetheless, although the simplicity and cost-effectiveness of RNAi, a major disadvantage of this gene knock-down technique is that the degree of disruption in the expression of the target gene may not be high enough to evoke loss-of-function phenotype. Iacobas and colleagues observed inconsistency in the level of Cx43 knock-down amongst their biological replicas using RNAi (Iacobas et al., 2008).

In this study, analysis of Cx43 expression in primary cultured astrocytes transduced with Cx43-targeting miRNAs showed no effect three days following transduction, which is the incubation time employed in the majority of the AVV-mediated transgene expression carried out during my PhD project. Although one apparent reason for this unsuccessful knock-down rate may be the lack of efficacy of the selected miRNAs, at least one out of the three miRNAs expressed in astrocytes would be expected to contribute to gene silencing. As previously detailed in this chapter, the three miRNAs were selected based in the highest probability of Cx43 knock-down success according to the optimisation algorithm provided by the manufacturer. Our group previously used similar RNAi approach to knock-down the expression of GPR37 and GPR37L in astrocytes (Liu et al., 2018). Employment of three miRNAs to target different regions of the target mRNA successfully decreased the expression of both GPR37 and GPR37L to non-detectable protein levels (Liu et al., 2018). Besides the fact that different proteins were targeted, our previous and current work also differed regarding the promoters used. Since in Liu et al. (2018) the miRNAs were meant to be used in a homogenous astrocytic cell culture, the CMV promoter was not swapped to sGFAP. In this investigation, however, a sGFAP promoter was employed so that we could use this tool in a more complex *in vitro* preparation or *in vivo* application. Even though a non-ubiquitous promoter was used in this project, this may not be reason for the lack

of Cx43 knock-down because analysis of the expression of the reporter gene suggested an adequate transcriptional rate driven by sGFAP (Figure 6.5).

In order to assure full establishment of miRNAs expression, we increased the incubation time and harvested the cells 5 and 9 days following AVV transduction. Preliminary results indicated that the knock-down rate of Cx43 proportionally increased over time, reaching approximately 50% at 9 days of AVV incubation. Intriguingly, Cx43 half-life, which is the time required for turnover of half the amount of the protein at steady-state levels, is relatively short. Reports of Cx43 expression in various cellular cultures suggested that the protein turnover ranges from 1 to 5 hours (Berthoud, Minogue, Laing, & Beyer, 2004; Falk, Bell, Kells Andrews, & Murray, 2016).

In conclusion, we do not know at this point the reasons for which the engineered pre-miRNAs targeting Cx43 mRNA did not result in protein knock-down. Since the level of Cx43 expression in astrocytes did not change substantially, we have not proceeded with *in vitro* validation experiments.

Chapter 7 – Thesis Discussion

7.1 Limitations in the study of astrocyte-derived L-lactate roles in the brain

It is now well accepted that astrocytes are active elements in the processing of information by the brain (Allen & Lyons, 2018). By perceiving neuronal activity and environmental conditions, astrocytes are able to respond to them through the release of neuroactive substances (Bazargani & Attwell, 2016). At the same time, astrocytes are the major regulators of brain metabolic homeostasis. These cells are endowed with the machinery to metabolise, store and dynamically shuttle energy substrates throughout the astrocytic network and to the extracellular space (Giaume et al., 2010).

LL, in particular, has gained increasing attention due to its dual function as a metabolic and signalling compound in the brain (Magistretti & Allaman, 2018). This molecule is mainly produced by astrocytes through the metabolism of glucose or glycogen and may be released to adjacent neurones in case of high energy demand (Magistretti & Allaman, 2015; Pellerin & Magistretti, 2012). Moreover, LL can selectively activate neuronal receptors and modulate the function of neurones, including excitability (Mosienko et al., 2018). By activating a Gs-coupled LL receptor in noradrenergic neurones, astrocyte-derived LL increases neuronal activity and NA release, resulting in enhanced sympathoexcitation and arterial blood pressure in rats *in vivo* (Marina et al., 2015; Tang et al., 2014).

Although astrocytes are reported to possess various elements that favour the glycolytic processing of glucose to produce pyruvate and LL, the actual role of astrocyte-derived LL in the brain is very controversial. Whilst some researchers have suggested that LL is shuttled from astrocytes to neurones in order to sustain the energetic requirements of neuronal function (Bélanger et al., 2011; Pellerin & Magistretti, 1994; Pellerin & Magistretti, 2012), others have consistently contested this hypothesis and even challenged whether the source of the increased LL levels that follow neuronal activation is in fact astrocytic (Díaz-García & Yellen, 2019; Dienel, 2012, 2017; Dıaz-Garcıa et al., 2017). Therefore, the main challenge in the investigation of the metabolic role of LL in the brain is to provide evidence of the cell type accountable for stimulation-induced LL release.

On the other hand, although the role of LL as a signalling molecule is not under dispute (but rather under scrutiny), the effects of LL in the brain are largely investigated

through acute application of high doses of LL. Decreased neuronal activity mediated by LL-induced activation of GPR81, for example, has been described following addition of supraphysiological levels of LL (Bozzo et al., 2013), In contrast, investigation of the effect of LL in memory formation has been contested partially because the amount of LL applied in the hippocampus is likely to be sustained only for a short duration due to the rapid metabolism of LL, making it less probably that it may influence memory consolidation (Dienel, 2012; Suzuki et al., 2011).

In fact, much of the research carried out on both metabolic and signalling effects of LL in the brain has used acute approaches to change aspects of LL production and release at short-term. These approaches include glucose deprivation and pharmacological interventions that inhibit glycogenolysis, astrocytic metabolism, LDH activity, transport of glucose or LL, as well as genetic manipulations to reduce expression of LL transporters and components of the glycolytic pathway (Clasadonte et al., 2017; Herrero-Mendez et al., 2009; Newman, Korol, & Gold, 2011; Parsons & Hirasawa, 2010; Sotelo-Hitschfeld et al., 2015; Suzuki et al., 2011; Walls, Heimbürger, Bouman, Schousboe, & Waagepetersen, 2009). Overall, although pharmacological compounds are of great use for manipulation of selective enzymes or transporters, they do not offer specificity towards the cell type to be targeted – unless the pharmacological targets are indisputably expressed in a single cell type – and their effects are transitory. Genetic manipulations, on the other hand, can offer improved cell specificity and lasting effects. Nonetheless, in some applications, such as the decrease of MCT expression used to study LL-mediated memory formation (Suzuki et al., 2011), the level of knock-down may not be enough to overcome the high capacity of the transporters, and other mechanisms of LL release, not well described yet, may be utilised (Dienel, 2017; Karagiannis et al., 2015; Sotelo-Hitschfeld et al., 2015).

7.2 Novel molecular tools to limit astrocytic L-lactate release and action

The advanced study of LL actions requires selective tools able to chronically modulate LL production and release specifically from astrocytes as well as to interfere with the effects of astrocyte-derived LL signalling in neurones. To address this, I have

developed during my PhD project work a range of viral vector-based molecular actuators that aim to target different aspects of astrocyte-derived LL action in the brain, which includes decreasing the intracellular LL pool in astrocytes, interfering with astrocyte-to-neurone LL signalling, and partial reduction of LL release.

For the design of these tools, we innovatively selected enzymes that are natively found in bacteria and made them specifically expressible in astrocytes. Accordingly, in order to create tools that reduce the astrocytic LL pool, we used the enzymes LOX and LMO, which irreversibly convert LL into pyruvate and hydrogen peroxide or acetate, water and CO_2, respectively. For the design of a tool to interfere with LL signalling, we selected the bacterial enzyme DLDH. This enzyme reduces pyruvate to DL, which has been described to antagonize the excitatory effect of LL in noradrenergic neurones in the brainstem (Tang et al., 2014). In addition, in an attempt to further investigate the mechanisms of astrocytic LL release and add to the tool kit for blocking it, we constructed a RNAi-based tool to drive the expression of miRNAs targeting Cx43 gene silencing specifically to astrocytes.

The ORF sequence of the LL catabolic enzymes LOX and LMO from *Aerococcus viridans* and *Mycobacterium smegmatis*, respectively, as well as the DL-producing enzyme DLDH from *Lactobacillus bulgaricus* were adapted to the mammalian codon usage and cloned under the control of a transcriptionally-enhanced astrocytic promoter. An expression vector that drives the expression of three engineered miRNAs targeting Cx43 gene under the control of the astrocyte-selective promoter was also constructed. Viral vectors were employed in order to deliver the expression of these enzymes to primary dissociated cultured astrocytes and to astrocytes in organotypic brainstem slices. Approaches that combine FRET-based sensors with real-time imaging techniques were adopted in order to analyse the functional effects of transgene expression in the intracellular glycolytic state of individual astrocytes. Moreover, enzyme-based LL biosensor and amperometric recordings were adopted to investigate the effects of the expression of the novel molecular tools in extracellular LL dynamics in the brain tissue. A cell-based NA sensor was also applied in order to evaluate how the expression of these enzymes influences LL-induced NA release from LC neurones.

7.2.1 Summary of the functional *in vitro* validation of the novel molecular tools

Investigation of the tonic LL or DL release from astrocytes expressing the novel molecular tools confirmed that the enzymes of bacterial origin are enzymatically active in mammalian cells. Primary cultured astrocytes expressing LOX or LMO decreased the constitutive release of LL, while expression of DLDH induced significant increase in the tonic release of DL to the extracellular space. Although DLDH-mediated production of DL utilizes the same substrate and coenzymes as the enzymatic reaction that leads to the generation of LL, the levels of LL were not altered by DLDH expression. A similar scenario was found in organotypic brainstem slices, in which expression of DLDH in astrocytes did not interfere with the LL tone of the slice. Astrocytic expression of LOX or LMO, on the other hand, consistently decreased the tonic release of LL from brainstem organotypic slices.

The effects of the expression of the novel enzyme-based molecular tools were also investigated on the LL release upon acute stimulation. Using a trans-acceleration protocol to force maximal LL extrusion, which involves the application of high doses of pyruvate, astrocytes showed decreased LL release when expressing LOX, LMO, or DLDH. On the other hand, in organotypic brainstem slices, only astrocytic expression of LOX resulted in significant reduction of LL release upon acute stimulation.

We further examined the effects of the expression of the genetically-encoded enzymatic tools on astrocytic metabolism. Since LL release is one of the factors that affect LDH-mediated LL production, we inhibited it in order to gain insight into LL and pyruvate handling by astrocytes expressing the novel molecular tools. Inhibition of LL release was performed by application of AR-C155858, which specifically blocks MCT1 in astrocytes. Importantly, AR-C155858 does not affect mitochondrial pyruvate uptake, in contrast to the broadly employed MCT inhibitor α-cyano-4-hydroxycinnamic (4-CIN) (Compan et al., 2015; Ovens et al., 2010). Blockade of pyruvate uptake by the mitochondria could potentially lead to increased glycolysis since oxidative phosphorylation of glucose would be impaired (Dienel, 2012; McKenna, Hopkins, & Carey, 2001). Although there is evidence for additional routes for LL extrusion from astrocytes (Karagiannis et al., 2015; Sotelo-Hitschfeld et al., 2015), MCTs are responsible for considerable LL transport across the astrocytic membrane under

steady-state conditions. In line with this, application of the MCT1 blocker AR-C155858 consistently increased intra-astrocytic LL concentration. Nonetheless, further increase in intracellular LL levels upon concomitant application of the MCT1 blocker with LL indicated that other LL transport pathways are present in astrocytes. Accumulation of LL in the astrocytic cytosol applies back-pressure on the LDH reaction until a new thermodynamic equilibrium is reached (Díaz-García & Yellen, 2019; Dienel, 2012).

Analysis of the rate of LL build-up showed no change in astrocytes expressing LOX or LMO, suggesting that the LDH reaction remains highly active when the enzymatic tools are expressed. However, surprisingly, the rate of pyruvate accumulation was decreased to the same extent in LOX- and LMO-expressing astrocytes, even though only LOX activity leads to additional pyruvate formation. This scenario led to speculation that there may be an increased drive towards LL formation in LOX or LMO expressing astrocytes which, in turn, slows down the rate of pyruvate accumulation. Such an increased LL production drive may be consistent with an alteration in LDH composition/activity due to compensation for the chronic LL sink imposed by LOX or LMO expression. In DLDH-expressing astrocytes, one factor that may contribute to the decreased rate of pyruvate build-up is the consumption of pyruvate by the DLDH enzymatic reaction. More experiments will be required to test these hypotheses, including the blockade of other specific metabolic processes, such LHD reaction, as well as detection of real-time fluctuations of cellular components that are closely involved in LL handling, such as NADH and NAD^+.

An additional strategy to limit LL actions in the brain refers to the partial inhibition of LL release from astrocytes. Since it has been shown that astrocytes release LL via connexin hemichannels (Karagiannis et al., 2015), we hypothesised that astrocyte-selective knock-down of Cx43, the major connexin type expressed by astrocytes, may contribute to the reduction of astrocytic LL release. A vector that drives the expression of three miRNAs that target different regions of Cx43 mRNA specifically in astrocytes was designed and constructed. However, when transduced in primary dissociated cultured astrocytes, the efficiency of Cx43 knock-down analysed at the protein level was minor. Preliminary results indicate that the Cx43 expression reduces proportionally to the time in which astrocytes were incubated with the Cx43 miRNA-carrying-AVV. This is a surprising result because Cx43 is known to be short lived,

exhibiting a quick turnover rate (Falk et al., 2016). Since the level of Cx43 expression did not considerably changed, no further characterization experiments were carried out using this tool.

7.2.1.1 Application of the novel molecular tools to inhibit L-lactate induced noradrenaline release

In order to investigate if the decreased intra-astrocytic LL pool or the release of DL by astrocytes expressing the novel molecular tools affect NA release, we employed a cell-based sensor for NA detection in LC organotypic slices (Muller et al., 2014). The same NA detection system, which translates noradrenergic volume transmission into fluorescence signals, has been previously used by our group and confirmed the prior finding obtained by fast-scan cyclic voltammetry, which is that LL evokes NA release from LC neurones (Mosienko et al., 2018). However, the challenge in the current project was to trigger selective release of LL or DL from the intra-astrocytic reservoir and assess if endogenous LL-driven NA release is different from the NA released following exogenous application of LL. Acute stimulation of LL release from the slice was triggered by the application of high doses of pyruvate (trans-acceleration). In slices whose astrocytes were expressing LOX, NA release triggered by pyruvate-driven LL extrusion was decreased as compared to the NA released following application of exogenous LL. On the other hand, neither LMO nor DLDH expression changed the amount of NA released by LC neurones.

7.2.2 Methodological considerations

In order to assess the functionality of the enzyme-based constructs, it was essential to induce intracellular LL depletion in cells. Since this is not possible using any known physiological stimulus, LL depletion has been achieved using the trans-acceleration protocol. One important caveat of the application of high doses of pyruvate to evoke LL release from astrocytes is the extreme nature of this stimulus, which does not directly reflect physiological LL efflux. Moreover, although application of high doses of pyruvate induces quick LL efflux, this effect comes at the expense of high

intracellular accumulation of pyruvate, which is directly involved in the pathways we are targeting with the expression of the enzyme-based tools. Accordingly, intracellular pyruvate can be converted to LL (and DL in the case of DLDH), which is broken down at different rates by LOX and LMO. In order to restrict LL formation following pyruvate application, glucose concentration in the superfusion buffer was reduced so that the generation of NADH through glycolysis was limited. Another issue with the trans-acceleration protocol in more complex brain tissue preparations such as organotypic brainstem slices is the non-selective nature of this stimulus. Many cells in the brain that are not targeted by the bacterial enzymes, such neurones and microglia, express MCTs, which would also contribute to the pyruvate-induced LL release. This may be the reason why in some experiments forced LL release was significantly decreased in dissociated astrocytes expressing the molecular tools but unchanged when measured in organotypic brainstem slices.

Moreover, trans-acceleration may not be the ideal approach to evoke DL release from astrocytes expressing DLDH in the assessment of LL-induced NA release in organotypic brainstem slices. Since DL affinity to MCTs is low, it seems likely that DL was not released from DLDH-expressing astrocytes in sufficient amounts, even with pyruvate-forced extrusion.

The validation experiments also required assessment of the glycolytic state of cells expressing the bacterial enzymes. However, it is highly complex to measure the dynamics of a variable that is in constant flux. LL is being constantly produced, released and catabolised. To make matters worse, blockade of one pathway can dynamically change other pathways. Blockade of MCT-mediated extrusion of LL, for example, drives by mass action LDH reaction towards pyruvate generation, which in turn impairs glycolysis (Dienel, 2018). LL formation, on the other hand, decreases pyruvate availability, which is an essential substrate of enzymatic reactions that ultimately lead to *de novo* synthesis of glutamate and GABA in astrocytes (Dienel, 2018). In the current study, we blocked MCTs in order to investigate the rate of intracellular LL and pyruvate accumulation. Nonetheless, we do not discard the possibility that other mechanisms related to LL flux may be changed due to the expression of the bacterial enzymes.

In vitro validation of the DLDH construct was hampered by the lack of technical means to directly measure DL dynamics in biological tissues. In fact, most of the results presented in my thesis report indirect effects of DLDH expression in astrocytes. Moreover, even though we successfully reported production and release of DL from astrocytes expressing DLDH, we proposed that improving astrocytic expression levels of DLDH would affect mechanisms in the brain that are sensitive to higher concentrations of DL as discussed below.

7.2.3 Future projections

Since LOX is the molecular tool that showed the most prominent results towards the decrease of LL release and action in the brain, this tool has been applied by our collaborators *in vivo* in the hippocampus and amygdala of mice in order to interrogate astrocyte-derived LL effects on behaviour patterns. Analysis of the morphology of cells expressing the reporter gene of the LVV driving LOX expression indicated predominant expression of the construct in astrocytes 4 weeks following LVV injections, indicating selective and long-lasting expression of the construct. Moreover, preliminary results showed that *in vivo* expression of LOX in astrocytes in the amygdala of mice enhanced anxiety-like behaviour. Therefore, LOX has potential to be employed *in vivo* in the study of the roles of astrocytic LL in the brain.

In order to enhance DLDH expression in astrocytes, our group is developing an AAV containing a ubiquitous promoter that drives the expression of a DLDH sequence flanked by Lox sites. This AAV will be used in a transgenic mouse in which Cre recombinase is regulated by the astrocyte-selective promoter Aldh1l1, resulting in selective expression of DLDH in astrocytes. Apart from antagonizing LL actions in noradrenergic neurones, DL has been suggested to act on other signalling pathways. Accordingly, DL was shown to decrease neuronal excitability through GPR81 activation with an EC_{50} value of approximately 3mM (Bozzo et al., 2013). Moreover, application of 4mM of DL has also been suggested to produce neuroprotective effects in ischemic models *in vitro* and *in vivo* (Castillo et al., 2015). Some researchers have also expressed interest in the utilization of an AAV for expression of LOX enzyme in a Cre/Lox system, which has already been constructed in our laboratory.

Overall, the genetically encoded LL-processing or DL-producing molecular tools show promise for future studies of the roles of astrocytic LL in the brain. LL-limiting tools represent a distinguishable approach to address many aspects of LL function in various physiological contexts. The viral vector-based molecular actuators, in particular LOX, decrease intra-astrocytic LL content and, consequently, LL release specifically from astrocytes. The selective nature of these tools is an essential requirement in the study of the metabolic compartmentalization of astrocytes and neurones. Moreover, these tools can be chronically expressed in the brain, changing LL dynamics at long-term, which has significant potential for the study of astrocyte-derived LL signalling.

Further arrangements in the vectors such as swapping of promoters can make these bacteria-derived enzymatic tools valuable in understanding the role of LL in other contexts such as in cancer cells, which have been extensively shown to favour LL formation (Ippolito, Morandi, Giannoni, & Chiarugi, 2019; Koppenol, Bounds, & Dang, 2011; Vander Heiden & DeBerardinis, 2017). To note, LMO may not be an ideal approach to be employed in this situation because the product of the reaction, acetate, is widely reported to be oxidized by cancer cells to be used as an additional energy substrate (Lin et al., 2018; Liu et al., 2018; Qiu et al., 2019).

7.3 Conclusion

In this thesis, I have described the development and functional validation of novel molecular tools to limit astrocyte-derived LL release and actions in the brain. As the ultimate goal, genetically encoded LL-processing or DL-producing microbial enzymes delivered selectively to astrocytes were designed to allow a better comprehension of the astrocytic function and its role in the regulation of neuronal activity. Application in different physiological contexts confirmed that these genetic tools, once expressed in mammalian cell lines, rat primary cultured astrocytes or cultured brainstem slices, are enzymatically active and change LL dynamics *in vitro*. Moreover, LL-limiting tools show potential for *in vivo* application in the study of LL roles in the metabolic and signalling coupling between astrocytes and neurones.

References

Agarwal, A., Wu, P. H., Hughes, E. G., Fukaya, M., Tischfield, M. A., Langseth, A. J., … Bergles, D. E. (2017). Transient Opening of the Mitochondrial Permeability Transition Pore Induces Microdomain Calcium Transients in Astrocyte Processes. *Neuron*, *93*(3), 587–605.e7. https://doi.org/10.1016/j.neuron.2016.12.034

Allen, N. J., & Lyons, D. A. (2018). Glia as architects of central nervous system formation and function. *Science*, *362*(6411), 181–185. https://doi.org/10.1126/science.aat0473

Ambros, V. (2004). The functions of animal microRNAs. *Nature*, *431*(7006), 350–355. https://doi.org/10.1038/nature02871

Amirache, F., Levy, C., Costa, C., Mangeot, P.-E., Torbett, B. E., Wang, C. X., … Verhoeyen, E. (2014). Mystery solved: VSV-G-LVs do not allow efficient gene transfer into unstimulated T cells, B cells, and HSCs because they lack the LDL receptor. *Blood*, *123*(9), 1422–1424.

Angelova, P. R., Kasymov, V., Christie, I., Sheikhbahaei, S., Turovsky, E., Marina, N., … Gourine, A. V. (2015). Functional oxygen sensitivity of astrocytes. *Journal of Neuroscience*, *35*(29), 10460–10473. https://doi.org/10.1523/JNEUROSCI.0045-15.2015

Aoki, C. (1992). Beta-adrenergic receptors: astrocytic localization in the adult visual cortex and their relation to catecholamine axon terminals as revealed by electron microscopic immunocytochemistry. *The Journal of Neuroscience*, *12*(3), 781–792. https://doi.org/10.1523/JNEUROSCI.12-03-00781.1992

Aoki, C., & Pickel, V. M. (1992). Ultrastructural relations between β-adrenergic receptors and catecholaminergic neurons. *Brain Research Bulletin*, *29*(3–4), 257–263. https://doi.org/10.1016/0361-9230(92)90055-3

Araque, A., Carmignoto, G., Haydon, P. G., Oliet, S. H. R., Robitaille, R., & Volterra, A. (2014). Gliotransmitters travel in time and space. *Neuron*, *81*(4), 728–739. https://doi.org/10.1016/j.neuron.2014.02.007

Aston-Jones, G., & Cohen, J. D. (2005). Adaptive gain and the role of the locus coeruleus-norepinephrine system in optimal performance. *The Journal of Comparative Neurology*, *493*(1), 99–110. https://doi.org/10.1002/cne.20723

Aston-Jones, G., Rajkowski, J., & Cohen, J. (1999). Role of locus coeruleus in attention and behavioral flexibility. *Biological Psychiatry*, *46*(9), 1309–1320. https://doi.org/10.1016/S0006-3223(99)00140-7

Bak, L. K., & Walls, A. B. (2018). CrossTalk opposing view: lack of evidence supporting an astrocyte-to-neuron lactate shuttle coupling neuronal activity to glucose utilisation in the brain. *Journal of Physiology*, *596*(3), 351–353. https://doi.org/10.1113/JP274945

Barros, L. F., Bolaños, J. P., Bonvento, G., Bouzier-Sore, A.-K., Brown, A., Hirrlinger, J., … Weber, B. (2017). Current technical approaches to brain energy metabolism. *Glia*, 1138–1159. https://doi.org/10.1002/glia.23248

Barros, L. F., & Weber, B. (2018). CrossTalk proposal: an important astrocyte-to-neuron lactate shuttle couples neuronal activity to glucose utilisation in the brain. *Journal of Physiology*, *596*(3), 347–350. https://doi.org/10.1113/JP274944

Bartel, D. P. (2004). MicroRNAs: Genomics, Biogenesis, Mechanism, and Function. *Cell*, *116*(2), 281–297. https://doi.org/10.1016/S0092-8674(04)00045-5

Bartel, D. P. (2009). MicroRNAs: Target Recognition and Regulatory Functions. *Cell*, *136*(2), 215–233. https://doi.org/10.1016/j.cell.2009.01.002

Bazargani, N., & Attwell, D. (2016). Astrocyte calcium signaling: The third wave. *Nature Neuroscience*, *19*(2), 182–189. https://doi.org/10.1038/nn.4201

Bekar, L. K., He, W., & Nedergaard, M. (2008). Locus Coeruleus -Adrenergic-Mediated Activation of Cortical Astrocytes In Vivo. *Cerebral Cortex*, *18*(12), 2789–2795. https://doi.org/10.1093/cercor/bhn040

Bélanger, M., Allaman, I., & Magistretti, P. J. (2011). Brain energy metabolism: Focus on Astrocyte-neuron metabolic cooperation. *Cell Metabolism*, *14*(6), 724–738. https://doi.org/10.1016/j.cmet.2011.08.016

Belanger, M., Yang, J., Petit, J., Laroche, T., Magistretti, P. J., & Allaman, I. (2011). Role of the Glyoxalase System in Astrocyte-Mediated, *31*(50), 18338–18352. https://doi.org/10.1523/JNEUROSCI.1249-11.2011

Benard, G., Bellance, N., Jose, C., & Rossignol, R. (2011). Relationships Between Mitochondrial Dynamics and Bioenergetics. In *Mitochondrial Dynamics and Neurodegeneration* (pp. 47–68). Dordrecht: Springer Netherlands. https://doi.org/10.1007/978-94-007-1291-1_2

Berg, J. M., Tymoczko, J. L., & Stryer, L. (2002). *Biochemistry* (Fifth edition). W. H. Freeman and Company.

Bergersen, L. H. (2015). Lactate transport and signaling in the brain: Potential therapeutic targets and roles in body-brain interaction. *Journal of Cerebral Blood Flow and Metabolism*, *35*(2), 176–185. https://doi.org/10.1038/jcbfm.2014.206

Berridge, C. W., & Waterhouse, B. D. (2003). The locus coeruleus–noradrenergic system: modulation of behavioral state and state-dependent cognitive processes. *Brain Research Reviews*, *42*(1), 33–84. https://doi.org/10.1016/S0165-0173(03)00143-7

Berridge, M. V., Herst, P. M., & Tan, A. S. (2005). Tetrazolium dyes as tools in cell biology: New insights into their cellular reduction (pp. 127–152). https://doi.org/10.1016/S1387-2656(05)11004-7

Berthoud, V. M., Minogue, P. J., Laing, J. G., & Beyer, E. C. (2004). Pathways for degradation of connexins and gap junctions. *Cardiovascular Research*, *62*(2), 256–267. https://doi.org/10.1016/j.cardiores.2003.12.021

Betley, J. N., & Sternson, S. M. (2011). Adeno-Associated Viral Vectors for Mapping, Monitoring, and Manipulating Neural Circuits. *Human Gene Therapy*, *22*(6), 669–677. https://doi.org/10.1089/hum.2010.204

Bett, A. J., Haddara, W., Prevec, L., & Graham, F. L. (1994). An efficient and flexible system for construction of adenovirus vectors with insertions or deletions in early regions 1 and 3. *Proceedings of the National Academy of Sciences of the United States of America*, *91*(19), 8802–8806. https://doi.org/10.1073/pnas.91.19.8802

Bewig, B., & Schmidt, W. E. (2000). Accelerated Titering of Adenoviruses. *BioTechniques*, *28*(5), 870–873. https://doi.org/10.2144/00285bm08

Bezzi, P., & Volterra, a. (2001). A neuron-glia signalling network in the active brain. *Current Opinion in Neurobiology*, *11*(3), 387–394. https://doi.org/10.1016/S0959-4388(00)00223-3

Bittar, P. G., Charnay, Y., Pellerin, L., Bouras, C., & Magistretti, P. J. (1996). Selective distribution of lactate dehydrogenase isoenzymes in neurons and astrocytes of human brain. *Journal of Cerebral Blood Flow and Metabolism*, *16*(6), 1079–1089. https://doi.org/10.1097/00004647-199611000-00001

Bolaños, J. P. (2016). Bioenergetics and redox adaptations of astrocytes to neuronal activity. *Journal of Neurochemistry*, *139*, 115–125. https://doi.org/10.1111/jnc.13486

Bozzo, L., Puyal, J., & Chatton, J.-Y. (2013). Lactate Modulates the Activity of Primary Cortical Neurons through a Receptor-Mediated Pathway. *PLoS ONE*, *8*(8), e71721. https://doi.org/10.1371/journal.pone.0071721

Brenner, M., Kisseberth, W. C., Su, Y., Besnard, F., & Messing, A. (1994). GFAP promoter directs astrocyte-specific expression in transgenic mice. *The Journal of Neuroscience*, *14*(3), 1030–1037. https://doi.org/10.1523/JNEUROSCI.14-03-01030.1994

Bröer, S., Bröer, A., Schneider, H.-P., Stegen, C., Halestrap, A. P., & Deitmer, J. W. (1999). Characterization of the high-affinity monocarboxylate transporter MCT2 in *Xenopus laevis oocytes*. *Biochemical Journal*, *341*(3), 529. https://doi.org/10.1042/0264-6021:3410529

Bröer, S., Schneider, H.-P., Bröer, A., Rahman, B., Hamprecht, B., & Deitmer, J. W. (1998). Characterization of the monocarboxylate transporter 1 expressed in *Xenopus laevis oocytes* by changes in cytosolic pH. *Biochemical Journal*, *174*, 167–174.

Bucher, E. S., & Wightman, R. M. (2015). Electrochemical Analysis of Neurotransmitters. *Annual Review of Analytical Chemistry*, *8*(1), 239–261. https://doi.org/10.1146/annurev-anchem-071114-040426

Cai, T., Ren, N., Jin, L., Cheng, K., Kash, S., Chen, R., … Waters, M. G. (2008). Role of GPR81 in lactate-mediated reduction of adipose lipolysis. *Biochemical and Biophysical Research Communications*, *377*(3), 987–991. https://doi.org/10.1016/j.bbrc.2008.10.088

Calì, C., Baghabra, J., Boges, D. J., Holst, G. R., Kreshuk, A., Hamprecht, F. A., … Magistretti, P. J. (2016). Three-dimensional immersive virtual reality for studying cellular compartments in 3D models from EM preparations of neural tissues. *Journal of Comparative Neurology*, *524*(1), 23–38. https://doi.org/10.1002/cne.23852

Carpenter, L., & Halestrap, A. P. (1994). The kinetics, substrate and inhibitor specificity of the lactate transporter of Ehrlich-Lettre tumour cells studied with the intracellular pH indicator BCECF. *The Biochemical Journal*, *304 (Pt 3*, 751–760. https://doi.org/10.1002/rra

Carter, M. E., Yizhar, O., Chikahisa, S., Nguyen, H., Adamantidis, A., Nishino, S., … De Lecea, L. (2010). Tuning arousal with optogenetic modulation of locus coeruleus neurons. *Nature Neuroscience*, *13*(12), 1526–1535. https://doi.org/10.1038/nn.2682

Castillo, X., Rosafio, K., Wyss, M. T., Drandarov, K., Buck, A., Pellerin, L., … Hirt, L. (2015). A probable dual mode of action for both L- and D-lactate neuroprotection in cerebral ischemia. *Journal of Cerebral Blood Flow & Metabolism*, (April), 1–9. https://doi.org/10.1038/jcbfm.2015.115

Chai, H., Diaz-Castro, B., Shigetomi, E., Monte, E., Octeau, J. C., Yu, X., … Khakh, B. S. (2017). Neural Circuit-Specialized Astrocytes: Transcriptomic, Proteomic, Morphological, and Functional Evidence. *Neuron*, *95*(3), 531–549.e9. https://doi.org/10.1016/j.neuron.2017.06.029

Chang, A. J., Ortega, F. E., Riegler, J., Madison, D. V, & Krasnow, M. A. (2015). Oxygen control of breathing by an olfactory receptor activated by lactate. *Nature*, *527*(7577), 240–244. https://doi.org/10.1038/nature15721

Cheeseman, A. J., & Clark, J. B. (1988). Influence of the Malate-Aspartate Shuttle on Oxidative Metabolism in Synaptosomes. *Journal of Neurochemistry*, *50*(5), 1559–1565. https://doi.org/10.1111/j.1471-4159.1988.tb03044.x

Chenal, J., & Pellerin, L. (2007). Noradrenaline enhances the expression of the neuronal monocarboxylate transporter MCT2 by translational activation via stimulation of PI3K/Akt and the mTOR/S6K pathway. *Journal of Neurochemistry*, *102*(2), 389–397. https://doi.org/10.1111/j.1471-4159.2007.04495.x

Chenal, J., Pierre, K., & Pellerin, L. (2007). Insulin and IGF-1 enhance the expression of the neuronal monocarboxylate transporter MCT2 by translational activation via stimulation of the phosphoinositide 3-kinase-Akt-mammalian target of rapamycin pathway. *European Journal of Neuroscience*, *27*(1), 53–65. https://doi.org/10.1111/j.1460-9568.2007.05981.x

Chiti, Z., & Teschemacher, A. G. (2007). Exocytosis of norepinephrine at axon varicosities and neuronal cell bodies in the rat brain. *The FASEB Journal*, *21*(10), 2540–2550. https://doi.org/10.1096/fj.06-7342com

Chojnacki, A. K., Mak, G. K., & Weiss, S. (2009). Identity crisis for adult periventricular neural stem cells: subventricular zone astrocytes, ependymal cells or both? *Nature Reviews Neuroscience*, *10*(2), 153–163. https://doi.org/10.1038/nrn2571

Christopher, M. M., Broussard, J. D., Fallin, C. W., Drost, N. J., & Peterson, M. E. (1995). Increased serum d-lactate associated with diabetic ketoacidosis. *Metabolism Clinical and Experimental*, *44*(3), 287–290.

Clasadonte, J., Scemes, E., Wang, Z., Boison, D., & Haydon, P. G. (2017). Connexin 43-Mediated Astroglial Metabolic Networks Contribute to the Regulation of the Sleep- Connexin 43-Mediated Astroglial Metabolic Networks Contribute to the Regulation of the Sleep-Wake Cycle. *Neuron*, 1–16. https://doi.org/10.1016/j.neuron.2017.08.022

Coleman, J. E., Huentelman, M. J., Kasparov, S., Metcalfe, B. L., Paton, J. F. R., Katovich, M. J., … Raizada, M. K. (2003). Efficient large-scale production and concentration of HIV-1-based lentiviral vectors for use in vivo. *Physiological Genomics*, *12*(3), 221–228. https://doi.org/10.1152/physiolgenomics.00135.2002

Compan, V., Pierredon, S., Vanderperre, B., Krznar, P., Marchiq, I., Zamboni, N., … Martinou, J. C. (2015). Monitoring Mitochondrial Pyruvate Carrier Activity in Real Time Using a BRET-Based Biosensor: Investigation of the Warburg Effect. *Molecular Cell*, *59*(3), 491–501. https://doi.org/10.1016/j.molcel.2015.06.035

Condorelli, D. F., Trovato-Salinaro, A., Mudò, G., Mirone, M. B., & Belluardo, N. (2003). Cellular expression of connexins in the rat brain: Neuronal localization, effects of kainate-induced seizures and expression in apoptotic neuronal cells. *European Journal of Neuroscience*, *18*(7), 1807–1827. https://doi.org/10.1046/j.1460-9568.2003.02910.x

Contreras, J. E., Sanchez, H. A., Eugenin, E. A., Speidel, D., Theis, M., Willecke, K., … Saez, J. C. (2002). Metabolic inhibition induces opening of unapposed connexin 43 gap junction hemichannels and reduces gap junctional communication in cortical astrocytes in culture. *Proceedings of the National Academy of Sciences*, *99*(1), 495–500. https://doi.org/10.1073/pnas.012589799

Crow, M. T. (1982). Chemical energetics of slow- and fast-twitch muscles of the mouse. *The Journal of General Physiology*, *79*(1), 147–166. https://doi.org/10.1085/jgp.79.1.147

D'Ascenzo, M., Fellin, T., Terunuma, M., Revilla-Sanchez, R., Meaney, D. F., Auberson, Y. P., … Haydon, P. G. (2007). mGluR5 stimulates gliotransmission in the nucleus accumbens. *Proceedings of the National Academy of Sciences of the United States of America*, *104*(6), 1995–2000. https://doi.org/10.1073/pnas.0609408104

Dale, N., Pearson, T., & Frenguelli, B. G. (2000). Direct measurement of adenosine release during hypoxia in the CA1 region of the rat hippocampal slice. *The Journal of Physiology*, *526*(1), 143–155. https://doi.org/10.1111/j.1469-7793.2000.00143.x

de Bari, L., Atlante, A., Guaragnella, N., Principato, G., & Passarella, S. (2002). D-Lactate transport and metabolism in rat liver mitochondria. *Biochemical Journal*, *365*(2), 391–403. https://doi.org/10.1042/bj20020139

de Bari, L., Moro, L., & Passarella, S. (2013). Prostate cancer cells metabolize D-lactate inside mitochondria via a D-lactate dehydrogenase which is more active and highly expressed than in normal cells. *FEBS Letters*, *587*(5), 467–473. https://doi.org/10.1016/j.febslet.2013.01.011

de Bari, L., Valenti, D., Atlante, A., & Passarella, S. (2010). L-Lactate generates hydrogen peroxide in purified rat liver mitochondria due to the putative L-lactate oxidase localized in the intermembrane space. *FEBS Letters*, *584*(11), 2285–2290. https://doi.org/10.1016/j.febslet.2010.03.038

de Castro Abrantes, H., Briquet, M., Schmuziger, C., Restivo, L., Puyal, J., Rosenberg, N., … Chatton, J.-Y. (2019). The lactate receptor HCAR1 modulates neuronal network activity through the activation of G α and G β ɣ subunits . *The Journal of Neuroscience*, *39*(23), 2092–18. https://doi.org/10.1523/jneurosci.2092-18.2019

Delvaeye, T., Vandenabeele, P., Bultynck, G., Leybaert, L., & Krysko, D. V. (2018). Therapeutic Targeting of Connexin Channels: New Views and Challenges. *Trends in Molecular Medicine*, *24*(12), 1036–1053. https://doi.org/10.1016/j.molmed.2018.10.005

Dermietzel, R., Hertberg, E. L., Kessler, J. A., & Spray, D. C. (1991). Gap junctions between cultured astrocytes: immunocytochemical, molecular, and electrophysiological analysis. *The Journal of Neuroscience*, *11*(5), 1421–1432.

Desguin, B., Goffin, P., Viaene, E., Kleerebezem, M., Martin-diaconescu, V., Maroney, M. J., … Hols, P. (2014). Lactate racemase is a nickel-dependent enzyme activated by a widespread maturation system. *Nature Communications*. https://doi.org/10.1038/ncomms4615

Di Castro, M. A., Chuquet, J., Liaudet, N., Bhaukaurally, K., Santello, M., Bouvier, D., … Volterra, A. (2011). Local Ca2+ detection and modulation of synaptic release by astrocytes. *Nature Neuroscience*, *14*(10), 1276–1284. https://doi.org/10.1038/nn.2929

Díaz-García, C. M., & Yellen, G. (2019). Neurons rely on glucose rather than astrocytic lactate during stimulation. *Journal of Neuroscience Research*, *97*(8), 883–889. https://doi.org/10.1002/jnr.24374

Dienel, G. A. (2012). Fueling and imaging brain activation. *Asn Neuro*, *4*(5), 267–321. https://doi.org/10.1042/AN20120021

Dienel, G. A. (2017). Lack of appropriate stoichiometry: Strong evidence against an energetically important astrocyte-neuron lactate shuttle in brain. *Journal of Neuroscience Research*, *95*(11), 2103–2125. https://doi.org/10.1002/jnr.24015

Dienel, G. A. (2018). Brain Glucose Metabolism: Integration of Energetics with Function. *Physiological Reviews*, *99*(1), 949–1045. https://doi.org/10.1152/physrev.00062.2017

Dienel, G. A., & Cruz, N. F. (2006). Astrocyte activation in working brain: Energy supplied by minor substrates. *Neurochemistry International*, *48*(6–7), 586–595. https://doi.org/10.1016/j.neuint.2006.01.004

Dienel, G. A., & Cruz, N. F. (2016). Aerobic glycolysis during brain activation: adrenergic regulation and influence of norepinephrine on astrocytic metabolism. *Journal of Neurochemistry*, 14–52. https://doi.org/10.1111/jnc.13630

Dimmer, K.-S., Friedrich, B., Lang, F., Deitmer, J. W., & Bröer, S. (2000). The low-affinity monocarboxylate transporter MCT4 is adapted to the export of lactate in highly glycolytic cells. *Biochemical Journal*, *350*(1), 219. https://doi.org/10.1042/0264-6021:3500219

Dıaz-Garcıa, C. M., Mongeon, R., Lahmann, C., Koveal, D., Zucker, H., & Yellen, G. (2017). Neuronal Stimulation Triggers Neuronal Glycolysis and Not Lactate Uptake Article Neuronal Stimulation Triggers Neuronal Glycolysis and Not Lactate Uptake, 361–374. https://doi.org/10.1016/j.cmet.2017.06.021

Doengi, M., Deitmer, J. W., & Lohr, C. (2008). New evidence for purinergic signaling in the olfactory bulb: A 2A and P2Y 1 receptors mediate intracellular calcium release in astrocytes. *The FASEB Journal*, *22*(7), 2368–2378. https://doi.org/10.1096/fj.07-101782

Doetsch, F., Caillé, I., Lim, D. A., García-Verdugo, J. M., & Alvarez-Buylla, A. (1999). Subventricular Zone Astrocytes Are Neural Stem Cells in the Adult Mammalian Brain. *Cell*, *97*(6), 703–716. https://doi.org/10.1016/S0092-8674(00)80783-7

Dringen, R., Brandmann, M., Hohnholt, M. C., & Blumrich, E. M. (2015). Glutathione-Dependent Detoxification Processes in Astrocytes. *Neurochemical Research*, *40*(12), 2570–2582. https://doi.org/10.1007/s11064-014-1481-1

Dringen, R., Kussmaul, L., Gutterer, J. M., Hirrlinger, J., & Hamprecht, B. (1999). The Glutathione System of Peroxide Detoxification Is Less Efficient in Neurons than in Astroglial Cells. *Journal of Neurochemistry*, *72*(6), 2523–2530. https://doi.org/10.1046/j.1471-4159.1999.0722523.x

Duale, H., Waki, H., Howorth, P., Kasparov, S., Teschemacher, A., & Paton, J. (2007). Restraining influence of A2 neurons in chronic control of arterial pressure in spontaneously hypertensive rats. *Cardiovascular Research*, *76*(1), 184–193. https://doi.org/10.1016/j.cardiores.2007.06.018

Duan, D., Sharma, P., Yang, J., Yue, Y., Dudus, L., Zhang, Y., … Engelhardt, J. F. (1998). Circular intermediates of recombinant adeno-associated virus have defined structural characteristics responsible for long-term episomal persistence in muscle tissue. *Journal of Virology*, *72*(11), 8568–8577. https://doi.org/10.1128/jvi.75.15.6969-6976.2001

El-Brolosy, M. A., & Stainier, D. Y. R. (2017). Genetic compensation: A phenomenon in search of mechanisms. *PLoS Genetics*, *13*(7), 1–17. https://doi.org/10.1371/journal.pgen.1006780

Esseltine, J. L., & Laird, D. W. (2016). Next-Generation Connexin and Pannexin Cell Biology. *Trends in Cell Biology*, *26*(12), 944–955. https://doi.org/10.1016/j.tcb.2016.06.003

Ewaschuk, J. B., Naylor, J. M., & Zello, G. A. (2005). Critical Review D -Lactate in Human and Ruminant Metabolism, (March), 1619–1625.

Falk, M. M., Bell, C. L., Kells Andrews, R. M., & Murray, S. A. (2016). Molecular mechanisms regulating formation, trafficking and processing of annular gap junctions. *BMC Cell Biology*, *17*(S1), S22. https://doi.org/10.1186/s12860-016-0087-7

Ferain, T., Garmyn, D., Bernard, N., Hols, P., & Delcour, A. J. (1994). Lactobacillus plantarum ldhL Gene : Overexpression and Deletion, *176*(3), 596–601.

Ferain, T., Hobbs, J. N., Richardson, J., Bernard, N., Garmyn, D., Hols, P., … Delcour, J. (1996). Knockout of the Two ldh Genes Has a Major Impact on Peptidoglycan Precursor Synthesis in Lactobacillus plantarum, *178*(18), 5431–5437.

Fernandez-Fernandez, S., Almeida, A., & Bolaños, J. P. (2012). Antioxidant and bioenergetic coupling between neurons and astrocytes. *Biochemical Journal*, *443*(1), 3–11. https://doi.org/10.1042/bj20111943

Fernández-moncada, I., Ruminot, I., Robles-maldonado, D., Alegría, K., & Deitmer, J. W. (2018). Neuronal control of astrocytic respiration through a variant of the Crabtree effect, *115*(7), 1623–1628. https://doi.org/10.1073/pnas.1716469115

Fiacco, T. A., & McCarthy, K. D. (2018). Multiple Lines of Evidence Indicate That Gliotransmission Does Not Occur under Physiological Conditions. *The Journal of Neuroscience*, *38*(1), 3–13. https://doi.org/10.1523/jneurosci.0016-17.2017

Fire, A., Xu, S., Montgomery, M. K., Kostas, S. A., Driver, S. E., & Mello, C. C. (1998). Potent and specific genetic interference by double-stranded RNA in Caenorhabditis elegans. *Nature*, *391*(6669), 806–811. https://doi.org/10.1038/35888

Fisenne, I. M., Razewsky, B., Hantke, H. J., Kologrov, R., Kulp, J. L., Queen, F. B., … Bean, H. W. (1961). Lactate Dehydrogenase Isozymes: Dissociation and Recombination of Subunit, *113*, 2–3.

Fishbein, W. N., Foellmer, J. W., Davis, J. I., Fishbein, T. M., & Armbrustmacher, A. P. (1988). Clinical Assay of the Human Erythrocyte Lactate Transporter. *BIOCHEMICAL MEDICINE AND METABOLIC BIOLOGY*, *39*, 338–350.

Flick, M. J., & Konieczny, S. F. (2002). Identification of putative mammalian D-lactate dehydrogenase enzymes. *Biochemical and Biophysical Research Communications*, *295*(4), 910–916.

Fox, P., Raichle, M., Mintun, M., & Dence, C. (1988). Nonoxidative glucose consumption during focal physiologic neural activity. *Science*, *241*(4864), 462–464. https://doi.org/10.1126/science.3260686

Furuichi, M., Suzuki, N., Dhakshnamoorhty, B., Minagawa, H., Yamagishi, R., Watanabe, Y., … Mizuno, H. (2008). X-ray Structures of Aerococcus viridans Lactate Oxidase and Its Complex with D -Lactate at pH 4 . 5 Show an α - Hydroxyacid Oxidation Mechanism, 436–446. https://doi.org/10.1016/j.jmb.2008.02.062

Fuxe, K., Agnati, L. F., Marcoli, M., & Borroto-Escuela, D. O. (2015). Volume Transmission in Central Dopamine and Noradrenaline Neurons and Its Astroglial Targets. *Neurochemical Research*, 2600–2614. https://doi.org/10.1007/s11064-015-1574-5

Gao, V., Suzuki, A., Magistretti, P. J., Lengacher, S., Pollonini, G., Steinman, M. Q., & Alberini, C. M. (2016). Astrocytic β2-adrenergic receptors mediate hippocampal long-term memory consolidation. *Proceedings of the National Academy of Sciences*, *113*(30), 8526–8531. https://doi.org/10.1073/pnas.1605063113

Garcia, C. K., Goldstein, J. L., Pathak, R. K., Anderson, R. G. W., & Brown, M. S. (1994). Molecular Characterization of a Membrane Transporter for Lactate, Pyruvate, and Other Monocarboxylates: Implications for the Cori Cycle. *Cell*, *76*, 665–673.

Gebert, L. F. R., & MacRae, I. J. (2019). Regulation of microRNA function in animals. *Nature Reviews Molecular Cell Biology*, *20*(1), 21–37. https://doi.org/10.1038/s41580-018-0045-7

Giaume, C., Koulakoff, A., Roux, L., Holcman, D., & Rouach, N. (2010). Astroglial networks: A step further in neuroglial and gliovascular interactions. *Nature Reviews Neuroscience*, *11*(2), 87–99. https://doi.org/10.1038/nrn2757

Giaume, C., Leybaert, L., Naus, C. C., & Sáez, J. C. (2013). Connexin and pannexin hemichannels in brain glial cells: Properties, pharmacology, and roles. *Frontiers in Pharmacology*, *4*(July), 1–17. https://doi.org/10.3389/fphar.2013.00088

Goffin, P., Deghorain, M., Mainardi, J., Tytgat, I., Champomier-Verges, M. C., Kleerebezem, M., & Hols, P. (2005). Lactate Racemization as a Rescue Pathway for Supplying D -Lactate to the Cell Wall Biosynthesis Machinery in *Lactobacillus plantarum*. Journal of Bacteriology, *187*(19), 6750–6761. https://doi.org/10.1128/JB.187.19.6750-6761.2005

Gourine, A. V., Dale, N., Korsak, A., Llaudet, E., Tian, F., Huckstepp, R., & Spyer, K. M. (2008). Release of ATP and glutamate in the nucleus tractus solitarii mediate pulmonary stretch receptor (Breuer-Hering) reflex pathway. *The Journal of Physiology*, *586*(16), 3963–3978. https://doi.org/10.1113/jphysiol.2008.154567

Gourine, A. V., & Funk, G. D. (2017). On the existence of a central respiratory oxygen sensor. *Journal of Applied Physiology (Bethesda, Md.: 1985)*, *123*(5), 1344–1349. https://doi.org/10.1152/japplphysiol.00194.2017

Gourine, A. V, Kasymov, V., Marina, N., Tang, F., Figueiredo, M. F., Lane, S., … Kasparov, S. (2010). Astrocytes control breathing through pH-dependent release of ATP. *Science*, *329*(5991), 571–575. https://doi.org/10.1126/science.1190721

Graham, F. L., & Prevec, L. (1995). Methods for construction of adenovirus vectors. *Molecular Biotechnology*, *3*, 207–220. https://doi.org/10.1007/BF02789331

Grimm, D. (2002). Production methods for gene transfer vectors based on adeno-associated virus serotypes. *Methods*, *28*(2), 146–157. https://doi.org/10.1016/S1046-2023(02)00219-0

Ha, M., & Kim, V. N. (2014). Regulation of microRNA biogenesis. *Nature Reviews Molecular Cell Biology*, *15*(8), 509–524. https://doi.org/10.1038/nrm3838

Halestrap, A. P. (1976). Transport of pyruvate and lactate into human erythrocytes. Evidence for the involvement of the chloride carrier and a chloride-independent carrier. *The Biochemical Journal*, *156*(2), 193–207. https://doi.org/10.1042/bj1560193

Halestrap, A. P. (2011). Monocarboxylic Acid Transport. In *Comprehensive Physiology* (Vol. 3, pp. 1611–1643). https://doi.org/10.1002/cphy.c130008

Halestrap, A. P., & Denton, R. M. (1974). Specific inhibition of pyruvate transport in rat liver mitochondria and human erythrocytes by α-cyano-4-hydroxycinnamate. *Biochemical Journal*, *138*(2), 313–316. https://doi.org/10.1042/bj1380313

Halestrap, A. P., & Price, N. T. (1999). The proton-linked monocarboxylate transporter (MCT) family: structure, function and regulation. *Biochemical Journal*, *343*(2), 281–299. https://doi.org/10.1042/bj3430281

Halestrap, A. P., & Wilson, M. C. (2012). The monocarboxylate transporter family-Role and regulation. *IUBMB Life*, *64*(2), 109–119. https://doi.org/10.1002/iub.572

Halim, N. D., Mcfate, T., Mohyeldin, A., Okagaki, P., Korotchkina, L. G., Patel, M. S., … Verma, A. (2010). Phosphorylation status of pyruvate dehydrogenase distinguishes metabolic phenotypes of cultured rat brain astrocytes and neurons. *Glia*, *58*(10), 1168–1176. https://doi.org/10.1002/glia.20996

Harris, A. L. (2007). Connexin Channel Permeability to Cytoplasmic Molecules. *Progress in Biophysics and Molecular Biology*, *94(1-2)*, 120–143. https://doi.org/10.1016/j.pbiomolbio.2007.03.011

Haustein, M. D., Kracun, S., Lu, X. H., Shih, T., Jackson-Weaver, O., Tong, X., … Khakh, B. S. (2014). Conditions and constraints for astrocyte calcium signaling in the hippocampal mossy fiber pathway. *Neuron*, *82*(2), 413–429. https://doi.org/10.1016/j.neuron.2014.02.041

Herrero-Mendez, A., Almeida, A., Fernández, E., Maestre, C., Moncada, S., & Bolaños, J. P. (2009). The bioenergetic and antioxidant status of neurons is controlled by continuous degradation of a key glycolytic enzyme by APC/C-Cdh1. *Nature Cell Biology*, *11*(6), 747–752. https://doi.org/10.1038/ncb1881

Hertz, L., Chen, Y., Gibbs, M. E., Zang, P., & Peng, L. (2004). Astrocytic adrenoceptors: a major drug target in neurological and psychiatric disorders? *Current Drug Targets. CNS and Neurological Disorders*, *3*, 239–267. https://doi.org/10.2174/1568007043337535

Hertz, L., Xu, J., Song, D., Du, T., Li, B., Yan, E., & Peng, L. (2015). Astrocytic glycogenolysis: mechanisms and functions. *Metabolic Brain Disease*, *30*(1), 317–333. https://doi.org/10.1007/s11011-014-9536-1

Hewinson, J., Paton, J. F. R., & Kasparov, S. (2013). Viral Gene Delivery: Optimized Protocol for Production of High Titer Lentiviral Vectors (pp. 65–75). https://doi.org/10.1007/978-1-62703-351-0_5

Hinckelmann, M.-V., Virlogeux, A., Niehage, C., Poujol, C., Choquet, D., Hoflack, B., … Saudou, F. (2016). Self-propelling vesicles define glycolysis as the minimal energy machinery for neuronal transport. *Nature Communications*, *7*(1), 13233. https://doi.org/10.1038/ncomms13233

Hiraka, K., Kojima, K., Lin, C. E., Tsugawa, W., Asano, R., La Belle, J. T., & Sode, K. (2018). Minimizing the effects of oxygen interference on L-lactate sensors by a single amino acid mutation in Aerococcus viridans L-lactate oxidase. *Biosensors and Bioelectronics*, *103*(December 2017), 163–170. https://doi.org/10.1016/j.bios.2017.12.018

Hofer, A., & Dermietzel, R. (1998). Visualization and functional blocking of gap junction hemichannels (connexons) with antibodies against external loop domains in astrocytes. *Glia*, *24*(1), 141–154. https://doi.org/10.1002/(SICI)1098-1136(199809)24:1<141::AID-GLIA13>3.0.CO;2-R

Holets, V. R., Hökfelt, T., Rökaeus, Å., Terenius, L., & Goldstein, M. (1988). Locus coeruleus neurons in the rat containing neuropeptide Y, tyrosine hydroxylase or galanin and their efferent projections to the spinal cord, cerebral cortex and hypothalamus. *Neuroscience*, 24(3), 893–906. https://doi.org/10.1016/0306-4522(88)90076-0

Huang, Y., You, C., & Liu, Z. (2017). Cloning of d-lactate dehydrogenase genes of Lactobacillus delbrueckii subsp. bulgaricus and their roles in d-lactic acid production. *3 Biotech*, *7*(3), 1–7. https://doi.org/10.1007/s13205-017-0822-6

Hung, Y. P., Albeck, J. G., Tantama, M., & Yellen, G. (2011). Imaging Cytosolic NADH-NAD + Redox State with a Genetically Encoded Fluorescent Biosensor. *Cell Metabolism*, *14*(4), 545–554. https://doi.org/10.1016/j.cmet.2011.08.012

Hung, Y. P., & Yellen, G. (2014). Live cell imaging of cytosolic NADH-NAD+ redox state using a genetically encoded fluorescent biosensor. *Investigative Ophthalmology and Visual Science*, *1071*, 83–95. https://doi.org/10.1007/978-1-62703-622-1

Hwang, D.-Y., Carlezon, W. A., Isacson, O., & Kim, K.-S. (2001). A High-Efficiency Synthetic Promoter That Drives Transgene Expression Selectively in Noradrenergic Neurons. *Human Gene Therapy*, *12*(14), 1731–1740. https://doi.org/10.1089/104303401750476230

Hyzinski-García, M. C., Rudkouskaya, A., & Mongin, A. A. (2014). LRRC8A protein is indispensable for swelling-activated and ATP-induced release of excitatory amino acids in rat astrocytes. *Journal of Physiology*, *592*(22), 4855–4862. https://doi.org/10.1113/jphysiol.2014.278887

Iacobas, D. A., Iacobas, S., Urban-Maldonado, M., Scemes, E., & Spray, D. C. (2008). Similar Transcriptomic Alterations in Cx43 Knockdown and Knockout Astrocytes. *Cell Communication & Adhesion*, *15*(1–2), 195–206. https://doi.org/10.1080/15419060802014222

Ippolito, L., Morandi, A., Giannoni, E., & Chiarugi, P. (2019). Lactate: A Metabolic Driver in the Tumour Landscape. *Trends in Biochemical Sciences*, *44*(2), 153–166. https://doi.org/10.1016/j.tibs.2018.10.011

Jang, S. K., Kräusslich, H. G., Nicklin, M. J., Duke, G. M., Palmenberg, A. C., & Wimmer, E. (1988). A segment of the 5' nontranslated region of encephalomyocarditis virus RNA directs internal entry of ribosomes during in vitro translation. *Journal of Virology*, *62*(8), 2636–2643. Retrieved from http://www.ncbi.nlm.nih.gov/pubmed/2839690%0Ahttp://www.pubmedcentral.nih.gov/articlerender.fcgi?artid=PMC253694

Jones, G. A., & Bradshaw, D. S. (2019). Resonance Energy Transfer: From Fundamental Theory to Recent Applications. *Frontiers in Physics*, *7*(July), 1–19. https://doi.org/10.3389/fphy.2019.00100

Jurič, D. M., Lončar, D., & Čarman-Kržan, M. (2008). Noradrenergic stimulation of BDNF synthesis in astrocytes: Mediation via α1- and β1/β2-adrenergic receptors. *Neurochemistry International*, *52*(1), 297–306. https://doi.org/10.1016/j.neuint.2007.06.035

Karagiannis, A., Sylantyev, S., Hadjihambi, A., Hosford, P. S., Kasparov, S., & Gourine, A. V. (2015). Hemichannel-mediated release of lactate. *Journal of Cerebral Blood Flow & Metabolism*, 36(7), 1202–1211. https://doi.org/10.1177/0271678X15611912

Kasparov, S. (2016). Are Astrocytes the Pressure-Reservoirs of Lactate in the Brain? *Cell Metabolism*, *23*(1), 1–2. https://doi.org/10.1016/j.cmet.2015.11.001

Kasparov, S., & Teschemacher, A. G. (2008). Altered central catecholaminergic transmission and cardiovascular disease. *Experimental Physiology*, *93*(6), 725–740. https://doi.org/10.1113/expphysiol.2007.041814

Kasparov, S., Teschemacher, A. G., Hwang, D.-Y., Kim, K.-S., Lonergan, T., & Paton, J. F. R. (2004). Viral vectors as tools for studies of central cardiovascular control. *Progress in Biophysics and Molecular Biology*, *84*(2–3), 251–277. https://doi.org/10.1016/j.pbiomolbio.2003.11.011

Kaufman, R. J., Davies, M. V., Wasley, L. C., & Michnick, D. (1991). Improved vectors for stable expression of foreign genes in mammalian cells by use of the untranslated leader sequence from EMC virus. *Nucleic Acids Research*, *19*(16), 4485–4490. https://doi.org/10.1093/nar/19.16.4485

Kay, M. A., Glorioso, J. C., & Naldini, L. (2001). Viral vectors for gene therapy: the art of turning infectious agents into vehicles of therapeutics. *Nature Medicine*, *7*, 33–40. https://doi.org/10.1038/83324

Khakh, B. S., & Deneen, B. (2019). The Emerging Nature of Astrocyte Diversity. *Annual Review of Neuroscience*, *42*(1), 187–207. https://doi.org/10.1146/annurev-neuro-070918-050443

Khakh, B. S., & Sofroniew, M. V. (2017). Diversity of astrocyte functions and phenotypes in neural circuits Introduction and historical perspective, *18*(7), 942–952. https://doi.org/10.1038/nn.4043

Khan, Z. U., Koulen, P., Rubinstein, M., Grandy, D. K., & Goldman-Rakic, P. S. (2001). An astroglia-linked dopamine D2-receptor action in prefrontal cortex. *Proceedings of the National Academy of Sciences*, *98*(4), 1964–1969. https://doi.org/10.1073/pnas.98.4.1964

Kimelberg, H. K., MacVicar, B. A., & Sontheimer, H. (2006). Anion channels in astrocytes: Biophysics, pharmacology, and function. *Glia*, *54*(7), 747–757. https://doi.org/10.1002/glia.20423

Koizumi, N., Kawabata, K., Sakurai, F., & Watanabe, Y. (2006). Modified Adenoviral Vectors Ablated for Coxsackievirus–Adenovirus Receptor, av Integrin, and Heparan Sulfate Binding Reduce In Vivo Tissue Transduction and Toxicity. *Human Gene Therapy*, *279*(March), 264–279.

Kondoh, Y., Kawase, M., Kawakami, Y., & Ohmori, S. (1992). Concentrations of D-lactate and its related metabolic intermediates in liver, blood, and muscle of diabetic and starved rats. *Experimental Medicine*, *192*, 407–414.

Koppenol, W. H., Bounds, P. L., & Dang, C. V. (2011). Otto Warburg's contributions to current concepts of cancer metabolism. *Nature Reviews Cancer*, *11*(5), 325–337. https://doi.org/10.1038/nrc3038

Latour, I., Gee, C. E., Robitaille, R., & Lacaille, J.-C. (2001). Differential mechanisms of Ca2+ responses in glial cells evoked by exogenous and endogenous glutamate in rat hippocampus. *Hippocampus*, *11*(2), 132–145. https://doi.org/10.1002/hipo.1031

Laughton, J. D., Charnay, Y., Belloir, B., Pellerin, L., Magistretti, P. J., & Bouras, C. (2000). Differential messenger RNA distribution of lactate dehydrogenase LDH-1 and LDH-5 isoforms in the rat brain. *Neuroscience*, *96*(3), 619–625. https://doi.org/10.1016/S0306-4522(99)00580-1

Lauritzen, K. H., Morland, C., Puchades, M., Holm-hansen, S., Hagelin, E. M., Lauritzen, F., … Bergersen, L. H. (2014). Lactate Receptor Sites Link Neurotransmission , Neurovascular Coupling , and Brain Energy Metabolism, (October), 2784–2795. https://doi.org/10.1093/cercor/bht136

Lee, Y., Messing, A., Su, M., & Brenner, M. (2008). GFAP promoter elements required for region-specific and astrocyte-specific expression. *Glia*, *56*(5), 481–493. https://doi.org/10.1002/glia.20622

Leung, R. K. M., & Whittaker, P. A. (2005). RNA interference: From gene silencing to gene-specific therapeutics. *Pharmacology and Therapeutics*, *107*(2), 222–239. https://doi.org/10.1016/j.pharmthera.2005.03.004

Lin, R. Y., Vera, J. C., Chaganti, R. S. K., & Golde, D. W. (1998). Human monocarboxylate transporter 2 (MCT2) is a high affinity pyruvate transporter. *Journal of Biological Chemistry*, *273*(44), 28959–28965. https://doi.org/10.1074/jbc.273.44.28959

Lin, S. Y., Zhang, C. S., & Lin, S. C. (2018). Carbohydrates: Not All that Bad? *Cell Metabolism*, *28*(5), 671–672. https://doi.org/10.1016/j.cmet.2018.10.004

Liu, B. H., Yang, Y., Paton, J. F. R., Li, F., Boulaire, J., Kasparov, S., & Wang, S. (2006). GAL4–NF-κB Fusion Protein Augments Transgene Expression from Neuronal Promoters in the Rat Brain. *Molecular Therapy*, *14*(6), 872–882. https://doi.org/10.1016/j.ymthe.2006.05.020

Liu, B., Mosienko, V., Vaccari Cardoso, B., Prokudina, D., Huentelman, M., Teschemacher, A. G., & Kasparov, S. (2018). Glio- and neuro-protection by prosaposin is mediated by orphan G-protein coupled receptors GPR37L1 and GPR37. *Glia*, *66*(11), 2414–2426. https://doi.org/10.1002/glia.23480

Liu, B., Paton, J. F., & Kasparov, S. (2008). Viral vectors based on bidirectional cell-specific mammalian promoters and transcriptional amplification strategy for use in vitro and in vivo. *BMC Biotechnology*, *8*, 49. https://doi.org/10.1186/1472-6750-8-49

Liu, C., Wu, J., Zhu, J., Kuei, C., Yu, J., Shelton, J., … Lovenberg, T. W. (2009). Lactate Inhibits Lipolysis in Fat Cells through Activation of an Orphan G-protein-coupled Receptor, GPR81. *Journal of Biological Chemistry*, *284*(5), 2811–2822. https://doi.org/10.1074/jbc.M806409200

Liu, X., Cooper, D. E., Cluntun, A. A., Warmoes, M. O., Zhao, S., Reid, M. A., … Locasale, J. W. (2018). Acetate Production from Glucose and Coupling to Mitochondrial Metabolism in Mammals. *Cell*, *175*(2), 502–513.e13. https://doi.org/10.1016/j.cell.2018.08.040

Lonergan, T., Teschemacher, A. G., Hwang, D. Y., Kim, K.-S., Pickering, A. E., & Kasparov, S. (2005). Targeting brain stem centers of cardiovascular control using adenoviral vectors: impact of promoters on transgene expression. *Physiological Genomics*, *20*(2), 165–172. https://doi.org/10.1152/physiolgenomics.00120.2004

Lopez-Fabuel, I., Le Douce, J., Logan, A., James, A. M., Bonvento, G., Murphy, M. P., … Bolaños, J. P. (2016). Complex I assembly into supercomplexes determines differential mitochondrial ROS production in neurons and astrocytes. *Proceedings of the National Academy of Sciences*, *113*(46), 13063–13068. https://doi.org/10.1073/pnas.1613701113

Löser, P., Jennings, G. S., Strauss, M., & Sandig, V. (1998). Reactivation of the previously silenced cytomegalovirus major immediate-early promoter in the mouse liver: involvement of NFkappaB. *Journal of Virology*, *72*(1), 180–190. Retrieved from http://www.ncbi.nlm.nih.gov/pubmed/9420214%0Ahttp://www.pubmedcentral.nih.gov/articlerender.fcgi?artid=PMC109363

Loughlin, S. E., Foote, S. L., & Grzanna, R. (1986). Efferent projections of nucleus locus coeruleus: Morphologic subpopulations have different efferent targets. *Neuroscience*, *18*(2), 307–319. https://doi.org/10.1016/0306-4522(86)90156-9

Lovatt, D., Sonnewald, U., Waagepetersen, H. S., Schousboe, A., He, W., Lin, J. H. C., … Nedergaard, M. (2007). The transcriptome and metabolic gene signature of protoplasmic astrocytes in the adult murine cortex. *Journal of Neuroscience*, *27*(45), 12255–12266. https://doi.org/10.1523/JNEUROSCI.3404-07.2007

Mächler, P., Wyss, M. T., Elsayed, M., Stobart, J., Gutierrez, R., von Faber-Castell, A., … Weber, B. (2016). In Vivo Evidence for a Lactate Gradient from Astrocytes to Neurons. *Cell Metabolism*, *23*(1), 94–102. https://doi.org/10.1016/j.cmet.2015.10.010

Maeda-Yorita, K., Aki, K., Sagai, H., Misaki, H., & Massey, V. (1995). L-lactate oxidase and L-lactate monooxygenase: Mechanistic variations on a common structural theme. *Biochimie*, *77*(7–8), 631–642. https://doi.org/10.1016/0300-9084(96)88178-8

Magistretti, P. J., & Allaman, I. (2015). A Cellular Perspective on Brain Energy Metabolism and Functional Imaging. *Neuron*, *86*(4), 883–901. https://doi.org/10.1016/j.neuron.2015.03.035

Magistretti, P. J., & Allaman, I. (2018). Lactate in the brain: from metabolic end-product to signalling molecule. *Nature Reviews Neuroscience*, *19*(4), 235–249. https://doi.org/10.1038/nrn.2018.19

Mank, M., Santos, A. F., Direnberger, S., Mrsic-Flogel, T. D., Hofer, S. B., Stein, V., … Griesbeck, O. (2008). A genetically encoded calcium indicator for chronic in vivo two-photon imaging. *Nature Methods*, *5*(9), 805–811. https://doi.org/10.1038/nmeth.1243

Manning Fox, J. E., Meredith, D., & Halestrap, A. P. (2000). Characterisation of human monocarboxylate transporter 4 substantiates its role in lactic acid efflux from skeletal muscle. *Journal of Physiology*, *529*(2), 285–293. https://doi.org/10.1111/j.1469-7793.2000.00285.x

Manome, A., Okada, S., Uchimura, T., & Komagata, K. (1998). The ratio of L -form to D -form of lactic acid as a criteria for the identification of lactic acid bacteria. *The Journal of General and Applied Microbiology*, *44*, 371–374.

Marina, N., Ang, R., Machhada, A., Kasymov, V., Karagiannis, A., Hosford, P. S., … Gourine, A. V. (2015). Brainstem hypoxia contributes to the development of hypertension in the spontaneously hypertensive rat. *Hypertension*, *65*(4), 775–783. https://doi.org/10.1161/HYPERTENSIONAHA.114.04683

Marina, N., Teschemacher, A. G., Kasparov, S., & Gourine, A. V. (2016). Glia, sympathetic activity and cardiovascular disease. *Experimental Physiology*, *101*(5), 565–576. https://doi.org/10.1113/EP085713

Marina, N., Turovsky, E., Christie, I. N., Hosford, P. S., Hadjihambi, A., Korsak, A., … Gourine, A. V. (2018). Brain metabolic sensing and metabolic signaling at the level of an astrocyte. *Glia*, *66*(6), 1185–1199. https://doi.org/10.1002/glia.23283

Markert, C., Shaklee, J., & Whitt, G. (1975). Evolution of a gene. Multiple genes for LDH isozymes provide a model of the evolution of gene structure, function and regulation. *Science*, *189*(4197), 102–114. https://doi.org/10.1126/science.1138367

Marriott, D. R., Hirst, W. D., & Ljungberg, M. C. (1995). Astrocytes. In J. Cohen & G. P. Wilkin (Eds.), *Neural cell culture - A practical approach* (pp. 85–96). Oxford University Press.

Martin, P. M., & O'Callaghan, J. P. (1995). A direct comparison of GFAP immunocytochemistry and GFAP concentration in various regions of ethanol-fixed rat and mouse brain. *Journal of Neuroscience Methods*, *58*(1–2), 181–192. https://doi.org/10.1016/0165-0270(94)00175-G

Matyash, V., & Kettenmann, H. (2010). Heterogeneity in astrocyte morphology and physiology. *Brain Research Reviews*, *63*(1–2), 2–10. https://doi.org/10.1016/j.brainresrev.2009.12.001

McCall, J. G., Al-Hasani, R., Siuda, E. R., Hong, D. Y., Norris, A. J., Ford, C. P., & Bruchas, M. R. (2015). CRH Engagement of the Locus Coeruleus Noradrenergic System Mediates Stress-Induced Anxiety. *Neuron*, *87*(3), 605–620. https://doi.org/10.1016/j.neuron.2015.07.002

McIver, S. R., Faideau, M., & Haydon, P. G. (2013). *Astrocyte–Neuron Communications*. *Neural-Immune Interactions in Brain Function and Alcohol Related Disorders*. (C. Cui, L. Grandison, & A. Noronha, Eds.). Boston, MA: Springer US. https://doi.org/10.1007/978-1-4614-4729-0

McKenna, M. C. (2013). Glutamate Pays Its Own Way in Astrocytes. *Frontiers in Endocrinology*, *4*. https://doi.org/10.3389/fendo.2013.00191

McKenna, M. C., Hopkins, I. B., & Carey, A. (2001). α-cyano-4-hydroxycinnamate decreases both glucose and lactate metabolism in neurons and astrocytes: Implications for lactate as an energy substrate for neurons. *Journal of Neuroscience Research*, *66*(5), 747–754. https://doi.org/10.1002/jnr.10084

McKenna, M. C., Waagepetersen, H. S., Schousboe, A., & Sonnewald, U. (2006). Neuronal and astrocytic shuttle mechanisms for cytosolic-mitochondrial transfer of reducing equivalents: Current evidence and pharmacological tools. *Biochemical Pharmacology*, *71*(4), 399–407. https://doi.org/10.1016/j.bcp.2005.10.011

Mederos, S., González-Arias, C., & Perea, G. (2018). Astrocyte–Neuron Networks: A Multilane Highway of Signaling for Homeostatic Brain Function. *Frontiers in Synaptic Neuroscience*. https://doi.org/10.3389/fnsyn.2018.00045

Merienne, N., Douce, J. Le, Faivre, E., Déglon, N., & Bonvento, G. (2013). Efficient gene delivery and selective transduction of astrocytes in the mammalian brain using viral vectors. *Frontiers in Cellular Neuroscience*, *7*(July), 1–13. https://doi.org/10.3389/fncel.2013.00106

Middeldorp, J., & Hol, E. M. (2011). GFAP in health and disease. *Progress in Neurobiology*, *93*(3), 421–443. https://doi.org/10.1016/j.pneurobio.2011.01.005

Miller, R. H., & Raff, M. C. (1984). Fibrous and Protoplasmic Astrocytes Are Biochemically and Developmentally Distinct. *Journal of Neuroscience*, *4*(2), 585–592.

Milner, T. A., Lee, A., Aicher, S. A., & Rosin, D. L. (1998). Hippocampal a2A-adrenergic receptors are located predominantly presynaptically but are also found postsynaptically and in selective astrocytes. *The Journal of Comparative Neurology*, *395*(3), 310–327. https://doi.org/10.1002/(SICI)1096-9861(19980808)395:3<310::AID-CNE4>3.0.CO;2-5

Mongeon, R., Venkatachalam, V., & Yellen, G. (2016). Cytosolic NADH-NAD + Redox Visualized in Brain Slices by Two-Photon Fluorescence Lifetime Biosensor Imaging . *Antioxidants & Redox Signaling*, *25*(10), 553–563. https://doi.org/10.1089/ars.2015.6593

Morland, C., Andersson, K. A., Haugen, Ø. P., Hadzic, A., Kleppa, L., Gille, A., … Bergersen, L. H. (2017). Exercise induces cerebral VEGF and angiogenesis via the lactate receptor HCAR1. *Nature Communications*, *8*(7491), 15557. https://doi.org/10.1038/ncomms15557

Mosienko, V., Rasooli-Nejad, S., Kishi, K., De Both, M., Jane, D., Huentelman, M., … Teschemacher, A. (2018). Putative Receptors Underpinning l-Lactate Signalling in Locus Coeruleus. *Neuroglia*, *1*(2), 365–380. https://doi.org/10.3390/neuroglia1020025

Mosienko, V., Teschemacher, A. G., & Kasparov, S. (2015). Is L-lactate a novel signaling molecule in the brain? *Journal of Cerebral Blood Flow and Metabolism : Official Journal of the International Society of Cerebral Blood Flow and Metabolism*, (January), 1–7. https://doi.org/10.1038/jcbfm.2015.77

Muller, A., Joseph, V., Slesinger, P. a, & Kleinfeld, D. (2014). Cell-based reporters reveal in vivo dynamics of dopamine and norepinephrine release in murine cortex. *Nature Methods*, *11*(12), 1245–1252. https://doi.org/10.1038/nmeth.3151

Nagy, J. I., Dudek, F. E., & Rash, J. E. (2004). Update on connexins and gap junctions in neurons and glia in the mammalian nervous system. *Brain Research Reviews*, *47*(1–3), 191–215. https://doi.org/10.1016/j.brainresrev.2004.05.005

Nagy, J. I., Patel, D., Ochalski, P. A. Y., & Stelmack, G. L. (1999). Connexin30 in rodent, cat and human brain: Selective expression in gray matter astrocytes, co-localization with connexin43 at gap junction and late developmental appearance. *Neuroscience*, *88*(2), 447–468. https://doi.org/10.1016/S0306-4522(98)00191-2

Nelson, D. L., & Cox, M. M. (2017). *Lehninger principles of biochemistry* (7th ed.). W. H. Freeman and Company.

Nettelbeck, D. M., Jérôme, V., & Müller, R. (1998). A strategy for enhancing the transcriptional activity of weak cell type-specific promoters. *Gene Therapy*, *5*(12), 1656–1664. https://doi.org/10.1038/sj.gt.3300778

Newman, L. A., Korol, D. L., & Gold, P. E. (2011). Lactate Produced by Glycogenolysis in Astrocytes Regulates Memory Processing. *PLoS ONE*, *6*(12), e28427. https://doi.org/10.1371/journal.pone.0028427

O'Brien, J., Kla, K. M., Hopkins, I. B., Malecki, E. A., & McKenna, M. C. (2007). Kinetic parameters and lactate dehydrogenase isozyme activities support possible lactate utilization by neurons. *Neurochemical Research*, *32*(4–5), 597–607. https://doi.org/10.1007/s11064-006-9132-9

O'Donnell, J., Zeppenfeld, D., McConnell, E., Pena, S., & Nedergaard, M. (2012). Norepinephrine: A Neuromodulator That Boosts the Function of Multiple Cell Types to Optimize CNS Performance. *Neurochemical Research*, *37*(11), 2496–2512. https://doi.org/10.1007/s11064-012-0818-x

Oberheim, N. A., Goldman, S. A., & Nedergaard, M. (2012). Heterogeneity of Astrocytic Form and Function. In R. Milner (Ed.), *Astrocytes. Methods in Molecular Biology (Methods and Protocols)* (Vol. 814, pp. 23–45). https://doi.org/10.1007/978-1-61779-452-0_3

Oberheim, N. A., Takano, T., Han, X., He, W., Lin, J. H. C., Wang, F., … Nedergaard, M. (2009). Uniquely Hominid Features of Adult Human Astrocytes. *Journal of Neuroscience*, *29*(10), 3276–3287. https://doi.org/10.1523/jneurosci.4707-08.2009

Okada, Y., Okada, T., Sato-Numata, K., Islam, M. R., Ando-Akatsuka, Y., Numata, T., … Sabirov, R. Z. (2019). Cell Volume-Activated and Volume-Correlated Anion Channels in Mammalian Cells: Their Biophysical, Molecular, and Pharmacological Properties. *Pharmacological Reviews*, *71*(1), 49–88. https://doi.org/10.1124/pr.118.015917

Ovens, M. J., Davies, A. J., Wilson, M. C., Murray, C. M., & Halestrap, A. P. (2010). AR-C155858 is a potent inhibitor of monocarboxylate transporters MCT1 and MCT2 that binds to an intracellular site involving transmembrane helices 7–10. *Biochemical Journal*, *425*(3), 523–530. https://doi.org/10.1042/BJ20091515

Pankratov, Y., & Lalo, U. (2015). Role for astroglial α1-adrenoreceptors in gliotransmission and control of synaptic plasticity in the neocortex. *Frontiers in Cellular Neuroscience*, *9*(June), 1–11. https://doi.org/10.3389/fncel.2015.00230

Parri, H. R., Gould, T. M., & Crunelli, V. (2001). Spontaneous astrocytic Ca2+ oscillations in situ drive NMDAR-mediated neuronal excitation. *Nature Neuroscience*, *4*(8), 803–812. https://doi.org/10.1038/90507

Parsons, M. P., & Hirasawa, M. (2010). ATP-Sensitive Potassium Channel-Mediated Lactate Effect on Orexin Neurons: Implications for Brain Energetics during Arousal. *Journal of Neuroscience*, *30*(24), 8061–8070. https://doi.org/10.1523/JNEUROSCI.5741-09.2010

Pellerin, L., & Magistretti, P. J. (1994). Glutamate uptake into astrocytes stimulates aerobic glycolysis: a mechanism coupling neuronal activity to glucose utilization. *Proceedings of the National Academy of Sciences*, *91*(22), 10625–10629. https://doi.org/10.1073/pnas.91.22.10625

Pellerin, L., & Magistretti, P. J. (2012). Sweet Sixteen for ANLS. *Journal of Cerebral Blood Flow & Metabolism*, *32*(7), 1152–1166. https://doi.org/10.1038/jcbfm.2011.149

Perea, G., & Araque, A. (2005). Properties of synaptically evoked astrocyte calcium signal reveal synaptic information processing by astrocytes. *Journal of Neuroscience*, *25*(9), 2192–2203. https://doi.org/10.1523/JNEUROSCI.3965-04.2005

Perea, G., Sur, M., & Araque, A. (2014). Neuron-glia networks: integral gear of brain function. *Frontiers in Cellular Neuroscience*, *8*(November), 378. https://doi.org/10.3389/fncel.2014.00378

Philp, N. J., Yoon, H., & Grollman, E. F. (1998). Monocarboxylate transporter MCT1 is located in the apical membrane and MCT3 in the basal membrane of rat RPE. *American Journal Of Physiology-Regulatory Integrative And Comparative Physiology*, *274*(6), R1824–R1828. https://doi.org/10.1007/s003399900078

Pierre, K., & Pellerin, L. (2005). Monocarboxylate transporters in the central nervous system: Distribution, regulation and function. *Journal of Neurochemistry*, *94*(1), 1–14. https://doi.org/10.1111/j.1471-4159.2005.03168.x

Poole, R. C., Cranmer, S. L., Halestrap, A. P., & Levi, A. J. (1990). Substrate and inhibitor specificity of monocarboxylate transport into heart cells and erythrocytes. Further evidence for the existence of two distinct carriers. *Biochemical Journal*, *269*(3), 827–829. https://doi.org/10.1042/bj2690827

Poole, R. C., & Halestrap, A. P. (1993). Transport of lactate and other monocarboxylates across mammalian plasma membranes. *American Journal of Physiology-Cell Physiology*, *264*(4), C761–C782. https://doi.org/10.1152/ajpcell.1993.264.4.C761

Poole, R. C., Sansom, C. E., & Halestrap, A. P. (1996). Studies of the membrane topology of the rat erythrocyte H+/lactate cotransporter (MCT1). *Biochemical Journal*, *320*(3), 817–824. https://doi.org/10.1042/bj3200817

Poulain, D. A., Oliet, S. H., & Piet, R. (2001). Control of glutamate clearance and synaptic efficacy by glial coverage of neurons. *Science*, *292*(5518), 923–926.

Qiu, J., Villa, M., Sanin, D. E., Buck, M. D., O'Sullivan, D., Ching, R., … Pearce, E. L. (2019). Acetate Promotes T Cell Effector Function during Glucose Restriction. *Cell Reports*, *27*(7), 2063–2074.e5. https://doi.org/10.1016/j.celrep.2019.04.022

Quistorff, B., & Grunnet, N. (2011). High brain lactate is not caused by a shift in the lactate dehydrogenase A/B ratio. *Proceedings of the National Academy of Sciences*, *108*(7), E21–E21. https://doi.org/10.1073/pnas.1017750108

Quistorff, B., & Grunnet, N. (2011). The isoenzyme pattern of LDH does not play a physiological role; except perhaps during fast transitions in energy metabolism. *Aging*, *3*(5), 457–460. https://doi.org/10.18632/aging.100329

Rae, C., Fekete, A. D., Kashem, M. A., Nasrallah, F. A., & Bröer, S. (2012). Metabolism, compartmentation, transport and production of acetate in the cortical brain tissue slice. *Neurochemical Research*, *37*(11), 2541–2553. https://doi.org/10.1007/s11064-012-0847-5

Rafiki, A., Boulland, J. L., Halestrap, A. P., Ottersen, O. P., & Bergersen, L. (2003). Highly differential expression of the monocarboxylate transporters MCT2 and MCT4 in the developing rat brain. *Neuroscience*, *122*(3), 677–688. https://doi.org/10.1016/j.neuroscience.2003.08.040

Ramos, M., del Arco, A., Pardo, B., Martínez-Serrano, A., Martínez-Morales, J. R., Kobayashi, K., … Satrústegui, J. (2003). Developmental changes in the Ca2+-regulated mitochondrial aspartate–glutamate carrier aralar1 in brain and prominent expression in the spinal cord. *Developmental Brain Research*, *143*(1), 33–46. https://doi.org/10.1016/S0165-3806(03)00097-X

Rash, J. E., Yasumura, T., Dudek, F. E., & Nagy, J. I. (2001). Cell-specific expression of connexins and evidence of restricted gap junctional coupling between glial cells and between neurons. *The Journal of Neuroscience*, *21*(6), 1983–2000. https://doi.org/10.1016/j.ajog.2008.08.044

Reaume, A., de Sousa, P., Kulkarni, S., Langille, B., Zhu, D., Davies, T., … Rossant, J. (2006). Cardiac malformation in neonatal mice lacking connexin43. *Science*, *267*(5205), 1831–1834. https://doi.org/10.1126/science.7892609

Retamal, M. A., Froger, N., Palacios-Prado, N., Ezan, P., Saez, P. J., Saez, J. C., & Giaume, C. (2007). Cx43 Hemichannels and Gap Junction Channels in Astrocytes Are Regulated Oppositely by Proinflammatory Cytokines Released from Activated Microglia. *Journal of Neuroscience*, *27*(50), 13781–13792. https://doi.org/10.1523/JNEUROSCI.2042-07.2007

Ribeiro, J. A., Fernandes, P. M. V., Pereira, C. M., & Silva, F. (2016). Electrochemical sensors and biosensors for determination of catecholamine neurotransmitters: A review. *Talanta*, *160*, 653–679. https://doi.org/10.1016/j.talanta.2016.06.066

Riis, B., Suresh, I. S., Derventzi, A., & Clark, B. F. C. (1990). Reduced levels of ADP-ribosylatable elongation factor-2 in aged and SV40-transformed human cell cultures. *FEBS Letters, 266(1–2),* 45–47. https://doi.org/10.1016/0014-5793(90)81502-F

Robertson, S. D., Plummer, N. W., De Marchena, J., & Jensen, P. (2013). Developmental origins of central norepinephrine neuron diversity. *Nature Neuroscience*, *16*(8), 1016–1023. https://doi.org/10.1038/nn.3458

Robinet, C., & Pellerin, L. (2010). Brain-Derived Neurotrophic Factor Enhances the Expression of the Monocarboxylate Transporter 2 through Translational Activation in Mouse Cultured Cortical Neurons. *Journal of Cerebral Blood Flow & Metabolism*, *30*(2), 286–298. https://doi.org/10.1038/jcbfm.2009.208

Rouach, N., Koulakoff, A., Abudara, V., Willecke, K., & Giaume, C. (2008). Astroglial Metabolic Networks Sustain Hippocampal Synaptic Transmission. *Science*, *322*(December), 1551–1555. https://doi.org/10.1126/science.1164022

Saab, A. S., & Nave, K. A. (2017). Myelin dynamics: protecting and shaping neuronal functions. *Current Opinion in Neurobiology*, *47*, 104–112. https://doi.org/10.1016/j.conb.2017.09.013

Saez, I., Duran, J., Sinadinos, C., Beltran, A., Yanes, O., Tevy, M. F., … Guinovart, J. J. (2014). Neurons have an active glycogen metabolism that contributes to tolerance to hypoxia. *Journal of Cerebral Blood Flow and Metabolism*, *34*(6), 945–955. https://doi.org/10.1038/jcbfm.2014.33

Sagara, J., Miura, K., & Bannai, S. (1993). Maintenance of Neuronal Glutathione by Glial Cells. *Journal of Neurochemistry*, *61*(5), 1672–1676. https://doi.org/10.1111/j.1471-4159.1993.tb09802.x

Sahoo, H. (2011). Förster resonance energy transfer - A spectroscopic nanoruler: Principle and applications. *Journal of Photochemistry and Photobiology C: Photochemistry Reviews*, *12*(1), 20–30. https://doi.org/10.1016/j.jphotochemrev.2011.05.001

San Martin, A., Ceball, S., Baeza-Lehnert, F., Lerchundi, R., Valdebenito, R., Contreras-Baeza, Y., … Barros, L. F. (2014). Imaging Mitochondrial Flux in Single Cells with a FRET Sensor for Pyruvate, *9*(1). https://doi.org/10.1371/journal.pone.0085780

San Martín, A., Ceballo, S., Ruminot, I., Lerchundi, R., Frommer, W. B., & Barros, L. F. (2013). A Genetically Encoded FRET Lactate Sensor and Its Use To Detect the Warburg Effect in Single Cancer Cells. *PLoS ONE*, *8*(2), e57712. https://doi.org/10.1371/journal.pone.0057712

Sandén, N., Thorlin, T., Blomstrand, F., Persson, P. A. ., & Hansson, E. (2000). 5-Hydroxytryptamine2B receptors stimulate Ca2+ increases in cultured astrocytes from three different brain regions. *Neurochemistry International*, *36*(4–5), 427–434. https://doi.org/10.1016/S0197-0186(99)00134-5

Sanders, J., Brandsma, M., Janssen, G. M. C., Dijk, J., & Möller, W. (1996). Immunofluorescence studies of human fibroblasts demonstrate the presence of the complex of elongation factor-1βγδ in the endoplasmic reticulum. *Journal of Cell Science*, *109*, 1113–1117.

Savtchouk, I., & Volterra, A. (2018). Gliotransmission: Beyond Black-and-White. *The Journal of Neuroscience*, *38*(1), 14–25. https://doi.org/10.1523/jneurosci.0017-17.2017

Schnepp, B. C., Jensen, R. L., Chen, C.-L., Johnson, P. R., & Clark, K. R. (2005). Characterization of Adeno-Associated Virus Genomes Isolated from Human Tissues. *Journal of Virology*, *79*(23), 14793–14803. https://doi.org/10.1128/JVI.79.23.14793-14803.2005

Schummers, J., Yu, H., & Sur, M. (2008). Tuned Responses of Astrocytes and Their Influence on Hemodynamic Signals in the Visual Cortex. *Science*, *320*(5883), 1638–1643. https://doi.org/10.1126/science.1156120

Schwarz, L. A., & Luo, L. (2015). Organization of the locus coeruleus-norepinephrine system. *Current Biology*, *25*(21), R1051–R1056. https://doi.org/10.1016/j.cub.2015.09.039

Shaner, N. C., Patterson, G. H., & Davidson, M. W. (2011). Advances in fluorescent protein technology. *Journal of Cell Science*, *124*(13), 2321–2321. https://doi.org/10.1242/jcs.094722

Shao, Y., & Sutin, J. (1991). Noradrenergic facilitation of motor neurons: Localization of adrenergic receptors in neurons and nonneuronal cells in the trigeminal motor nucleus. *Experimental Neurology*, *114*(2), 216–227. https://doi.org/10.1016/0014-4886(91)90038-E

Shin, J.-H., Yue, Y., & Duan, D. (2012). Recombinant Adeno-Associated Viral Vector Production and Purification. In J. X. DiMario (Ed.), *Myogenesis. Methods in Molecular Biology (Methods and Protocols)* (Vol. 798, pp. 267–284). https://doi.org/10.1007/978-1-61779-343-1_15

Sinclair, J. H., Baillie, J., Bryant, L. A., Taylor-Wiedeman, J. A., & Sissons, J. G. P. (1992). Repression of human cytomegalovirus major immediate early gene expression in a monocytic cell line. *Journal of General Virology*, *73*(2), 433–435. https://doi.org/10.1099/0022-1317-73-2-433

Smith, S. J. (1992). Chapter 10: Do astrocytes process neural information? (pp. 119–136). https://doi.org/10.1016/S0079-6123(08)61744-6

Sotelo-Hitschfeld, T., Niemeyer, M. I., Machler, P., Ruminot, I., Lerchundi, R., Wyss, M. T., … Barros, L. F. (2015). Channel-Mediated Lactate Release by K+-Stimulated Astrocytes. *Journal of Neuroscience*, *35*(10), 4168–4178. https://doi.org/10.1523/JNEUROSCI.5036-14.2015

Sotelo, C., & Palay, S. L. (1968). The Fine Structure of the Lateral Vestibuar Nucleus in the Rat. *The Journal of Cell Biology*, *36*(1), 151–179. https://doi.org/10.1083/jcb.36.1.151

Souza, D. G., Almeida, R. F., Souza, D. O., & Zimmer, E. R. (2019). The astrocyte biochemistry. *Seminars in Cell and Developmental Biology*, (April), 1–9. https://doi.org/10.1016/j.semcdb.2019.04.002

Stehberg, J., Moraga-Amaro, R., Salazar, C., Becerra, A., Echeverria, C., Orellana, J. A., … Retamal, M. A. (2012). Release of gliotransmitters through astroglial connexin 43 hemichannels is necessary for fear memory consolidation in the basolateral amygdala. *The FASEB Journal*, *26*(9), 3649–3657. https://doi.org/10.1096/fj.11-198416

Stone, E. A., & Ariano, M. A. (1989). Are glial cells targets of the central noradrenergic system? A review of the evidence. *Brain Research Reviews*, *14*(4), 297–309. https://doi.org/10.1016/0165-0173(89)90015-5

Straub, S. V., & Nelson, M. T. (2007). Astrocytic Calcium Signaling: The Information Currency Coupling Neuronal Activity to the Cerebral Microcirculation. *Trends in Cardiovascular Medicine*, *17*(6), 183–190. https://doi.org/10.1016/j.tcm.2007.05.001

Stryer, L. (1995). *Biochemistry*. New York, NY: W.H. Freeman and Co.

Subbarao, K. V., & Hertz, L. (1990). Effect of adrenergic agonists on glycogenolysis in primary cultures of astrocytes. *Brain Research*, *536*(1–2), 220–226. https://doi.org/10.1016/0006-8993(90)90028-A

Sullivan, J. M., Traynelis, S. F., Chen, H.-S. V., Escobar, W., Heinemann, S. F., & Lipton, S. A. (1994). Identification of two cysteine residues that are required for redox modulation of the NMDA subtype of glutamate receptor. *Neuron*, *13*(4), 929–936. https://doi.org/10.1016/0896-6273(94)90258-5

Supplie, L. M., Düking, T., Campbell, G., Diaz, F., Moraes, C. T., Götz, M., … Nave, K.-A. (2017). Respiration-Deficient Astrocytes Survive As Glycolytic Cells *In Vivo*. *The Journal of Neuroscience*, *37*(16), 4231–4242. https://doi.org/10.1523/JNEUROSCI.0756-16.2017

Suzuki, A., Stern, S. a, Bozdagi, O., Huntley, G. W., Ruth, H., Magistretti, P. J., & Alberini, C. M. (2011). Astrocyte-neuron lactate transport is required for long-term memory formation. *Cell*, *144*(5), 810–823. https://doi.org/10.1016/j.cell.2011.02.018.Astrocyte-neuron

Swanson, R. A., Morton, M. M., Sagar, S. M., & Sharp, F. R. (1992). Sensory stimulation induces local cerebral glycogenolysis: Demonstration by autoradiography. *Neuroscience*, *51*(2), 451–461. https://doi.org/10.1016/0306-4522(92)90329-Z

Swiderek, K., & Paneth, P. (2011). Differences and similarities in binding of pyruvate and L-lactate in the active site of M4 and H4 isoforms of human lactate dehydrogenase. *Archives of Biochemistry and Biophysics*, *505*(1), 33–41. https://doi.org/10.1016/j.abb.2010.10.010

Tabernero, A., Giaume, C., & Medina, J. M. (1996). Endothelin-1 regulates glucose utilization in cultured rat astrocytes by controlling intercellular communication through gap junctions. *Glia*, *16*, 187–195.

Tang, F., Lane, S., Korsak, A., Paton, J. F. R., Gourine, A. V, Kasparov, S., & Teschemacher, A. G. (2014). Lactate-mediated glia-neuronal signalling in the mammalian brain. *Nature Communications*, *5*, 3284. https://doi.org/10.1038/ncomms4284

Teschemacher, A. G., Paton, J. F. R., & Kasparov, S. (2005). Imaging living central neurones using viral gene transfer. *Advanced Drug Delivery Reviews*, *57*(1), 79–93. https://doi.org/10.1016/j.addr.2004.05.004

Tijsterman, M., Ketting, R. F., & Plasterk, R. H. A. (2002). The Genetics of RNA Silencing. *Annual Review of Genetics*, *36*(1), 489–519. https://doi.org/10.1146/annurev.genet.36.043002.091619

Torres-Torrelo, H., Ortega-Sáenz, P., Macías, D., Omura, M., Zhou, T., Matsunami, H., … López-Barneo, J. (2018). The role of Olfr78 in the breathing circuit of mice. *Nature*, *561*(7724), E33–E40. https://doi.org/10.1038/s41586-018-0545-9

Tsuchiya, R., Yoshiki, F., Kudo, Y., & Morita, M. (2002). Cell type-selective expression of green fluorescent protein and the calcium indicating protein, yellow cameleon, in rat cortical primary cultures. *Brain Research*, *956*(2), 221–229. https://doi.org/10.1016/S0006-8993(02)03518-7

Turovsky, E., Theparambil, S. M., Kasymov, V., Deitmer, J. W., Del Arroyo, A. G., Ackland, G. L., … Gourine, A. V. (2016). Mechanisms of CO2/H+ sensitivity of astrocytes. *Journal of Neuroscience*, *36*(42), 10750–10758. https://doi.org/10.1523/JNEUROSCI.1281-16.2016

Umena, Y., Yorita, K., Matsuoka, T., Kita, A., Fukui, K., & Morimoto, Y. (2006). The crystal structure of L-lactate oxidase from Aerococcus viridans at 2.1 A˚ resolution reveals the mechanism of strict substrate recognition, *350*, 249–256. https://doi.org/10.1016/j.bbrc.2006.09.025

Uribarri, J., Oh, M. S., & Carroll, H. J. (1998). D-Lactic Acidosis: A Review of Clinical Presentation, Biochemical Features, and Pathophysiologic Mechanisms. *Medicine (Baltimore)*, *77*(2), 73–82.

Vander Heiden, M. G., & DeBerardinis, R. J. (2017). Understanding the Intersections between Metabolism and Cancer Biology. *Cell*, *168*(4), 657–669. https://doi.org/10.1016/j.cell.2016.12.039

Vélez-Fort, M., Audinat, E., & Angulo, M. C. (2012). Central Role of GABA in Neuron–Glia Interactions. *The Neuroscientist*, *18*(3), 237–250. https://doi.org/10.1177/1073858411403317

Verkhratsky, A., & Nedergaard, M. (2018). Physiology of Astroglia. *Physiological Reviews*, *98*(1), 239–389. https://doi.org/10.1152/physrev.00042.2016

Vilchez, D., Ros, S., Cifuentes, D., Pujadas, L., Vallès, J., García-Fojeda, B., … Guinovart, J. J. (2007). Mechanism suppressing glycogen synthesis in neurons and its demise in progressive myoclonus epilepsy. *Nature Neuroscience*, *10*(11), 1407–1413. https://doi.org/10.1038/nn1998

Volkenhoff, A., Weiler, A., Letzel, M., Stehling, M., Klämbt, C., & Schirmeier, S. (2015). Glial glycolysis is essential for neuronal survival in drosophila. *Cell Metabolism*, *22*(3), 437–447. https://doi.org/10.1016/j.cmet.2015.07.006

Walls, A. B., Heimbürger, C. M., Bouman, S. D., Schousboe, A., & Waagepetersen, H. S. (2009). Robust glycogen shunt activity in astrocytes: Effects of glutamatergic and adrenergic agents. *Neuroscience*, *158*(1), 284–292. https://doi.org/10.1016/j.neuroscience.2008.09.058

Wang, D., & Bordey, A. (2008). The astrocyte odyssey. *Progress in Neurobiology*, *86*(4), 342–367. https://doi.org/10.1016/j.pneurobio.2008.09.015

Waniewski, R. A., & Martin, D. L. (1998). Preferential Utilization of Acetate by Astrocytes Is Attributable to Transport, *18*(14), 5225–5233.

Weber, B., & Barros, L. F. (2015). The astrocyte: Powerhouse and recycling center. *Cold Spring Harbor Perspectives in Biology*, *7*(12), 1–15. https://doi.org/10.1101/cshperspect.a020396

Wheeler, D. G., & Cooper, E. (2001). Depolarization Strongly Induces Human Cytomegalovirus Major Immediate-Early Promoter/Enhancer Activity in Neurons. *Journal of Biological Chemistry*, *276*(34), 31978–31985. https://doi.org/10.1074/jbc.M103667200

Wickham, T. J. (2000). Targeting adenovirus vectors. *Nature Biotechnology*, *7*, 110–114. https://doi.org/10.1038/70161

Wilson, G. S., & Johnson, M. A. (2008). In-Vivo Electrochemistry: What Can We Learn about Living Systems? *Chemical Reviews*, *108*(7), 2462–2481. https://doi.org/10.1021/cr068082i

Yang, J., Ruchti, E., Petit, J.-M., Jourdain, P., Grenningloh, G., Allaman, I., & Magistretti, P. J. (2014). Lactate promotes plasticity gene expression by potentiating NMDA signaling in neurons. *Proceedings of the National Academy of Sciences*, *111*(33), 12228–12233. https://doi.org/10.1073/pnas.1322912111

Yellen, G. (2018). Fueling thought: Management of glycolysis and oxidative phosphorylation in neuronal metabolism. *Journal of Cell Biology*, *217*(7), 2235–2246. https://doi.org/10.1083/jcb.201803152

Ying, S. Y., Chang, D. C., & Lin, S. L. (2008). The MicroRNA (miRNA): Overview of the RNA genes that modulate gene function. *Molecular Biotechnology*, *38*(3), 257–268. https://doi.org/10.1007/s12033-007-9013-8

Yuan, T. T. T., Toy, P., McClary, J. A., Lin, R. J., Miyamoto, N. G., & Kretschmer, P. J. (2001). Cloning and genetic characterization of an evolutionarily conserved human olfactory receptor that is differentially expressed across species. *Gene*, *278*(1–2), 41–51. https://doi.org/10.1016/S0378-1119(01)00709-0

Zeisel, A., Munoz-Manchado, A. B., Codeluppi, S., Lonnerberg, P., La Manno, G., Jureus, A., … Linnarsson, S. (2015). Cell types in the mouse cortex and hippocampus revealed by single-cell RNA-seq. *Science*, *347*(6226), 1138–1142. https://doi.org/10.1126/science.aaa1934

Zhang, J., Gong, G., Wang, X., Zhang, H., & Tian, W. (2015). Positive selection on D-lactate dehydrogenases of Lactobacillus delbrueckii subspecies bulgaricus. *IET Systems Biology*, *9*(4), 172–179. https://doi.org/10.1049/iet-syb.2014.0056

Zhang, Y., Chen, K., Sloan, S. A., Bennett, M. L., Scholze, A. R., O'Keeffe, S., … Wu, J. Q. (2014). An RNA-Sequencing Transcriptome and Splicing Database of Glia, Neurons, and Vascular Cells of the Cerebral Cortex. *Journal of Neuroscience*, *34*(36), 11929–11947. https://doi.org/10.1523/JNEUROSCI.1860-14.2014

Zhang, Y., Sloan, S. A., Clarke, L. E., Caneda, C., Plaza, C. A., Blumenthal, P. D., … Barres, B. A. (2016). Purification and Characterization of Progenitor and Mature Human Astrocytes Reveals Transcriptional and Functional Differences with Mouse. *Neuron*, *89*(1), 37–53. https://doi.org/10.1016/j.neuron.2015.11.013

Zhao, Y., Jin, J., Hu, Q., Zhou, H., Yi, J., Yu, Z., … Yang, Y. (2011). Genetically Encoded Fluorescent Sensors for Intracellular NADH Detection. *Cell Metabolism*, *14*(4), 555–566. https://doi.org/10.1016/j.cmet.2011.09.004

Zhao, Y., Xin, Y., He, Z., & Hu, W. (2018). Function of Connexins in the Interaction between Glial and Vascular Cells in the Central Nervous System and Related Neurological Diseases. *Neural Plasticity*, *2018*, 1–13. https://doi.org/10.1155/2018/6323901

Zielke, H. R., Zielke, C. L., & Baab, P. J. (2009). Direct measurement of oxidative metabolism in the living brain by microdialysis: A review. *Journal of Neurochemistry*, *109*(SUPPL. 1), 24–29. https://doi.org/10.1111/j.1471-4159.2009.05941.x

Zorec, R., Araque, A., Carmignoto, G., Haydon, P. G., Verkhratsky, A., & Parpura, V. (2012). Astroglial excitability and gliotransmission: An appraisal of Ca2+ as a signalling route. *ASN Neuro*, *4*(2), 103–119. https://doi.org/10.1042/AN20110061